UNIVERSIDADE DE LISBOA
INSTITUTO SUPERIOR TÉCNICO

Wave-current modelling at local and regional scales

Maria João Rodrigues Teles Sampaio

Supervisor: **Doctor** António Alberto Pires Silva
Co-supervisor: **Doctor** Michel Benoit

Thesis specifically prepared to obtain the PhD degree in Civil Engineering

Draft

September 2013

UNIVERSIDADE DE LISBOA
INSTITUTO SUPERIOR TÉCNICO

Wave-current modelling at local and regional scales

Maria João Rodrigues Teles Sampaio

Supervisor: **Doctor** António Alberto Pires Silva
Co-supervisor: **Doctor** Michel Benoit

Thesis specifically prepared to obtain the PhD degree in Civil Engineering

Draft

September 2013

Resumo

O principal objectivo desta tese é modelar os efeitos resultantes da interacção entre ondas e correntes às escalas local e regional, essencialmente à escala de um canal e de uma zona costeira baixa arenosa, tipo praia.

Primeiro, a modelação das ondas e correntes é feita sem separar os dois tipos de escoamento, considerando também o campo da turbulência. Para tal, foi usado um modelo CFD, o *Code_Saturne* (Archambeau et al., 2004). Algumas adaptações tiveram de ser realizadas, de modo a tornar o código mais adequado para modelar este tipo de escoamentos. Os resultados numéricos foram comparados com medições realizadas por Klopman (1994) e Umeyama (2005) em canais de ondas com capacidade de sobrepôr correntes.

De seguida, o objectivo focou-se na caracterização dos mesmos efeitos da interacção mas à escala regional (em águas costeiras). Neste caso é feita a separação entre as contribuições das ondas e das correntes. Para este fim, foi desenvolvido um novo sistema acoplado entre o modelo hidrodinâmico tridimensional, o TELEMAC-3D (Hervouet, 2007) e o modelo de ondas espectral, TOMAWAC (Benoit et al., 1996). Os resultados numéricos foram comparados com dados laboratoriais obtidos numa bacia de ondas, onde num caso estava reproduzida uma praia plana (Hamilton and Ebersole, 2001) e, noutro caso, uma praia com um sistema de barras (Haller et al. (2002), Haas and Svendsen (2002)).

Na primeira parte do trabalho, o CFD mostrou capacidade na modelação das alterações do perfil vertical da velocidade horizontal média e tensões de Reynolds quando um campo de ondas é sobreposto, no mesmo sentido ou em sentido oposto à corrente. Na segunda parte do trabalho, o novo sistema acoplado desenvolvido mostrou dar bons resultados na modelação de correntes geradas por ondas e nos respectivos efeitos de interacção.

Palavras chave: Interacções entre ondas e correntes, Modelação CFD, Modelação da turbulência, *Code_Saturne*, Acoplamento 3D, glm2z-RANS, TELEMAC-3D, TOMAWAC, Correntes induzidas pelas ondas, Zona litoral

Abstract

The main purpose of this thesis is to model the effects of wave and current interactions at local and regional scales.

In the first part of the research, the waves and currents were modelled simultaneously including turbulence effects. An advanced CFD model, the *Code_Saturne* software (Archambeau et al., 2004) was used. Some adaptations had to be made in order to render the code suitable to model this kind of flow. The numerical results are compared with data obtained on wave flumes by Klopman (1994) and Umeyama (2005).

In the second part of the thesis the purpose was to characterize this combined environment in coastal waters. Therefore, instead of solving the total motion simultaneously, a separation was made between the waves and current parts. A new coupled system between a three-dimensional hydrodynamic model, TELEMAC-3D (Hervouet, 2007) and a spectral wave model, TOMAWAC (Benoit et al., 1996) was developed. The numerical results are compared with data obtained on a plane beach (Hamilton and Ebersole, 2001) and on a barred beach (Haller et al. (2002), Haas and Svendsen (2002)).

In the first task, the CFD model showed to be capable of well reproducing the changes in the vertical profiles of mean horizontal velocity and shear stress, when waves are superimposed on a turbulent current, either following or opposing the current. Then, in the second task the development of the coupled system was shown to give good results in wave-induced currents modelling and interaction effects.

Key words: Wave-current interactions, *Code_Saturne*, CFD modelling, Turbulence modelling, 3D coupling system, glm2z-RANS, TELEMAC-3D, TOMAWAC, Wave-induced currents, Coastal zone

Acknowledgments

My first acknowledgment goes to my supervisors, António Pires Silva and Michel Benoit. It was decisive in this thesis having your scientific guidance. Moreover, I would like to thank you for all the encouragement and support that you gave me throughout these years.

Furthermore I would like to thank all my co-workers, either during my stay in Paris or in Lisbon.

For the first year in Paris, I would like to thank all the group of Laboratoire de Saint-Venant which have received me so nicely and warmly. Amélie, Élodie , Cédric, Antoine, Andrés, Christophe, thanks for all the talks, good sense of humour, and coffee breaks that inspired me and helped me to feel welcomed in your group.

Durante todo este percurso, tenho uma quantidade inimaginável de pessoas a quem gostaria de agradecer. Entre eles, aos meus colegas do Técnico, agradeço ao Edgar que acompanhou esta jornada desde o seu início, pela boa disposição e apoio que me deu durante estes anos. À Ana Margarida, que passado um ano chegou da Suiça com um sorriso sempre presente, tenho muito a agradecer pela amizade e companhia! À Mariana, que tendo chegado na etapa final, foi a vítima dos meus desesperos, tenho a dizer um grande obrigado por tudo e pela nova amizade que me proporcionou! Ao Artur, Nelson, Nuno, Andrea, Ricardo pelas pausas de café que tanto bem me souberam.

Fora do Técnico, toda a companhia, apoio e paciência de todos os meus amigos e amigas foram essenciais para partilhar os bons e superar os maus momentos destes últimos anos. Entre eles, um especial agradecimento à minha prima Rita, Inês, Joaninha, JT, Johnny, Anita, Filipinha, Joana C., Mary, Raquelinha, Rita, JP, Guillaume, Olivier, Luisa e Mário.

Ao Victor um grande obrigado por toda a paciência, ajuda, apoio, companhia e optimismo essenciais para conseguir atingir todos os meus objectivos.

Por fim, e não menos importante, quero agradecer os encorajamentos imprescindiveis e todo o apoio incondicional, do meu pai, mãe e irmão a quem eu dedico esta tese.

Contents

List of Figures

List of Tables

List of Symbols

Notation	SI units	Definition
a	m	Wave amplitude
B		Depth-induced breaking coefficient
B_l	m	Channel width
$C = \frac{\sigma}{k}$	ms^{-1}	Phase velocity
C_g	ms^{-1}	Wave group velocity
C_{g0}	ms^{-1}	Wave group velocity in deep waters
C_h		Chézy coefficient
C_f		Friction coefficient
C_{fwc}		Friction coefficient with effects of waves and currents included
C_{ij}		Surface of interface (i, j) common to cells i and j
D_h	m	Hydraulic diameter
$D = h + \overline{\eta}$	m	Total mean water depth
$\overline{D}^L$		Generalized Lagrangian mean material derivative
E	Jm^{-2}	Wave energy per unit area
$f_r = \frac{\sigma}{2\pi}$	Hz	Relative or intrinsic wave frequency
$f_c = (f_1, f_2, f_3)$	ms^{-2}	Coriolis force
$F_{cs}, F_{ss}, F_{cc}, F_{sc}$		Vertical profile functions
F_x, F_y	ms^{-2}	Buoyancy source terms per unit mass
$F(\theta, f_r)$	$m^2Hz^{-1}rad^{-1}$	Variance density directional spectrum
F_i	ms^{-2}	Body forces that act on the mean flow per unit mass
g_i	ms^{-2}	Gravity acceleration vector
G	$kgm^{-1}s^{-3}$	Turbulence buoyancy term for kinetic energy

G_ϵ		Turbulence buoyancy term for dissipation
h	m	Still water depth
H	m	Wave height
H_s	m	Significant wave height
H_m	m	Maximum wave height compatible with the water depth
H_{mean}	m	Mean wave height
h_0	m	Offshore still water depth
Id		Identity matrix
J	m^2s^{-2}	Wave-induced pressure per unit mass
J_a		Jacobian of the mapping $(\mathbf{x},t) \rightarrow (\mathbf{x}+\boldsymbol{\xi}(\mathbf{x},t),t)$
$k = \frac{1}{2}\overline{u_i'u_i'}$	m^2s^{-2}	Kinetic turbulence energy per unit mass
$k = \frac{2\pi}{L}$	m^{-1}	Wave number
K_S		Shoaling coefficient
k_s	m	Nikuradse roughness
l_t	m	Turbulence length scale
l_m	m	Mixing length scale
L	m	Wave length
M^w	$kgm^{-1}s^{-1}$	Depth-integrated wave pseudomomentum
M^{tot}	$kgm^{-1}s^{-1}$	Depth-integrated total momentum
M^m	$kgm^{-1}s^{-1}$	Depth-integrated mean momentum
$\dot{m}_{fs}$	$kgs^{-1}m^{-2}$	Mass flux when the free surface is represented in a fixed mesh
$N = F(\theta, f_r)/\sigma$	kgs^{-1}	Wave action
$Neighbrs(i)$		Set of cells j sharing at least an interface (i,j) with cell i
p	$kgm^{-1}s^{-2}$	Pressure
p_a	$kgm^{-1}s^{-2}$	Atmospheric pressure
$P = 2\mu_t S_{ij}S_{ij}$	$kgm^{-1}s^{-3}$	Turbulence production term
P	$kgm^{-2}s^{-1}$	Wave pseudomomentum
Q	Jm^{-2}	Source and sink terms in the wave action balance equation
Q_b		Fraction of breaking waves
$R_{ij} = \overline{u_i'u_j'}$	m^2s^{-2}	Reynolds stress tensor per unit mass
R_{xx}, R_{yy}, R_{zz}	m^2s^{-2}	Reynolds normal stresses per unit mass
R_{xz}	m^2s^{-2}	Reynolds shear stress per unit mass

S_f		Unit free surface vector
$S_{ij} = \frac{1}{2}\left(\frac{\partial u_i}{\partial x_j} + \frac{\partial u_j}{\partial x_i}\right)$	Hz	Strain rate tensor
S_{ij}	kgs^{-2}	Radiation stress
S_x, S_y	ms^{-2}	Horizontal momentum source terms in the hydrodynamic model per unit mass
t	s	Time
T	s	Wave period
(u,v,w)	ms^{-1}	Velocity vector components
$\hat{u}$	ms^{-1}	Quasi-Eulerian velocity
$\tilde{u}_\alpha$	ms^{-1}	Wave-induced horizontal velocity
u'	ms^{-1}	Velocity fluctuating part
u_*	ms^{-1}	Friction velocity
u_1	ms^{-1}	Near surface cross-shore velocity
u_m^{n+1}	ms^{-1}	Velocity at time instant t^{n+1} calculated in the known mesh at time instant t^n
(U,V)	ms^{-1}	Mean horizontal velocity components
U_s, V_s, W_s	ms^{-1}	Stokes drift components
U_r		Ursell number
v_{max}	ms^{-1}	Maximum longshore velocity
w_m	ms^{-1}	Mesh velocity
x_0	m	Initial position
x_{br}	m	Location where waves start to break
$\hat{X}_i$	$kgm^{-1}s^{-1}$	Diabatic source of momentum
z_0	m	Physical roughness related parameter
z_a	m	Apparent roughness
z^+		Dimensionless z-coordinate
δ	m	Viscous sublayer thickness
δ_{ij}		Kronecker delta
ε	m^2s^{-3}	Turbulence kinetic energy dissipation
ϵ		Wave slope
$\epsilon_{ijk}A_jB_k$		Component i of the vector product $A \times B$
γ_b		Adjacent boundary cells
γ		Depth-induced breaking coefficient
γ_e		Peak enhancement factor
η	m	Free surface elevation
φ	rad	Wave phase
Φ	kgs^{-3}	Pressure-velocity correlation tensor

μ	$kgm^{-1}s^{-1}$	Dynamic molecular viscosity
μ_t	$kgm^{-1}s^{-1}$	Dynamic turbulence viscosity
ν	m^2s^{-1}	Kinematic molecular viscosity
ν_t	m^2s^{-1}	Kinematic turbulence viscosity
ν_{wbz}	m^2s^{-1}	Wave-enhanced vertical diffusion coefficient
ν_H	m^2s^{-1}	Horizontal diffusion velocity coefficient
ν_z	m^2s^{-1}	Vertical diffusion velocity coefficient
ρ	kgm^{-3}	Mass per unit volume
$\Delta\rho$	kgm^{-3}	Mass per unit volume variation
$\sigma = \sqrt{gktanh(kD)}$	$rads^{-1}$	Relative angular frequency
σ_r	$kgm^{-1}s^{-2}$	Stress tensor
θ	$degrees$	Wave direction
θ_m	$degrees$	Mean wave direction
τ	$kgm^{-1}s^{-2}$	Viscous stress tensor
τ_{wind}	$kgm^{-1}s^{-2}$	Wind stress
τ_{watm}	$kgm^{-1}s^{-2}$	Stress induced by atmosphere transferred to the ocean
τ_{wbr}	$kgm^{-1}s^{-2}$	Stress induced by dissipation of depth-induced breaking waves
τ_{bot}	$kgm^{-1}s^{-2}$	Bottom friction induced stress in the hydrodynamic model
τ_{wbot}	$kgm^{-1}s^{-2}$	Stress induced by waves dissipation by bottom friction
$\xi = (\xi_1, \xi_2, \xi_3)$	m	Wave-induced displacement
$\Xi = x + \xi$	m	Disturbed position
$\omega = \sigma + \vec{k}\vec{U}$	$rads^{-1}$	Absolute angular wave frequency
$\omega \approx \frac{\epsilon}{k}$	s^{-1}	Specific turbulence dissipation
κ		von Karman constant
Ω_i		Cell i
$\|\Omega_i\|$		Volume of cell i
ζ	m	Free surface cell vertex displacement

Chapter 1

Introduction

1.1 Motivation

The World's population has always had the tendency to be concentrated close to the sea shore, and this trend is still strong in the present day. In Europe, for instance, 40% of the population live in coastal areas (EUROSTAT). In Portugal, in particular, it can be seen that there is clear distinction of the population density between inland and coastal zones (Figure 1.1).

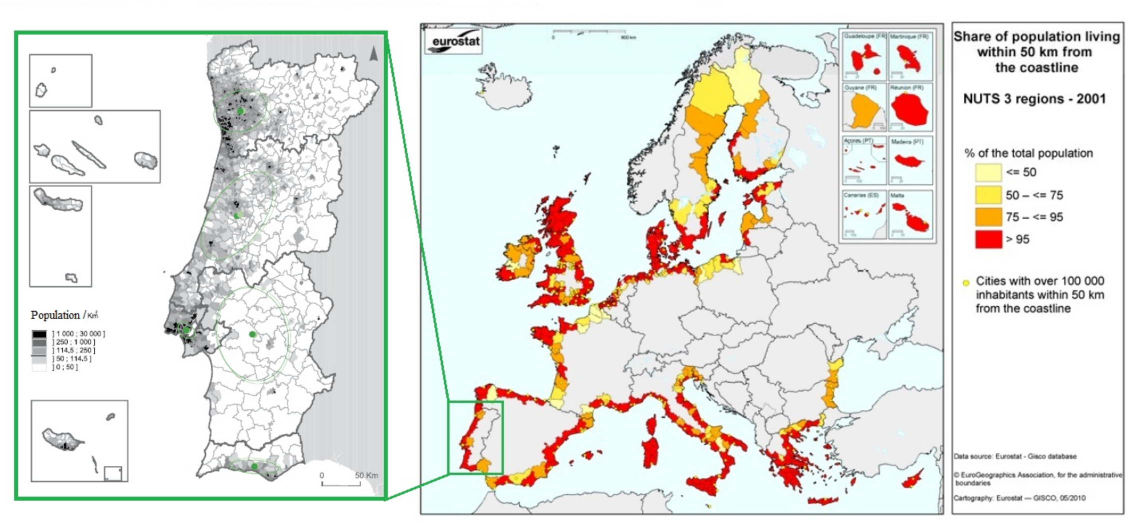

Figure 1.1: Population density in Portugal (on the left) and percentage of population living within 50 *km* of the coastline (on the right). Sources: INE and EUROSTAT.

This high concentration of population brings environmental, social and economic issues to coastal zones that cannot be ignored. In order to obtain a safe and sustainable area, different human intervention is needed and made. For instance, the construction of ports or structures for commercial reasons or to simply protect the coast line, such as the case of breakwaters.

The Gross Domestic Product (GDP) in Europe has a contribution of 40% from the littoral zones with 75% of Europe′s foreign trade done by sea. Together with the increase of tourists in coastal zones, where three fifths of the total bed places in hotels are located in the coastal region (EUROSTAT), a high amount of employment, related to maritime industries, is generated.

From the point of view of tourism, several procedures are made, namely the creation of artificial reefs to get better surf conditions, or the depositing sand on the beaches. Nevertheless, a number of problems can occur or it can become too expensive when for example the beaches are restored.

Additionally, nowadays, there has been constant interest of finding alternatives to fossil resources. The exploitation of wind, solar, fluvial or maritime energy is a possible solution. Once again another potential is found in the maritime region.

The population concentration in the coastal zone inevitably also brings an increase in pollution in this area. Furthermore, disasters such as unfortunate wrecks and consequently, in some cases, oil spill are a concern that one has to be aware of.

Even if there is no human activity, there is constant interaction between the ocean and the coastal zone. This interaction is dynamic and can induce several changes in the littoral domain. Incident waves on the beach can induce strong currents that can have a marked impact on the littoral morphodynamics. Storm surges can, for instance, destroy several structures and even be fatal. Moreover, climate change contributes to a mean sea level raise that one has to bear in mind, since it interacts with infrastructure located within the coastal zone.

There are, therefore, a number of issues to be concerned with and, consequently, constant and increasing efforts are being made in order to achieve a good management of the coastal domain. The problem is that this is not a simple task, since several factors have to be taken into account.

Due to the issues encountered to achieve good management, great interest has been placed by the scientific and engineering community on understanding the different phenomena that co-exist in the littoral zones, in order to contribute to sustainable development in these areas.

The problem is that the coastal domain is a complex system where several phenomena with different time and spatial scales interact. From offshore to the coast, processes like tides, wind, currents, waves and turbulence are characterized by distinct time-scales. Therefore describing the interaction among these different scales is difficult to achieve.

Among the different processes, it is crucial to take into account the surface waves and the currents to get a good description of the littoral domain. These two processes induce several changes in the morphodynamics and hydrodynamics of coastal waters. For instance, breaking waves in the coastal zone can generate currents. Depending on the bottom morphology or the incident waves field, the induced currents have different characteristics. If obliquely incident waves break on a plane beach, a longshore current is generated. If the beach has for example, sand bars or cusps, rip currents can be generated. These currents have great impact on sediment transport directed alongshore or offshore. Furthermore, this wave-current environment can become dangerous for humans, since swimmers can be dragged offshore by the currents or into hazardous areas.

The propagation of wind-generated waves with varying spatial and time currents is a special case of an inhomogeneous and unsteady environment. In coastal waters, these features are enhanced by bathymetry with variable depths, triggering a number of modifications in the wave field like refraction and breaking. Furthermore, ambient currents (either general circulation currents, tidal currents, discharge currents or wave-induced currents) may have an effect on wave propagation. They modify the wave number of the waves and frequency (the so-called Doppler effect) and lead to refraction in the case of heterogeneous flow fields. Additionally, they have an influence on the bottom and surface stresses in combined wave-flow conditions. On the other, the wave-induced mass transport and gradients of the excess momentum flux force the mean flow, originating the build up of pressure gradients and changes in the mean water level and driving currents, like the Stokes drift. In particular, in the surf zone there are intense transfers from the organized wave motion to the mean flow. Therefore, it is essential to assess and study the interaction between waves and currents.

For that purpose, there are two options: either through observations/measurements in the field or in laboratory facilities, or by modelling the different phenomena. Although the first option is extremely useful, it can sometimes become too expensive. The instrumentation, support, maintenance, and human resources bring several costs to a measurement campaign.

Therefore, numerical modelling appears as a possible solution to get the description of the different processes. Several scenarios and set-ups can be tested to get the optimal solution. Moreover, predictions for the littoral domain in the short and long term can be achieved. Consequently it is crucial to have access to a numerical platform that computes and characterizes the different phenomena and interaction between them. Nevertheless, several difficulties are also encountered in the prediction and modelling and consequent management of the coastal domain due to the complexity in the co-existing environment already mentioned above. Attention has to be put on the way that these phenomena are described in the numerical codes to better understand the output results.

From a modelling perspective there are mainly two possible approaches to address wave-current interaction. The first one relies on solving a single set of (primitive) equations that describe the resulting total motion while the second approach is based on a partitioning of the total motion into wave motion and mean flow motion.

Within the second approach, for many years, in order to get the description of the waves and current co-existing environment, the theories based on the work developed by Longuet-Higgins (1953), Longuet-Higgins and Stewart (1962, 1964) were largely used. This was possible within a two-dimensional (2D) approach. The concept of radiation stress (Longuet-Higgins (1953), Longuet-Higgins and Stewart (1962, 1964)) reported important contributions for understanding and predicting, for instance, the wave set-up and wave-breaking induced currents.

Nevertheless over the past decade a great effort has been made to get a three-dimensional (3D) description of the current field when waves are superimposed. Through different measurements (Kemp and Simons (1982, 1983), Klopman (1994, 1997), Umeyama (2005)) it was confirmed that the vertical profile of the mean flow throughout the water depth as well as shear stresses undergo several changes when waves are present.

A number of numerical studies (McWilliams et al. (2004), Newberger and Allen (2007a)) were carried out, from a Eulerian point of view. Nevertheless, a problem arises when the region between the crest and trough has to be taken into account. Sometimes there is water, and other times simply air.

Ardhuin et al. (2008b) took the set of GLM (Generalized Lagrangian Mean) equations derived from Andrews and McIntyre (1978a) and deduced a new set applied to water wave problems - the glm2z-RANS equations. The GLM approach combines Lagrangian information with a field coordinates framework. Using this approach, the problem in the region between air and water is solved.

1.2 Aims and Scope

The work carried out in the thesis is focused on wave-current interaction in nearshore areas. That means that both effects of waves on currents and effects of currents on waves considering turbulence effects are assessed. This will be important for marine renewable energy extraction, especially to optimize tidal current energy devices, harbour layout design, lagoon inlet stabilization and morphodynamics in coastal areas. As the vertical profile of the mean velocity field is essential for the good prediction of the wave-current environment effects, a 3D approach is followed.

When a single set of equations is solved to describe the total motion, sophisticated 3D free surface models are required. They can be applied at a very fine scale and the appropriate turbulence models have to be chosen.

For the proper application of a CFD model, a number of questions are raised:

- what are the proper boundary conditions, particularly on the free surface?
- which is the most adequate turbulence closure model to simulate this combined flow?
- how is the vertical profile of the mean flow and shear stress changed in the presence of the waves?
- what are the main contributions that cause those modifications?

In the first part of this thesis, these aspects are addressed with a RANS type (Reynolds-Averaged Navier-Stokes) numerical model on a local scale basis. The work was done by using an existing model, *Code_Saturne* (Archambeau et al., 2004). Some adaptations had to be made in order to make the code suitable to model these free surface flows and particularly the wave-current environment. The aim is to study the exchanges and fluxes of momentum, energy and mass between the mean flow and the waves. The influence of various schemes for modelling turbulence effect is studied and tested. Here, non-breaking waves are focused. Therefore, no effects induced by waves breaking are taken into account.

The main purpose of this first part is the modelling of the deformation of the vertical profile of a mean flow in the presence of following or opposing waves. The numerical results obtained with *Code_Saturne* are compared with data measured by Klopman (1994) and Umeyama (2005), which, among others, performed experiments addressing these interactions.

In the end, the output of this part is an improved RANS model for the simulation of combined flow dynamics under the effect of mean flow and non-linear waves.

The above-mentioned modelling approach can be used for academic and local scale applications in order to improve the understanding of physical processes, but it can not be applied for real application at regional scale, at least at the moment, due to the high computational cost.

The alternative, is to separate the total motion into wave motion and mean flow motion and each component being solved by a separate model, applied with appropriate space and time resolutions. For that purpose, both models need to be coupled to simulate the interaction effects. Using this approach, existing models for wave and hydrodynamic modelling at regional scales can be employed.

The second main purpose of this research is to improve the coupling of these models.

In the second part of the thesis a number of questions are raised:

- which is the most appropriate theoretical framework to work with the combined environment?
- what are the main advantages of taking into account the 3D effects?
- in which zones are those 3D effects more important?
- how can we/one quantify and describe the existing exchanges of energy between waves and currents?
- what are the dominant effects to be considered and modelled in this coupling?

In this step, attention was paid to the determination of the proper way to couple the models.

A critical review of theoretical approaches to decompose the total flow into two components and the resulting set of equations was made. After an extensive literature review, it was decided to work with the recent formulation proposed by Ardhuin et al. (2008b), the glm2z-RANS approach. Other codes based on the same theoretical framework of Ardhuin et al. (2008b) were developed and validated against real applications (Michaud et al. (2012), Delpey (2012)).

Here, the main purpose was to develop a new numerical platform to model the waves and currents environment. The models used in this research are integrated in the TELEMAC-MASCARET hydroinformatics system developed at the Research and Development Department of Electricité de France (EDF). They are TELEMAC-3D (Hervouet, 2007) (for real 3D flows, based on the Navier-Stokes equations) and TOMAWAC for the spectral wave modelling (Benoit et al., 1996).

The study domain was mainly focused on the littoral and surf zones. This region is essential to study for a number of reasons, one of them clearly being the interface that it represents between the mainland and the ocean.

In conclusion, the specific and main objectives of this research work are:

- to perform a comprehensive review of wave-current modelling at a local and refined scale, specially RANS type (Reynolds-Averaged Navier-Stokes) models and GLM (Generalized Lagrangian Mean) formulations;
- to model waves and currents simultaneously including turbulence effects;
- to access the influence on the choice of the turbulence closure model to simulate this kind of combined flows;
- to improve the knowledge of the vertical distribution of the mean velocity field and shear stresses in the presence of waves;
- to get a better representation of these subscale phenomena for possible coastal and harbour applications;
- to implement a new two-way coupled model in a nearshore scale;
- to assess the influence of the different parametrizations included in the wave and hydrodynamic models;
- to make a contribution to characterize hydrodynamics in coastal waters.

1.3 Outline of the thesis

The thesis is divided into two distinct parts.

In the first part of the research (**Part I**), the changes on the vertical profile of the mean horizontal velocity, mean horizontal velocity amplitude and shear stresses are studied on a local scale. Here, a numerical flume is used and a Computational Fluid Dynamics (CFD) model is tested to simulate the combined wave-current environment. The study is focused on non-breaking waves propagating over a turbulent current.

After this introductory section, in **Chapter 2**, the description of the used CFD code is made, namely *Code_Saturne* (Archambeau et al., 2004). Since turbulence effects are to be taken into account, a brief description of the existing turbulence closure models in *Code_Saturne* is given. Then the model set-up to simulate wave-current interaction is described, particularly for application in a numerical flume.

On **Chapter 3**, the combined environment of wave-current interaction is modelled on a local scale with *Code_Saturne* and numerical results are compared with laboratory data obtained by Klopman (1994) and Umeyama (2005). The vertical profiles of horizontal mean velocities, horizontal amplitude velocity profiles and shear stresses are analysed. The changes of the vertical profiles when waves are superimposed in the turbulent current, either in the opposing or in the same direction are studied. Furthermore, sensitivity tests regarding the turbulence closure model that best suits this kind of modelling are assessed.

In the second part of the research (**Part II**), the main objective is to develop a new numerical platform, where the spectral wave model TOMAWAC (Benoit et al., 1996) is coupled with the hydrodynamics model TELEMAC-3D (Hervouet, 2007). To achieve this purpose, the recent equations proposed by Ardhuin et al. (2008b) together with the simplifications made by Bennis and Ardhuin (2011) were implemented in the hydrodynamic model. Furthermore, parametrizations from the waves non-conservative forces were included in the coupling system.

In **Chapter 4**, a review of the existing wave-mean interaction theories is made. These are, essentially, parametrizations schemes to provide approximations to the effects of the waves upon the larger scales, as Bühler and McIntyre (1998) put it. First the 2D approach is assessed with the description of the associated theories. Then, a brief overview of the 3D theories is made together with a more detailed description of the GLM equations Andrews and McIntyre (1978a) and the theoretical framework approach from Ardhuin et al. (2008b).

In **Chapter 5**, the models used to develop the full coupling system are described, the hydrodynamics model TELEMAC-3D (Hervouet, 2007) and the spectral wave model TOMAWAC (Benoit et al., 1996). Then the implementation of the new equations is presented together with the different choices for the parametrization of the different phenomena of the wave action on the mean flow. The chapter is finalized with an adiabatic test proposed in Bennis and Ardhuin (2011), from which was possible to make a first validation of the coupled system.

In **Chapter 6** two realistic test cases are made in order to verify and validate the coupled system. First, the numerical results are compared with measurements obtained on a plane beach from the Laboratory Facility of Sediment Transport (LSTF) (Hamilton and Ebersole, 2001). Then, with data obtained from a barred beach on the wave basin installed at Delaware University (Haller et al. (2002) and Haas and Svendsen (2002)), it was possible to test the model capability to reproduce a rip current system together with the modelling of the vertical profiles of the rip current.

Finally, in **Chapter 7**, the final and general conclusions taken from this research work are outlined and some perspectives are made.

Part I

Local scale

Chapter 2

Computational Fluid Dynamics modelling in a combined wave-current environment

2.1 General context

The combined effects of waves and currents on free surface flows has been the subject of many studies due to its impact on coastal hydrodynamics. In this environment, horizontal and vertical velocities, as well as shear stresses, depend greatly on this interaction. The vertical profiles of these variables are modified and these are major issues in nearshore wave and current modelling.

In recent decades, many efforts have been made to improve the description of the interactions between the waves and the current. These studies are based on either purely analytical approaches with simple models of the wave boundary layer (in particular, relying on the concept of an eddy viscosity), or numerical simulations to accommodate more sophisticated models of the primitive equations.

The work of Grant and Madsen (1979) follows the first approach, stating that the influence of waves on steady currents above the wave boundary layer can be parametrized by an apparent increase in the roughness experienced by the current. Additional examples of simplified wave boundary models include: Christoffersen and Jonsson (1985) with an eddy-viscosity approach (also a wealth of references on previous studies, particularly on purely oscillatory boundary layers), You (1996) with a parabolic distribution of the turbulence viscosity, Nielsen and You (1996), who explicitly take into account the wave-induced Reynolds stresses, Huang and Mei (2003) who formulate a boundary-layer theory, and Yang et al. (2006) with a simplified mixing-length hypothesis.

Numerical approaches range from the inclusion of the Craik-Leibovich vortex force in the mean-current equations (Dingemans et al., 1996), to the Generalized Lagrangian Mean approach (GLM) (Groeneweg and Klopman (1998), Groeneweg and Battjes (2003)), or to a three-dimensional Navier-Stokes equation model (e.g. Olabarrieta et al., 2010).

In this combined environment there are important exchanges and fluxes of momentum, energy and mass between the mean flow and the wave component. For instance, when waves are superimposed on a turbulent current, either in the same or opposite direction, the vertical mean velocity profile undergoes several important modifications.

It is desired not only the to know the changes that occur on the mean flow when waves propagate over it, but also the effects of turbulence on this combined flow. Therefore choosing the appropriate turbulence modelling is essential.

The increase in computing capacity and the expansion of Computational Fluid Dynamics (CFD) software as a simulation tool has led to the possibility of solving complex and varied fluid flow problems, including the simulation of three-dimensional time-varying flows. One advantage of using a RANS-based model is that the number of underlying hypotheses is quite low. Additionally, not only the non-linear flow characteristics are obtained, as turbulence is also considered. Therefore, the CFD models give the ideal framework to perform this kind of numerical modelling.

In the present work, one of the main purposes is to model wave-current interaction and study its three-dimensional effects at a local and refined scale. This is essential to better know and understand the different phenomena that occur when waves interact with currents. Thus, one of the purposes is to verify the capability of a RANS-type model to model the combined wave-current environment in a numerical flume. Numerical flumes show a great advantage to study wave transformation and associated physical properties within different time scales.

To accomplish the wave-current interaction modelling, a sophisticated free surface 3D model was needed and used to solve a single set of equations that describe the resulting total motion.

The *Code_Saturne* software (Archambeau et al., 2004) was the chosen CFD model to pursue this study. A number of reasons led to the choice of this model. Firstly, *Code_Saturne* is based on RANS equations and applies a co-located finite volume approach to solve them. It is a free, open source software, giving the possibility of interacting and changing the code concerning the user necessities. Furthermore it has a large range of turbulence models. For the free surface representation the Arbitrary Lagrangian Eulerian

(ALE) methodology (Archambeau et al., 1999), incorporated in the code, can also be used.

Therefore, *Code_Saturne* (version 2.0.2) was applied in a numerical channel to model free surface flows, where waves are superimposed on a turbulent current. A number of adaptations had to be made to render the model suitable for studying wave and current interactions considering turbulence effects in free surface flows.

In a CFD model, the overall procedure is based on three main stages. First, in the pre-processing step, the geometry of the problem has to be defined. A mesh must be created, and the volume occupied by the fluid discretized in several cells. After the mesh generation, the physical properties of the flow and the boundary conditions are defined. At a second stage, the Navier-Stokes equations, which are the mathematical background of CFD models are solved iteratively. Finally, at a post-processing stage, the model results are treated and analysed by the user.

Bearing in mind the overall procedure to use a CFD model, the present chapter is organized in order to give a general framework to a user that wants to apply a CFD model, specifically, for the modelling of a combined wave-current environment on a numerical flume.

Therefore, after the above introduction, the *Code_Saturne* model is presented (section 2.2). A brief overview of turbulence RANS-based models is then made in section 2.3. In section 2.4 the model set-up applied to study the combined wave-current flow in a numerical flume is described.

2.2 *Code_Saturne* model

2.2.1 Governing equations

The *Code_Saturne* model (Archambeau et al., 2004) is a CFD code that solves the Navier-Stokes equations for laminar and turbulent flows in two and three-dimensional domains. It is based on a finite volume approach that works within structured or unstructured meshes. To handle with moving meshes, it has a module implemented with the Arbitrary Lagrangian Eulerian methodology.

Due to the main features and degree of sophistication of the *Code_Saturne* model, this software was chosen to carry out this study. In the section below a general description of the mathematical and numerical backgrounds included in *Code_Saturne* is made. For more details please refer to *Code_Saturne* documentation (2013).

The numerical model is divided into the *Kernel*, which solves the Navier-Stokes and turbulence equations, and the *shell*, which deals with the mesh and post processing. The mass (2.1) and momentum (2.2) equations are written in a conservative form and then integrated over control volumes with a co-located method (all variables are considered at the cell centre). For incompressible flows and considering turbulence effects, they read:

$$\nabla.(\mathbf{u}) = 0 \tag{2.1}$$

$$\rho\frac{\partial \mathbf{u}}{\partial t} + \nabla.(\rho\mathbf{u}\otimes\mathbf{u}) = \nabla.(\sigma_r) + \rho\mathbf{g} \tag{2.2}$$

$\mathbf{u}$ denotes the three components of the fluid velocity, ρ is the fluid density and σ_r represents the stress tensor and includes the effects of pressure (p) and the viscous stress tensor (τ). σ_r is a symmetric tensor and for a Newtonian fluid it is expressed by the relation $\sigma_r = \tau - pId$ with $\tau = 2\mu S - \frac{2}{3}\mu tr(S)Id$. μ is the dynamic molecular viscosity and $S = \frac{1}{2}(\nabla\mathbf{u} +^t \nabla\mathbf{u})$ the strain rate tensor. Here the body forces that act on the fluid element are considered to be consisted only by the gravity acceleration $\mathbf{g}$.

2.2.2 Time and space discretization

The Navier-Stokes equations are discretized in space and time for each time-step using the finite volume method and the pressure-velocity coupling through a predictor-corrector scheme.

The time discretization used to solve the incompressible mass and momentum equations is made using a fractional-step scheme (predictor-corrector scheme), similar to the SIMPLEC (Semi IMPlicit Linked Equations) algorithm. The time scheme can be chosen between a first order implicit Euler scheme or a second order implicit Cranck Nicolson scheme.

In the following, the source terms, including the viscous terms that depend on ${}^t\nabla\mathbf{u}$, are grouped together into a term S_u, which is written as $S_u = \mathbf{A} + B.u$. It is considered the time step n, going from $t = t^n$ to $t = t^{n+1}$. The time step value, defined by the user, is given by $\Delta t = t^{n+1} - t^n$.

At a first stage, the predictor step, the velocity components are predicted by solving equation (2.2) with an explicit pressure gradient. With an Euler implicit scheme, it solves for the time step t^n the following:

$$
\begin{cases} \frac{(\rho\mathbf{u})^{n+1/2}-(\rho\mathbf{u})^{n}}{\Delta t} + \nabla.\left(\mathbf{u}^{n+1/2}\otimes(\rho\mathbf{u})^{n} - \mu\nabla\mathbf{u}^{n+1/2}\right) = -\nabla p^{n} + \mathbf{A}^{n} + B^{n}.\mathbf{u}^{n+1/2} \\ p^{n+1/2} = p^{n} \end{cases} \tag{2.3}
$$

At a second stage (corrector step) the predicted velocity is corrected by taking into account the pressure variation in (2.2). The variation of convection and diffusion terms are neglected at this stage. The pressure p^n is updated by adding an increment Δp^{n+1} such that $\Delta p^{n+1} = p^{n+1} - p^n$. The mass conservation is enforced by taking it into account.

$$
\begin{cases} \frac{(\rho\mathbf{u})^{n+1}-(\rho\mathbf{u})^{n+1/2}}{\Delta t} = -\nabla(p^{n+1} - p^{n}) \\ \nabla.(\rho\mathbf{u})^{n+1} = 0 \end{cases} \tag{2.4}
$$

In order to get the pressure variation, the divergence is taken from the first equation of (2.4) and the second equation is used to eliminate $\rho\mathbf{u}^{n+1}$:

$$
\nabla.\left[\Delta t\nabla\left(p^{n+1} - p^{n}\right)\right] = \nabla.(\rho\mathbf{u})^{n+1/2} \tag{2.5}
$$

If turbulence closure models (which will be referred in sub-section 2.3) are used, the turbulence variables are solved after the second stage (the corrector step). For the $k-\varepsilon$ model, an additional step is needed to couple the source terms. The k and ε equations are solved at the same time to take into account the equilibrium between the two variables. In Reynolds Stress Models (RSM), the turbulence stresses and dissipation are solved sequentially without coupling. For the numerical discretization regarding the turbulence terms please refer to *Code_Saturne* documentation (2013).

Finally, once the variable values are known for the time step t^{n+1}, the algorithm can carry on for the next time step.

Following the finite volume method, the momentum equation is discretized in space by partitioning the domain, Ω, in control volumes, Ω_i. The integration of the equations is made on each cell of the mesh. The finite volume approach is used with a co-located arrangement of all variables. It is applied to the set of equations obtained through the discretization in time presented above.

In Figure 2.1 it is possible to identify the geometric entities used in the numerical model. F_{ij} is the centre of face (i,j). I and J are the mass centres of cells i and j, respectively. The point O_{ij} is the intersection of face (i,j) and the line (IJ). By projecting I and J orthogonally on the line normal to face (i,j), the points I' and J' are obtained. $Neigh(i)$

are the neighbouring cells of cell i, which share at least an interface (i, j) with it.

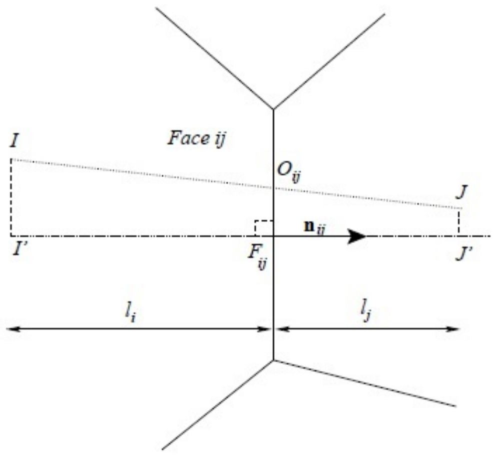

Figure 2.1: Representation of the geometric features for face (i, j). Source: Archambeau et al. (2004).

b_i^n represents the mean value of a continuous variable $b(\mathbf{x},t)$, calculated over cell i at time $t = t^n$:

$$b_i^n = \frac{1}{|\Omega_i|} \int_{\Omega_i} b(\mathbf{x}, t^n) d\Omega \tag{2.6}$$

$b_{i'}^n$ is the approximate value of $b(\mathbf{x},t)$ at point I' and time $t = t^n$. If the discrete gradient of the variable b is known at cell i, $b_{i'}^n$ is obtained, using a first order approximation:

$$b_{i'}^n = b_i^n + \mathbf{II}'.(\nabla b)_i \tag{2.7}$$

Assuming that ∇b is continuous, the operator G gives the discrete gradient of b at cell i:

$$G_i(b) = (\nabla b)_i \tag{2.8}$$

The normal gradient at face (i, j) is given by $\mathtt{G}_{n,ij}$:

$$\mathtt{G}_{\mathbf{n},ij}(b) = \frac{b_{j'} - b_{i'}}{\mathbf{IJ}.\mathbf{n}_{ij}} \tag{2.9}$$

The momentum equation is integrated over cell i, and through the Gauss theorem, it is transformed into:

$$\frac{|\Omega_i|}{\Delta t}\left((\rho\mathbf{u})_i^{n+1/2}-(\rho\mathbf{u})_i^n\right)+\sum_{j\in Neigh(i)}\mathbf{u}_{ij}^{n+1/2}\left((\rho\mathbf{u})^n.\mathbf{n}\right)_{ij}C_{ij}-$$
$$\sum_{j\in Neigh(i)}\left(\mu\nabla\mathbf{u}^{n+1/2}.\mathbf{n}\right)_{ij}C_{ij}=-|\Omega_i|G_i(p^n)+|\Omega_i|\mathbf{A}_i^n+|\Omega_i|B_i^n.\mathbf{u}^{n+1/2} \quad (2.10)$$

C_{ij} is the shared face (i,j) between cells i and j.

The diffusion term is defined as:

$$\left(\mu\nabla\mathbf{u}^{n+1/2}.\mathbf{n}\right)_{ij}=\mu_{ij}\mathtt{G}_{\mathbf{n},ij}(\mathbf{u}^{n+1/2}) \quad (2.11)$$

To calculate the face values for the velocity $(\mathbf{u}^{n+1/2})_{ij}$, *Code_Saturne* has three numerical convective schemes available: the first order UPWIND scheme, a second order centred scheme (used in the present work) and the Second Order Linear Upwind scheme (SOLU).

The mass flux values, $((\rho\mathbf{u})^n.\mathbf{n})_{ij}$, through the face (i,j) are obtained from the previous pressure correction step.

The pressure increment term, as defined above, is integrated as:

$$\Delta t\sum_{j\in Neigh(i)}(\nabla(\Delta p).\mathbf{n})_{ij}C_{ij}=\sum_{j\in Neigh(i)}\left((\rho\mathbf{u})^{n+1/2}.\mathbf{n}\right)_{ij}C_{ij} \quad (2.12)$$

After the equation for the pressure increment being solved, the mass flux values through the faces is updated:

$$\left((\rho\mathbf{u})^{n+1}.\mathbf{n}\right)_{ij}=\left((\rho\mathbf{u})^{n+1/2}.\mathbf{n}\right)_{ij}-\Delta t\mathtt{G}_{\mathbf{n},ij}(\Delta p) \quad (2.13)$$

Finally, the momentum at cell centres and pressure are corrected for the next time step, respectively, as the following:

$$(\rho\mathbf{u})_i^{n+1}=(\rho\mathbf{u})_i^{n+1/2}-\Delta tG_i(\Delta p) \quad (2.14)$$

$$p_i^{n+1}=p_i^{n+1/2}+\Delta p_i \quad (2.15)$$

2.2.3 ALE module

Free surface boundaries can be handled using a fixed-mesh or a moving-mesh approach. Muzaferija and Peric (1997) or Apsley and Hu (2003) show examples of applications of a moving-mesh approach to model free surface flows using the finite volume method.

The *Code_Saturne* model uses the Arbitrary Lagrangian Eulerian (ALE) methodology (Archambeau et al., 1999), which allows the mesh to follow the moving boundaries. The basic principle of this method is the separation between the mesh velocity from the fluid velocity field. The ALE method is compromised between the Lagrangian approach, where the mesh velocity ($\mathbf{w_m}$) is equal to the fluid velocity ($\mathbf{u}$) and an Eulerian fixed mesh ($\mathbf{w_m} = 0$).

With this module, the Navier-Stokes equations gain a new term in the transport type terms which accounts for the vertical velocity of the mesh ($\mathbf{w_m}$). For an incompressible flow within a moving domain, the new equations are expressed below.

$$\nabla.(\mathbf{u}) = 0 \tag{2.16}$$

$$\rho\frac{\partial \mathbf{u}}{\partial t} + \nabla.(\rho(\mathbf{u} - \mathbf{w_m}) \otimes \mathbf{u}) = \nabla.(\sigma_r) + \mathbf{u}\nabla.(\rho(\mathbf{u} - \mathbf{w_m})) + \rho\mathbf{g} \tag{2.17}$$

Recently, Cozzi (2010) adapted the ALE method for representing wave propagation in free surface flows in *Code_Saturne* version 1.3.3. At each time step, the mesh is updated with the vertical velocity of the mesh, constrained to guarantee a zero net mass flux at the free surface. Since there is some arbitrariness in the transformation from the physical domain to the computational domain, these type of constrains are essential to specify a particular problem. Therefore the following kinematic condition is imposed:

$$w_m = \frac{\mathbf{u}.\mathbf{S_f}}{\mathbf{e_z}.\mathbf{S_f}} = \frac{\dot{m}_{fs}}{\rho S_{fz}} \tag{2.18}$$

The mesh velocity is represented by $\mathbf{w_m} = w_m.e_z$, considering that the mesh moves only in the vertical direction. $\dot{m}_{fs}$ would be the mass flux if the free surface was represented by a fixed mesh, and S_{fz} is the vertical component of the unit free surface vector, $\mathbf{S_f}$.

The overall algorithm implemented in *Code_Saturne* model, with the ALE free surface module included, is explained hereby:

- At the free surface, the mesh velocity is equal to the flow velocity at time step t^n, and the pressure equal to the atmospheric pressure.

- The Navier-Stokes equations are solved in the known geometry at time t^n in two stages (prediction-correction). In the prediction step, they include two extra terms related to the mesh velocity;

- The velocity field and mass flow values through the free surface faces are obtained;

- Convergence loop in the mass flow values through the free surface faces to enforce the kinematic boundary condition (2.18) imposed at the free surface;

- After the mesh being updated, the values for the mass flow at the free surface faces ($\dot{m}_{fs}^{n+1}$), velocity mesh (w_m^{n+1}), pressure (p^{n+1}) and velocity field (u^{n+1}) are known for t^{n+1};

- After knowing the boundary displacements at t^{n+1}, the internal cell vertices displacements are calculated. This is done such that an internal cell vertex displacement (ζ_j) below the free surface cell vertex displacement (ζ_i) is related through the initial ratio between the two vertices elevations (h_i for the free surface vertex and h_j for the internal vertex). The relation is the following:

$$\zeta_j = \zeta_i \frac{h_j}{h_i} \tag{2.19}$$

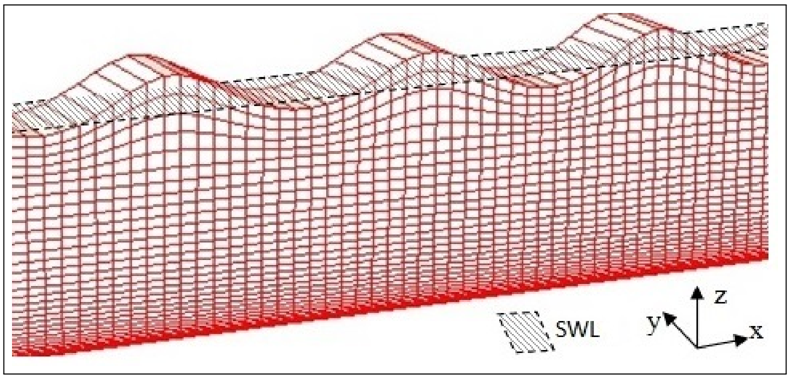

Figure 2.2: Application of the ALE module to the free surface moving mesh representation. SWL is the still water depth.

For more detailed information about the adaptation of the ALE module in *Code_Saturne*, please refer to Archambeau et al. (1999) and Cozzi (2010).

2.3 Turbulence modelling

2.3.1 Reynolds decomposition

For many years, a number of studies have been carried out for a better knowledge and understanding of the turbulence effects existent in the flow. The first attempt to study the turbulence was made by Leonardo da Vinci through the placement of obstructions in water and observation of the induced effects.

"Observe the motion of the surface of the water, which resembles that of hair, which has two motions, of which one is caused by the weight of the hair, the other by the direction of the curls; thus the water has eddying motions, one part of which is due to the principal current, the other to random and reverse motion. " (Leonardo da Vinci, 1510) (translation by Ugo Piomelli, University of Maryland).

Later, Osborne Reynolds was the first to investigate the transition from laminar flow to turbulent flow through the well-known Reynolds experiments (Reynolds, 1895). In particular, Reynolds concluded that if turbulence effects were to be taken into account, the instantaneous fluid velocity ($\mathbf{u}$) should be decomposed in a time average part ($\overline{\mathbf{u}}$) and a fluctuating part ($\mathbf{u}'$).

$$\mathbf{u} = \overline{\mathbf{u}} + \mathbf{u}' \tag{2.20}$$

After applying the decomposition (2.20) to the Navier-Stokes equations, the resulting equations are time-averaged. Finally, the so-called Reynolds Averaged Navier-Stokes (RANS) equations (2.21) and (2.22) are obtained. For an incompressible flow they read:

$$\nabla.(\overline{\mathbf{u}}) = 0 \tag{2.21}$$

$$\rho \frac{\partial \overline{\mathbf{u}}}{\partial t} + \nabla.(\rho \overline{\mathbf{u}} \otimes \overline{\mathbf{u}}) = -\nabla \overline{p} + \nabla.(\overline{\tau}_{ij} - \rho R_{ij}) + \rho \mathbf{g} \tag{2.22}$$

A new term appears in the RANS equations, relative to the Navier-Stokes equations - the non-linear Reynolds stress term $R_{ij} = \overline{u_i' u_j'}$. The indices i and j range from the values 1 to 3. The Reynolds stress tensor represents the transport of momentum by the velocity fluctuations. The sum of this last term with the viscous stresses, mean pressure field and body forces balances the rate of change of the mean momentum (left hand side of (2.22)).

The system of the above equations (2.21 and 2.22) is underdetermined. There are four equations (the three components of RANS equations for velocity and the mean continuity equation) for more than four unknowns (the three components of the velocity, the mean pressure and the Reynolds stresses). Therefore, the Reynolds stress tensor needs to be determined by a turbulence closure model to close the RANS equations. For that purpose, there has been a constant development of different turbulence closure models.

Turbulence modelling is essential in a number of applications. It is a complex problem since in a turbulent flow the energy spectrum is characterized by a wide range of length scales.

Depending on the kind of application and degree of accuracy that the user wants to describe the different characteristics of the flow, several turbulence models have been developed to better fit user needs, ranging from the simplest ones to ones with a high degree of complexity.

In most engineering problems, RANS-based models are used to describe the flow quantities since usually they are usually adequate and sufficient to model the turbulence effects. The RANS-based models can be divided into two main groups: the eddy viscosity models, where the turbulence stress tensor is evaluated from the mean deformation rate tensor, and the Reynolds Stress Models (RSM), where a transport equation is solved for each of the turbulence stress tensor components.

Nevertheless, in a number of applications, the description of the flow becomes more complex and the approach based on RANS models has to be abandoned. Therefore, other turbulence models have been made available by/for the scientific community, such as the LES (Large Eddy Simuation) or the DNS (Direct Numerical Simulation) models. In LES models, the Navier-Stokes equations are not averaged. A spatial filter is applied, and the smaller scales are modelled and the larger scales resolved. In DNS models there is no modelling at all, all the turbulence contained in the flow is resolved. Despite the accuracy of these kinds of models, finer grids are needed and consequently the computational cost is increased.

In *Code_Saturne*, a large range of first and second order turbulence closure models are implemented. In the range of eddy viscosity models the numerical model has implemented the one equation mixing length model, the Spalart Allmaras model (Spalart and Allmaras, 1992), the two-equation models $k-\varepsilon$ (Launder and Spalding, 1974), the $k-\varepsilon$ LP (Linear Production) version (Guimet and Laurence, 2002), the $k-\omega$ SST (Menter, 1994) and a v^2-f model, with the ϕ model version (Uribe, 2006). It has also two RSM models available, for instance the second-order Reynolds stress transport model $R_{ij}-\varepsilon$ SSG (Speziale et al., 1991) and the $R_{ij}-\varepsilon$ LRR (Launder et al., 1975). Apart from the RANS models, it has the possibility of dealing with the turbulent flows using LES models.

In the following sub-sections, the RANS-based turbulence closure models are focused, since they were the ones chosen to work with.

2.3.2 Eddy viscosity models

The eddy viscosity models use the turbulence viscosity hypothesis - the Boussinesq assumption (Boussinesq, 1877). It relates the Reynolds stress tensor $\overline{u_i'u_j'}$ with the mean flow straining field (2.23).

$$\overline{u_i'u_j'} - \frac{2}{3}k\delta_{ij} = -\nu_t\left(\frac{\partial \overline{u}_i}{\partial x_j} + \frac{\partial \overline{u}_j}{\partial x_i}\right) = -2\nu_t\overline{S}_{ij} \tag{2.23}$$

Where ν_t is the kinematic turbulence viscosity and δ_{ij} is the Kronecker delta. $\overline{S}_{ij} = \frac{1}{2}\left(\frac{\partial \overline{u}_i}{\partial x_j} + \frac{\partial \overline{u}_j}{\partial x_i}\right)$ represents the mean deformation rate tensor.

The mean kinetic energy per unit mass in the fluctuating field is the turbulence kinetic energy per unit mass, k :

$$k = \frac{1}{2}\overline{u_i'u_i'} \tag{2.24}$$

Within the Boussinesq assumption, the turbulence viscosity represents a degree of freedom in the set of equations, thus needing to be specified. The turbulence viscosity has an important role in fluid mechanics. It controls the mixing effects of the different water properties. Consequently, to calculate the turbulence viscosity, a number of models were developed.

Boussinesq (1877) proposed the simplest approach to model the turbulence viscosity, which consists in assuming it a constant value. Other models with higher complexity levels were developed, for instance the models with zero, one or two equations.

2.3.2.1 Zero-equation models

In zero-equation models, such as the Prandtl model (Prandtl, 1925), the main assumption states that the turbulence structures are directly linked with the flow mean quantities. In fact, from laboratory experiments it was verified that the flow mixing was larger if the turbulence eddies were also larger and that it had a larger velocity if the turbulence kinetic energy assumed also a greater value.

Therefore, the largest turbulence eddies are first associated within the integral scale, which is linked to the dimensions of the domain. Then, the equilibrium hypothesis is made. It is considered that the turbulence production equals the turbulence dissipation.

The turbulence viscosity is finally expressed by (2.25). The dependence on mean velocity can be seen, and a characteristic length scale, the so-called mixing length, l_m.

$$\nu_t = \frac{\mu_t}{\rho} = l_m^2 \sqrt{2\overline{S}_{ij}\overline{S}_{ij}} \tag{2.25}$$

μ_t is the dynamic turbulence viscosity and l_m depends on the nature of the flow and has to be prescribed as a function of space. In general it is assumed that the turbulence structures dimension is limited by the presence of walls and that faraway from them their dimension tends to stabilize.

2.3.2.2 One-equation models

In one-equation models, the turbulence viscosity is not directly deduced from the mean flow quantities. To determine the turbulence viscosity (2.26), it is considered that the turbulence length-scale (l_t) is known and an extra equation for the description of the turbulence kinetic energy transport (2.27) has to be solved. To deduce this equation, the momentum RANS equations are subtracted from the momentum Navier-Stokes equations obtaining the equation for the evolution of velocity fluctuations. Then the resulting equation is multiplied by the velocity fluctuation (u_i') and then time averaged.

$$\nu_t = \sqrt{k} l_t \tag{2.26}$$

$$\rho \frac{\partial k}{\partial t} + \nabla . \left[\rho \mathbf{u} k - \left(\mu + \frac{\mu_t}{\sigma_k} \right) \nabla k \right] = P - \rho \varepsilon + G \tag{2.27}$$

σ_k is a constant that usually is assumed to be equal to one, P is the turbulence production due to viscous forces, G a production term due to gravity effects and the dissipation term (ε) is related to the turbulence length-scale by the following:

$$\varepsilon = C_\mu \frac{k^{3/2}}{l_t} \tag{2.28}$$

with $C_\mu = 0.09$.

2.3.2.3 Two-equation models

Among the models applying the Boussinesq assumption, the two-equation models are widely used for their simplicity (comparing with more complex turbulence closure models) and relatively accuracy.

The two-equation models take into account an extra equation. The second equation varies depending on what the user wants to apply as a turbulence model. Usually, the second variable to be transported is either the turbulence dissipation, ε or the so-called specific dissipation, $\omega \approx \frac{\varepsilon}{k}$. The choice between the two variables leads to the most commonly used two two-equation models, $k-\varepsilon$ (Launder and Spalding, 1974) and $k-\omega$ (Wilcox, 1993) models. With these two quantities, the mixing length is no longer required. The application of these models results in a more accurate prediction of the quantities linked to turbulence viscosity (2.29). In the following, the equations for the $k-\varepsilon$ model (Launder and Spalding, 1974) are shown.

$$\nu_t = C_\mu \frac{k^2}{\varepsilon} \tag{2.29}$$

$$\rho \frac{\partial k}{\partial t} + \nabla . \left[\rho \mathbf{u} k - \left(\mu + \frac{\mu_t}{\sigma_k} \right) \nabla k \right] = P - \rho \varepsilon + G \tag{2.30}$$

$$\rho \frac{\partial \varepsilon}{\partial t} + \nabla . \left[\rho \mathbf{u} \varepsilon - \left(\mu + \frac{\mu_t}{\sigma_\varepsilon} \right) \nabla \varepsilon \right] = \frac{\varepsilon}{k} C_{\varepsilon 1} \left(P + (1 - C_{\varepsilon 3}) G \right) - \rho C_{\varepsilon 2} \frac{\varepsilon^2}{k} \tag{2.31}$$

P is the turbulence production due to viscous forces modelled by:

$$P = -\rho \overline{u_i' u_j'} \frac{\partial u_i}{\partial x_j} \tag{2.32}$$

and G the production term due to gravity effects:

$$G = -\frac{1}{\rho} \frac{\mu_t}{\sigma_t} g_i \frac{\partial \rho}{\partial x_i} \tag{2.33}$$

Table 2.1: Constants used in $k-\epsilon$ model (Launder and Spalding, 1974).

C_μ	$C_{\varepsilon 1}$	$C_{\varepsilon 2}$	σ_k	σ_ε	σ_t
0.09	1.44	1.92	1	1.3	1

$C_{\varepsilon 3} = 0$ if $G \geq 0$ and $C_{\varepsilon 3} = 1$ if $G < 0$.

Several developments have been made both on $k-\varepsilon$ leading to different versions of this model. One example of these versions, which will be used in the present work, is the $k-\varepsilon$ LP (Linear Production) model (Guimet and Laurence, 2002) in which there is a linearization of the production term.

In the $k-\omega$ model (Wilcox, 1993), equation (2.30) is solved for k, but the dissipation is estimated using a so-called specific dissipation $\omega = \frac{\varepsilon}{\beta^* k}$, where $\beta^* = 0.09$ is a constant. Menter (1994) proposed another version of $k-\omega$ model in which a modified expression for the turbulence viscosity is used, and a blending function (F_1) is applied to combine $k-\varepsilon$ and $k-\omega$ models. He obtained the $k-\omega$ SST (Shear Stress Transport) model.

The turbulence viscosity is calculated in the following way:

$$\nu_t = \frac{a_1 k}{max(a_1 \omega; 2\sqrt{S_{ij}S_{ij}}F_2)} \tag{2.34}$$

with:

$$F_2 = tanh(arg_2)^2 \tag{2.35}$$

$$arg_2 = max\left(\frac{\sqrt{2k}}{\beta^* \omega y}; \frac{500\nu}{y^2 \omega}\right) \tag{2.36}$$

The evolution for the specific dissipation solved in $k-\omega$ SST model is expressed below.

$$\begin{aligned} \rho\frac{\partial \omega}{\partial t} + \nabla.\left[\rho \mathbf{u} \omega - (\mu + \sigma_{\omega 3}\mu_t)\nabla\omega\right] = \\ -\rho\beta_3\omega^2 + \frac{a_3}{\nu_t}\left(P + (1 - C_{\varepsilon 3})\,G\right) + 2\,(1 - F_1)\,\rho\frac{\sigma_{\omega 2}}{\omega}\nabla k \nabla \omega \end{aligned} \tag{2.37}$$

with the blending function:

$$F_1 = tanh(arg_1)^4 \tag{2.38}$$

with:

$$arg_1 = min\left[max\left(2\frac{\sqrt{k}}{\beta^*\omega y};\frac{500\nu}{y^2\omega}\right);\frac{4\rho\sigma_{\omega 2}k}{CD_{k\omega}y^2}\right] \tag{2.39}$$

$$CD_{k\omega} = max\left(2\rho\frac{\sigma_{\omega 2}}{\omega}\nabla k\nabla\omega;10^{-20}\right) \tag{2.40}$$

The coefficients of the $k-\omega$ SST model are obtained by:

$$\phi_3 = F_1\phi_1 + (1-F_1)\phi_2 \tag{2.41}$$

Table 2.2: Constants used in $k-\omega$ SST model (Menter, 1994).

a_1	a_2	β_1	β_2	β^*	$\sigma_{\omega 1}$	$\sigma_{\omega 2}$
$\frac{5}{9}$	0.44	0.075	0.0828	0.09	0.5	0.856

Most of the CFD models include the above mentioned eddy viscosity models. They are applied depending on the different natures of flows.

Despite the good performance and prediction of these models, no eddy-viscosity model accounts for the anisotropy of turbulence. Hence the introduction of Reynolds Stress Models overcome some of the limitations that the eddy-viscosity models have.

2.3.3 Reynolds Stress Models (RSM)

As computer resources increased, it was possible to develop more complex turbulence models. An example is the development of the Reynolds Stress Models (RSM), a second order closure model. Contrary to first order turbulence models, in RSM the Reynolds stress transport (2.42) accounts for the directional effects of the Reynolds stress fields, and the eddy viscosity hypothesis, the Boussinesq assumption, is discarded. Here, there are six transport equations for the six independent components of the Reynolds stress tensor, $R_{ij} = \overline{u'_i u'_j}$, and one equation for the dissipation rate (2.31). Below, the equations for the $R_{ij}-\varepsilon$ LRR (Launder, Reece and Rodi) model (Launder et al., 1975) are presented.

$$\rho\frac{\partial R_{ij}}{\partial t} + \nabla.\left(\rho\mathbf{u}R_{ij} - \mu\nabla R_{ij}\right) = P_{ij} + G_{ij} + d_{ij} + \Phi_{ij} - \rho\varepsilon_{ij} \tag{2.42}$$

$$\rho\frac{\partial\varepsilon}{\partial t} + \nabla.\left(\rho\mathbf{u}\varepsilon - \mu\nabla\varepsilon\right) = d_\varepsilon + C_{\varepsilon 1}\frac{\varepsilon}{k}\left[P + G_\varepsilon\right] - \rho C_{\varepsilon 2}\frac{\varepsilon^2}{k} \tag{2.43}$$

The first term in the R.H.S. of (2.42) is the turbulence production tensor, P_{ij} expressed by:

$$P_{ij} = -\rho \left[R_{ik} \frac{\partial u_j}{\partial x_k} + R_{jk} \frac{\partial u_i}{\partial x_k} \right] \tag{2.44}$$

The gravity effects terms G_{ij} and G_ε are, respectively:

$$G_{ij} = \left[\mathtt{G}_{ij} - C_3 \left(\mathtt{G}_{ij} - \frac{1}{3} \delta_{ij} \mathtt{G}_{kk} \right) \right] \tag{2.45}$$

with

$$\mathtt{G}_{ij} = -\frac{3}{2} \frac{C_\mu}{\sigma_t} \frac{k}{\epsilon} \left(R_{ik} \frac{\partial \rho}{\partial x_k} g_j + R_{jk} \frac{\partial \rho}{\partial x_k} g_i \right) \tag{2.46}$$

$$G_\varepsilon = max \left(0, \frac{1}{2} G_{ll} \right) \tag{2.47}$$

The turbulence diffusion terms are denoted by d_{ij} and d_ε.

$$d_{ij} = C_S \frac{\partial}{\partial x_k} \left(\rho \frac{k}{\varepsilon} R_{km} \frac{\partial R_{ij}}{\partial x_m} \right) \tag{2.48}$$

$$d_\varepsilon = C_\varepsilon \frac{\partial}{\partial x_k} \left(\rho \frac{k}{\varepsilon} R_{km} \frac{\partial \varepsilon}{\partial x_m} \right) \tag{2.49}$$

Φ_{ij} represents the correlation between the pressure fluctuations (p') and the velocity fluctuation (u') gradient.

$$\Phi_{ij} = \frac{1}{\rho} \overline{p' \left(\frac{\partial u'_j}{\partial x_j} + \frac{\partial u'_j}{\partial x_i} \right)} \tag{2.50}$$

The constants used in the RSM LRR model are presented on Table 2.3.

Table 2.3: Constants used in the $R_{ij} - \varepsilon$ LRR model (Launder et al., 1975).

C_1	C_2	C_3	C_S	C_ε
1.8	0.6	0.55	0.22	0.18

To model Φ_{ij}, two versions of RSM models can be applied: a linear model, the $R_{ij} - \varepsilon$

LRR (Launder et al., 1975) and a quasi-linear model, the $R_{ij}-\varepsilon$ SSG (Speziale et al., 1991). In the present work the RSM SSG (Speziale et al., 1991) was used.

2.4 Model setup

2.4.1 Wave generation and dissipation

In the present study, the *Code_Saturne* was applied with the objective of studying wave-current interactions, taking into account the effects of turbulence on free surface flows. A numerical flume was reproduced for that purpose (Figure 2.3).

In order to generate the waves in the numerical flume, a horizontal movement of the mesh is imposed at the upstream lateral wall. To minimize undesirable free super-harmonic and sub-harmonic waves, a second-order piston-type wave boundary condition can be applied. If waves propagate in positive x-direction, the following expression for the wave board (represented by the upstream lateral wall of the numerical flume) motion displacement $X_0\left(t\right)$ in equation (2.51) (Dean and Dalrymple, 1991) is introduced:

$$X_0\left(t\right)=\frac{H}{2m_1}sin\left(\frac{2\pi}{T}t\right)+\frac{H^2}{32h}\left(\frac{3cosh(kh)}{sinh^3(kh)}-\frac{2}{m_1}\right)sin\left(2t\frac{2\pi}{T}\right) \tag{2.51}$$

with m_1 given by:

$$m_1=\frac{4sinh(kh)}{sinh(2kh)+2kh}\left[sin(kh)+\frac{(1-cosh(kh))}{kh}\right] \tag{2.52}$$

k represents the wave number, h the water depth, H the wave height, T the wave period, and t the time. To avoid a sudden movement of the mesh and thus mesh crossover, the signal at the lateral boundary (2.51) has to be progressively imposed over time.

The energy of waves can be dissipated if the waves propagate into a more viscous fluid. Following this idea, the downstream boundary can be extended by about six wave lengths with a less refined mesh and a linear increasing viscosity distribution can be imposed in the extension of the numerical flume.

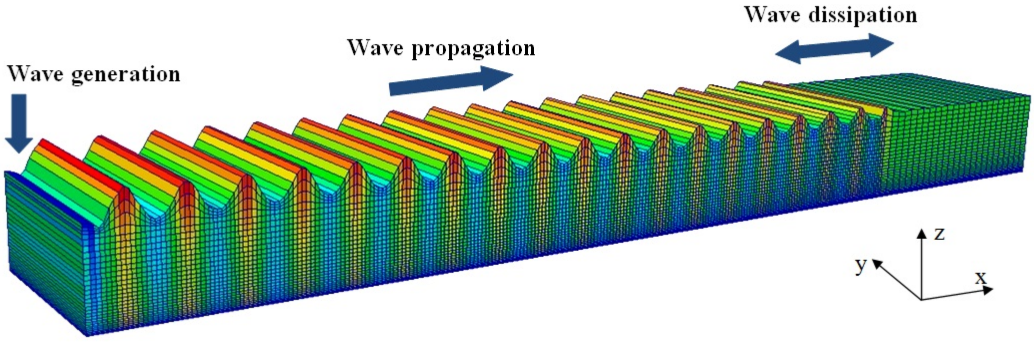

Figure 2.3: Scheme of the numerical channel with waves generation, propagation and dissipation.

2.4.2 Mesh generation

The mesh generation is subject to a number of conditions that the modeller has to take into account. On one hand, in order to ensure a good representation of the waves, it is necessary to have about 10-15 cells per wavelength. On the other hand, the mesh resolution cannot be too fine next to the moving wall (representative of the wave board motion) to avoid mesh crossover and the divergence of the simulation.

Mesh resolution in the vicinity of boundaries where a no-slip condition applies (i.e. near the bottom in this study) requires special attention when using CFD codes. There are basically two main approaches that can be followed by such codes: in the first one, usually referred to as *Low Reynolds* number model, the CFD model is used throughout the boundary layers (including the viscous sublayer in the vicinity of the boundary) and above, with a very refined grid in order to resolve the structure of the flow (which is strongly sheared) when approaching the boundary. In the second one, the actual use of the CFD code (where the first grid point lies) starts at a given (small) distance from the wall and an additional wall function is applied in order to correctly handle the viscous effects at the boundary. In this case, the resolution of the grid close to the boundary is coarser compared to the previous approach. This approach is usually referred to as *High Reynolds* number model, or “wall function approach ”.

With the present version of *Code_Saturne*, the second modelling strategy (*High Reynolds* number model) was adopted and a wall function close to the bottom was used. This was motivated by two main reasons: first, *Code_Saturne* is designed to be used preferably with this modelling strategy and more experience is available on this side, and secondly it was desired to keep the computational effort relatively moderate.

Since *High Reynolds* number models were used in *Code_Saturne* in the present work, there were therefore some constraints on the mesh generation. One of them was to define the relative size of the cells near the bottom. It is necessary to ensure that $z^+ > 2.5$, but it is preferential that $30 < z^+ < 100$, where z^+ is the dimensionless z-coordinate normalized by the thickness of the viscous sublayer $\left(\delta = \frac{\nu}{u_*}\right)$. At the same time, some important effects were to be analysed in this region, such as the influence of the roughness on the vertical profile of the measured quantities, so adequate spatial resolution was required.

2.4.3 Boundary conditions

The definition of boundary conditions for the computational variables is needed for the calculation of convection and diffusion terms and cell gradients. There are a number of available coded boundary conditions in *Code_Saturne*. In Figure 2.4 the boundary conditions type for the velocity and pressure variables are defined for each boundary face of the numerical flume.

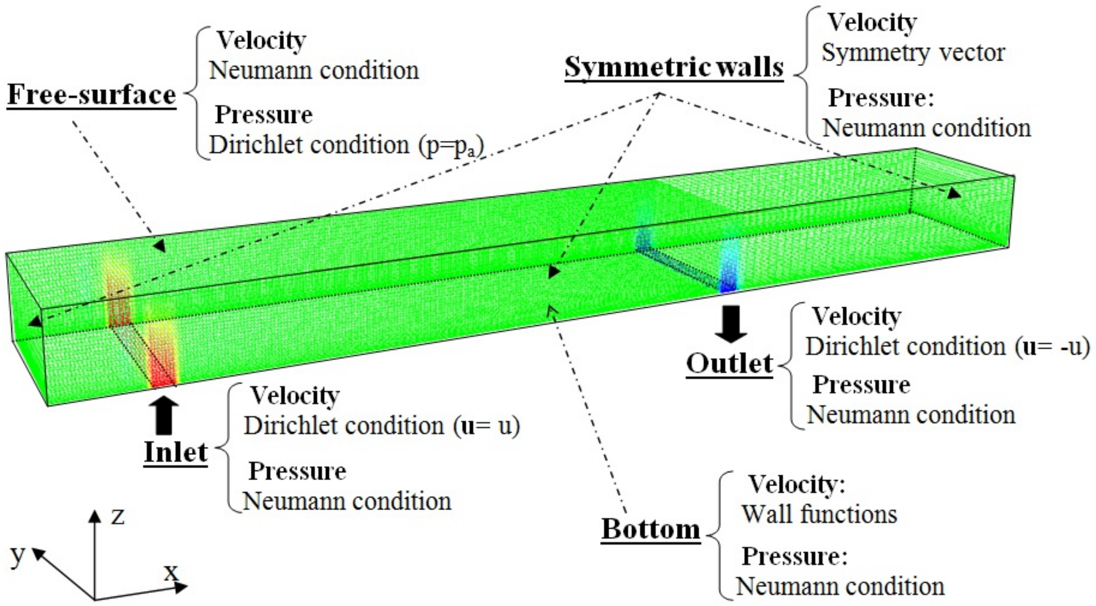

Figure 2.4: Boundary conditions types for the velocity and pressure imposed at each boundary face of the numerical flume.

Please note that in sub-section 2.2.3 a specific condition imposed by the ALE methodology was already introduced.

An additional condition (2.53), proposed by Celik and Rodi (1984), had to be imposed on the free surface.

$$\varepsilon = \frac{k^{3/2}}{h\alpha} \tag{2.53}$$

The turbulence dissipation, ε, and the turbulence kinetic energy, k, are the values at the free surface and $\alpha = 0.18$ is an empirical constant. Although the RSM model does not compute explicitly the turbulence energy k, this variable is estimated as half the sum of the normal stresses. In the $k-\omega$ model, ε is replaced by $\omega\beta^{*}k$ in (2.53).

This boundary condition accounts for the reduction of the length scale of turbulence near the free surface, which is physically consistent behaviour and has been observed experimentally by Nezu and Rodi (1986). With this boundary condition, the turbulence dissipation, which determines the turbulence length scale, will be higher than the value obtained when using a zero-gradient surface boundary condition (Nezu and Nakagawa, 1993). Hence from equation (2.29), it can be seen that the eddy viscosity decreases toward the free surface.

Additionally, a Neumann condition for the Reynolds stresses and the turbulence kinetic energy is also defined at the free surface:

$$\frac{\partial R_{ij}}{\partial z} = 0 \tag{2.54}$$

$$\frac{\partial k}{\partial z} = 0 \tag{2.55}$$

In the case of inlet boundaries (from which the flow enters in the domain), besides the value of the velocity, the turbulence variables also needed to be specified. With the friction velocity (u_*) known from, for example, the experimental data, the other turbulence variables are defined by the following:

$$k = \frac{u_*^2}{\sqrt{C_\mu}} \tag{2.56}$$

$$\varepsilon = \frac{u_*^{3/2}}{\kappa 0.1 D_h} \tag{2.57}$$

$$R_{ij} = \frac{2}{3}\frac{u_*^2}{\sqrt{C_\mu}}\delta_{ij} \tag{2.58}$$

With D_h equal to the hydraulic diameter and k estimated as half the sum of the normal stresses.

Regarding the wall-type boundary conditions, as *Code_Saturne* works with *"High Reynolds"* number turbulence closure models, wall functions are needed and used. *"High Reynolds"* number models are not adequate to be applied in the viscous boundary layer and thus it is avoided that equations are solved within this boundary layer. The wall functions are analytical laws, which integrated over the first cell of the grid above the bottom, allowing the behaviour of the boundary layer to be represented. In Figure 2.5 a representation of a boundary cell of the computational domain in *Code_Saturne* is shown.

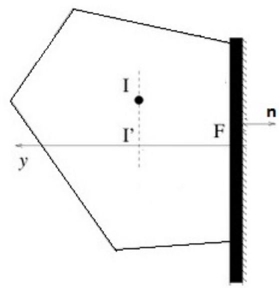

Figure 2.5: Boundary cell representation. Source: *Code_Saturne* documentation (2013).

In the case of having a smooth wall, the function below is applied:

$$f(z) = \frac{1}{\kappa} ln(z) + 5.2 \tag{2.59}$$

The von Karman constant is $\kappa = 0.41$.

For the other turbulence variables the following boundary conditions are applied near the wall:

$$\nabla(R_{ii}).n = 0; R_{12} = u_* u_k; R_{13} = R_{23} = 0 \tag{2.60}$$

$$\epsilon = \frac{u_k^3}{\kappa z} \tag{2.61}$$

$$k = \frac{u_k^2}{\sqrt{C_\mu}} \tag{2.62}$$

The unit vector normal to the boundary, oriented outwards, is represented by n and u_k is an estimate of u_* obtained from the turbulence kinetic energy.

In the case of having a rough wall the expression below is applied in function of $z_p = \overline{I'F}$ which is the distance from the wall defined by the size of the first cell. z_0 is a parameter related to the wall roughness that has to be defined by the user.

$$f(z_p) = \frac{1}{\kappa} ln \left(\frac{z_p + z_0}{z_0} \right) \tag{2.63}$$

Chapter 3

Numerical modelling of waves and current interaction at a local scale

A significant part of this chapter is the subject of the papers Teles et al. (2013a) and Teles et al. (2013b).

3.1 Introduction

In the past, some experiments have been designed to evaluate the modifications that occur in the wave-current environment. The experiments were initially driven by the motivation to understand how these interactions affect the bottom boundary layer and the near bed shear stresses, which may have consequences on sediment transport. Therefore, these experiments were focused on the bottom boundary layer.

Kemp and Simons (1982) and Kemp and Simons (1983) carried out laboratory experiments in a flume with rough and smooth beds, and with waves following and opposing currents, over the entire depth. They observed that when waves were following the current, the mean horizontal velocity reached a maximum value at a level between the bottom boundary layer and the wave trough. On the other hand, when waves were opposing the current, the mean horizontal velocity reached a maximum at the free surface which is higher than the value observed with the logarithmic profile for a only current case. The reader is also referred to the references therein for a discussion of previous experiments.

Similar results were obtained by Klopman (1994) in a series of experiments in a wave flume with a rough bed. His measurements included both the mean horizontal velocity and the horizontal-velocity amplitude for regular and irregular waves with (i) waves opposing currents, (ii) waves following currents, (iii) only waves, and (iv) only currents. Klopman (1994) also reported a reduction in the near-bed velocities and the presence of a wave-induced streaming. In the case of only currents, more detailed observations were made, including shear and normal stresses. The observed velocity shear is in agreement with the conclusions of Kemp and Simons (1982) and Kemp and Simons (1983). Albeit the high quality of Klopman′s (1994) experiments, they were mainly focused on the characteristics of the mean horizontal velocity. The tests with waves and currents provided no data on the Reynolds stresses.

More recently, Umeyama (2005) conducted experiments in a laboratory flume with a smooth bed for the purpose of measuring turbulence properties with only currents, only waves, and waves following and opposing currents, for different incident wave conditions (by varying the wave height and/or wave period). For the mean horizontal velocity, he presented the same conclusions as Klopman (1994), but also identified the importance of the wave period. His results concerning near-bed mean velocities differ partially from Klopman′s (1994) measurements.

Over the last decades there has been a constant and increasing demand for the analysis of environmental or safety studies, essential in a number of domains and for several kind of applications. The physical modelling appears as a possible solution to make this kind of studies. Although experimental studies are absolutely necessary to understand and know better a varied set of phenomena in different natures of flows, they show some disadvantages. For instance, important costs are associated with physical modelling: the necessity for the repeatability of experiments or when large-scale experiments are used. Furthermore, scale effects, Froude and Reynolds similarity incompatibility are issues difficult to deal with.

As introduced in the previous chapter the numerical modelling can be a powerful solution to overcome the disadvantages of using experimental facilities. Therefore, in the present work the numerical modelling is the chosen tool to study the effects of waves and currents. *Code_Saturne* model is used to model waves and currents simultaneously at a local scale.

Firstly, changes in the mean horizontal velocity and the horizontal velocity amplitude profiles are studied when waves are superimposed on currents. The influence of various first and second order turbulence closure models is addressed. Among the turbulence closure models available in *Code_Saturne*, the choice was made to evaluate the first-order $k-\varepsilon$ LP version and $k-\omega$ SST models, which are widely used because of their simplicity, and the second-order Reynolds stress transport model $R_{ij}-\varepsilon$ SSG. The results of the numerical simulations are compared to the experimental data of Klopman (1994) and

Umeyama (2005). Secondly, a more detailed study of the shear stresses and the turbulence viscosity vertical profile changes is also pursued when waves and currents interact. This analysis is completed using the data from Umeyama (2005). A tentative parameterisation of the turbulence viscosity in terms of the Ursell number will be proposed using the results of the numerical simulations obtained by *Code_Saturne*.

This chapter is organized in the following way. After this introductory section, the laboratory measurements used to verify the model are introduced in Section 3.2. Section 3.3 analyses the accuracy of the mean horizontal velocity profiles, preceded by a sensitivity analysis of the turbulence closure models. In Section 3.3.3, a discussion of turbulence intensities modelling is presented. The conclusions are then summarized.

3.2 Laboratory Data

Klopman (1994) carried out a series of laboratory experiments with two computer controlled wave boards (one generating waves and another absorbing the waves) and a flow circulation circuit able to provide a constant discharge of about $Q \approx 80\ ls^{-1}$. The channel was 46 m long (x direction), 1 m wide (y direction) and the water depth was 0.5 m (z direction) (Figure 3.1). Waves were generated with a second order signal to minimize free long waves. Based on the mean flow velocity, the flow was characterized by a Reynolds number of approximately 67000.

Numerical simulations were carried out for the test cases with currents only, waves only, and monochromatic waves following and opposing currents. The wave height was $H = 0.12\ m$, and the wave period was $T = 1.44\ s$. During each test, mean horizontal velocity profiles and horizontal velocity amplitudes were measured by a laser-Doppler velocimeter (LDV) at the middle of the channel ($x = 22.5\ m$ and $y = 0.5\ m$). For the case with only currents, a description of the shear stress was also made through the LDV measurements.

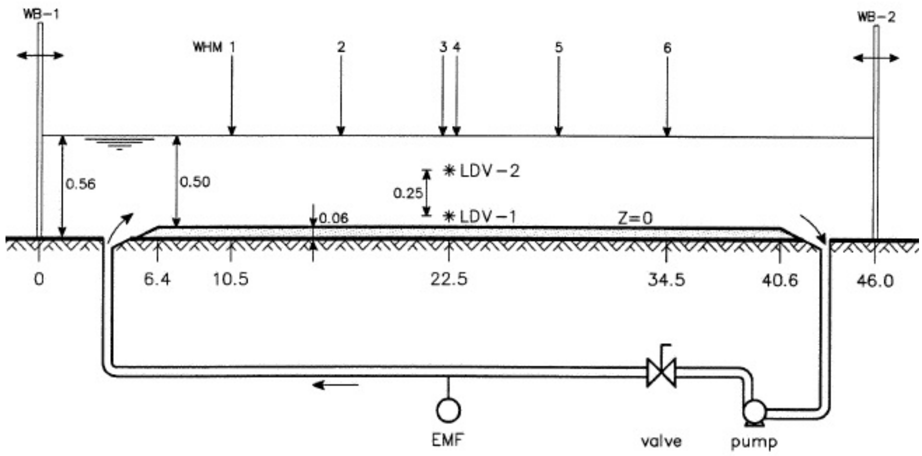

Figure 3.1: Wave flume scheme from Klopman (1994) experiments.

The experiments from Umeyama (2005) were completed in a channel 25 *m* long and 0.7 *m* wide, with a water depth of 0.2 *m* (Figure 3.2). Regular waves were generated with a piston-type wave maker and dissipated with a wave absorber at the opposite end of the channel. Four combinations of wave height and wave period used in tests with only waves, waves following currents, and waves opposing currents (Table 1). The mean flow velocity in the channel was about 12 cms^{-1}. For each test, the horizontal and vertical velocities were measured by a Laser Doppler Anemometer (LDA) 10.5 *m* from the wave generator. Mean velocity profiles and shear stresses were obtained.

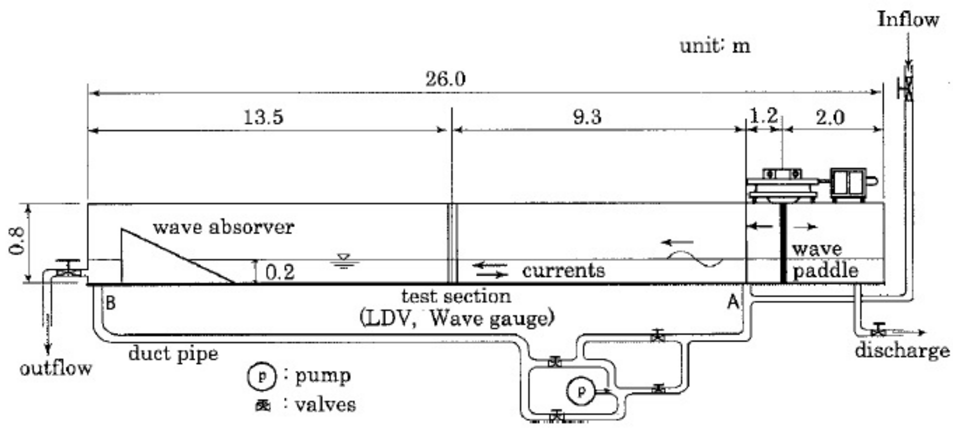

Figure 3.2: Wave flume scheme from Umeyama (2005) experiments.

Table 3.1: Wave heights and wave periods for the four test cases of Umeyama (2005).

Tests	T1	T2	T3	T4
Wave height (m)	0.0202	0.0251	0.0267	0.028
Wave period (s)	0.9	1	1.2	1.4

For Klopman (1994) and Umeyama (2005), the relative wave heights were approximately $H/h \approx 0.24$ and $H/h \approx 0.1$, respectively, which qualifies them as intermediate non linear waves. With dimensionless depth $kh \approx 1$, these experiments are typically characterized as intermediate water depth.

To satisfy the conditions specified in section 2.4.2 regarding the mesh generation, the vertical discretization of the mesh had a varying resolution of $0.005\ m < \Delta z < 0.025\ m$ for the simulations of Klopman′s channel and $0.001\ m < \Delta z < 0.005\ m$ for the simulations of Umeyama′s channel. In the end, the computational domains for Klopman′s and Umeyama′s channels had approximately 18500 and 24000 cells, respectively.

3.3 Mean horizontal velocity profile

3.3.1 Turbulence closure model sensitivity

3.3.1.1 The “only currents”case

An important step evaluation of the ability of a full RANS equations model (e.g. *Code_Saturne*) to represent wave-current interaction, is a sensitivity study of the built-in turbulence closure models. Throughout this sub-section, the Klopman (1994) data was used for that purpose. Klopman (1994) found in the only current experiment a value of $z_0 = 0.04\ mm$. Therefore, the same value was imposed in *Code_Saturne*. The numerical model output corresponds to the phase-averaged values, from which it was possible to estimate the contributions of the mean flow and the waves. For the cases with waves propagating in the channel, results were analysed for fifty wave cycles within the 600 s of the total simulation time.

It should be highlighted that this sensitivity test is made with the default parameters set in the *Code_Saturne* turbulence models. Thus, no optimization of the constants of the model was attempted for any of the turbulence closure models. For all models, the same mesh was used, and the same free surface (2.53) boundary conditions was imposed. The time step for each simulation was set to 0.02 s.

The first test case had only currents. The simulation runs until a stationary current is achieved. Figures 3.3 (linear scale) and 3.4 (semi-log scale) show the comparison of the mean horizontal current profiles calculated with the $k-\varepsilon$ LP version, $k-\omega$ SST version and $R_{ij}-\varepsilon$ SSG turbulence closure models. Good agreement is found between the simulations with *Code_Saturne* and the laboratory data.

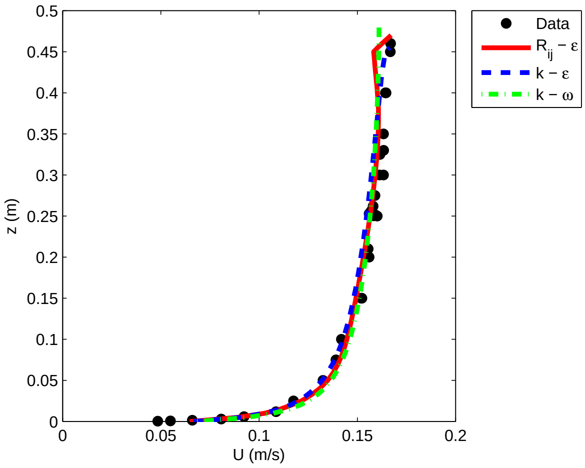

Figure 3.3: Vertical profiles of the mean horizontal velocity for only currents: linear scale. Data from Klopman (1994).

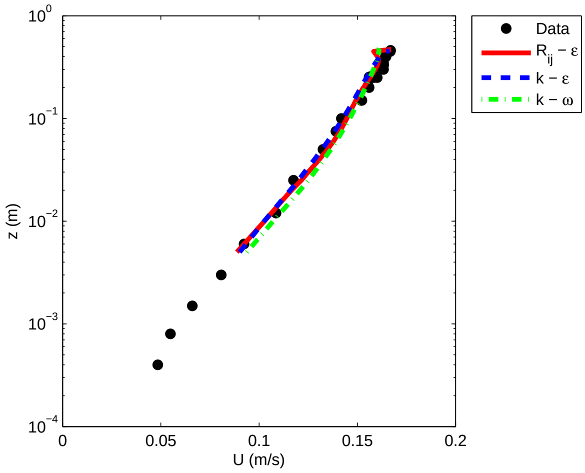

Figure 3.4: Vertical profiles of the mean horizontal velocity for only currents: semi-log scale. Data from Klopman (1994).

Near the free surface, there is a slight curvature in the vertical profile of the mean horizontal velocity when the $R_{ij}-\varepsilon$ model is applied. This behaviour is not observed with the two other turbulence models. It could be due to the impact of the side walls on the mean flow and the three-dimensionality of the flow, since the ratio between the channel width (B) and water depth (h) is $\frac{B_l}{h}=2$. This effect was also observed by Song (1994) for a turbulent current without waves and with the same range of values for $\frac{B_l}{h}$.

Of the three turbulence closure models, it is possible that the $R_{ij} - \varepsilon$ model is the only one capable of reproducing these effects, since it takes into account the turbulence anisotropy.

3.3.1.2 The "only waves"case

The second test case investigated the propagation of waves (along the positive x axis) in the channel without currents. Figures 3.5 (linear scale) and 3.6 (semi-log scale) present the numerical results and the experimental data for the mean horizontal velocity profiles. Near the bed, around $z \approx 0.02\ m$, the mean horizontal velocity changes sign, becoming negative. Below this level, there is a layer where the velocity is positive and in the direction of wave propagation, representing wave-induced streaming. These are second-order steady mean velocity fields that arise in any oscillatory flow. They are a consequence of viscosity and spatial variation of the velocity field outside this layer. This was first described by Longuet-Higgins (1953) for sinusoidal surface water waves. Holmedal et al. (2009) studied different mechanisms causing streaming, in particular, the importance of the mass transport beneath second-order Stokes waves.

In Figure 3.5 it can be observed that neither model can reproduce the wave streaming effect. Nevertheless the second order $R_{ij} - \varepsilon$ model seems to fit better the observations. The negative velocities in the middle of the water column are due to the undertow, and they compensate for the positive mass flux between the wave trough and the wave crest (i.e. the Stokes drift (not shown here)) since conservation of mass is guaranteed.

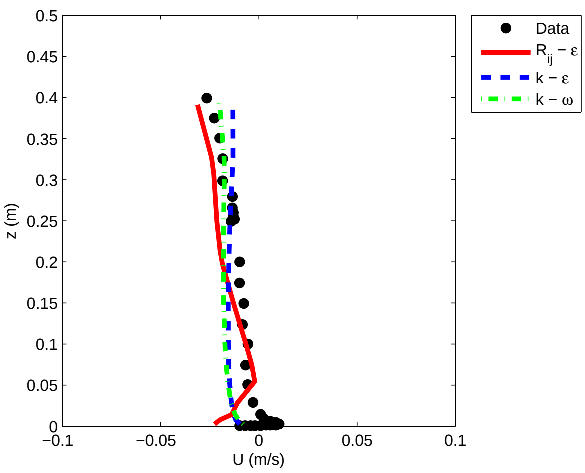

Figure 3.5: Vertical profiles of mean horizontal velocity for waves only: linear scale. Data from Klopman (1994).

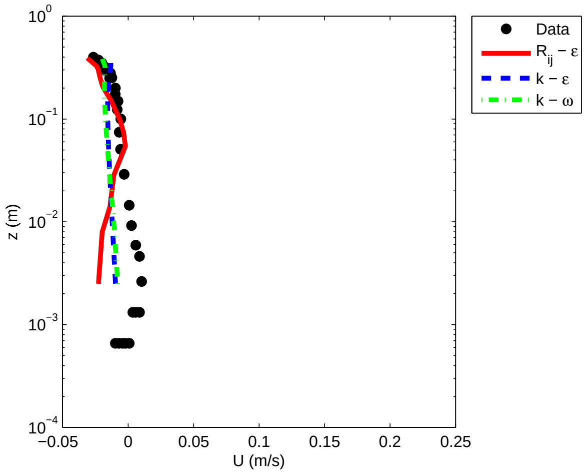

Figure 3.6: Vertical profiles of mean horizontal velocity for waves only: semi-log scale. Data from Klopman (1994).

The horizontal velocity amplitude profile is presented in Figures 3.7 (linear scale) and 3.8 (semi-log scale). The $k-\omega$ and $R_{ij}-\varepsilon$ models overestimate the horizontal velocity amplitude. Even though, the key features of the vertical profile, i.e. the cosine hyperbolic shape above the boundary layer and the overshooting before reaching this shape, are fairly well reproduced.

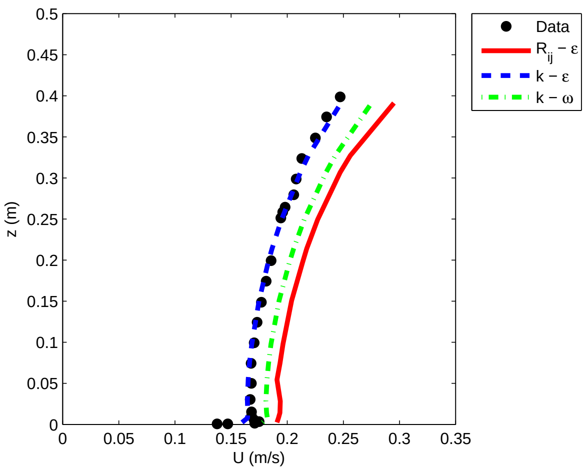

Figure 3.7: Horizontal velocity amplitude profile for only waves: linear scale. Data from Klopman (1994).

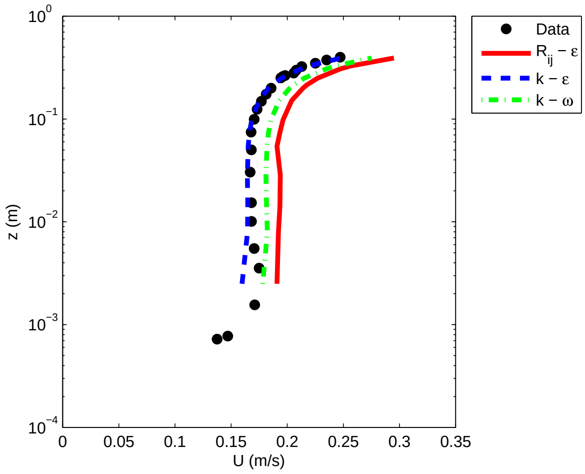

Figure 3.8: Horizontal velocity amplitude profile for only waves: semi-log scale. Data from Klopman (1994).

3.3.1.3 The “waves following currents”case

The vertical profile of the mean horizontal velocity is significantly changed by the presence of the waves, as seen by comparing Figure 3.9 with Figure 3.3.

In the case of waves following currents, the velocity shear in the upper half of the water column decreases and become negative. Figure 3.9 shows that the $R_{ij} - \varepsilon$ turbulence model was the only model capable of simulating the reduction in the velocity near the free surface. The simulations agreed well with the experiments not only near the bottom but also near the free surface.

The change in the velocity gradient near the free surface can be caused by different effects. A number of authors (e.g. Groeneweg and Klopman (1998), Groeneweg and Battjes (2003), Huang and Mei (2003), You (1996), Nielsen and You (1996)) attributed this change in the mean horizontal velocity profile mainly to the wave induced Reynolds stress when waves propagate in a flume. Due to oscillations induced by the superposition of waves the mean flow is modified.

When waves are superimposed on a turbulent current flowing in the same direction, the current shear velocity is positive. When approaching the free surface (where the wave induced stresses are more important) the wave related propagation contributions have opposite sign with the current contribution resulting in a decrease of the mean velocity shear. It can be even negative as in the present study.

Yang et al. (2006) analysed other possible effects, such as the non-uniformity of the flow (existence of a free surface slope along the channel) and/or secondary currents induced by sidewall effects. They concluded that both contributions also caused a change in mean horizontal velocity profile.

The decay of waves when propagating along the channel could cause a variation of the mean surface elevation and thus giving a non-uniformity character to the flow.

Klopman (1997) repeated the same experiments as in Klopman (1994), but this time he completed measurements along the cross section. He concluded that the secondary circulation cells predicted by the Craik-Leibovich vortex force theory existed in the flume. However, Groeneweg and Battjes (2003) concluded that this effect have a secondary influence on the change of the mean horizontal velocity profile.

The first order turbulence models, $k-\varepsilon$ and $k-\omega$, were not able to reproduce the reduction of mean horizontal velocity near the free surface. The accurate results obtained by the $R_{ij}-\varepsilon$ model are a natural consequence of the fact that the turbulence dissipation and the Reynolds stresses are computed explicitly and hence the model is able to take into account the anisotropy of the flow. In the first-order turbulence closure models, the Boussinesq approximation does not take into account the anisotropy of the flow due to the isotropic eddy viscosity assumption.

Comparing Figures 3.4 and 3.10 a reduction of the near-bed velocities is observed. Again, the $R_{ij}-\varepsilon$ model simulations approach the data better.

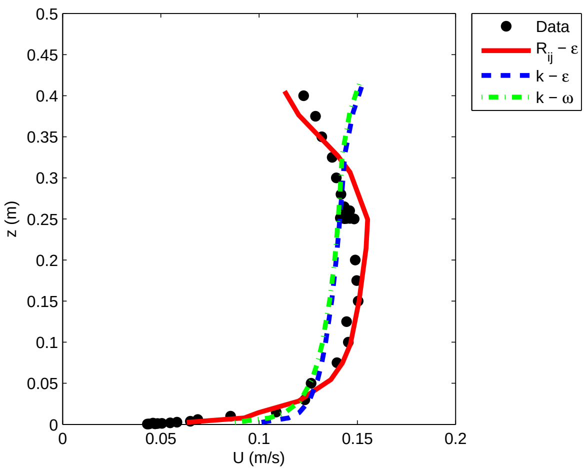

Figure 3.9: Vertical profiles of mean horizontal velocity for waves following currents: linear scale. Data from Klopman (1994).

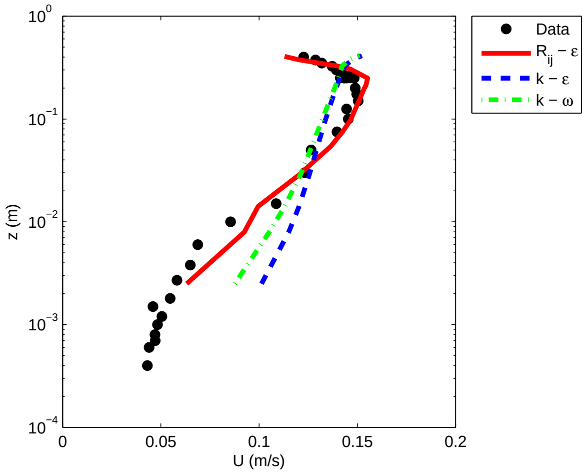

Figure 3.10: Vertical profiles of mean horizontal velocity for waves following currents: semi-log scale. Data from Klopman (1994).

Figures 3.11 (linear scale) and 3.12 (semi-log scale) show the horizontal velocity amplitude profile. All numerical simulations slightly underestimate the measurements, and the $R_{ij} - \varepsilon$ approach shows the best performance. The above-mentioned overshooting is not well represented in this case.

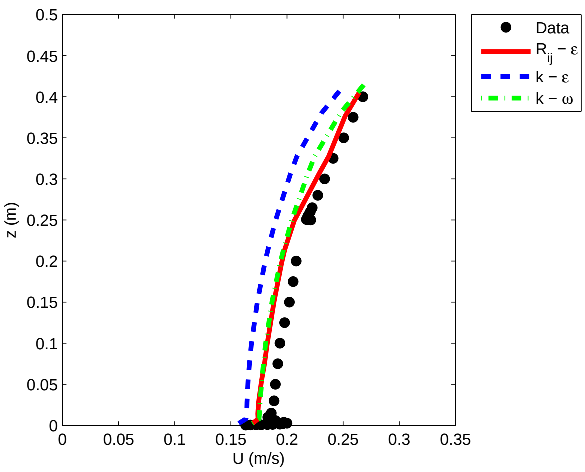

Figure 3.11: Horizontal velocity amplitude profile for waves following currents: linear scale. Data from Klopman (1994).

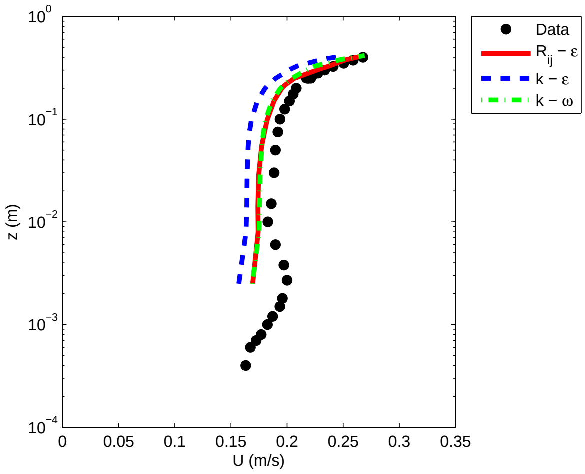

Figure 3.12: Horizontal velocity amplitude profile for waves following currents: semi-log scale. Data from Klopman (1994).

3.3.1.4 The "waves opposing currents"case

In the case of waves opposing the current, an increase in the velocity near the surface was observed by Klopman (1994) and others, such as Kemp and Simons (1983). Similar to the case of waves following currents, the $R_{ij} - \varepsilon$ model showed the best performance, even if the increase of the mean velocity in the upper part of the water column was slightly underestimated and the mean current profile in the middle of the water column was overestimated (Figures 3.13 (linear scale) and 3.14 (semi-log scale)). Nevertheless, the mean horizontal velocity profile showed good agreement through the water column.

Contrary to the waves following the current case, when waves are opposing the mean flow, the current shear velocity is negative and therefore with the same sign of wave induced Reynolds stress contribution. Hence, the mean velocity gradient is going to increase when approaching the free surface.

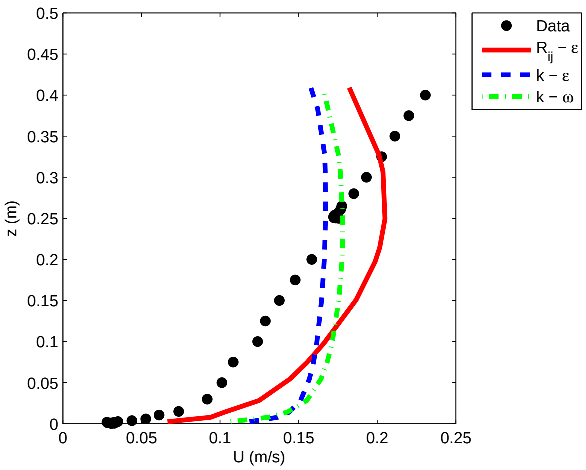

Figure 3.13: Vertical profiles of mean horizontal velocity for waves opposing currents: linear scale. Data from Klopman (1994).

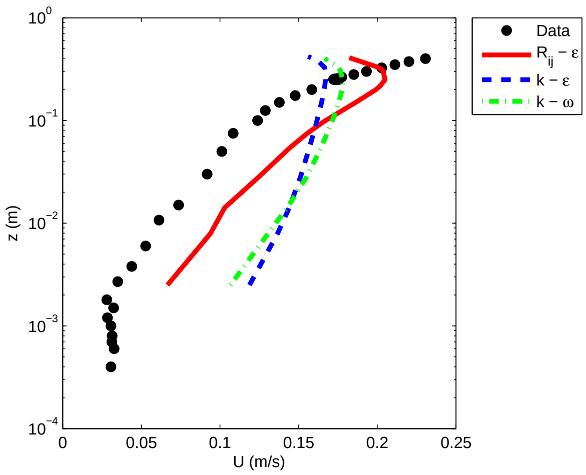

Figure 3.14: Vertical profiles of mean horizontal velocity for waves opposing currents: semi-log scale. Data from Klopman (1994).

The mean horizontal velocity amplitude profile in the case of waves opposing the current is shown in Figures 3.15 (linear scale) and 3.16 (semi-log scale). It can be verified that the $k-\varepsilon$ and $k-\omega$ models underestimate it comparing to the measurements. Even if slightly overestimated, the $R_{ij}-\varepsilon$ shows the best results.

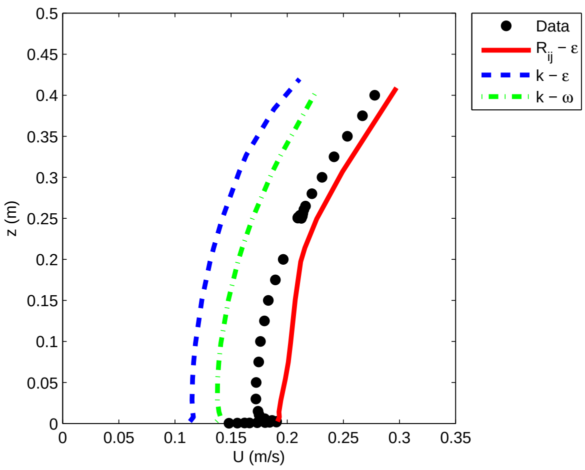

Figure 3.15: Horizontal velocity amplitude profile for waves opposing currents: linear scale. Data from Klopman (1994).

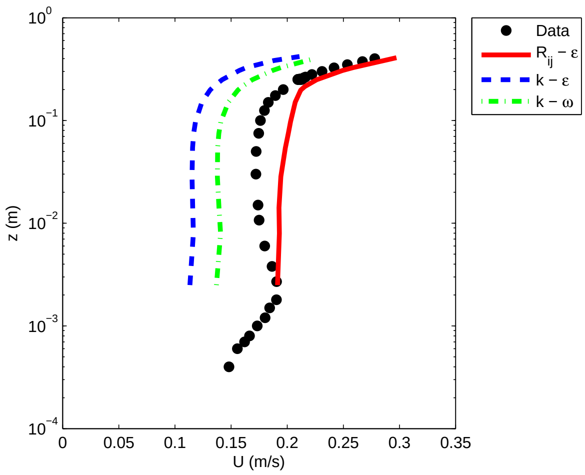

Figure 3.16: Horizontal velocity amplitude profile for waves opposing currents: semi-log scale. Data from Klopman (1994).

3.3.2 Brief discussion about the apparent roughness

For combined waves and currents, the variable z_a is the analogue of the standard roughness length z_0. It is an apparent roughness that plays an important role in the interaction of waves and currents with the bottom boundary layer. It was already identified by Lundgren (1972) by the association of a reduction of the current velocity in the presence of waves, to the increase of the viscosity in the wave boundary layer. It was formalised by Grant and Madsen (1979) and has been used since by a number of researchers (Christoffersen and Jonsson (1985); Soulsby et al. (1993); Fredsœet al. (1999); Houwman and van Rijn (1999); Perlin and Kit (2002); Holmedal et al. (2003); Huang and Mei (2003); Van Rijn (2007);

Olabarrieta et al. (2010)). In these studies, it is clear that the apparent roughness is the dominant roughness factor and a measure of the effect of the waves on the mean current profile above the boundary layer.

The wave induced velocity field increases the turbulence in the wave boundary layer and a reduction of near-bed mean horizontal velocities is observed. This effect is equivalent to an increase of the roughness of the physical bottom boundary and could be parametrized with a high value of the Nikuradse roughness or, which is equivalent, an additional roughness experienced by the current (see Fredsœet al. (1999) for an account of the mechanism responsible for the change of the apparent roughness).

The experimental data obtained by Klopman (1994) showed an increase in the apparent roughness when waves opposed the current as compared to the case with only currents. No such clear increase could be identified in the case of waves following the current. In Figure 3.17 the values of z_a shown were obtained by linear extrapolation of the mean horizontal velocities estimated from the data.

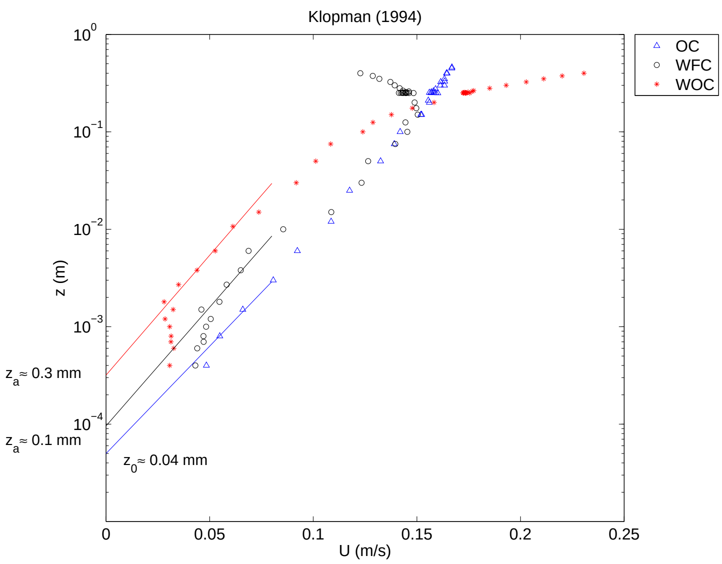

Figure 3.17: Comparison of the vertical profiles of the mean horizontal velocity in a semi-log scale for the cases “only current ”(OC), “waves following the current ”(WFC) and “waves opposing the current ”(WOC). Data from Klopman (1994).

As pointed out, in the present study *Code_Saturne* was applied using a *High Reynolds* number modelling strategy (i.e. a wall function approach in the vicinity of the bottom) and therefore the model is not able to fully resolve the bottom boundary layer. It can be seen from Figure 3.18 that the values obtained by linear extrapolation of the mean horizontal velocities estimated from the *Code_Saturne* model are higher than the initially imposed physical roughness (z_0), both for the waves following and waves opposing the currents cases. This increase is related to the apparent roughness concept.

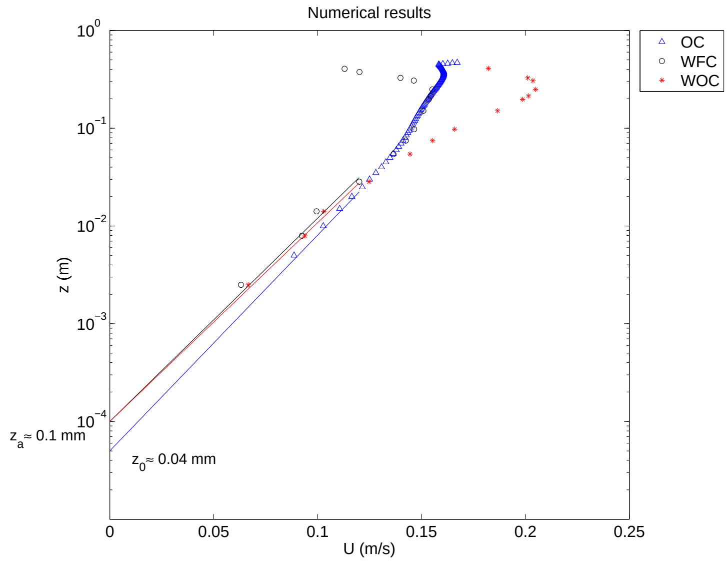

Figure 3.18: Numerical results of the vertical profiles of the mean horizontal velocity in a semi-log scale for the cases “only current ”(OC), “waves following the current ”(WFC) and “waves opposing the current ”(WOC).

3.3.3 Influence of external parameters

3.3.3.1 The “only waves”case

A sensitivity test similar to the one presented previously concerning the choice of the turbulence closure model was also made for Umeyama′s experiments. The same conclusions were achieved and so they are not presented here. More details can be found on Teles et al. (2013a). Therefore, the $R_{ij} - \varepsilon$ turbulence closure model will be used in the *Code_Saturne* for the remainder of this section.

In an experimental flume (described in section 3.2) with waves and currents, Umeyama (2005) measured the vertical profile of the mean horizontal velocity and Reynolds stresses. Four different wave heights and wave periods were considered for the test cases with only waves, waves following currents, and waves opposing currents. The channel had a smooth bed and, contrary to Klopman′s experiments, the z_a parameter did not have an important role.

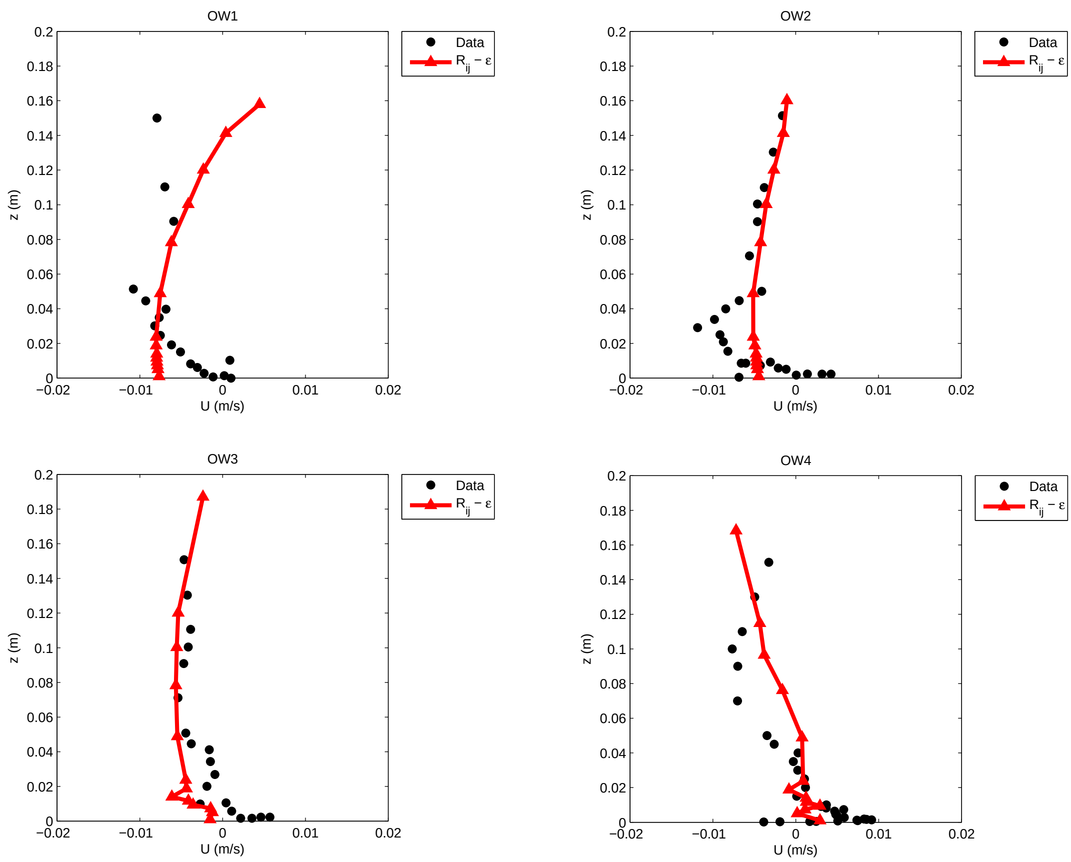

Figure 3.19: Mean velocity vertical profile for only waves: OW1 ($H = 0.0202$ m; $T = 0.9$ s); OW2 ($H = 0.0251$ m; $T = 1$ s); OW3 ($H = 0.0267$ m; $T = 1.2$ s) and OW4 ($H = 0.0280$ m; $T = 1.4$ s). Data from Umeyama (2005).

Figure 3.19 shows the vertical distribution of the mean horizontal velocity for four different wave conditions (in the case of only waves). Again, the model is capable of predicting well the mean horizontal velocity profiles for each case. It is also evident that when the wave height increases, the wave boundary layer effects become more significant.

3.3.3.2 The "waves following currents"case

Figure 3.20 shows the mean horizontal velocity vertical profile when waves are superposed on a turbulent current. For the four different conditions of waves following currents, the velocity increases near the bed and then decreases near the free surface.

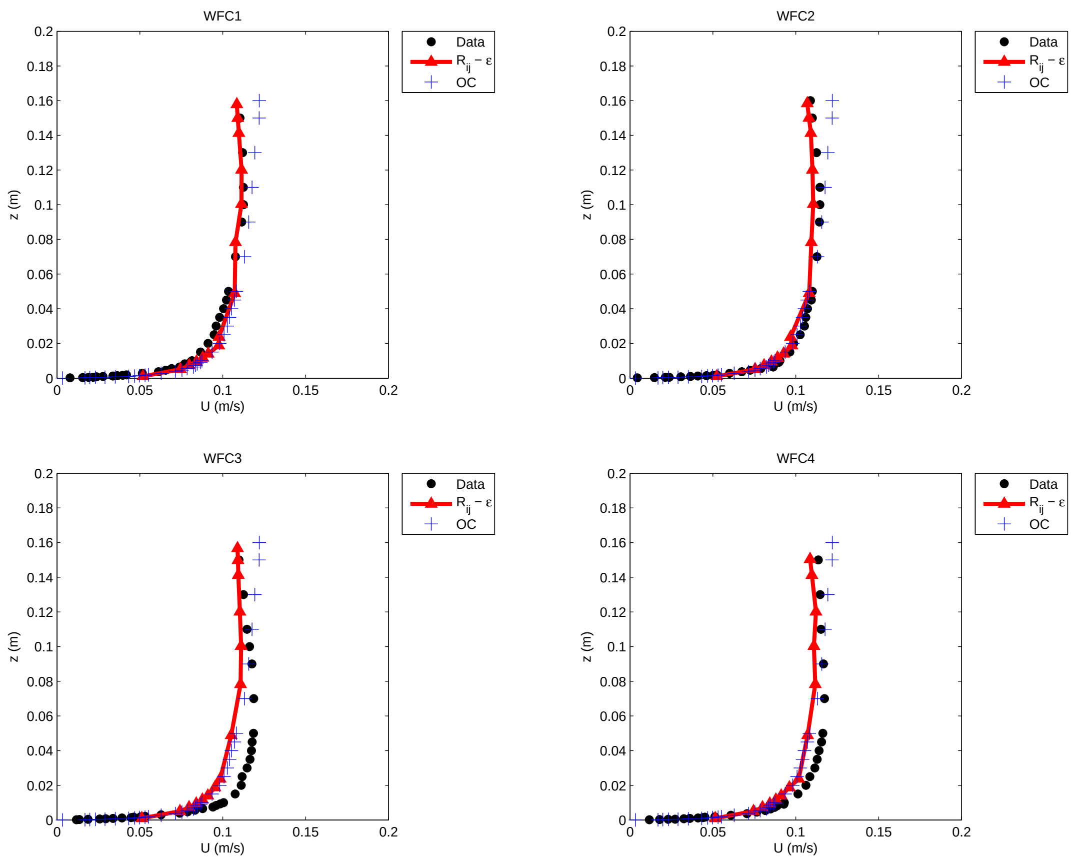

Figure 3.20: Mean velocity vertical profile for only currents (OC) and for waves following currents: WFC1 ($H = 0.0202\ m$; $T = 0.9\ s$); WFC2 ($H = 0.0251\ m$; $T = 1\ s$); WFC3 ($H = 0.0267\ m$; $T = 1.2\ s$) and WFC4 ($H = 0.0280\ m$; $T = 1.4\ s$). Data from Umeyama (2005).

The phase-averaged Reynolds stresses induced by the waves represent the phase-averaged correlation between the horizontal and vertical velocities. In intermediate waters (like in these experiments), Olabarrieta et al. (2010) pointed out that as the wave height increases, this correlation increases, and a sharp decrease in the mean horizontal velocity can be seen. However, as the wave period increases, the vertical component of the particle motion decreases, causing a reduction of Reynolds stresses. The effects of the wave height and wave period oppose each other, which could explain why the decrease in mean velocity does not vary significantly between the experiments. When compared with the experimental results, it can be concluded that the *Code_Saturne* model reproduces well these effects.

3.3.3.3 The "waves opposing currents"case

For waves opposing currents (Figure 3.21), the velocity profile is initially logarithmic, but it begins to deviate, and the velocity shear increases near the free surface. The mean velocity gradient seems to increase with an increase in wave height and wave period. This behaviour is very well reproduced by the numerical simulations in the two more energetic cases. However for the two lower wave conditions some discrepancies are found. Near the free surface the modelled velocity gradient becomes even negative ($H = 0.0202$ m) or approaches to zero ($H = 0.0251$ m). Just above the boundary layer the slight decrease in $\frac{dU}{dz}$ cannot be observed in the model results.

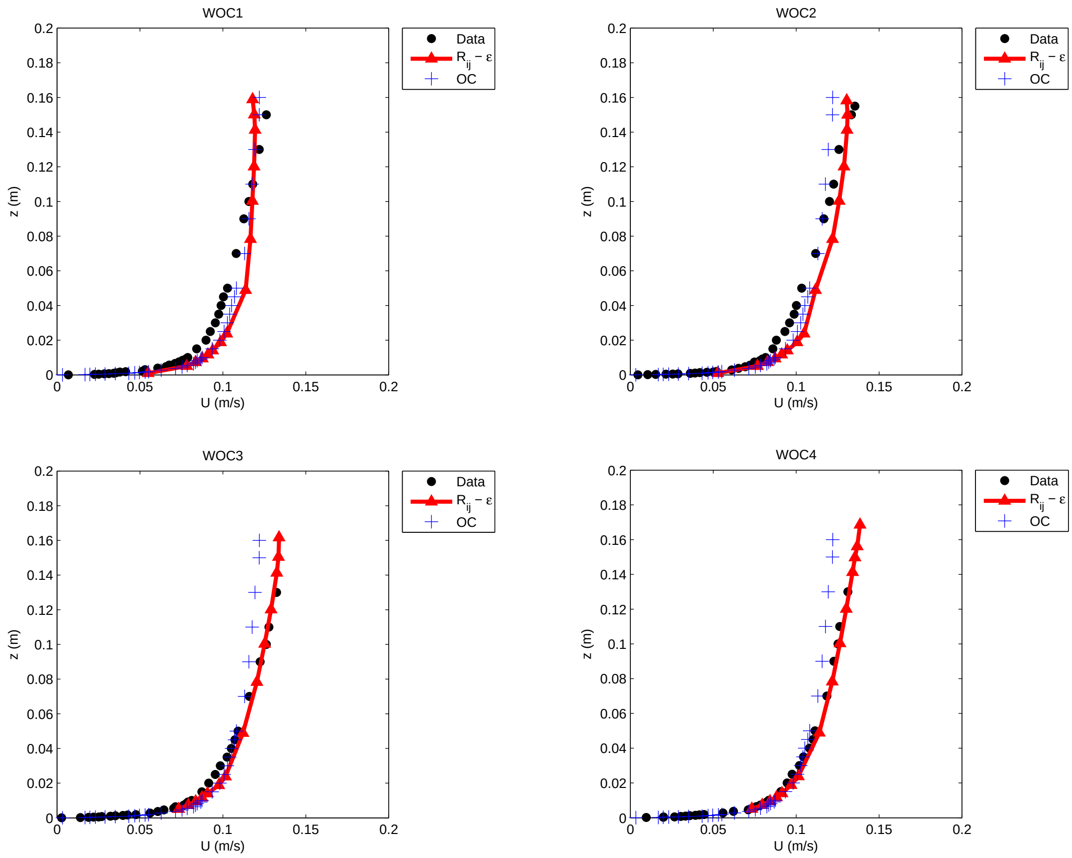

Figure 3.21: Mean velocity vertical profile for only currents (OC) and for waves opposing currents: WOC1 ($H = 0.0202$ m; $T = 0.9$ s); WOC2 ($H = 0.0251$ m; $T = 1$ s); WOC3 ($H = 0.0267$ m; $T = 1.2$ s) and WOC4 ($H = 0.0280$ m; $T = 1.4$ s). Data from Umeyama (2005).

3.4 Vertical profiles of Reynolds stresses and turbulence viscosity

3.4.1 Vertical profile of the R_{xz} Reynolds stress

3.4.1.1 The "only currents"case

It was also of great interest to analyse the capacity of the *Code_Saturne* model to reproduce the vertical profile of the Reynolds shear stress $R_{xz} = - < u'w' >$, and therefore to understand better the different mechanisms that occur in a turbulent flow, such as in a wave-current environment. Firstly, the vertical profile of the Reynolds stress R_{xz} with "only currents"was tested. A comparison was made between the shear stress profile obtained by Klopman (1994) and the results of the *Code_Saturne* model using the three turbulence closure models evaluated in section 3.3. Figure 3.22 shows that the results obtained with both the $k-\varepsilon$, $k-\omega$ and $R_{ij}-\varepsilon$ models agree well with Klopman$'$s data for the entire water column.

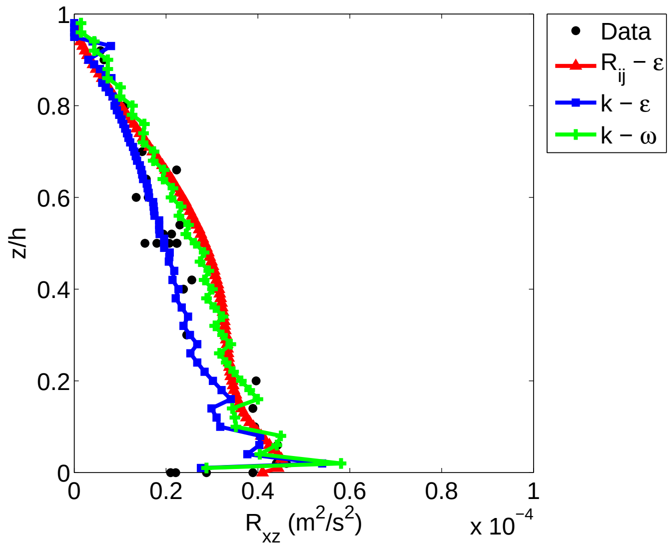

Figure 3.22: Vertical profiles of the Reynolds shear stress $R_{xz} = - < u'w' >$ for the "only currents"case using the three turbulence closure models in *Code_Saturne*. Data from Klopman (1994).

The Reynolds stress vertical profile obtained by the turbulence closure model $R_{ij}-\varepsilon$ was used to evidence the effects of the free surface boundary condition given in (2.53) on the ability of *Code_Saturne* to represent other turbulence related variables. In Figure 3.23, the comparison between numerical results applying and without applying the boundary condition (2.53) is shown. It can be seen that the zero-gradient free surface boundary condition is insufficient to get the decrease of the Reynolds shear stress towards zero. Only the additional empirical conditions proposed by Nezu and Rodi (1986) bring the *Code_Saturne* to a correct behaviour.

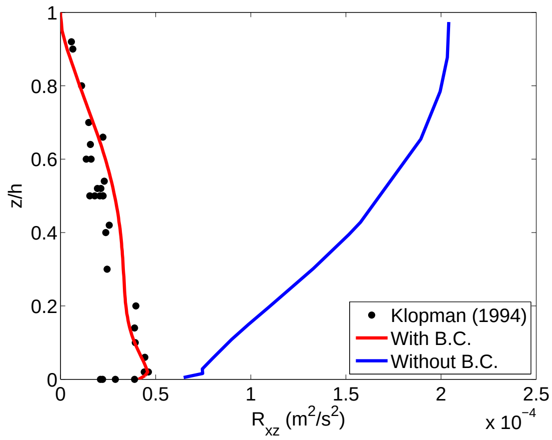

Figure 3.23: Vertical profiles of the Reynolds shear stress $R_{xz} = - < u'w' >$ for the "only currents"case with (With B.C.) and without (Without B.C.) imposing the boundary condition defined in (2.53). Data from Klopman (1994).

The figures below show simulated profiles, for only a current in the channel, of the dimensionless turbulent kinetic energy and the dimensionless dissipation rate (Figure 3.24) with the three turbulence closure models. Semi-empirical formulas (Nezu and Nakagawa, 1993) were also included and used to estimate the dimensionless turbulent kinetic energy (3.1) and dissipation rate (3.2). The comparison of the numerical simulations with the semi-empirical curves shows, in general, the same order of magnitude, particularly close to the surface. It can be observed that the profiles of the non-dimensional turbulent intensities have a similar development over the water depth for each turbulence closure model, with exception of $k-\omega$ SST model. This last model shows, in general, an overestimation for the non-dimensional turbulence kinetic energy, relatively to the $k-\varepsilon$ and $R_{ij}-\varepsilon$ models.

$$\frac{k}{u_*^2} = 4.78e^{-\frac{2z}{h}} \tag{3.1}$$

$$\frac{\varepsilon}{u_*^3} = 9.8\left(\frac{z}{h}\right)^{-\frac{1}{2}} e^{-\frac{3z}{h}} \tag{3.2}$$

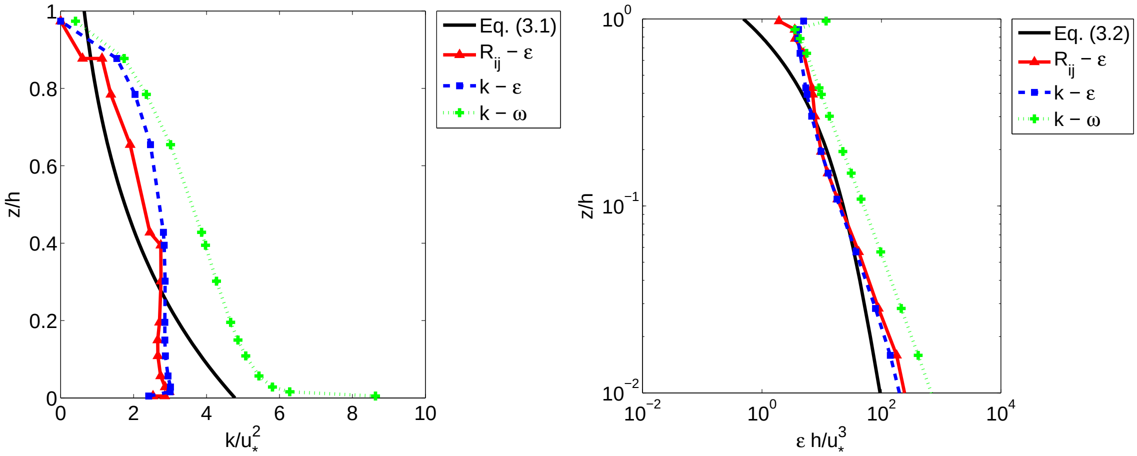

Figure 3.24: Vertical profiles of the non-dimensional turbulence kinetic energy (left panel) and turbulence dissipation (right panel) for the "only current"case using the three turbulence closure models in *Code_Saturne* and semi-empirical formulas. Numerical results obtained for Klopman (1994) experiments.

Following the previous analysis made for Klopman′s data it was also conducted a sensitivity analysis regarding the differences obtained between the three turbulence closure models in the case of Umeyama′s data. The vertical profiles of the non-dimensional Reynolds shear stress, non-dimensional turbulence kinetic energy and non-dimensional turbulence dissipation are presented. It can be verified that both $k-\epsilon$, $k-\omega$ and $R_{ij}-\epsilon$ models reproduce well the non-dimensional Reynolds shear stress throughout the water depth (Figure 3.25).

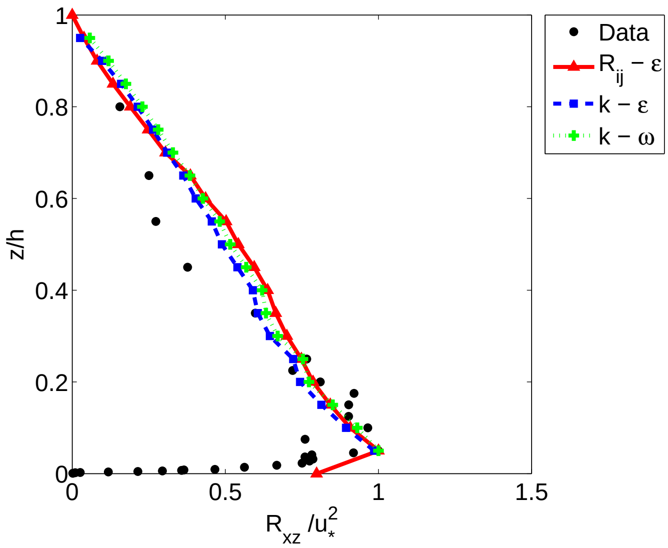

Figure 3.25: Vertical profiles of the non-dimensional Reynolds shear stress $R_{xz} = -\frac{<u'w'>}{u_*^2}$ for the "only currents"case using the three turbulence closure models in *Code_Saturne*. Data from Umeyama (2005).

Once again, the results obtained with the semi-empirical formulas for the dimensionless turbulent kinetic energy (3.1) and dissipation rate (3.2) are compared with numerical results for the three turbulence closure models. It can be seen that in the case of the non-dimensional turbulence kinetic energy (Figure 3.26, on the left), the three turbulence models give similar results between each other. When observing the non-dimensional turbulence dissipation vertical profile (Figure 3.26, on the right) it can be verified that the three turbulence closure models fit quite well the semi-empirical curve calculated by (3.2).

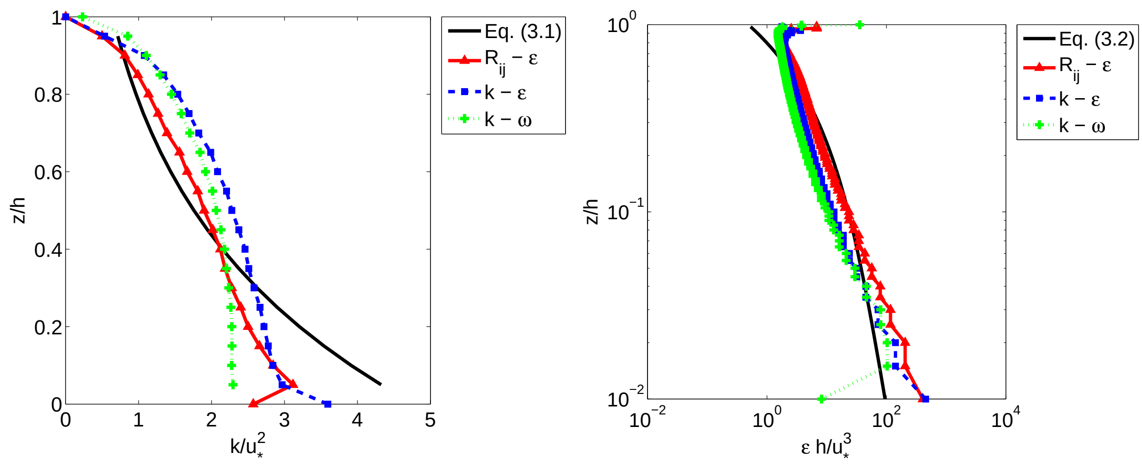

Figure 3.26: Vertical profiles of the dimensionless turbulence kinetic energy (left panel) and turbulence dissipation (right panel) for the "only current"case using the three turbulence closure models in *Code_Saturne* and semi-empirical formulas. Numerical results obtained for Umeyama (2005) experiments.

3.4.1.2 The "only waves"case

Since the Klopman (1994) shear stress data only include the currents only case, the remainder of the comparisons in this section will be completed with the Umeyama (2005) data. The numerical simulations of the *Code_Saturne* will use the $R_{ij} - \varepsilon$ closure approach. As seen in Figure 3.27, the shear stress is almost zero when there are only waves in the flume. In fact, in the only waves case, the flow is characterized by an almost potential flow. It can be verified that the model is able to reproduce the expected monotonic behaviour over the water column. Also the close to zero values computed are what to be expected. However, it can be concluded that in the bottom boundary layer *Code_Saturne* may have some difficulties in representing the shear stress when only waves are present.

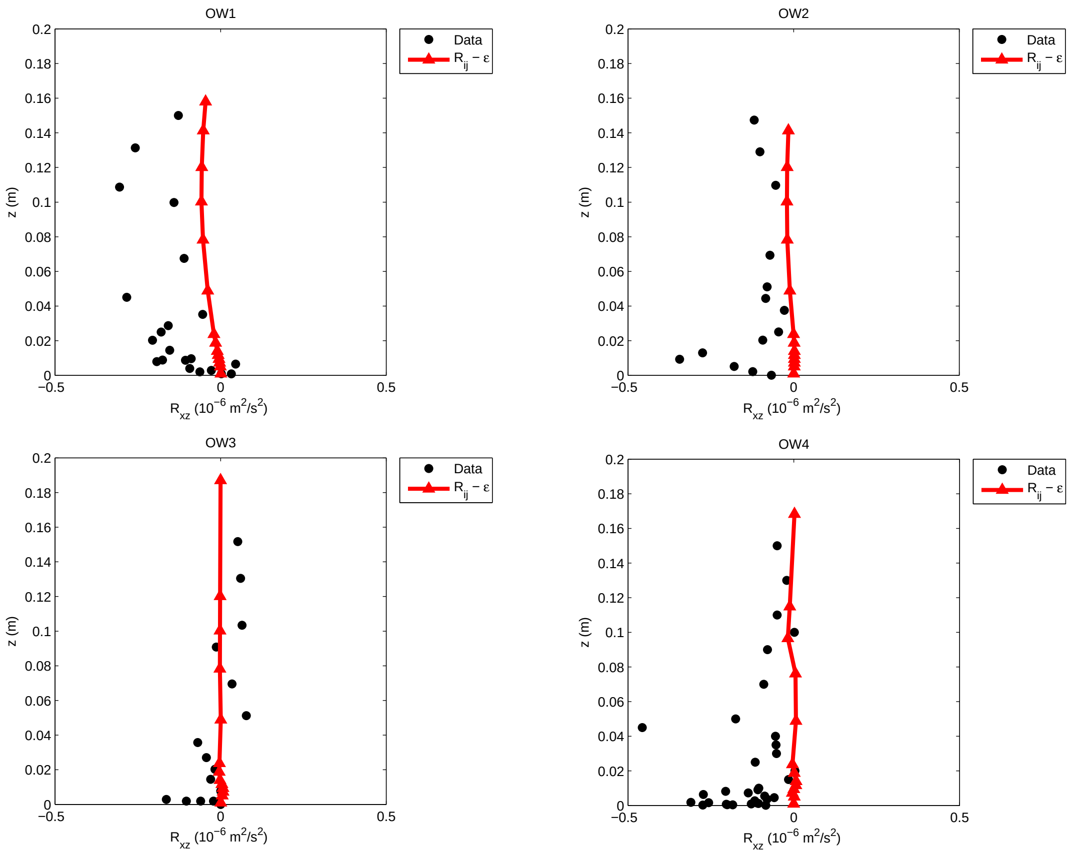

Figure 3.27: Vertical profiles of the Reynolds shear stress $R_{xz} = - < u'w' >$ for "only waves"cases: OW1 ($H = 0.0202\ m$; $T = 0.9\ s$); OW2 ($H = 0.0251\ m$; $T = 1\ s$); OW3 ($H = 0.0267\ m$; $T = 1.2\ s$) and OW4 ($H = 0.0280\ m$; $T = 1.4\ s$). Data from Umeyama (2005).

3.4.1.3 The "waves following currents"and "waves opposing currents"cases

Figures 3.28 and 3.29 present the changes of the vertical profile of the Reynolds stress R_{xz} when progressive waves are superimposed on a current in a flume. The striking feature in Figures 3.28 and 3.29 is the decrease in the Reynolds shear stress in comparison with the values obtained from the only currents experiment (indicated by the + symbol in these figures). The superposition of waves caused a reduction in the turbulence stresses, not only near the bottom, but also over the whole water column. This behaviour was also observed by Kemp and Simons (1982). They refer that somehow the generation of turbulence is also periodic (because of the waves). For this reason part of the turbulence intensities are going to be absorbed into the phase averaged values and do not appear as measured turbulence intensities.

The Reynolds stress intensity has the same average order of magnitude over the water column and does not change significantly with the wave direction. The numerical simulations reproduce well this behaviour, especially in the "waves opposing currents"case (Figure 3.29).

In Figure 3.28, a difference in the modelled and measured Reynolds stresses is observed in the more energetic cases. In particular, the model does not simulate the observed reverse in sign of the Reynolds stress near the surface.

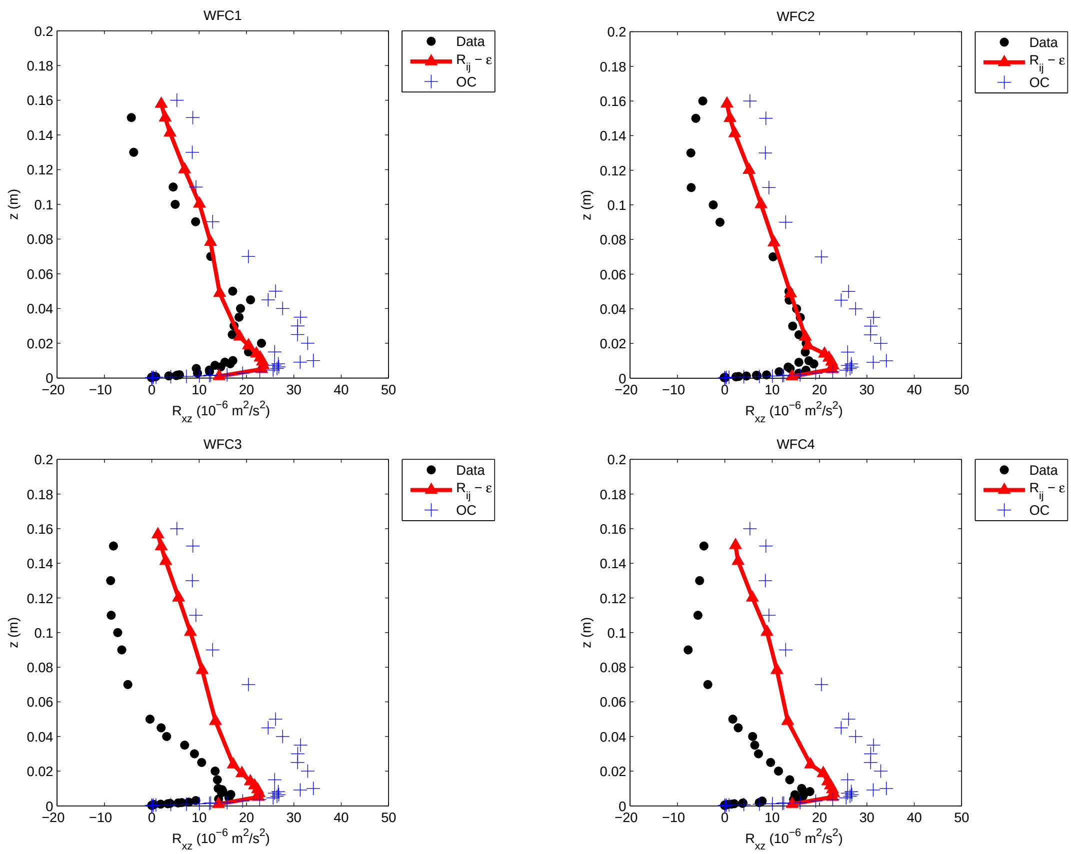

Figure 3.28: Vertical profiles of the Reynolds shear stress $R_{xz} = - < u'w' >$ for only currents (OC) and for "waves following currents"cases: WFC1 ($H = 0.0202\ m$; $T = 0.9\ s$); WFC2 ($H = 0.0251\ m$; $T = 1\ s$); WFC3 ($H = 0.0267\ m$; $T = 1.2\ s$) and WFC4 ($H = 0.0280\ m$; $T = 1.4\ s$). Data from Umeyama (2005).

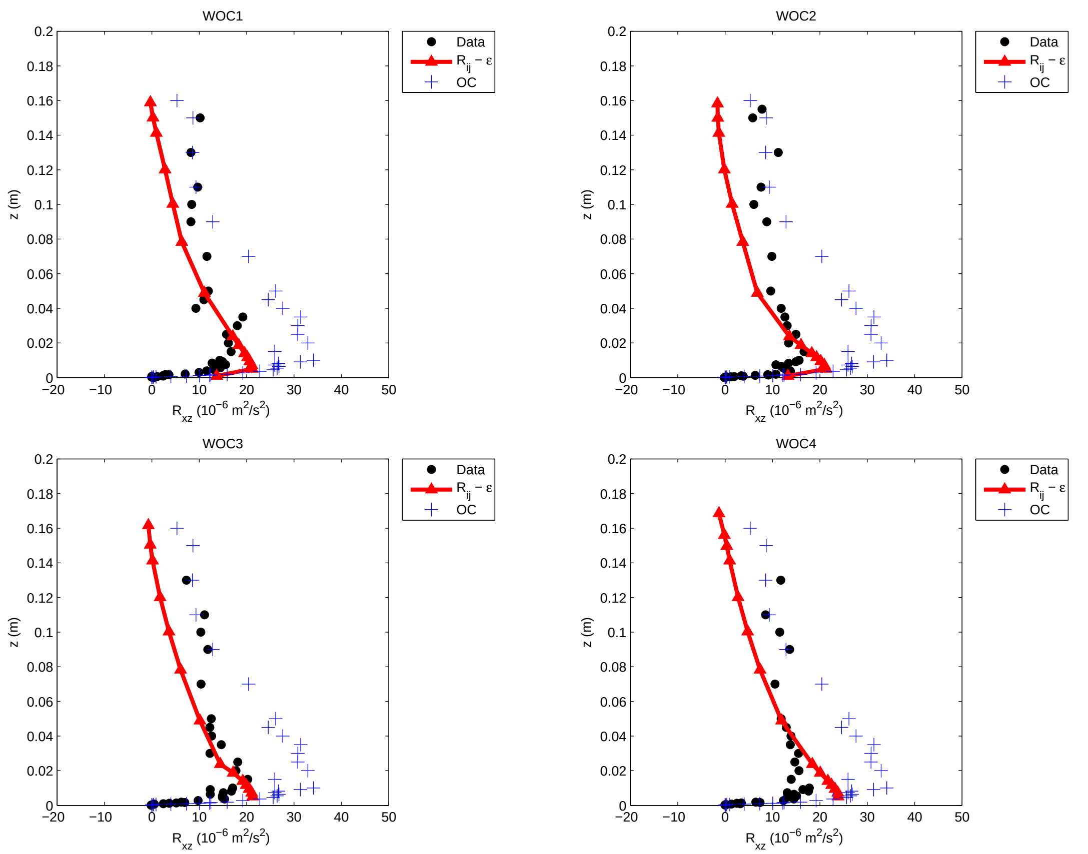

Figure 3.29: Vertical profiles of the Reynolds shear stress $R_{xz} = -<u'w'>$ for only currents (OC) and for "waves opposing currents"cases: WOC1 ($H = 0.0202\ m$; $T = 0.9\ s$); WOC2 ($H = 0.0251\ m$; $T = 1\ s$); WOC3 ($H = 0.0267\ m$; $T = 1.2\ s$) and WOC4 ($H = 0.0280\ m$; $T = 1.4\ s$). Data from Umeyama (2005).

In general, the *Code_Saturne* had some difficulties modelling the shear stress near the free surface. The observed differences could be caused by neglecting to model the shear stress at the free surface due to interactions between the water and the air (Dore, 1978). In and above the wave boundary layer (in the lower panels of Figure 3.28) no reasons were found for the mismatches observed between the numerical results and experimental data.

Moreover, it was decided to make the comparison between the dimensionless Reynolds shear stress obtained with the three turbulence closure models for the "waves following current "and the "waves opposing current "cases and Umeyama'*s* data. This was done only with the first test case from Umeyama′s data.

It can be observed that in both "waves following current "(Figure 3.30) and the "waves opposing current "(Figure 3.31) cases, the three turbulence closure models give similar results between each other throughout the water depth.

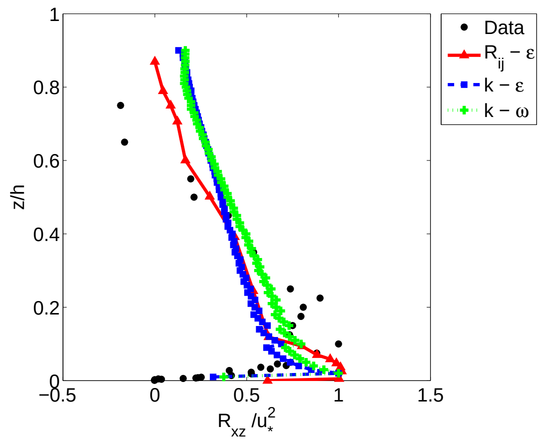

Figure 3.30: Vertical profiles of the non-dimensional Reynolds shear stress for the “waves following current ”case using the three turbulence closure models in *Code_Saturne*. Data from Umeyama (2005).

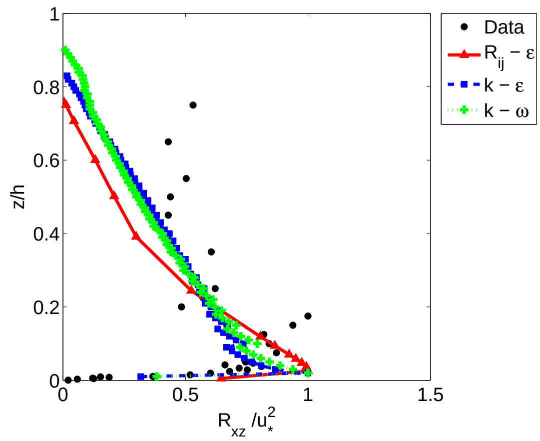

Figure 3.31: Vertical profiles of the non-dimensional Reynolds shear stress for the “waves opposing current ”case using the three turbulence closure models in *Code_Saturne*. Data from Umeyama (2005).

3.4.2 Vertical profile of turbulence viscosity

As previously mentioned, analytical expressions for the vertical profile of the turbulence viscosity in environments with waves and currents have been proposed (e.g. Christoffersen and Jonsson (1985); Huang and Mei (2003)).

The turbulence closure model $R_{ij} - \varepsilon$ has the advantage of solving for the turbulence dissipation ε and the Reynolds stresses R_{ij}, without relying on the eddy viscosity assumption. Nevertheless, one may estimate the value of the eddy viscosity a posteriori from the $R_{ij} - \varepsilon$ model results. In the *Code_Saturne* model, this estimate is obtained with equation (10), where k is computed as:

$$k = \frac{1}{2}\left(R_{xx} + R_{yy} + R_{zz}\right) \tag{3.3}$$

These estimates of the turbulence viscosity will be used to determine a parameterisation over the entire depth in relation to external variables. First, the conditions of the Nezu and Rodi (1986) experiments, an “only current”(OC) experiment, were considered and presented in Figure 3.32. In this figure, z is the elevation from the bottom, h is the water depth, and u_* is the friction velocity. At the bottom and at the (moving) free surface the turbulence viscosity is zero, and it has a parabolic shape over the water depth. These features were well modelled by the *Code_Saturne*, partially showing the effect of the boundary condition (2.53).

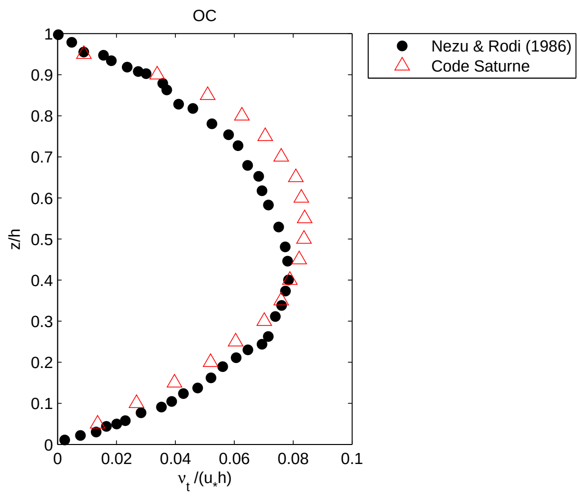

Figure 3.32: Comparison between measured and modelled vertical profiles of non-dimensional eddy viscosity for an open channel flow with only currents (OC). Data from Nezu and Rodi (1986).

Next, waves were superimposed on the current for different values of the wave height and period, as in Umeyama (2005), and the results are shown in Figure 3.33. The general shape of the turbulence viscosity profile does not change significantly when compared to the profile of the “only currents”case. Note that Huang and Mei (2003) also considered a parabolic and continuous profile when dealing with smooth bottoms.

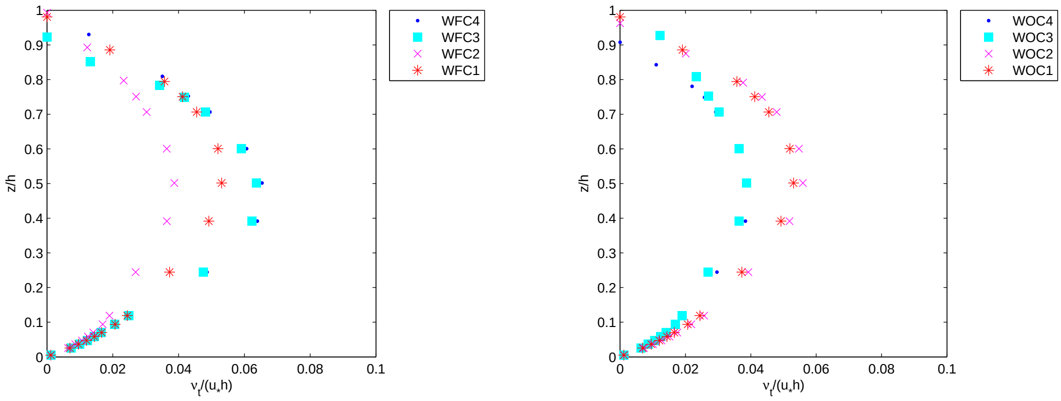

Figure 3.33: Vertical profiles of the non-dimensional turbulence viscosity obtained by the *Code_Saturne* using the $R_{ij}-\varepsilon$ SSG turbulence closure model for tests with different wave heights and wave periods for “waves following currents ”cases (WFC, left panel) and “waves opposing currents ”cases (WOC, right panel).

The relative similarity of the vertical profiles of the non-dimensional eddy viscosity observed in this set of experiments motivated us to search for a simple parameterisation of the eddy viscosity in combined wave-current flows. This parameterisation could then be used as an input in more simplified numerical models.

We therefore sought out a (simple) dimensionless relation between the turbulence viscosity (ν_t), acceleration due to gravity (g), mean velocity (U), water depth (h), elevation from the bottom (z), wave period (T), wave length (L) and wave height (H). After considering several possible relations, it was found that the non-dimensional eddy viscosity $\frac{\nu_t}{gUT^2}$ at each relative elevation z/h appears to decrease approximately linearly with the so-called Ursell number ($U_r = \frac{HL^2}{h^3}$), as illustrated in Figure 3.34. The plotted values correspond to the results of the simulations made with *Code_Saturne* using the Reynolds stress transport model $R_{ij}-\varepsilon$.

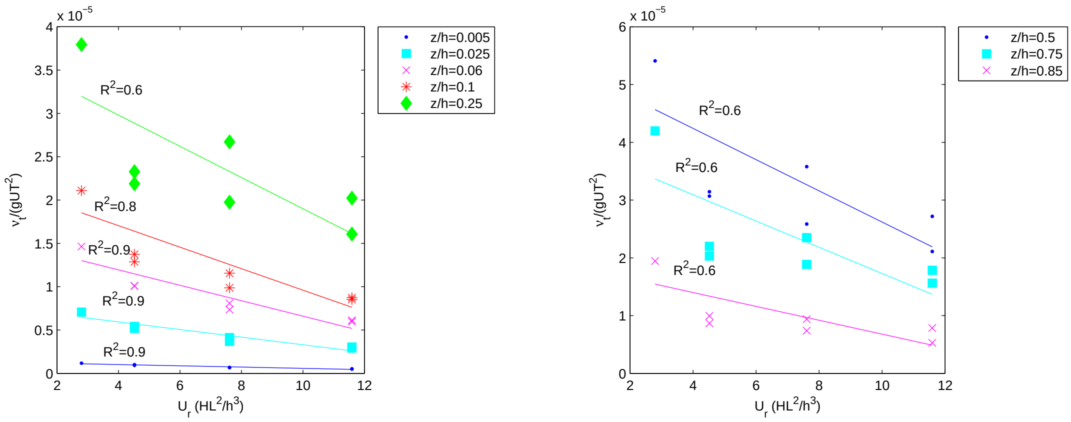

Figure 3.34: Variation of the non-dimensional turbulence viscosity $\frac{\nu_t}{gUT^2}$ for each z/h level as a function of the Ursell number $U_r = \frac{HL^2}{h^3}$.

The trends observed in Figure 3.34 can be used to write an expression for the vertical distribution of the nondimensional eddy viscosity as a function of the Ursell number.

$$\begin{aligned}\frac{\nu_t}{gUT^2}\left(\frac{z}{h}\right) = &\left(10^{-5}U_r - 2\times 10^{-4}\right)\left(\frac{z}{h}\right)^2 \\ &+\left(-10^{-5}U_r + 2\times 10^{-4}\right)\left(\frac{z}{h}\right) + \left(10^{-7}U_r - 2\times 10^{-6}\right)\end{aligned} \tag{3.4}$$

Figure 3.35 shows the vertical profile of the non-dimensional turbulence viscosity (from (3.4)) for the wave-current interaction simulations. Here, four different wave conditions ($OW1$, $OW2$, $OW3$, $OW4$), corresponding to four different Ursell numbers (U_{r1}, U_{r2}, U_{r3}, U_{r4}), were superimposed on a current.

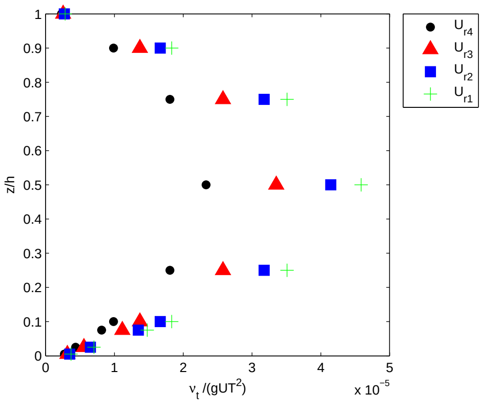

Figure 3.35: Vertical distribution of the non-dimensional turbulence viscosity $\frac{\nu_t}{gUT^2}$ in function of non-dimensional water depth z/h for different Ursell numbers (U_{r1}, U_{r2}, U_{r3}, U_{r4}) corresponding to the four test wave conditions ($OW1$, $OW2$, $OW3$, $OW4$).

However, we stress that this tentative parameterisation of the eddy viscosity needs to be validated with a more extensive set of data. Once validated, it could be used in simplified models that rely on the eddy viscosity assumption for the turbulence closure scheme.

3.5 Conclusions of Part I

With the aim of studying wave-current interaction in a detailed manner, an existing CFD solver based on the RANS equations [the *Code_Saturne* (Archambeau et al., 2004)] was applied to model combined wave-current free surface turbulent flows. The wave and current hydrodynamics were thus solved simultaneously at an intra-wave scale. The Arbitrary Lagrangian-Eulerian (ALE) method was used to model the time-varying free surface dynamics.

Four different hydrodynamic conditions were considered: only currents, only waves, waves following currents, and waves opposing currents. Laboratory data from Klopman (1994) and Umeyama (2005) was used to verify the numerical results, with particular attention paid to the vertical profiles of the mean flow velocity, as well as the amplitudes of the horizontal orbital velocity and shear stresses for each of the test cases.

A sensitivity analysis of turbulence closure models in *Code_Saturne* was completed to determine the appropriate model for simulating wave-current interaction. The results were obtained without any modification of the default values of the parameters in the turbulence schemes. A boundary condition for the turbulence dissipation was imposed at the free surface. Celik and Rodi (1984)'s expression for the turbulence dissipation at the free surface was used, and it was shown to be essential to reproduce correctly the vertical profile of the Reynolds stresses and turbulence viscosity. In *Code_Saturne*, the second-order Reynolds Stress Transport turbulence model (the $R_{ij} - \varepsilon$ SSG version by Speziale et al. (1991)) showed the best performance in the modelling of wave-current interaction when compared to the results obtained with first-order $k - \varepsilon$ and $k - \omega$ two-equation models. For these types of flows, the second-order $R_{ij} - \varepsilon$ model has the advantage that the Reynolds stresses are solved directly, and the model does not have to make any a priori assumptions about the turbulence viscosity.

As a general conclusion, the various comparisons showed that the model is capable of resolving the vertical structure of the combined flows. The model reproduced well the change in the vertical gradient of the mean horizontal velocity profile caused by the presence of waves following or opposing a mean flow. When waves are superimposed in the same direction as the current, there is a significant reduction in the mean horizontal velocity near mid-depth. When waves propagate in the opposite direction of the current, the vertical shear of the horizontal velocity increases. Yang et al. (2006) stated that the wave induced Reynolds stresses, non uniformity of the flow, and secondary currents all contribute to this effect.

When comparing the model results with the data from Umeyama (2005) a good agreement was also obtained. However, no general conclusions could be made concerning the changes in the vertical mean current profiles since the wave height and wave period increases have opposing effects.

It was also observed that the values obtained by linear extrapolation of the mean horizontal velocities estimated from the *Code_Saturne* model are higher than the initially imposed physical roughness (z_0), both for the waves following and waves opposing the currents cases. This effect is a common feature of the wave and current combined environment. This is equivalent to an enhanced roughness which is the so-called apparent roughness.

It is worth to point out that, as a consequence of using a *High Reynolds* number modelling strategy in *Code_Saturne* (i.e. a wall function approach in the vicinity of the bottom, the model is not able to fully resolve the bottom boundary layer. In order to reach a fully predictive model throughout the whole water column, several options might be considered: one relies on using existing formulas/relationships to predict the apparent roughness from the geometrical roughness and bulk parameters for waves and current (e.g. Perlin and Kit (2002); Van Rijn (2007)) to be used in a *High Reynolds* number CFD code for the wall function, a second one could be to couple the *High Reynolds* number CFD with a BBL model (such as the one proposed for instance by Fredsœ (1984)), and a third option would be to move to a *Low Reynolds* number modelling strategy with the CFD code. Some of these possibilities will be explored in the near future to improve the present model.

With the data from Umeyama (2005), it was also possible to explore the change in the vertical profile of shear stress for the combined wave-current environment. It was shown that the change of the bed shear stress is important independent of the relative direction of wave propagation. With the superposition of waves and currents a reduction of turbulence stresses is observed not only near the bottom but also throughout the water column.

Since the $R_{ij} - \varepsilon$ turbulence closure model offers the advantage of solving for the turbulence dissipation and Reynolds stresses, we also attempted to exploit the numerical results of the second-order scheme to propose a parameterisation of the turbulence viscosity profile as a function of the Ursell number.

The knowledge gained from this study on the effects of wave-current interaction at local scales, will be used in the forthcoming step of our work to model wave-current interaction at larger scales by using two types of models (one for the mean flow and one for the waves), which will then have to be coupled properly.

Part II

Regional scale

Chapter 4

Wave-current environment theories

4.1 General context

In the first part of the thesis, a local analysis is made for modelling waves and current interaction effects. For that purpose the RANS equations are solved and there is no separation of the two contributions (waves and currents). The flow is entirely solved within the scale of the oscillatory motion of waves. Waves and currents are modelled simultaneously, including turbulence effects.

The effects of the propagation of surface waves on the mean current was scrutinized. It was observed that when waves are superimposed on a turbulent current, important changes occur on the vertical structure of the mean horizontal velocity, amplitude of the mean horizontal velocity and Reynolds shear stress.

This kind of analysis shows a great advantage in modelling the combined flow. It helps to improve the understanding of the physical processes. This kind of approach is quite interesting and advantageous for academic and/or refined scale applications but it is impractical to apply it in regional applications. Particularly at a regional scale, there is a great computer demand to run the simulations. And yet, modelling in larger domains is essential in practical engineering works.

Therefore, the main purpose of the second part of the thesis is to be able to model the three-dimensional (3D) effects of waves and current interactions at a regional scale.

Within the description of the combined wave-current environment at this scale, a number of difficulties can arise. In fact, from offshore to the coast, several effects associated with tides, winds and waves are present in the flow, which is necessarily turbulent.

The nearshore dynamics are dominated by wave-induced and wind-induced forcing terms (Battjes et al., 1990). The coastal waters are an heterogeneous environment and the wind-generated waves propagation is, in general, unsteady. In addition, spatial and time-varying currents can occur due to large scale oceanic circulation, tides or river discharges. Consequently, there are interactions and exchanges of momentum between the wave and current fields.

For these reasons, the waves undergo several modifications when propagating from offshore towards the coast. Shoaling, refraction and diffraction (Figure 4.1) or breaking (Figure 4.2) are just examples of those depth-induced modifications.

Figure 4.1: Photos of shoaling (on the left), refraction and diffraction (on the right) effects when waves propagate towards the coast. Sources: www.surfline.com and www.geographyfieldwork.com.

Figure 4.2: Photo of waves breaking on a beach. Source: www.giantrelease.com.

The wave-induced mass transport and gradients of the excess momentum flux force the mean flow originating the build up of pressure gradients and changes on the mean water level. Furthermore, the loss of momentum by waves due to breaking in the surf zone generates driving currents, with both cross-shore and longshore components. For instance, the longshore currents along the littoral zone are generated by an oblique incidence of propagating waves, relative to the coastline (Figure 4.3, on the left). A larger incident angle of waves induces a stronger current. Also, if the waves propagate towards different beaches morphologies, such as barred or cusped beaches, this can generate currents that pass through the channels that link the bars or cusps. These so-called rip currents are directed offshore (Figure 4.3, on the right) and can attend large velocities ($O(1)\ ms^{-1}$).

Figure 4.3: Photos of longshore currents (on the left) and rip currents (on the right) induced by waves propagation and breaking. Sources: www.ozcoasts.gov.au and www.noaa.gov.

The orbital motion of water particles due to wave propagation can induce a current near the bottom, with the same direction of wave propagation - the streaming effect, a second-order effect that puts in evidence the role of viscosity. This effect originates changes in the bottom morphology and it influences the bottom stress and thus it can have a great influence on the analysis of sediment transport.

Additionally, the propagation of waves induces a mean flow, the so-called Stokes drift, also a high-order effect that will be formalized latter in this chapter. The concept of Stokes drift was first described by Stokes (1847). Schematically, it can be said that the path made by the fluid particles is not completely closed.

Moreover, the interaction of the wave field with an ambient current (either general circulation currents, tidal currents, discharge currents or wave-induced currents) also induce several important changes on wave propagation. They modify some characteristics of the wave field. They can lead, for instance, to refraction in the case of heterogeneous flow fields and modification of the wave-number and the frequency (the so-called Doppler effect).

Therefore, the presence of waves and currents in a combined environment induces changes not only on the mean flow characteristics but also on wave propagation.

Due to its importance for understanding coastal hydrodynamics, the wave-current interaction environment in free surface flows has been the subject of several studies. Moreover, a number of coastal numerical models have undergone considerable development in the last decades.

Particularly in the surf zone there are intense transfers from the organized wave motion to the mean flow. Therefore, it is necessary to assess the partitioning between the two components of the water motion (waves and currents), with influence of turbulence effects.

At nearshore, incident wave periods are typically in the range between of 2.5 s to 25 s. The natural lengths are typically $1/k$ in the horizontal scale ($k = \frac{2\pi}{L}$ is the wave number and L the wave length) and the water depth (h) in the vertical scale. In what concerns the large motions of the oceans for instance tidal currents, they are typically characterized by a time scale of hours and developed in a larger spatial domain. Therefore different time and space scales can co-exist in the coastal domain (Figure 4.4).

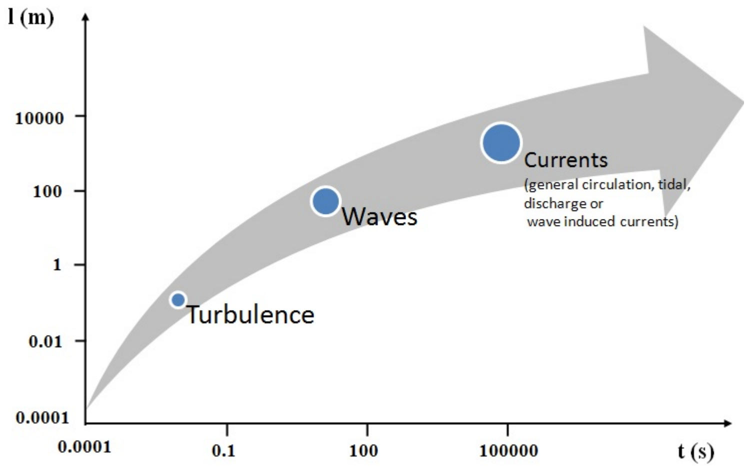

Figure 4.4: Different characteristic time (t (s)) and spatial (l (m)) scales for turbulence, waves and currents.

When waves and currents interact, a problem arises since the separation of the two contributions (currents and waves) is not so evident. As mentioned previously, different time and spatial scales co-exist in this combined environment. Therefore, to deal with this kind of combined environment, an averaging technique over the higher frequency waves and turbulence is used to get a separation of the total motion (Phillips (1977), Mei (1989), Dingemans (1997)).

If the average is performed in the time domain, it will be done over several wave periods (T), and represents a time scale much lower than the time scale of the mean motion variability (Dingemans, 1997).

The pioneer works on dealing with waves and current interactions and their numerical modelling were focused on a two-dimensional (2D) description. The effects of waves were taken into account on a depth-integrated and time-averaged mean flow.

Although the great contribution of 2D, depth-integrated currents approaches, there is a lack of information regarding the vertical structure of the flow. Furthermore, it has been shown that a considerable current shear over depth exists when waves and current interact (Ardhuin et al., 2008b). For this reason a number of theories have been proposed in the past decade to describe the fully 3D wave-current interaction effects. Different approaches are considered and exposed, depending on the way the equations are dealt with: from a Eulerian mean, a Lagrangian mean or a generalized Lagrangian mean (GLM) point of view (Figure 4.5).

The present chapter is divided in the following way. Firstly, the effects of waves on the mean current are focused. For this purpose, a review was first made within the 2D approaches to better understand the phenomena of the effects of waves on the mean flow (section 4.2). This is followed by section 4.3, where a review of the existing 3D theories of the combined wave-current environment is made. The objective was to find the approach that would best suit our main purpose for this second part of the thesis: the modelling of wave-current interaction at a regional scale. On subsections 4.3.2 and 4.3.3, the theoretical framework chosen in this work is described in more detail. Finally, the effects of currents on the wave field are addressed in section 4.4.

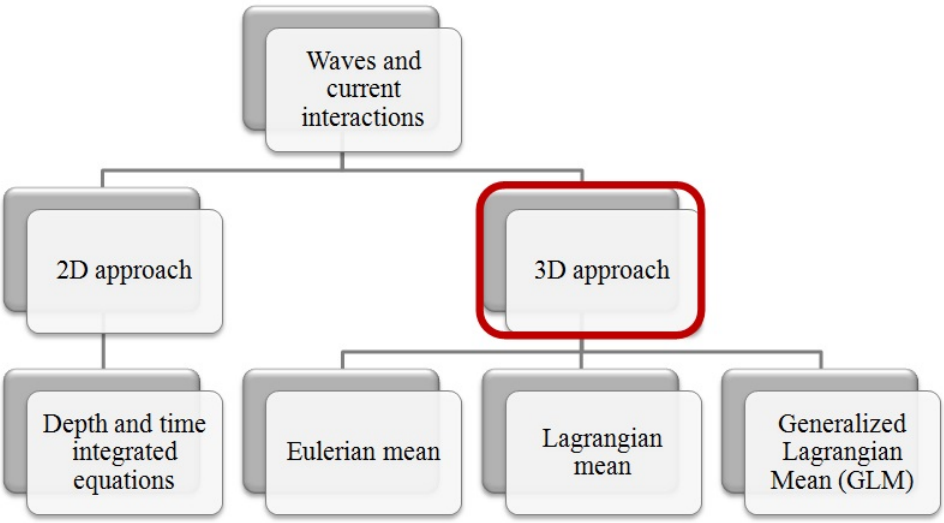

Figure 4.5: Different approaches to deal with the wave-current environment.

4.2 Effects of waves on the mean current - 2D description

4.2.1 Starting point equations

The starting point for the description of water waves interacting with the mean flow are the governing equations of motion for an incompressible fluid. The water density variation is neglected within a fluid parcel and therefore for incompressible flows, the continuity (4.1) and the momentum equations (4.2 and 4.3) per unit volume read:

$$\frac{\partial u_j}{\partial x_j} + \frac{\partial w}{\partial z} = 0 \tag{4.1}$$

$$\frac{\partial \rho u_i}{\partial t} + \frac{\partial \rho u_i u_j}{\partial x_j} + \frac{\partial \rho u_i w}{\partial z} = -\frac{\partial p}{\partial x_i} + \frac{\partial \tau_{ji}}{\partial x_j} + \frac{\partial \tau_{3i}}{\partial z} \tag{4.2}$$

$$\frac{\partial \rho w}{\partial t} + \frac{\partial \rho u_j w}{\partial x_j} + \frac{\partial \rho w^2}{\partial z} = -\frac{\partial (p+\rho g z)}{\partial z} + \frac{\partial \tau_{j3}}{\partial x_j} + \frac{\partial \tau_{33}}{\partial z} \tag{4.3}$$

The body forces (per unit mass) that act on the fluid element are considered here to consist only of the acceleration gravity vector $g = [0,0,-g]^T$. The horizontal velocity components are expressed by u_i or u_j, where the indices i and j assume the values 1 and 2. w is the vertical velocity component, p the pressure and ρ the specific mass. The components of the viscous stress tensor are represented by $\tau_{ji}, \tau_{3i}, \tau_{33}$. For a Newtonian fluid, the stress tensor is $\sigma_{ij} = -p\delta_{ij} + \tau_{ij}$, where $\tau_{ij} = \mu \left(\frac{\partial u_i}{\partial x_j} + \frac{\partial u_j}{\partial x_i} \right)$.

The above equations are valid from the bottom level $z = -h(x,y)$ to the instantaneous free surface elevation $z = \eta(x,t)$. In Figure 4.6 some variables are defined, such as $\overline{\eta}$ representative of the mean surface elevation, h the still water depth and $D = h + \overline{\eta}$ the total mean water depth.

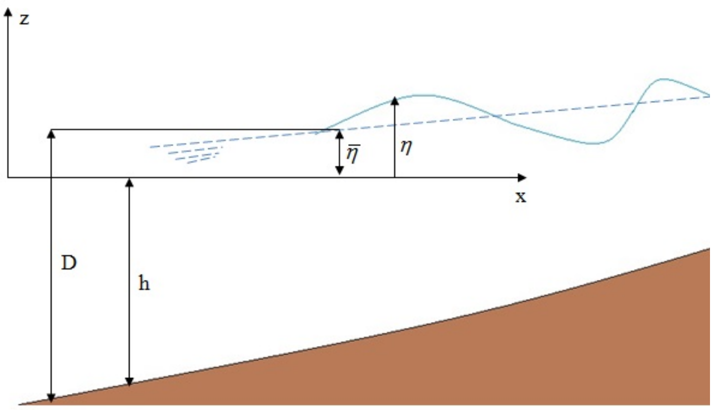

Figure 4.6: Definition of different variables.

Regarding the boundary conditions, both air-water interface (free surface) and the bottom surface must be specified. The free surface is defined as a moving impermeable boundary in which the velocity of the fluid perpendicular to the boundary is equal to the normal velocity of the boundary itself. It is considered that the bottom is impermeable and that does not vary with time. The kinematic boundary conditions defined at the free surface (4.4) and the bottom (4.5) are then the following:

$$w|_{z=\eta} = \frac{\partial \eta}{\partial t} + u_j \frac{\partial \eta}{\partial x_j} \tag{4.4}$$

$$w|_{z=-h} = -u_j \frac{\partial h}{\partial x_j} \tag{4.5}$$

In what concerns the dynamic free surface condition, it is considered that the interface between the two fluids is continuous and the pressure for $z = \eta(x,t)$ is equal to the atmospheric pressure p_a.

$$p|_{z=\eta} = p_a \tag{4.6}$$

4.2.2 Mean flow equations

4.2.2.1 Depth-integrated and time-averaged mass conservation equation

In the following sections, the symbol $\overline{(.)}$ represents the time average of a function over the wave period T of a monochromatic wave (4.7).

$$\overline{\phi} = \frac{1}{T}\int_{t-T/2}^{t+T/2} \phi dt \tag{4.7}$$

In a Eulerian framework, $\overline{u}_i$ is the time-averaged horizontal Eulerian velocity. The horizontal velocity is then decomposed into a mean (time-averaged) component ($\overline{u}_i$) and a residual component ($\tilde{u}_i$) (4.8).

$$u_i = \overline{u}_i + \tilde{u}_i \tag{4.8}$$

In order to describe the mean horizontal motion, equations (4.1), (4.2) and (4.3) are depth-integrated throughout the water depth and then time-averaged.

First, to obtain the depth-integrated equations, the Leibnitz$'$ rule has to be introduced:

$$\frac{\partial}{\partial x}\int_{\alpha}^{\beta} \phi(x,z)dz = \int_{\alpha}^{\beta} \frac{\partial \phi(x,z)}{\partial x}dz + \phi(x,\beta)\frac{\partial \beta}{\partial x} - \phi(x,\alpha)\frac{\partial \alpha}{\partial x} \tag{4.9}$$

With the help of (4.9) and applying the vertical integral to (4.1), the mass conservation equation integrated over depth is obtained:

$$\begin{aligned} &\int_{-h}^{\eta}\left(\frac{\partial u_j}{\partial x_j} + \frac{\partial w}{\partial z}\right)dz = 0 \Leftrightarrow \int_{-h}^{\eta}\frac{\partial u_j}{\partial x_j}dz + w|_{z=\eta} - w|_{z=-h} = 0 \\ &\Leftrightarrow \frac{\partial}{\partial x_j}\int_{-h}^{\eta} u_j dz - \left[u_j\frac{\partial \eta}{\partial x_j} - w\right]_{\eta} + \left[-u_j\frac{\partial (h)}{\partial x_j} - w\right]_{-h} = 0 \end{aligned} \tag{4.10}$$

Applying the kinematic boundary conditions (4.4) and (4.5), equation 4.10 is simplified:

$$\frac{\partial \eta}{\partial t} + \frac{\partial}{\partial x_j}\int_{-h}^{\eta} u_j dz = 0 \tag{4.11}$$

The time-averaged and depth-integrated mass conservation equation is then:

$$\frac{\partial \overline{\eta}}{\partial t} + \frac{\partial}{\partial x_j}\overline{\int_{-h}^{\eta} u_j dz} = 0 \tag{4.12}$$

4.2.2.2 Depth-integrated and time-averaged momentum conservation equations

First, the horizontal momentum equation (4.2) is integrated over depth. For that purpose, the kinematic boundary conditions (4.4) and (4.5) are used and the Leibnitz rule (4.9) is applied. The left hand side (L.H.S) and right hand side (R.H.S) of the horizontal momentum equation become, respectively:

$$\int_{-h}^{\eta}\left(\frac{\partial\rho u_i}{\partial t}+\frac{\partial\rho u_i u_j}{\partial x_j}+\frac{\partial\rho u_i w}{\partial z}\right)dz=\frac{\partial}{\partial t}\int_{-h}^{\eta}\rho u_i dz+\frac{\partial}{\partial x_j}\int_{-h}^{\eta}\rho u_i u_j dz \tag{4.13}$$

$$\begin{aligned}\int_{-h}^{\eta}(-\frac{\partial p}{\partial x_i}+\frac{\partial\tau_{ji}}{\partial x_j}+\frac{\partial\tau_{3i}}{\partial z})dz=\\ -\frac{\partial}{\partial x_i}\int_{-h}^{\eta}pdz+p_a\frac{\partial\eta}{\partial x_i}+p|_{z=-h}\frac{\partial h}{\partial x_i}\\ +\frac{\partial}{\partial x_j}\int_{-h}^{\eta}\tau_{ji}dz-\tau_{ji}|_{z=\eta}\frac{\partial\eta}{\partial x_j}-\tau_{ji}|_{z=-h}\frac{\partial h}{\partial x_j}+\tau_{3i}|_{z=\eta}-\tau_{3i}|_{z=-h}\end{aligned} \tag{4.14}$$

The viscous stress terms at the free surface and at the bottom can be represented, respectively, by $\tau_j^F=-\tau_{ji}|_{z=\eta}\frac{\partial\eta}{\partial x_j}+\tau_{3i}|_{z=\eta}$ and $\tau_j^B=\tau_{ji}|_{z=-h}\frac{\partial h}{\partial x_j}+\tau_{3i}|_{z=-h}$.

Putting together the L.H.S. (4.13) and R.H.S.(4.14) of the equation, the horizontal momentum equation integrated over depth is obtained.

$$\begin{aligned}\frac{\partial}{\partial t}\int_{-h}^{\eta}\rho u_i dz+\frac{\partial}{\partial x_j}\int_{-h}^{\eta}\rho u_i u_j dz=\\ -\frac{\partial}{\partial x_i}\int_{-h}^{\eta}pdz+\frac{\partial}{\partial x_j}\int_{-h}^{\eta}\tau_{ji}dz+p_a\frac{\partial\eta}{\partial x_i}+p|_{z=-h}\frac{\partial h}{\partial x_i}+(\tau_j^F-\tau_j^B)\end{aligned} \tag{4.15}$$

To obtain the bottom pressure, the vertical momentum equation (4.3) is integrated over depth.

A time average is then applied to (4.15). With the decomposition (4.8) and taking into account that $\overline{\tilde{u}}=0$, we have that $\overline{u_i u_j}=\bar{u}_i\bar{u}_j+\overline{\tilde{u}_i\tilde{u}_j}$. The depth-integrated and time-averaged horizontal momentum L.H.S and R.H.S of the horizontal momentum equations become, respectively:

$$\frac{\partial}{\partial t}\overline{\int_{-h}^{\eta}\rho u_i dz} + \frac{\partial}{\partial x_j}\overline{\int_{-h}^{\eta}\rho u_i u_j dz} =$$
$$\frac{\partial}{\partial t}\int_{-h}^{\overline{\eta}}\overline{\rho u_i}dz + \frac{\partial}{\partial t}\overline{\int_{\overline{\eta}}^{\eta}\rho u_i dz}$$
$$+\frac{\partial}{\partial x_j}\int_{-h}^{\overline{\eta}}\rho \overline{u}_i \overline{u}_j dz + \frac{\partial}{\partial x_j}\overline{\int_{\overline{\eta}}^{\eta}\rho u_i u_j dz} + \frac{\partial}{\partial x_j}\int_{-h}^{\overline{\eta}}\overline{\rho \tilde{u}_i \tilde{u}_j}dz \tag{4.16}$$

$$-\frac{\partial}{\partial x_i}\overline{\int_{-h}^{\eta}pdz} + \overline{p_a\frac{\partial \eta}{\partial x_i}} + \overline{p|_{z=-h}\frac{\partial h}{\partial x_i}} + \frac{\partial}{\partial x_j}\overline{\int_{-h}^{\eta}\tau_{ji}dz} =$$
$$-\frac{\partial}{\partial x_i}\overline{\int_{-h}^{\eta}pdz} + \frac{\partial}{\partial x_j}\overline{\int_{-h}^{\eta}\tau_{ji}dz} + \overline{p_a\frac{\partial \eta}{\partial x_i}} + \overline{p}|_{z=-h}\frac{\partial h}{\partial x_i} + (\overline{\tau_j}^F - \overline{\tau_j}^B) \tag{4.17}$$

Finally the complete equation of the mean horizontal momentum equation (4.15) reads:

$$\frac{\partial}{\partial t}\overline{\int_{-h}^{\eta}\rho u_i dz} + \frac{\partial}{\partial x_j}\int_{-h}^{\overline{\eta}}\rho \overline{u}_i \overline{u}_j dz + \frac{\partial}{\partial x_j}\overline{\int_{\overline{\eta}}^{\eta}\rho u_i u_j dz} + \frac{\partial}{\partial x_j}\int_{-h}^{\overline{\eta}}\overline{\rho \tilde{u}_i \tilde{u}_j}dz =$$
$$-\frac{\partial}{\partial x_i}\overline{\int_{-h}^{\eta}pdz} + \frac{\partial}{\partial x_j}\overline{\int_{-h}^{\eta}\tau_{ji}dz} + \overline{p_a\frac{\partial \eta}{\partial x_i}} + \overline{p}|_{z=-h}\frac{\partial h}{\partial x_i} + (\overline{\tau_j}^F - \overline{\tau_j}^B) \tag{4.18}$$

Longuet-Higgins (1953) and Longuet-Higgins and Stewart (1962, 1964) defined the radiation stress as the mean momentum flux caused by the waves only, S_{ij}.

$$S_{ij} = \overline{\int_{-h}^{\eta}(\rho \tilde{u}_i \tilde{u}_j + p\delta_{ij})dz} - \frac{1}{2}\rho g(h+\overline{\eta})^2\delta_{ij} \tag{4.19}$$

The radiation stress represents the time average of the local momentum fluxes. In the case of non-breaking waves, it can be obtained as a second order quantity from the first order small amplitude wave theory. The concept of radiation stress has been used for several proposes, for instance for wave set-up and wave set-down evaluation, for coastal and rip current analysis or to model the wave-induced currents. When the radiation stress concept is included in (4.18) the final mean horizontal momentum reads:

$$\frac{\partial}{\partial t}\overline{\int_{-h}^{\eta}\rho u_i dz} + \frac{\partial}{\partial x_j}\int_{-h}^{\overline{\eta}}\rho \overline{u}_i \overline{u}_j dz + \frac{\partial}{\partial x_j}\overline{\int_{\overline{\eta}}^{\eta}\rho u_i u_j dz} =$$
$$-\frac{\partial S_{ij}}{\partial x_j} + \overline{p}|_{z=-h}\frac{\partial h}{\partial x_i} - \rho g(h+\overline{\eta})\left(\frac{\partial h}{\partial x_i} + \frac{\partial \overline{\eta}}{\partial x_i}\right) + \overline{p_a\frac{\partial \eta}{\partial x_i}} + \frac{\partial}{\partial x_j}\overline{\int_{-h}^{\eta}\tau_{ij}dz} + (\overline{\tau}_j^F - \overline{\tau}_j^B) \tag{4.20}$$

4.2.3 Two-dimensional approaches

The interaction between waves and current has been subject of several studies due to its importance for the knowledge and understanding of hydrodynamic processes in the nearshore area.

Longuet-Higgins (1953) and Longuet-Higgins and Stewart (1962, 1964) made a seminal contribution to the description of the driving forces of the wave-induced currents for depth uniform currents. They introduced the concept of radiation stress in a Eulerian framework and implemented the idea that any loss of the oscillatory motion momentum should be transferred to the mean flow momentum and the other way around.

The mean flow equations of mass and momentum conservation, in a wave-current environment, can be dealt taking into account the total momentum (Phillips, 1977) or separating the contributions of each phenomenon (Garret (1976), Smith (2006), Ardhuin (2006)).

Phillips (1977) rewrote the horizontal momentum equations for the total motion, without any separation of the contributions of the mean flow and waves. In his work, those equations are simplified, considering that the mean current is uniform over depth. His approach was one of the seminal theories for dealing with wave current interactions with time-averaged and depth-integrated equations.

Nevertheless, a number of problems arise when the wave forcing terms are expressed in the total momentum equations (Hasselmann (1971), Garret (1976), Smith (2006), Ardhuin et al. (2008b)). For instance, within this framework, the radiation stress concept is complex to define since the effects induced by waves are not distinguished in the two momentum contributions (waves and current). Moreover, the description of the two phenomena, using the same parametrization, with such distinct temporal and spatial scales becomes difficult to achieve when dealing with the total contribution of the momentum flux. For instance, the advection velocities from waves and currents are too distinct. Also, in what concerns the eddy viscosity scales of both phenomena, the Stokes drift is not mixed by turbulence, unlike the mean flow. Therefore, working with the total momentum can lead to errors in the turbulence closure (Ardhuin et al., 2008b).

Therefore, these later works highlight the great interest in working with the separation of the momentum flux due to currents and momentum induced by the waves.

In order to overcome the problems that arose within the total momentum equations, Garret (1976) presented a new approach to deal with the mean flow equations. The total momentum flux (M_i^{tot}) is split into the momentum flux linked to the mean flow (M_i^m) and the momentum flux linked to the waves (M_i^w).

$$\underbrace{\overline{\int_{-h}^{\eta} u_i dz}}_{M_i^{tot}} = \underbrace{\int_{-h}^{\overline{\eta}} \overline{u}_i dz}_{M_i^m} + \underbrace{\overline{\int_{\overline{\eta}}^{\eta} u_i dz}}_{M_i^w} \tag{4.21}$$

His work was pioneering in separating and deriving a set of equations for the contribution of waves and currents. The wave forcing terms that act on the mean flow were deduced by taking into account the changes in the wave momentum flux and subtracting them from the radiation stress divergence. A mechanism for the generation of the Languimir circulation (Figure 4.7) was addressed. The wave refraction due to the current shear induces a change in the wave momentum flux. This change is to be compensated by the vortex force (Craik and Leibovich, 1976) integrated over depth.

Figure 4.7: Photo of Langmuir circulations. Source: www.ldeo.columbia.edu.

Recently, following the work of Garret (1976), other authors (Ardhuin (2006), Smith (2006)) represented the interaction phenomena by deducing the wave forcing terms. These terms are then imposed on the mean flow equations. Consequently, the two different contributions are clearly distinguished.

Smith (2006) evaluates the wave momentum budget to second order in wave quantities. He uses the dispersion, wave number evolution and conservation of wave action to take into account the variability of wave momentum flux. The wave momentum budget is subtracted from the total one and the wave effects on the mean flow are deduced. Afterwards, they are once again injected into the evolution of the total momentum flux. Hence, Smith (2006) made an analysis of wave and current interactions by making a clear distinction between the Eulerian mean, wave mean and the interaction terms. In this work, the depth-induced effects are included in comparison to the work proposed by Garret (1976). Additionally, some expressions reflecting the vertical structure of each forcing term on the mean flow due to waves are deduced. Within the same theoretical framework, Ardhuin (2006) made explicit the wave source and sink terms in the mean flow momentum equations.

There are several issues related to the way the decomposition (4.21) is performed, in particular regarding the averaging of fluid motion in the area comprised between the wave trough and wave crest.

If no separation is made between the wave and mean current contributions, as made by Phillips (1977) no problem is found, and the vertical integral (M_i^{tot}) can be well defined. Nevertheless, when making the separation between both contributions of momentum fluxes from waves and currents, the definition of the vertical integral represented by M_i^w is somehow ambiguous. Particularly, when $\eta < \overline{\eta}$, there is no water, only air. As a result, the Eulerian mean operator becomes difficult to apply beyond the region below the wave trough. For this area, between the wave trough and wave crest, Ardhuin (2006) proposes an extension of the velocity profile from the mean water level up to the free surface.

Even if the contributions in a 2D framework were essential to model the wave effects on the mean flow, they have an important limitation: they are not able to describe the vertical structure of those effects.

The question that arises is: what is the relevance of the 3D effects description in a combined wave-current environment? In the following section a brief overview of the existent 3D theories is presented. The main motivations for the need of a complete description of the flow structure are explained.

4.3 Vertical structure of the mean flow

4.3.1 Three-dimensional approaches

In the above section, a method to separate the two contributions by applying a method of averaging over wave phases was explained (Phillips (1977), Garret (1976), Smith (2006)). Although the great contribution of this kind of approach there is an important limitation: the mean current is considered uniform over the water depth.

In the past decade, several authors have pointed out the relevance of describing 3D effects of waves and current interaction.

The complete description of the flow structure is essential to represent the vertical current shear and mixing effects (Putrevu and Svendsen, 1999). A strong shear of the current is observed outside the surf zone (Haas and Svendsen, 2002). Moreover, the Stokes drift is strongly sheared throughout the water column inside and outside the surf zone (Ardhuin et al., 2008b).

Additionally, the interactions between the oscillatory motion and the turbulence vertical mixing are quite important to be considered when a 3D description of the flow is made (Craig and Banner (1994), Terray et al. (1996)). When waves break they induce an enhanced vertical mixing that contributes to the vertical mixing of the mean flow, particularly near the free surface. Throughout the water depth the vertical diffusion is modified towards the bottom. Consequently there is a contribution to the homogenization of the mean current vertical profile and therefore to the mixing of the different water properties. One practical example of improvement in results by taking into account the wave-enhanced vertical mixing is the modelling of the tracer dispersion, namely pollutants.

The full representation of these phenomena in a 3D way has several advantages. The vertical profile of the current is obtained, giving information about sediment transport since it is linked to the value of the velocities near the bottom. The knowledge of 3D flow characteristics can also be important to assess wave power availability at a certain point.

Nonetheless, to get a complete and correct description of 3D effects, several difficulties are encountered (Dingemans, 1997). One of the main difficulties with the 3D modelling of waves and current interactions is to deal with the air-water interface.

Within a 3D framework, different approaches were presented either in a Eulerian, Lagrangian or Generalized Lagrangian Mean (GLM) coordinate system.

If a Eulerian coordinate system is chosen, some difficulties arise in defining the region between wave trough and wave crest: sometimes there is water and sometimes not. Within this framework the question of the air-water interface can be overcome by using an asymptotic theory where a Taylor extension of the mean flow properties is applied through the free surface (McWilliams et al. (2004), Newberger and Allen (2007a)). Nevertheless, this solution does not describe the real flow in that region and therefore does not give the real flow quantities. Additionally, the definition of the free surface boundary conditions is difficult to define since the level at which they should be applied is rather ambiguous, as it is described by either air or water (Ardhuin et al., 2008b).

Another possible solution for dealing with the air-water interface in 3D is to work within a Lagrangian framework (Pierson (1962), Chang (1969)). Nevertheless, Jenkins (1989) showed that this framework shows some inconveniences. For instance, as time goes on, there is a strong current shear throughout the water depth. Therefore this shear can induce strong distortions in the coordinate system.

Several authors (Xia et al. (2004), Mellor (2003, 2005, 2008, 2011a, 2011b, 2013)) used a Lagrangian description of the combined flow by considering an horizontal displacement equal to zero, but not the vertical one.

A solution to deal with the air-water interface can also lie in the application of the generalized Lagrangian Mean (GLM) theory (Andrews and McIntyre, 1978a). For instance, Groeneweg (1999) and Ardhuin et al. (2008b) worked in the basis of this theoretical framework. Within the GLM theory, a Lagrangian coordinate is used, following the water particle displacement when waves propagate with an associated mean operator.

Likewise, the 2D approaches, the 3D theories for the wave and current interactions description are based either on the description of the total flux momentum (Groeneweg (1999), Mellor (2003), (2005, 2008, 2011a, 2011b, 2013)), or they make the clear separation between the waves and current momentum contributions (McWilliams et al. (2004), Newberger and Allen (2007a), Ardhuin et al. (2008b)) (Figure 4.8).

In the same way as in the 2D approaches, when solving the equations for the total motion, the same parametrization for both waves and current contributions is used. This is quite ambiguous since the wave and current fields have different behaviours. For instance, the separation of the oscillatory motion from the turbulent fluctuations is important since their physical nature is different. While the oscillatory motion is associated with wave propagation, the turbulent eddies are advected along with the fluid particles (Ardhuin et al., 2008b).

In addition, when solving the equations for the total motion, the computational time cost increases. A very refined mesh near the free surface is needed to properly reproduce the vertical shear of the total motion since there is a strong shear of the Stokes drift near the free surface. On the other hand, if the separation between both momentum contributions is made, such a refined mesh is no longer needed, reducing the computation time.

Another disadvantage of working with the total motion, and no less important, is related to the wave momentum flux that exists through the lower and upper faces of the fluid control volume. Within the equations for the total motion, Ardhuin et al. (2008a) and Bennis and Ardhuin (2011) did extensive work showing that important additional momentum fluxes appear when dealing with a bottom slope, relative to a horizontal bottom. If those supplementary momentum fluxes are not taken into account, erroneous results can be obtained. Therefore, they stated that to properly implement this kind of approach, higher order of wave kinematics should be used for some practical applications, such as situations where there is a bottom slope or wave field gradients.

Consequently, the 3D ocean models based on the radiation stress concept (Longuet-Higgins (1953), Longuet-Higgins and Stewart (1962, 1964)) within the total momentum flux equations, should be avoided (at least until nowadays) since they can cause spurious circulations (Ardhuin et al. (2008a), Bennis and Ardhuin (2011), Kumar et al. (2011), Moghimi et al. (2013)).

Recently, many authors replaced the use of the radiation stress concept with equations based on the vortex-force formalism.

Lane et al. (2007) make a clear comparison between the two theoretical frameworks. If the radiation stress concept is used, the following equality is applied:

$$u.\nabla u = \nabla.(uu) + u\underbrace{(\nabla.u)}_{=0} \tag{4.22}$$

If, instead, the vortex force is applied:

$$u.\nabla u = \underbrace{\nabla\frac{|u|^2}{2}}_{\text{Bernoulli head gradient}} + \underbrace{(\nabla \times u) \times u}_{\text{Vortex force}} \tag{4.23}$$

Lane et al. (2007) highlight the advantage of the vortex force formalism compared to the radiation stress concept for clearly representing some phenomena, namely a gradient of the Bernoulli head and a vortex force. The Bernoulli head is a pressure adjustment due to the effects of waves. The vortex force expresses the interaction between the vorticity of the flow and the Stokes drift. Furthermore, the vortex force formalism is better in representing the flux of waves momentum due to non-conservative wave effects, such as wave breaking or wave dissipation due to bottom friction, in the mean flux momentum (Lane et al., 2007).

In the past few years, a number of numerical models have been developed to describe the 3D effects of waves and current interactions based on vortex-force formalism (Newberger and Allen (2007b), Uchiyama et al. (2010), Kumar et al. (2012), Michaud et al. (2012), Delpey (2012)).

Ardhuin et al. (2008b), for instance, deduced new equations based on the generalized Lagrangian Mean (GLM) set of equations for the mean flow (Andrews and McIntyre, 1978a). In the GLM framework, the coordinate system is described by a hybrid Eulerian-Lagrangian approach. Here, the velocities above the wave trough are dealt as quasi-Eulerian velocities, giving a correct description of wave-induced velocities throughout all the water depth. The quasi-Eulerian velocities were first introduced by Jenkins (1989), defined by the difference between the Lagrangian mean velocity and the wave pseudomomentumn.

Ardhuin et al. (2008b) took the advantage of the clear distinction between the oscillatory and the mean motion that the GLM equations provide together with the quasi-Eulerian velocity concept. They were able to get expressions for the wave forcing terms on the mean motion needed to close the GLM equations. Through a change in the vertical GLM coordinates to Cartesian coordinates, they obtained the so-called glm2z-RANS equations. As a result, the problem of the air-water interface and the separation of the wave and current contributions are solved with the 3D modelling of wave-current interaction.

All the disadvantages presented above from different theories together with the advantages provided by the glm2z-RANS equations gave the motivation to choose the glm2z-RANS theoretical framework to work with (Figure 4.8). Additionally, the simplifications of those equations proposed by Bennis and Ardhuin (2011) were followed.

After this introductory section about the different 3D theories, the GLM general properties and particularly the new approach deduced by Ardhuin et al. (2008b), together with simplifications made by Bennis and Ardhuin (2011), are described in more detail.

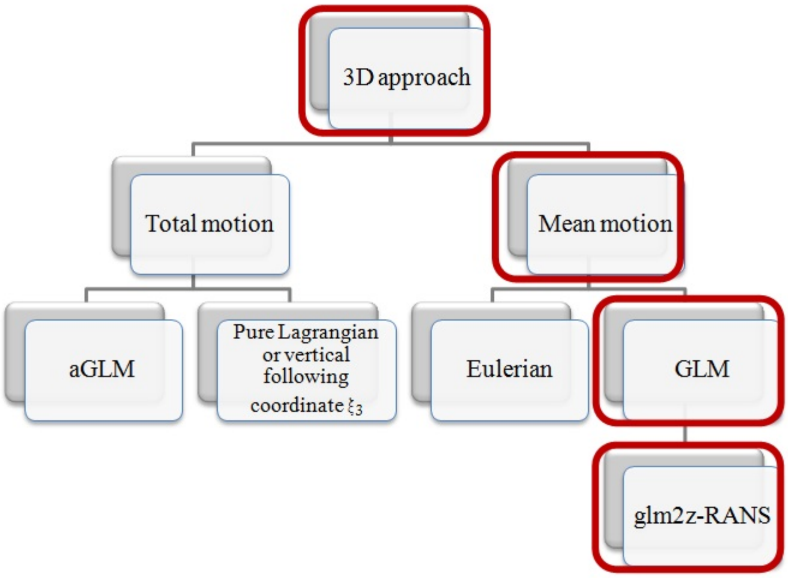

Figure 4.8: Choice of the momentum variable and coordinate system to deal with the 3D wave-current environment.

4.3.2 The GLM theory

4.3.2.1 Overview

Andrews and McIntyre (1978a) derived an exact theory for the mean flow for the case of a stratified, rotating fluid with allowance for self-gravitational effects and an external gravitational field. They derived the so-called Generalized Lagrangian Mean (GLM) equations.

A Lagrangian coordinate is used following the water particle displacement when waves propagate with an associated mean operator. Therefore, the GLM flow gives a correct description in the region between wave crest and wave trough, without being needed to make any sort of analytical developments through this region. As non asymptotic analysis is needed, two sets of exact averaged equations were presented. While the first set of equations describe the evolution of the mean momentum motion, the second one refers to the evolution of the total flow momentum, the so-called alternative generalized Lagrangian mean equations.

The Lagrangian mean flow is described through a hybrid Eulerian-Lagrangian description of the motion. The description of the mean flow is made with position $\mathbf{x}$ and t as independent variables. The difference between the classical Eulerian mean and Lagrangian mean is given by the Stokes correction. In addition, Andrews and McIntyre (1978a) identified the wave flux momentum, the so-called wave pseudomomentum.

When applying the GLM to the continuity and momentum equations, originally written in Eulerian coordinates, it is possible to get a precise separation between the mean flow and wave motion and clearly identify the effects of waves on the current field.

As a result, the GLM equations give an ideal framework to identify the effects of the wave forcing on the mean motion. Consequently, several authors (Uittenbogaard (1992), Dingemans (1997)) applied the exact equations by Andrews and McIntyre (1978a) for the case of water wave problems. This deduction was made under some assumptions, namely incompressibility of the fluid, constant gravity acceleration and no frictional forces.

Later, Groeneweg (1999) and Ardhuin et al. (2008b) applied the GLM to RANS equations in order to get a better description of the 3D effects of wave-current interaction phenomena. From this deduction, it is essential to get a clear distinction of the driving forces of the wave field, which are expressed in terms of mean momentum wave fluxes.

Bühler and McIntyre (1998) gave a clear physical interpretation of the GLM flow. The variables in **bold** denote vectors. In the following Latin indices i, j assume the values 1, 2 or 3.

Consider that a particle has a trajectory that starts at $\mathbf{x}_0$. The velocity, $\mathbf{u}$, is assumed to be averaged over the turbulent motion and thus the trajectory is the ensemble-averaged trajectory, $\frac{d\mathbf{x}}{dt} = \mathbf{u}(\mathbf{x},t)$. When time averaging, two distinct paths for each particle appear: one is the rapidly varying trajectory (the actual trajectory) and the other is given by its mean, the slowing varying part of the trajectory (Figure 4.9).

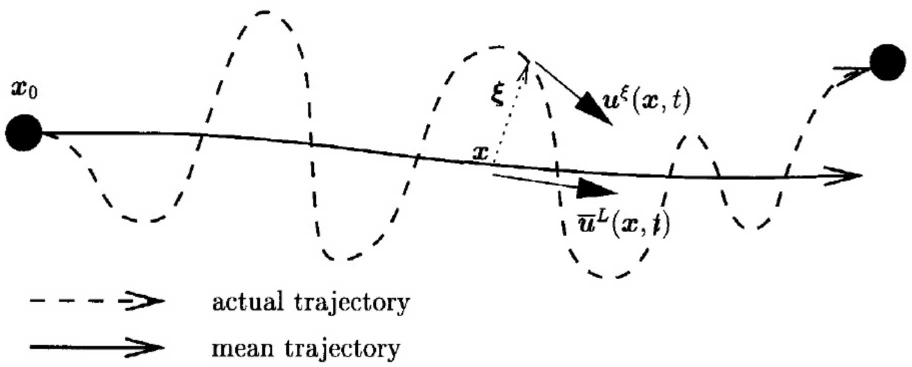

Figure 4.9: GLM representative scheme. The continuous line represents the mean position of the water particles and the interrupted line the instantaneous positions. Source: Bühler and McIntyre (1998).

The two trajectories are linked by the GLM operator through a disturbance-associated particle displacement field $\boldsymbol{\xi}(\mathbf{x},t)$, which in the ensemble averaged set is determined by the wave motion. In the GLM framework, the position $\mathbf{x}$ at time t is considered as a mean position that has one and only one associated actual particle position $\mathbf{x}+\boldsymbol{\xi}(\mathbf{x},t)$.

The generalized Lagrangian velocity, $\mathbf{u}^{\xi}$ (4.24), is evaluated at the actual position but relatively to the mean position.

$$\mathbf{u}^{\xi}(\mathbf{x},t) = \mathbf{u}(\mathbf{x}+\boldsymbol{\xi}(\mathbf{x},t),t) \tag{4.24}$$

The generalized Lagrangian mean velocity, $\overline{\mathbf{u}}^L$ is obtained by taking the mean of (4.24).

If $\boldsymbol{\xi} = 0$ (no waves), it can be seen that the Eulerian ($\mathbf{u}$) and the generalized Lagrangian ($\mathbf{u}^{\xi}$) velocities are equal.

As discussed in section 4.3.1, when dealing with a Eulerian or pure Lagrangian frameworks, some problems arise for the description of wave-current interaction effects. For instance, the definition of the Eulerian mean in the region between the wave trough and the wave crest and the coordinate system distortions that occur within a pure Lagrangian approach (Jenkins, 1989).

In a GLM framework, the free surface is given as a GLM elevation, and even if the chosen coordinate system follows the wave motion, it does not distort with the mean current. Therefore, with this approach the issue of the definition of the flow in the region between wave trough and wave crest is solved. Additionally, it has the advantage of treating all points at location $\mathbf{x}$ as a time dependent reference space for both mean and actual trajectories.

4.3.2.2 General properties of the GLM

The main idea behind the GLM theory is to average over positions displaced by a disturbance motion. The resulting equations are neither purely Lagrangian nor purely Eulerian. The description of the flow is rather characterized by a hybrid Eulerian-Lagrangian approach. It is based on a Lagrangian coordinate and a mean operator associated to it.

In the following a brief description about the main properties of GLM equations is given.

If a Cartesian coordinate system is considered, Andrews and McIntyre (1978a) made the hypothesis that there is a particle displacement associated with a disturbance of the mean field.

Let ϕ be a quantity to be averaged (over wave phase, time, space or ensemble average). Only when the type of flow has to be defined, the mean operator has also to be specified (Dingemans, 1997). The Eulerian mean operator is assigned at position $\mathbf{x}$ and time t as $\overline{\phi} = \overline{\phi(\mathbf{x},t)}$. The Langrangian mean of ϕ is expressed as follows:

$$\overline{\phi}^L(\mathbf{x},t) = \overline{\phi(\mathbf{x},t)}^L = \overline{\phi(\mathbf{x}+\boldsymbol{\xi}(\mathbf{x},t),t)} = \overline{\phi(\mathbf{x},t)^{\xi}} \tag{4.25}$$

$\overline{()}^L$ represents the exact GLM operator. $\overline{\phi}^L(\mathbf{x},t)$ is the generalized Lagrangian mean of the quantity ϕ, i.e., the mean of the quantity ϕ at its disturbed position. $\boldsymbol{\xi}(\mathbf{x},t)$ is the disturbance displacement of the fluid parcel.

A different notation for the disturbed position is used for convenience, such that $\Xi(\mathbf{x},t) = \mathbf{x}+\boldsymbol{\xi}(\mathbf{x},t)$.

One of the assumptions in the GLM approach is that the mapping $(\mathbf{x},t) \rightarrow (\mathbf{x}+\boldsymbol{\xi}(\mathbf{x},t),t)$ is invertible. This means that there is only one mean trajectory that passes through each point $\mathbf{x}$ at a given time t. There is only one mean position ($\mathbf{x}$) associated to the actual position ($\mathbf{x}+\boldsymbol{\xi}$) and vice-versa.

This property of the GLM flow has some consequences in the chain rule, which is:

$$\frac{\partial \phi^{\xi}}{\partial x_i} = \frac{\partial \phi}{\partial \Xi_j}\frac{\partial \Xi_j}{\partial x_i} \tag{4.26}$$

$$\left(\frac{\partial \phi}{\partial x_i}\right)^{\xi} = \frac{\partial \phi^{\xi}}{\partial x_j}\frac{\partial x_j}{\partial \Xi_i} \tag{4.27}$$

The GLM description requires that $\boldsymbol{\xi}(\mathbf{x},t)$ is a true disturbance-associated quantity and therefore:

$$\overline{\boldsymbol{\xi}(\mathbf{x},t)} = 0 \tag{4.28}$$

The generalized Lagrangian mean material derivative ($\overline{D}^L$) is defined as:

$$\overline{D}^L = \frac{\partial}{\partial t} + \overline{u}_j^L \frac{\partial \phi}{\partial x_j} \tag{4.29}$$

One of the properties of the generalized Lagrangian mean material derivative is that:

$$\left(\overline{\frac{D\phi}{Dt}}\right)^L = \overline{D}^L(\overline{\phi}^L); \left(\frac{D\phi}{Dt}\right)^l = \overline{D}^L(\phi^l) \tag{4.30}$$

where,

$$\phi^l = \phi^{\xi} - \overline{\phi}^L \tag{4.31}$$

If we replace the variable ϕ by the velocity field $\mathbf{u}$, the Lagrangian disturbance velocity ($\mathbf{u}^l$) is introduced (Andrews and McIntyre, 1978a), defined as the difference between the actual velocity of a particle $(\mathbf{u}(\boldsymbol{\Xi},t))$ and its velocity at the mean position $\left(\overline{\mathbf{u}}^L(\mathbf{x},t)\right)$:

$$\mathbf{u}^l(\mathbf{x},t) = \mathbf{u}(\mathbf{x}+\boldsymbol{\xi}(\mathbf{x},t),t) - \overline{\mathbf{u}(\mathbf{x},t)}^L = \mathbf{u}(\boldsymbol{\Xi},t) - \overline{\mathbf{u}(\mathbf{x},t)}^L \tag{4.32}$$

$$\mathbf{u}(\boldsymbol{\Xi},t) = \mathbf{u}^{\xi} = \overline{D}^L\boldsymbol{\Xi} \tag{4.33}$$

$$\overline{\mathbf{u}}^L(\mathbf{x},t) = \overline{D}^L\mathbf{x} \tag{4.34}$$

The Lagrangian disturbance velocity ($\mathbf{u}^l$) is then defined by:

$$\mathbf{u}^l(\mathbf{x},t) = \overline{D}^L \boldsymbol{\xi} = \left(\frac{\partial}{\partial t} + \overline{\mathbf{u}}^L \frac{\partial}{\partial x_j}\right) \boldsymbol{\xi} \tag{4.35}$$

4.3.2.3 The Stokes correction

The so-called Stokes correction $\left(\overline{\phi(\mathbf{x},t)}^S\right)$ is defined as the difference between the Lagrangian $\left(\overline{\phi(\mathbf{x},t)}^L\right)$ and the Eulerian means $\left(\overline{\phi(x,t)}\right)$.

$$\overline{\phi(\mathbf{x},t)}^S = \overline{\phi(\mathbf{x},t)}^L - \overline{\phi(\mathbf{x},t)} \tag{4.36}$$

When ϕ denotes the velocity field, $\mathbf{u}$, the Stokes correction is the so-called Stokes drift, $\overline{\mathbf{u}}^S$, and $\overline{\mathbf{u}}^L$ represents the velocity of the water particles mean position.

The perturbation ξ and the perturbed velocity u^l are small quantities that scale with the wave motion, which has an amplitude a and length scale k. The wave amplitude is assumed to be small relatively to the water depth and/or to the wave length. With $\epsilon = ka$ the measure for the wave motion is of $O(\epsilon)$ (Dingemans, 1997).

The Stokes correction is given by Andrews and McIntyre (1978a). Its deduction starts with the following definition:

$$\phi^{\xi}(\mathbf{x},t) = \phi(\mathbf{x} + \xi(\mathbf{x},t),t) \tag{4.37}$$

An expansion in Taylor series is applied on the R.H.S, obtaining:

$$\phi^{\xi} = \phi(\mathbf{x},t) + \xi_j \frac{\partial \phi}{\partial x_j} + \frac{1}{2}\xi_j \xi_k \frac{\partial^2 \phi}{\partial x_j \partial x_k} + O(a^3) \tag{4.38}$$

If a mean is taken from (4.38) and (4.36) is recalled, the Stokes correction is obtained:

$$\overline{\phi}^S = \overline{\xi_j \frac{\partial \tilde{\phi}}{\partial x_j}} + \frac{1}{2}\overline{\xi_j \xi_k} \frac{\partial^2 \overline{\phi}}{\partial x_j \partial x_k} + O(a^3) \tag{4.39}$$

with an implicit summation over repeated indices.

The above relation shows that the Stokes correction is at least of second order in wave slope.

If (4.31) is recalled, another consequence of (4.38) is that:

$$\phi^l = \tilde{\phi} + \xi_j \frac{\partial \overline{\phi}}{\partial x_j} + O(a^2) \tag{4.40}$$

4.3.2.4 Governing equations for water wave problems

Andrews and McIntyre (1978a) derived the exact GLM equations for the compressible Navier-Stokes equations. Later, several authors (Uittenbogaard (1992), Dingemans (1997)) applied the GLM equations for water wave problems.

Let′s rewrite the mass (4.1) and momentum equations (4.2, 4.3) so that for an incompressible flow, it reads:

$$\frac{\partial u_i}{\partial x_i} = 0 \tag{4.41}$$

$$\frac{Du_j}{Dt} + \frac{1}{\rho}\frac{\partial p}{\partial x_j} = X_j + F_j \tag{4.42}$$

The viscous and turbulence effects are represented by X_i and the body forces that act on the mean flow by F_i.

In the present section, the purpose is not to completely derive the governing equations, but rather to give some of the steps made on that derivation. The resulting mass (4.43) and momentum equations (4.45) expressed in terms of GLM variables are presented as in Groeneweg (1999).

$$\frac{\partial \overline{u}_i^L}{\partial x_i} = -\overline{D}^L log(J_a) \tag{4.43}$$

The Jacobian (J_a) of the mapping $(\mathbf{x},t)$ to $(\mathbf{x}+\xi(\mathbf{x},t),t)$ is expressed by (4.44).

$$J_a = \left| \frac{\partial \Xi_j}{\partial x_i} \right| \tag{4.44}$$

Contrary to the Eulerian velocity field divergence-free in an incompressible flow, it can be seen from (4.43) that the GLM velocity field $\overline{\mathbf{u}}^L$ is divergent.

To obtain the momentum equation it is necessary to first rewritten equation (4.42) at its disturbed position:

$$\overline{D}^L u_j^\xi + \frac{1}{\rho^\xi}\left(\frac{\partial p}{\partial x_j}\right)^\xi = F_j^\xi + X_j^\xi \tag{4.45}$$

The matrix $\frac{\partial \Xi_j}{\partial x_i}$ is multiplied by each term of equation (4.45) to write all quantities in their GLM form and the chain rule defined in (4.26) is used.

$$\frac{\partial \Xi_j}{\partial x_i}\overline{D}^L(u_j^\xi) + \frac{1}{\rho}\frac{\partial p^\xi}{\partial x_i} = F_j^\xi\frac{\partial \Xi_j}{\partial x_i} + X_j^\xi\frac{\partial \Xi_j}{\partial x_i} \tag{4.46}$$

The operator $\frac{\partial \Xi_j}{\partial x_i}$ is then brought under $\overline{D}^L$ and relation (4.33) is used. The first term of (4.46) is then expressed by:

$$\frac{\partial \Xi_j}{\partial x_i}\overline{D}^L(u_j^\xi) = \overline{D}^L(u_i^\xi) + \overline{D}^L\left(\frac{\partial \xi_j}{\partial x_i}u_j^\xi\right) - u_j^\xi\frac{\partial u_j^\xi}{\partial x_i} + u_j^\xi\frac{\partial \overline{u}_j^L}{\partial x_i} + u_j^\xi\frac{\partial \xi_j}{\partial x_k}\frac{\partial \overline{u}_k^L}{\partial x_i} \tag{4.47}$$

The averaged momentum equation in terms of GLM variables is obtained by replacing (4.47) in (4.46) and averaging it:

$$\overline{D}^L\overline{u}_i^L + \frac{1}{\rho}\frac{\partial \overline{p}^L}{\partial x_i} - \overline{X}_i^L - \overline{F}_i^L = \frac{1}{2}\frac{\partial \overline{u_j^l u_j^l}}{\partial x_i} + \overline{D}^L\overline{P}_i^L + \overline{P}_j^L\frac{\partial \overline{u}_j^L}{\partial x_i} + \overline{\frac{\partial \xi_j}{\partial x_i}X_j^l} + \overline{\frac{\partial \xi_j}{\partial x_i}F_j^l} \tag{4.48}$$

On the R.H.S of (4.48), the fluctuating quantities are represented.

The so-called wave pseudomomentum per unit mass ($\overline{P}^L$) is defined as (Andrews and McIntyre, 1978b):

$$\overline{P}_i^L = -\overline{\frac{\partial \xi_j}{\partial x_i}u_j^\xi} = -\overline{\frac{\partial \xi_j}{\partial x_i}u_j^l} \tag{4.49}$$

Andrews and McIntyre (1978a) showed the importance of the wave pseudomomentum as a only wave quantity that is forced on the mean motion. For further description about the wave pseudomomentum, please refer to Andrews and McIntyre (1978b).

Furthermore, the relation between the wave pseudomomentum and the Stokes drift was established. Andrews and McIntyre (1978a) showed that if the Eulerian mean velocity is of second order in wave amplitude, the difference between the wave pseudomomentum and Stokes drift is of third order for an irrotational flow.

When the viscous and turbulence effects are left in their general form, it can be affirmed that the GLM equations are exact, i.e., they do not need any asymptotic analyses. If viscous and turbulence effects are to be taken into account, an asymptotic analysis needs to be carried out.

4.3.2.5 Boundary conditions

With the governing equations established within the GLM theory, only the boundary conditions are missing to define a particular problem.

The kinematic boundary conditions, expressed in Eulerian coordinates, considered at the free surface (4.4) and the bottom (4.5), become within the GLM variables:

$$\overline{w}^L|_{z=\overline{\eta}^L} = \frac{\partial \overline{\eta}^L}{\partial t} + \overline{u}_i^L \frac{\partial \overline{\eta}^L}{\partial x_i} \tag{4.50}$$

$$\overline{w}^L|_{z=-\overline{h}^L} = -\overline{u}_i^L \frac{\partial \overline{h}^L}{\partial x_i} \tag{4.51}$$

The dynamic boundary condition is expressed by:

$$\overline{p}^L = \overline{p}_a^L \tag{4.52}$$

4.3.3 Ardhuin et al. (2008b) proposition

4.3.3.1 Methodology and hypothesis

The generalized Lagrangian mean theory can give a correct description for the wave turbulence and current interactions in three dimensions. Different approaches within the GLM framework are referred to, particularly regarding the way the equations are approximated, in what concerns specifying the wave forcing terms.

Andrews and McIntyre (1978a) presented two related sets of averaged equations. One of the set of equations distinguishes the wave momentum from the mean momentum and the other (the so-called alternative GLM equation) uses the total momentum flux.

Groeneweg (1999) used the alternative generalized Lagrangian mean equations (corresponding to Eq.(8.7a) from Andrews and McIntyre (1978a)), approximated to second order in wave slope. On the other hand, Ardhuin et al. (2008b) applied the first set of equations (equation (3.8) from Andrews and McIntyre (1978a)) and found analytical expressions for the wave-induced forcing terms to second order in wave slope needed to explicitly approximate these terms present in the exact equations.

Ardhuin et al. (2008b) dealt with the concept of quasi-Eulerian velocities. This concept was first introduced by Jenkins (1989). He defined the quasi-Eulerian current as the difference between the Lagrangian mean current ($\overline{\mathbf{u}}^L$) from the wave pseudomomentum ($\mathbf{P}$).

$$\hat{\mathbf{u}} = \overline{\mathbf{u}}^L - \mathbf{P} \tag{4.53}$$

The Ardhuin et al. (2008b) proposal has as its starting point equations (4.43) and (4.48), equivalent (with ρ = constant) to the following expressions:

$$\frac{\partial J_a}{\partial t} + \frac{\partial (J_a \overline{u}_i^L)}{\partial x_i} + \frac{\partial (J_a \overline{w}^L)}{\partial z} = 0 \tag{4.54}$$

$$\overline{D}^L \left(\overline{u}_i^L - \overline{P}_i^L \right) = -\frac{\partial}{\partial x_i} \left(\frac{\overline{p}^L}{\rho} - \frac{\overline{u_j^l u_j^l}}{2} \right) - g\delta_{i3} - \epsilon_{i3j} f_3 \overline{u}_j^L + \hat{X}_i + \overline{P}_j^L \frac{\partial \overline{u}_j^L}{\partial x_i} \tag{4.55}$$

$\hat{X}_i$ term is defined as the sum of the dissipative forces with the induced fluctuations and the body force term $\hat{F}_i$ is defined by the Coriolis effect in the horizontal direction and gravitational acceleration in the vertical direction.

$$\hat{X}_i = \overline{X}_i^L + \overline{\frac{\partial \xi_j}{\partial x_i} X_j^l} \tag{4.56}$$

$$\hat{F}_i = \overline{F}_i^L + \overline{\frac{\partial \xi_j}{\partial x_i} F_j^l} = -g\delta_{i3} - \epsilon_{i3j} f_3 \overline{u}_j^L \tag{4.57}$$

If viscous and turbulence effects are to be taken into account, an asymptotic analysis is necessary. It was seen in section 4.39 that the Stokes correction is a quantity with an order equal or greater than two in wave slope. Therefore, if an asymptotic formulation is desired for a small wave slope, the GLM equations need also to be expressed with an order equal to or greater than two.

Hereinafter, the indices α, β refer to the horizontal components and the index 3 to the vertical component.

The overall procedure made by Ardhuin et al. (2008b) is divided into four main steps:

1. The velocity perturbations (u_α^l, w^l) and displacements (ξ_α^l, ξ_3^l) induced by the presence of waves are initially derived at first order in wave amplitude;

2. With the expressions for the fluctuations induced by waves, the wave forcing terms are found to second order in wave slope. These are the horizontal and vertical wave pseudo-momentum (P_α, P_3), the Lagrangian mean Bernoulli head ($\frac{1}{2}\overline{u_j^l u_j^l}$) and the GLM free surface elevation ($\overline{\eta}^L$);

3. Then the wave-induced forcing terms obtained at second order and using (4.53) substituted in the GLM equations (4.54) and (4.55), obtaining what they called glm2-RANS equations. These equations are valid from $z = -h$ to $z = \overline{\eta}^L$;

4. As the resulting glm2-RANS equations are divergent, a change in the vertical coordinate is made taking into account the GLM-induced vertical displacements and correcting the expressions derived before. The final equations are the so-called glm2z-RANS equations.

For an extensive derivation of the glm2z-RANS approach please refer to Ardhuin et al. (2008b) or Delpey (2012). The main steps of this deduction and hypotheses made are once again repeated here.

First, a number of hypotheses were assumed by Ardhuin et al. (2008b) to be able to derive the wave forcing terms needed to close the GLM equations. In order to get explicit expressions for the wave-induced effects, first monochromatic waves are considered with the wave energy equal to $E = \frac{a^2}{2}$. The waves are characterized by the amplitude a, local wave number $\mathbf{k} = (k_x, k_y)$, radian frequency, ω, and local wave phase, φ. The wave slope is $\epsilon = ka$. The intrinsic wave frequency (σ) is assumed to verify the dispersion relationship, $\sigma = \sqrt{gktanh(kD)}$. $D = h + \overline{\eta}$ is the local mean water depth defined by the sum of the bottom local depth (h) with the mean free surface elevation ($\overline{\eta}$). The nabla symbol (∇) represents the horizontal gradient operator. Hereinafter the hypotheses made by Ardhuin et al. (2008b) are enumerated. In the following $\epsilon = max\epsilon_i$.

- The wave slope is small compared to unity;

$$\epsilon_1 \approx max(|\nabla\eta|) << 1 \tag{4.58}$$

- The Ursell number is small, $Ur = (a/D)/(kD)^2 < 1$;

- Derivations are restricted to first order in the slow spatial scale ϵ_2;

$$\epsilon_2 \approx max\left(\left|\frac{1}{ka}\frac{\partial a}{\partial x_\alpha}\right|, \left|\frac{1}{\sigma}\frac{\partial \bar{u}}{\partial x_\alpha}\right|, \left|\frac{\partial D}{\partial x_\alpha}\right|\right) \tag{4.59}$$

$$\epsilon_2 \approx max\left(\left|\frac{1}{a\sigma}\frac{\partial a}{\partial t}\right|, \left|\frac{1}{\sigma^2}\frac{\partial k\bar{u}}{\partial t}\right|, \left|\frac{k}{\sigma}\frac{\partial D}{\partial t}\right|\right); \tag{4.60}$$

- The curvature of the current is weak or concentrated in a thin boundary layer, i.e., ϵ_3 is smaller than an unity;

$$\epsilon_3 = \frac{1}{\omega sinh(kD)}\int_{-h}^{\eta}\left|\frac{\partial^2 u}{\partial z^2}\right| sinh\left(2k(z+h)\right)dz << 1; \tag{4.61}$$

- Additionally they assume that:

$$a^2\left[\partial^3 \bar{u}_\alpha/\partial z^3/(\sigma)\right] \leq \epsilon_3; \tag{4.62}$$

- The mean flow is assumed to follow the hydrostatic hypothesis. Consequently, the vertical velocity $\hat{w}$ is neglected in the vertical momentum equation for the mean flow momentum.

Moreover, in the work developed in this thesis, an additional hypothesis was made for simplicity in the implementation of the glm2z-RANS theory in the numerical models. This particular hypothesis follows the work of Bennis and Ardhuin (2011), in which they made the assumption that the velocity vertical shear is weak relatively to the oscillatory motion scale (4.63).

$$\epsilon_4 \approx \left|\frac{1}{\sigma}\frac{\partial \bar{u}_\alpha}{\partial z}\right| << 1 \tag{4.63}$$

4.3.3.2 Wave-induced forcing terms

In this subsection, the main purpose is to expose the wave-induced forcing terms that will after be replaced in the GLM momentum equation (4.55). The resulting GLM equations will be approximated to second order in wave amplitude.

First, the wave-induced pressure ($\tilde{p}$) and wave-induced horizontal and vertical velocities ($\tilde{u_\alpha}$ and $\tilde{w}$), given by linear theory are expressed below.

$$\tilde{p} = \rho g a \left[F_{cc} cos\varphi + O(\epsilon) \right] \tag{4.64}$$

$$\tilde{u}_\alpha = a\sigma \frac{k_\alpha}{k} \left[F_{cs} cos\varphi + O(\epsilon) \right] \tag{4.65}$$

$$\tilde{w} = a\sigma \left[F_{ss} sin\varphi + O(\epsilon) \right] \tag{4.66}$$

The water density ρ is considered constant. Fcc, Fcs, Fss are expressed by:

$$F_{cc} = cosh(kz + kD)/cosh(kD) \tag{4.67}$$

$$F_{cs} = cosh(kz + kD)/sinh(kD) \tag{4.68}$$

$$F_{ss} = sinh(kz + kD)/sinh(kD) \tag{4.69}$$

Within the hypotheses made by Ardhuin et al. (2008b), the expressions for the vertical and horizontal Lagrangian velocity perturbations (w^l, u^l_α) and vertical and horizontal displacement (ξ_3, ξ_α) are obtained to first order in wave amplitude.

First the vertical Lagrangian velocity perturbation (w^l) is calculated by recalling (4.40) and replacing the variable ϕ by the vertical velocity w. To lowest order in wave amplitude, the vertical Lagrangian perturbation becomes:

$$w^l = \tilde{w} \tag{4.70}$$

With the above expression obtained for the vertical Lagrangian velocity perturbation together with the relation obtained in (4.35) regarding the mean material derivative, the following equation is achieved:

$$\frac{\partial \xi_3}{\partial t} + \overline{u}^L_\alpha \frac{\partial \xi_3}{\partial x_\alpha} = \tilde{w} \tag{4.71}$$

The hypothesis (4.60) is then applied obtaining the expression for vertical displacement, ξ_3:

$$\xi_3 = am(\mathbf{x}, t) F_{ss} cos\varphi \tag{4.72}$$

With $m(\mathbf{x},t) = \frac{\sigma}{\omega - \mathbf{k}_\alpha - \overline{\mathbf{u}_\alpha}^L}$. The shear correction parameter m differs from the unity by a quantity of order $\sigma^{-1} \frac{\partial \overline{u}}{\partial z}$ (Ardhuin et al., 2008b). This means that if the additional hypothesis made by Bennis and Ardhuin (2011) (4.63) is assumed, the $m(\mathbf{x},t)$ function tends to the unity.

Regarding the horizontal Lagrangian velocity perturbation (u^l_α), this term is calculated by recalling (4.40) and replace the variable ϕ by the horizontal velocity u_α.

$$u^l_\alpha = \tilde{u}_\alpha + \xi_\beta \frac{\partial \overline{u}_\alpha}{\partial x_\beta} + \xi_3 \frac{\partial \overline{u}_\alpha}{\partial z} + O\left(\epsilon^2\right) \tag{4.73}$$

Here, it is considered (4.59). Furthermore, the expressions for the wave-induced horizontal velocity (4.65) and for the vertical displacement (4.72) are replaced in (4.73). Finally u^l_α reads:

$$u^l_\alpha = a\left(\sigma \frac{k_\alpha}{k} F_{cs} cos\varphi + m(\mathbf{x},t) F_{ss} \frac{\partial \overline{u}_\alpha}{\partial z} cos\varphi\right) + O\left(\epsilon^2\right) \tag{4.74}$$

If the additional hypothesis (4.63) is made, the terms that have the vertical current shear associated to them can be neglected to first order in wave slope. Therefore (4.74) becomes:

$$u^l_\alpha = a\sigma \frac{k_\alpha}{k} F_{cs} cos\varphi + O\left(\epsilon^2\right) \tag{4.75}$$

The horizontal displacement (ξ_α) is obtained through the expression obtained above for the horizontal Lagrangian velocity (4.74), the relation defined in (4.35) and assuming hypothesis (4.62).

$$\xi_\alpha = -am(\mathbf{x},t)\left(\frac{k_\alpha}{k} F_{cs} sin\varphi + \frac{m(\mathbf{x},t)}{\sigma} F_{ss} \frac{\partial \overline{u}_\alpha}{\partial z} sin\varphi\right) + O\left(\epsilon^2\right) \tag{4.76}$$

Once again, the hypothesis (4.63) is also applied, the horizontal displacement, ξ_α, can be approximated to:

$$\xi_\alpha = -a \frac{k_\alpha}{k} F_{cs} sin\varphi + O\left(\epsilon^2\right) \tag{4.77}$$

In the following the wave-induced terms represented in the GLM momentum equation (4.55), namely the horizontal and vertical components of the wave pseudomomentum and the Lagrangian mean Bernoulli head, are expressed to second order in wave slope.

The wave pseudomomentum is defined in (4.49). The resulting first order wave-induced motions obtained above are replaced in (4.49) and the horizontal components of the wave pseudodmomentum are expressed to second order in wave slope:

$$P_\alpha = -\overline{\frac{\partial \xi_\beta}{\partial x_\alpha} u^l_\beta} - \overline{\frac{\partial \xi_3}{\partial x_\alpha} w^l} = \frac{ma^2}{4sinh^2(kD)} \left(2\sigma k_\alpha cosh(2kz+2kh)\right)$$
$$+\frac{ma^2}{4sinh^2(kD)}\left[2\frac{k_\alpha}{k} msinh(2kz+2kh)k_\beta \frac{\partial \overline{\mathbf{u}}}{\partial z} + 2m^2\frac{k_\alpha}{\sigma} sinh^2(kz+kh)\left(\frac{\partial \overline{\mathbf{u}}}{\partial z}\right)^2\right]$$
$$+O\left(\epsilon^3\right) \quad (4.78)$$

When the hypothesis (4.63) is applied, the wave pseudodmomentum is approximated to:

$$P_\alpha = \sigma k_\alpha E \frac{cosh\left(2kz+2kh\right)}{sinh^2(kD)} + O\left(\epsilon^3\right) \quad (4.79)$$

The vertical wave pseudomomentum can be calculated through the horizontal components of the wave pseudomomentum. If $m = 1$ and in the limit of small surface slopes, the wave pseudomomentum is non-divergent, leading to the following expression for P_3:

$$P_3 = -P_\alpha\left(z=-h\right)\frac{\partial h}{\partial x_\alpha} - \int_{-h}^{z} \frac{\partial P_\alpha(z')}{\partial x_\alpha} dz' \quad (4.80)$$

Ardhuin et al. (2008b) note that, in the general case, for $m \neq 1$ and nonlinear waves, the corrections that have to be made are of higher order.

The Lagrangian mean Bernoulli head term is also expressed to second order in wave slope and it is obtained from the first order wave-induced motions (w^l and u^l_α) obtained before:

$$\frac{1}{2}\overline{u^l_j u^l_j} = \frac{gkE}{2}\left(F_{cc}F_{cs} + F_{sc}F_{ss}\right) + \frac{E\sigma k_\alpha}{k}\frac{\partial \overline{\mathbf{u}}}{\partial z} mF_{cs}F_{ss} + \frac{Em^2}{2}\left(\frac{\partial \overline{\mathbf{u}}}{\partial z}\right)^2 F^2_{ss} + O\left(\epsilon^3\right) \quad (4.81)$$

where,

$$F_{sc} = sinh(kz+kD)/cosh(kD) \quad (4.82)$$

Once again, the hypothesis (4.63) is applied and the Lagrangian mean Bernoulli head term is expressed to second order:

$$\frac{1}{2}\overline{u_j^l u_j^l} = \frac{gkE}{2}\left(F_{cc}F_{cs} + F_{sc}F_{ss}\right) + O\left(\epsilon^3\right) \tag{4.83}$$

Finally the GLM free surface position is also obtained through its Stokes correction ($\overline{\eta}^S$). Without and within the hypothesis (4.63), it reads, respectively:

$$\begin{aligned}\overline{\eta}^L = \overline{\eta} + \overline{\eta}^S = \overline{\eta} + \overline{\frac{\partial \eta}{\partial x_\alpha}\xi_\alpha|_{z=\overline{\eta}}} + O\left(\epsilon^3\right) = \\ \overline{\eta} + \frac{ma^2}{2}\left(\frac{k}{tanh(kD)} + \frac{mk_\alpha}{\sigma}\frac{\partial \overline{\mathbf{u}}}{\partial z}|_{z=\overline{\eta}}\right) + O\left(\epsilon^3\right)\end{aligned} \tag{4.84}$$

$$\overline{\eta}^L = \overline{\eta} + \frac{Ek}{tanh(kD)} + O\left(\epsilon^3\right) \tag{4.85}$$

If only the hypotheses made by Ardhuin et al. (2008b) are assumed, the difference between the Stokes drift ($\overline{u}_\alpha^S$) and the horizontal component of the wave pseudomomentum (P_α) is given by the current vertical shear.

Consequently, the quasi-Eulerian mean velocity ($\hat{u}_\alpha = \overline{u}_\alpha^L - P_\alpha$) differs from the Eulerian mean velocity ($\overline{u}_\alpha = \overline{u}_\alpha^L - \overline{u}_\alpha^S$) in the same way (Ardhuin et al., 2008b):

$$\hat{u}_\alpha = \overline{u}_\alpha + \frac{1}{2}\overline{\xi}_3^2\frac{\partial^2 \overline{u}_\alpha}{\partial z^2} + O(\epsilon^3) \tag{4.86}$$

When hypothesis (4.63) is considered, together with the relations obtained for the wave-induced forcing terms, the Stokes drift becomes:

$$\overline{u}_\alpha^S = \sigma k_\alpha E\frac{cosh\left(2kz + 2kh\right)}{sinh^2(kD)} + O\left(\epsilon^3\right) \tag{4.87}$$

If (4.87) is compared with the expression for the horizontal wave pseudomomentum (4.79) it can be seen that the difference between the wave pseudomomentum (P_α) and Stokes velocity ($\overline{u}^S$) becomes:

$$P_\alpha = \overline{u}_\alpha^S + O\left(\epsilon^3\right) \tag{4.88}$$

and therefore,

$$\hat{u}_\alpha = \overline{u}_\alpha + O\left(\epsilon^3\right) \tag{4.89}$$

Replacing the wave forcing terms deduced at second order in wave slope, namely the components of the wave pseudomomentum and the Lagrangian mean Bernoulli head, in the set of equations (4.54 and 4.55), a new set of equations, the glm2-RANS equations are obtained. Hereinafter, the main steps of this deduction are focused.

4.3.3.3 glm2z-RANS equations

The equation for the quasi-Eulerian conservation of mass is obtained from (4.54):

$$\frac{\partial J_a}{\partial t}+\frac{\partial(J_a\overline{u}^L_\alpha)}{\partial x_\alpha}+\frac{\partial(J_a\overline{w}^L)}{\partial z}=0\Leftrightarrow\frac{\partial J_a}{\partial t}+\frac{\partial(J_a\hat{u}_\alpha)}{\partial x_\alpha}+\frac{\partial(J_a\hat{w})}{\partial z}=-\frac{\partial(J_aP_\alpha)}{\partial x_\alpha}-\frac{\partial(J_aP_3)}{\partial z} \tag{4.90}$$

Considering the momentum equation given in (4.55), the evolution for the vertical component of the quasi-Eulerian velocity $\left(\hat{w}=\left(\overline{w}^L-\overline{P}^L_3\right)\right)$ can be re-written by using expression (4.83) and re-calling the hydrostatic hypothesis.

$$-\frac{1}{\rho}\frac{\partial}{\partial z}\left(\overline{p}^L+\rho gz-\rho\frac{gkE}{2}(F_{cc}F_{cs}+F_{sc}F_{ss})\right)+P_\beta\frac{\partial}{\partial z}\left(\hat{u}_\beta+P_\beta\right)+P_3\frac{\partial P_3}{\partial z}=0 \tag{4.91}$$

The two last terms in (4.91) can be neglected to a second order approximation when the definition given for the horizontal components of the wave pseudomomentum (4.79) is used together with the hypothesis made in (4.58) and (4.63), since they result in terms of higher order.

After the simplifications made, (4.91) is integrated over depth and the dynamic boundary condition (4.52) is used. Furthermore, the expression obtained for $\overline{\eta}^L$ (4.85) is applied. At second order in wave slope, the expression for GLM pressure is established:

$$\frac{\overline{p}^L}{\rho}=g\left(\overline{\eta}-z\right)+\frac{\overline{p}_a}{\rho}+gkEF_{cc}F_{cs} \tag{4.92}$$

The quasi-Eulerian pressure that enters in the horizontal momentum equation is then:

$$\hat{p}=\overline{p}^L-\frac{\rho\overline{u^l_ju^l_j}}{2}=\rho g\left(\overline{\eta}-z\right)+\overline{p}_a+\rho J=\overline{p}^H+\rho J \tag{4.93}$$

$\overline{p}_H$ is the hydrostatic pressure and J represents the wave-induced kinematic pressure, depth-uniform over depth, obtained already in Smith (2006).

$$J = \frac{gkE}{sinh2kD} \tag{4.94}$$

Now, for the quasi-Eulerian horizontal velocity evolution equation, expression (4.93) is injected in the momentum equation (4.55), giving:

$$\frac{\partial \hat{u}_\alpha}{\partial t} + \left(\hat{u}_\beta + P_\beta\right) \frac{\partial \hat{u}_\alpha}{\partial x_\beta} + \left(\hat{w} + P_3\right) \frac{\partial \hat{u}_\alpha}{\partial z} =$$
$$-\frac{1}{\rho}\frac{\partial \overline{p}^H}{\partial x_\alpha} - \frac{\partial J}{\partial x_\alpha} - \epsilon_{\alpha 3 \beta} f_3 \left(\hat{u}_\beta + \hat{X}_\alpha + P_\beta\right) + P_\beta \frac{\partial \overline{u}^L_\beta}{\partial x_\alpha} + P_3 \frac{\partial \overline{w}^L}{\partial x_\alpha} \tag{4.95}$$

Within the hypothesis made, the last two terms of (4.95) can be simplified, to second order in wave slope and considering the hydrostatic hypothesis, to $P_\beta \frac{\partial \hat{u}_\beta}{\partial x_\alpha}$.

Finally, all the terms including P_β are grouped and the equation for the horizontal GLM momentum expressed to second order becomes:

$$\frac{\partial \hat{u}_\alpha}{\partial t} + \hat{u}_\beta \frac{\partial \hat{u}_\alpha}{\partial x_\beta} + \hat{w} \frac{\partial \hat{u}_\alpha}{\partial z} = -\frac{1}{\rho}\frac{\partial \overline{p}^H}{\partial x_\alpha} - \frac{\partial J}{\partial x_\alpha} + \hat{X}_\alpha - \epsilon_{\alpha 3 \beta}\left(f_3 \hat{u}_\beta + (f_3 + \omega_3) P_\beta\right) - P_3 \frac{\partial \hat{u}_\alpha}{\partial z} \tag{4.96}$$

$\epsilon_{\alpha 3 \beta} \omega_3 P_\beta$ represents the vortex force, defined by the product between the wave pseudomomentum (**P**) and the mean flow vertical vorticity (ω_3) (Ardhuin et al., 2008b). The vortex force includes the flux of momentum resulting from the quasi-Eulerian momentum advected by the wave motion. It is a momentum flux divergence that compensates the change of the wave momentum flux due to wave refraction (Garret (1976), Ardhuin et al. (2008b)).

The set of equations (4.90) and (4.96) are valid for the hypothesis made and for the entire water column that ranges from $z = -h$ to $z = \overline{\eta}^L$. They represent, asymptotically, the evolution of the quasi-Eulerian flow to second order in the wave non-linearity.

In the above set of equations, the quasi-Eulerian velocity is not divergence-free (please see 4.90). For the use of numerical models, it is rather preferable to have non-divergent variables to solve the primitive equations. Moreover, it is also better to have a local water column that does not change with the local wave height (Ardhuin et al., 2008b).

To overcome these problems raised for practical numerical modelling, Ardhuin et al. (2008b) proposed to transform the glm2-RANS mass (4.90) and momentum (4.96) equations (except for the mean pressure $\overline{p}^L$ which is not defined as a GLM average, but rather as Eulerian) within a change of the vertical coordinate. The vertical coordinate is corrected for the GLM-induced vertical displacements, such that the Jacobian associated to the GLM transformation is equal to the unity, i.e., a non-divergent GLM flow.

For a detailed description of the change of the glm2-RANS equations to z-coordinates please refer to Ardhuin et al. (2008b) and Delpey (2012). The derived glm2z-RANS equations in z-coordinate, with a non-divergent GLM velocity field are shown below.

$$\frac{\partial \hat{u}_\alpha}{\partial x_\alpha} + \frac{\partial \hat{w}}{\partial z} = 0 \tag{4.97}$$

$$\frac{\partial \hat{u}_\alpha}{\partial t} + \hat{u}_\beta \frac{\partial \hat{u}_\alpha}{\partial x_\beta} + \hat{w} \frac{\partial \hat{u}_\alpha}{\partial z} = -\frac{1}{\rho} \frac{\partial \overline{p}^H}{\partial x_\alpha} - \frac{\partial J}{\partial x_\alpha} + \hat{X}_\alpha - \epsilon_{\alpha 3 \beta} \left(f_3 \hat{u}_\beta + (f_3 + \omega_3) P_\beta \right) - P_3 \frac{\partial \hat{u}_\alpha}{\partial z} \tag{4.98}$$

4.3.3.4 Boundary conditions

The boundary conditions have also to be transformed by the vertical coordinate change.

Through the change made in the vertical coordinate for the Lagrangian vertical displacement, the free surface GLM position ($\overline{\eta}^L$) comes back to its mean Eulerian position ($\overline{\eta}$).

The kinematic boundary condition for the free surface is then expressed by:

$$(\hat{w} + P_3)|_{z=\overline{\eta}} = \frac{\partial \overline{\eta}}{\partial t} + (\hat{u}_\alpha + P_\alpha) \frac{\partial \overline{\eta}}{\partial x_\alpha} \tag{4.99}$$

At the bottom the kinematic boundary condition becomes:

$$(\hat{w} + P_3)|_{z=-h} = -(\hat{u}_\alpha + P_\alpha) \frac{\partial h}{\partial x_\alpha} \tag{4.100}$$

In what concerns the dynamic boundary conditions for the quasi-Eulerien flow, the momentum transfers between the atmosphere and waves are influenced by the waves field. A part of these momentum fluxes goes to the ocean through the wind stress τ_{wind}, and another part goes into the wave field (τ_{watm}). Additionally, all the momentum flux lost by waves, due to wave breaking, is a source of momentum for the mean flow. Therefore the momentum flux transferred by the wind to the waves (τ_{watm}) has to be subtracted from the total momentum transferred by the atmosphere to the ocean (τ_{wind}). Here, the source of momentum is injected as a surface stress, τ_{wbr}, modifying the free surface boundary condition:

$$\rho \nu_z \left.\frac{\partial \hat{u}_\alpha}{\partial z}\right|_{z=\hat{\eta}} = \tau_{wind,\alpha} - \tau_{watm,\alpha} + \tau_{wbr,\alpha} \tag{4.101}$$

If the bottom boundary layer is resolved, the bottom stress becomes:

$$\rho \nu_z \left.\frac{\partial \hat{u}_\alpha}{\partial z}\right|_{z=-h} = \tau_{bot,\alpha} + \tau_{wbot,\alpha} \tag{4.102}$$

The variable ν_z represents the vertical turbulent viscosity associated to a given turbulence closure model. $\tau_{bot,\alpha}$ is the bottom stress calculated by friction effects in the hydrodynamic model, and $\tau_{wbot,\alpha}$ is the wave momentum flux lost by bottom friction that is added to the mean momentum flux within the bottom boundary layer.

4.4 Effects of currents on the wave field

The effects of currents on wave propagation was the subject of a number of theoretical studies (Longuet-Higgins and Stewart (1961), Peregrine and Jonsson (1983), Mei (1989), Ris and Holthuijsen (1996)) and on laboratory experiments (Chawla and Kirby, 2002).

The frequency of incoming waves from offshore can be shifted by the interaction with an ambient current. This is related to the so-called Doppler effect. Therefore a variable ambient current can modify the waves phase velocity and induce their refraction. It occurs a change in the wave energy propagation direction from wave direction.

If a uniform current profile over depth is considered, the Doppler-shift relation (4.103) is used. The absolute frequency (ω) is calculated through the addition of the relative or intrinsic frequency (σ) with the current velocity (U) times the wave number.

$$\omega = \sigma + kUcos\alpha \tag{4.103}$$

α is the angle between k and U.

When waves are following or opposing the currents, they undergo different effects. The dispersion relationship (4.104) can be represented graphically (Figure 4.10).

$$\sigma = \omega - kUcos\alpha = \pm(gktanhkh)^{\frac{1}{2}} \tag{4.104}$$

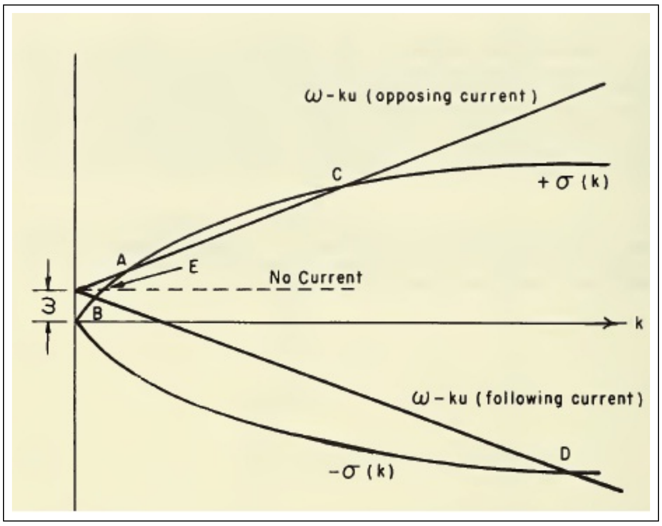

Figure 4.10: Representative scheme of the wave changes due to an ambient current. Source: Peregrine and Jonsson (1983).

For the case where waves are perpendicular with the current ($cos\alpha = 0$), the solution is given by point E. Here there are no changes induced by the current on waves.

For both solutions A and B, energy propagates in the wave direction, while for solutions C and D energy changes direction by the effect of the current.

For waves following the current ($Ucos\alpha > 0$), the waves propagate from the region without currents (point E) to solutions B and D. The wave number decreases from point E to point B, i.e. the wave length increases when waves are following the current.

On the other hand, if waves are opposing the current ($Ucos\alpha < 0$), two situations can occur: either the waves can propagate against the current, since they have a group velocity larger than the velocity current (until solution A), or waves are blocked by the opposing current (solution C) for having a group velocity equal to the velocity current. From solution E to A, the wave number increases, i.e., the wave length decreases when waves are opposing the current.

A number of spectral wave models (among others, WAM (WAMDI-Group, 1988) SWAN (Booij et al., 1996), TOMAWAC (Benoit et al., 1996), WWIII (Tolman, 2002)) have included the effects of an ambient current in wave modelling due to the importance of taking into account the changes induced by the currents on waves.

Chapter 5

Wave 3D-flow two-way coupling system

5.1 On the need for a numerical platform

In the past few years, different numerical models have been developed due to the necessity of finding and choosing strategies for the sustainable management of the littoral environment. The design of port and coastal structures or the study of morphodynamics, such as erosion or accretion phenomena on beaches are examples that show that it is essential not only to have a safe coastal zone but also to reach economic prosperity. Therefore, an increased and constant demand from coastal engineers occurs for the coastal zone, since that is the region where human activities are mainly focused.

Consequently, it is necessary to have access to a numerical platform able to be applied at regional scale, to take into account the different processes that co-exist in the maritime environment, such as the modelling of tides, waves, currents and atmosphere together with sediment transport and morphodynamics.

A number of commercial codes are available for this purpose. Some examples are the MIKE 21 (developed at DHI, Denmark), the SMC (Sistema Modelado Costero) (from the University of Cantabria, Spain) or the SMS (Surface Water Modeling System) (developed at the Environmental Modeling Research Laboratory (EMRL) at Brigham Young University in cooperation with the U.S. Army Corps of Engineers Waterways Experiment Station (USACE-WES), and the US Federal Highway Administration (FHWA)).

Computer resources of higher performance, together with the development of numerical methods, make numerical modelling a powerful tool with an increased range of applications. Additionally, with the improved knowledge of the different physical phenomena, it is possible to use a numerical tool applied to larger domains with finer discretization, matching the level of refinement and accuracy that users need. The continuous research of ocean modelling can bring answers to coastal engineers.

The formalism on which the coupling between hydrodynamics and wave models is based (radiation stress or vortex force formalism), differentiates the existing numerical models. This can be done in a two-dimensional (2D), quasi-3D, or fully three-dimensional (3D) way. Some of the different approaches and theories that are commonly used to describe the wave-current environment, either in 2D or 3D way, were already cited and mentioned in the previous chapter.

For many years, the numerical models, used to describe wave-current interaction effects, have been based on the radiation stress concept and were within a two-dimensional coupling system (among others: MARS2D (Model for Applications at Regional Scale)/SWAN (Simulating WAves Nearshore) by Bruneau (2009), SELFE/WWM-II by Roland et al. (2012) or TELEMAC-2D/TOMAWAC). The coupling between wave and hydrodynamic models, taking into account the effects of the source of wave momentum (radiation stress) on the mean flow, showed that it had great importance in describing phenomena such as the wave set-up, surf beats or the generation of alongshore currents.

However, in order to take into account the variation of the vertical structure of the current profile, Putrevu and Svendsen (1999) proposed a quasi-3D approach in which the vertical profile of the current is solved analytically. The result is applied in a 2D model, leading to what is called a “quasi-3D”approach. It has the advantage of considering the vertical variability of the flow by applying the depth-integrated equations. Thus, the required computer effort is lower. This type of quasi-3D approach was implemented in the nearshore circulation model SHORECIRC to reproduce wave-induced currents (Haas et al. (2003), Haas and Warner (2009)).

But, as mentioned before, in the last ten years several efforts have been made to get a fully 3D description of wave effects on the current within the littoral zone. In Table 5.1 some of the existing coupled systems between 3D hydrodynamic and wave models are presented.

Hydrodynamic model	**Wave model**	**Coupling system** (Theoretical framework)
POM Blumberg and Mellor (1987)	**SWAN** Booij et al. (1996)	**Xie et al. (2001)** (Lewis, 1997)
POM	**WW3** Tolman (2002)	**Newberger and Allen (2007b)** (Newberger and Allen, 2007a)
POM	**WW3**	**Tang et al. (2007)** (Jenkins, 1987)
ROMS Shchepetkin and McWilliams (2005)	**SWAN**	**Warner et al. (2008)** (Mellor 2003, 2005)
Delft3D Delft3D-FLOW (2012)	**SWAN**	**Walstra et al. (2000)** (Groeneweg, 1999)
ROMS	**SWAN**	**Uchiyama et al. (2010)** (McWilliams et al., 2004)
POLCOMS Holt and James (2001)	**WAM** WAMDI-Group (1988)	**Bolanos et al. (2011)** (Mellor 2003, 2005)
CH3D Sheng (1986)	**SWAN**	**Sheng and Liu (2011)** (Mellor, 2008)
MARS3D Lazure and Dumas (2008)	**WW3** Tolman (2002), Ardhuin et al. (2010)	**Bennis and Ardhuin (2011)** (Ardhuin et al., 2008b)
ROMS	**SWAN**	**Kumar et al. (2012)** (McWilliams et al., 2004)
SYMPHONIE Marsaleix et al. (1998)	**WW3**	**Michaud et al. (2012)** (Ardhuin et al., 2008b)
MOHID Martins (2000)	**WW3**	**Delpey (2012)** (Ardhuin et al., 2008b)
GETM Burchard and Bolding (2002)	**SWAN**	**Moghimi et al. (2013)** (Mellor (2011a), Ardhuin et al. (2008b))

The main purpose of this project is to get a 3D two-way coupled system able to model the 3D circulation in coastal and surf zones accurately. The wave-current interaction is emphasised. The final objective would be to get a coupling numerical platform based on a recent and appropriate theoretical framework.

The TELEMAC-MASCARET system (www.opentelemac.org) was the chosen numerical platform for this research. It has been developed by the Research and Development Department of Electricité de France (EDF) since 1987. It offers a 2D and 3D numerical tool to model free surface flows in maritime and fluvial domains. It is distributed as open-source software since mid 2011.

It has several modules with which different hydrodynamic processes can be modelled (Figure 5.1). Some of the modules are already coupled. The coupling between the 3D hydrodynamic model and wave model is missing, at least in an accurate way (until now the coupling between the wave and the 3D hydrodynamic model was made through the forces induced by the radiation stresses based on the 2D theory of Longuet-Higgins (1953), Longuet-Higgins and Stewart (1962, 1964) and uniformly distributed over depth).

Therefore, the third generation wave model, TOMAWAC (Benoit et al., 1996), and the three-dimensional hydrodynamic model, TELEMAC-3D (Hervouet, 2007), were coupled in the present work through the implementation of the set of equations proposed by Ardhuin et al. (2008b) with the simplified equations presented in Bennis and Ardhuin (2011).

With the TELEMAC-MASCARET system it is possible to achieve a free, open-source numerical platform that is essential for the coastal management. Both models are indeed open-source and available at www.opentelemac.org.

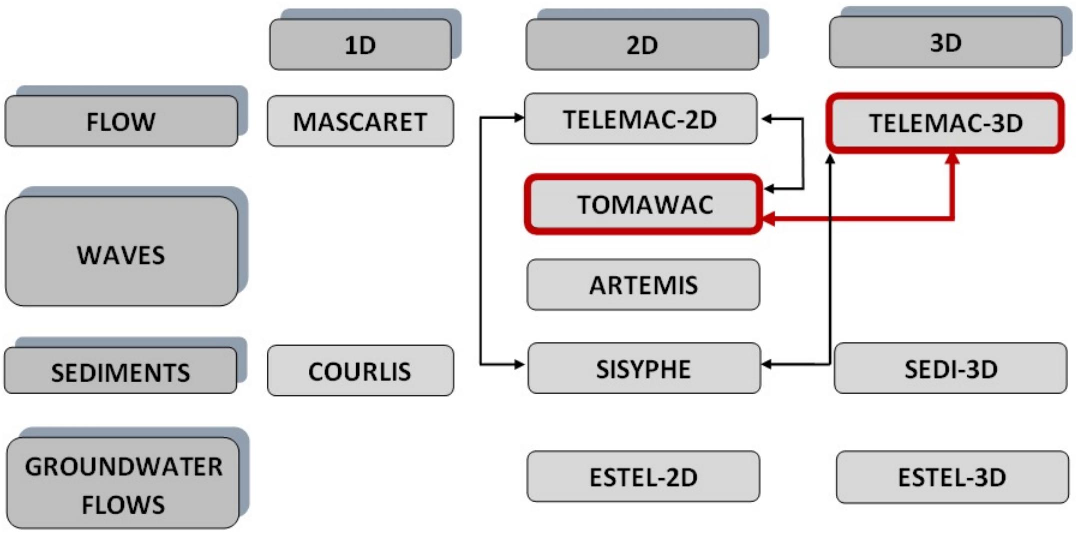

Figure 5.1: Available modules in the TELEMAC-MASCARET system. Adapted from TELEMAC modelling system documentation (2004).

All the available modules are based on an internal library of finite element numerical framework and solvers, the BIEF library. Here, the finite element technique is used within unstructured grids based on triangular elements. The BIEF library has a number of subroutines that include methods for solving, for instance, the advection and diffusion equations.

This chapter is organized in the following way. The hydrodynamic and spectral wave models used to build the coupled system are first described, in sections 5.2 and 5.3, respectively. Then in section 5.4, the modifications implemented in TELEMAC-3D and new terms included in TOMAWAC are presented. In section 5.5 the way how the coupling system works is showed. Finally, in section 5.6, the coupled system is first tested and validated against an academic test study, which consists of an adiabatic test presented in Bennis and Ardhuin (2011).

5.2 Hydrodynamic circulation model - TELEMAC-3D

5.2.1 Flow equations in the fluid domain

The TELEMAC-3D module, version v6p2, was used to develop the numerical platform for modelling wave-current interaction 3D effects. The following description of the hydrodynamic circulation model features is mainly based on the literature by Hervouet (2007).

TELEMAC-3D solves three-dimensional water flow equations (with or without the hydrostatic hypothesis) and the transport of dissolved substances. This is made by a finite-element technique over unstructured grids of elements with triangular basis in the horizontal plane. Within the hydrostatic hypothesis, and for an incompressible and Newtonian fluid of constant and homogeneous density ρ, the equations of mass (5.1) and horizontal momentum conservation ((5.2) and (5.3)) are solved at each node of the computational domain.

$$\frac{\partial u}{\partial x}+\frac{\partial v}{\partial y}+\frac{\partial w}{\partial z}=0 \tag{5.1}$$

$$\frac{\partial u}{\partial t}+u\frac{\partial u}{\partial x}+v\frac{\partial u}{\partial y}+w\frac{\partial u}{\partial z}=S_x-g\frac{\partial \eta}{\partial x}+\frac{\partial}{\partial x}\left(\nu_H\frac{\partial u}{\partial x}\right)+\frac{\partial}{\partial y}\left(\nu_H\frac{\partial u}{\partial y}\right)+\frac{\partial}{\partial z}\left(\nu_z\frac{\partial u}{\partial z}\right) \tag{5.2}$$

$$\frac{\partial v}{\partial t}+u\frac{\partial v}{\partial x}+v\frac{\partial v}{\partial y}+w\frac{\partial v}{\partial z}=S_y-g\frac{\partial \eta}{\partial y}+\frac{\partial}{\partial x}\left(\nu_H\frac{\partial v}{\partial x}\right)+\frac{\partial}{\partial y}\left(\nu_H\frac{\partial v}{\partial y}\right)+\frac{\partial}{\partial z}\left(\nu_z\frac{\partial v}{\partial z}\right) \tag{5.3}$$

$$p=p_a+\rho_0 g\left(\eta-z\right) \tag{5.4}$$

(u, v , w) are the three velocity components, η is the free surface elevation, p_a is the atmospheric pressure, g is the acceleration due to gravity and ρ_0 is the reference density. S_x and S_y represent the hydrodynamic model horizontal source or sink terms of momentum, for instance, the Coriolis force, wind drag at the free surface and bottom friction. ν_H and ν_z are the horizontal and vertical diffusion velocity coefficients, respectively. They represent the values of both molecular and turbulence viscosities.

The velocity diffusion coefficient values can either be prescribed by the user or computed by a turbulence closure model. For the horizontal diffusion velocity coefficient, two choices are available: the user prescribes a constant value (the choice in this work) or the Smagorinsky model (Smagorinsky, 1963) can be activated. Regarding the vertical diffusion velocity coefficient, TELEMAC-3D offers the possibility of applying the simplest models, in which a constant value is assumed, the mixing length models (here several choices are also made available for the determination of the mixing length distribution throughout the water depth) or the two-equations model $k-\varepsilon$ (which will be the choice in this work).

The total water depth $D=h+\eta$ is obtained by integrating the pressure-continuity terms along the vertical. The $\overline{(.)}$ operator refers to the depth-integrated variable.

$$\frac{\partial \eta}{\partial t}+\frac{\partial \overline{u}D}{\partial x}+\frac{\partial \overline{v}D}{\partial y}=0 \tag{5.5}$$

5.2.2 Boundary conditions

The boundary conditions have to be specified for the free surface, bottom, walls or boundaries that do not correspond to any physical boundary, for instance, the open sea or the upstream and downstream sides of a river.

Open boundaries are artificial boundaries and can be difficult to deal with and thus some additional information is required on, for example, the pressure, water depth or velocity. TELEMAC-3D has the option for the user to choose boundaries of Thompson type (Thompson, 1987).

The free surface is defined such that there is no fluid crossing the surface (kinematic boundary condition) and it evolves as time goes on.

The following boundary condition is defined at the free surface:

$$w|_{z=\overline{\eta}} = \frac{\partial \overline{\eta}}{\partial t} + u|_{z=\overline{\eta}} \frac{\partial \overline{\eta}}{\partial x} + v|_{z=\overline{\eta}} \frac{\partial \overline{\eta}}{\partial y} \tag{5.6}$$

The wind forcing is taken into account as a surface stress ($\vec{\tau}_{wind}$).

$$\vec{\tau}_{wind} = \rho_{air} a_{wind} ||v_w|| \vec{v}_w \tag{5.7}$$

ρ_{air} is the density of air, $\vec{v}_w$ is the wind velocity 10 m above the water and a_{wind} a dimensionless coefficient (e.g. Flather (1976)).

At the bottom, the boundary conditions are expressed by:

$$w|_{z=-h} = -u|_{z=-h} \frac{\partial h}{\partial x} - v|_{z=-h} \frac{\partial h}{\partial y} \tag{5.8}$$

$$\vec{\tau}_{bot} = -\frac{1}{2} \rho C_f ||u_{z=-h}|| \vec{u} \tag{5.9}$$

$\vec{\tau}_{bot}$ is the bottom shear stress and C_f a dimensionless friction coefficient. TELEMAC-3D offers different friction laws to model the bottom friction, for instance, Chézy, Strickler, Manning or Nikuradse law.

5.2.3 Time and space discretization

Within the hydrostatic hypothesis, TELEMAC-3D solves the RANS equations using a fractional-step method which consists of solving the equations with different steps.

More precisely, the overall algorithm of TELEMAC-3D is divided into four main steps. First, the advected velocities are computed by solving the advected terms in the momentum equations. After, taking into account the diffusion and source terms in the momentum equations, new intermediate velocities are calculated. At a third stage the water depth is computed through the vertical integration of the continuity equation and momentum equations, excluding pressure terms. Finally the vertical velocity is obtained from the continuity equation and the pressure is calculated.

Let be ϕ a certain variable, for instance, the velocity, the turbulence kinetic energy, the dissipation of turbulence energy or a tracer.

The discretization in time of the variable ϕ is expressed as:

$$\frac{\partial \phi}{\partial t} = \frac{\phi^{n+1} - \phi_D + \phi_D - \phi_C + \phi_C - \phi^n}{\Delta t} \tag{5.10}$$

The algorithm for the numerical solution of this equation is based on three fractional steps:

- Advection step $\frac{\phi_C - \phi^n}{\Delta t}$ = advection terms;
- Diffusion step $\frac{\phi_D - \phi_C}{\Delta t}$ + diffusion terms = source terms;
- Pressure-continuity step $\frac{\phi^{n+1} - \phi_D}{\Delta t}$ = pressure terms

  The continuity equation is solved and the water depth and vertical velocity are computed.

As time goes on, the free surface evolves. In this way, the quantities ϕ^{n+1}, ϕ^n, ϕ_C and ϕ_D are not defined in the same mesh in the vertical direction. In order to overcome this problem a change of variables is performed along the vertical through the sigma transform, in which a fixed transformed mesh is obtained.

The space discretization is made by the finite-element method. For 3D simulations the computational domain is discretized in prisms with a triangular basis. Therefore, passing from the 2D to 3D meshes is relatively easy, only being needed to add horizontal planes on the vertical direction (Figure 5.2).

One has to note however that this discretization scheme restricts the range of application of the code to flows for which the water column is continuous from the bottom to the free surface. Complex flows, overturning waves, submerged bodies can not be modelled.

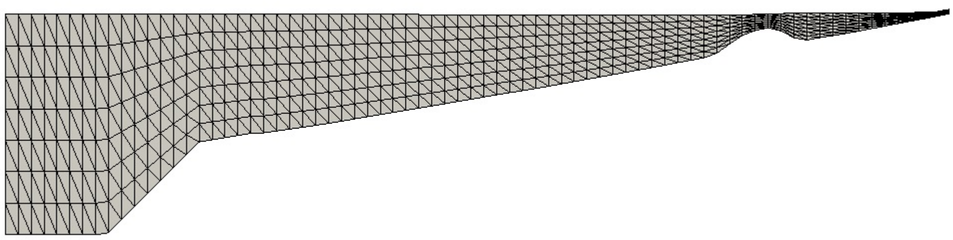

Figure 5.2: Scheme of a three-dimensional mesh. View in the x-z plane.

TELEMAC-3D offers several methods available to solve the advection step: the method of characteristics (which is the chosen method to work with in this study), the streamline-upwind Petrov-Galerkin scheme (SUPG) or a number of distributive schemes.

The method of characteristics has the great advantage of being unconditionally stable and giving monotonic solutions. It is however prone to numerical diffusion, and conservation of advected quantities can not be guaranteed.

The velocity field, which is needed to calculate the characteristics path, is given by:

$$\vec{u}(t) = \vec{u}^n + \frac{t - t^n}{\Delta t}\vec{u}^{n+1} \tag{5.11}$$

Before the end of the time step, the advection field is still an unknown at time t^{n+1}. Therefore, the advection field is used at time t^n. The advection step is performed in the fixed transformed mesh (by the sigma transform).

Due to numerical features, the diffusion step is solved in the real mesh, i.e., evolving free surface in time (Hervouet, 2007). At this stage, the prism is no longer used as the finite element. Instead, the prism is divided into three tetrahedra to reduce numerical errors that the prismatic element can bring (Hervouet, 2007). After the calculation of elements matrices in the tetrahedra, the prismatic element matrix can be once again restored.

When assuming the hydrostatic hypothesis and a constant density, the horizontal pressure gradients are given by the free surface slope effect ($-g\nabla\eta$).

Moreover, the effect of atmospheric pressure is added at the free surface. These source terms are integrated subsequently in the source terms S_x and S_y and they are divided into a barotropic and baroclinic part, and calculated on the mesh at time t^n.

Finally, the pressure-continuity step is also solved after the advection and diffusion steps. At this stage the momentum equations are integrated over depth, without taking into account any advection, diffusion, source or friction terms. The resulting equations are solved between t^n and t^{n+1}. A new water depth value and averaged horizontal velocities at the time instant t^{n+1} are obtained. With these quantities a new mesh is calculated, as well as the horizontal velocities u and v at time t^{n+1}. Through the continuity equation the vertical velocity w can be obtained.

Within the hydrostatic hypothesis, w is required only in the advection stage for the next time step. As the advection step is solved in the fixed mesh, the three-dimensional continuity equation is also solved in the fixed mesh to avoid the passing between the real and the fixed mesh.

5.3 Spectral wave model - TOMAWAC

5.3.1 Action balance equation

The wave model used in this project was the third generation spectral model TOMAWAC (TELEMAC-based Operational Model Addressing Wave Action Computation) (Benoit et al., 1996), version v6p2, which is incorporated in the TELEMAC-MASCARET system. TOMAWAC solves the propagation of wind-generated waves in the time and space domains. The applicability domain ranges from oceanic to coastal zones.

The wave model solves the action balance equation in Cartesian (x, y) (5.12) or spherical spatial coordinates. The wave action density (N) is conserved in the presence of non-homogeneous and unsteady environment.

All the points of the mesh must have a positive water depth, since only the maritime domain is discretized. Moreover, TOMAWAC follows the nautical convention, i.e., the wave direction is defined from the geographic North in the clockwise direction.

$$\frac{\partial N}{\partial t} + \dot{x}\frac{\partial N}{\partial x} + \dot{y}\frac{\partial N}{\partial y} + \dot{k_x}\frac{\partial N}{\partial k_x} + \dot{k_y}\frac{\partial N}{\partial k_y} = Q(x,y,k_x,k_y,t) \tag{5.12}$$

The wave number vector components are $(k_x, k_y) = (ksin\theta, kcos\theta)$ and the transfer rates of each variable, $\dot{x}$, $\dot{y}$, $\dot{k_x}$ and $\dot{k_y}$, are given by linear wave theory. The wave number is calculated by the wave linear dispersion relation σ^2 =gk $tanh$(kD). σ is the relative angular wave frequency. The source and sink terms are represented by $Q(x,y,k_x,k_y,t)$.

In the Cartesian coordinate system, equation (5.12) can be re-written , switching the spectral variables (k_x, k_y) to (f_r, θ), where $\sigma = 2\pi f_r$:

$$\frac{\partial \tilde{B}\tilde{F}}{\partial t} + \dot{x}\frac{\partial \tilde{B}\tilde{F}}{\partial x} + \dot{y}\frac{\partial \tilde{B}\tilde{F}}{\partial y} + \dot{\theta}\frac{\partial \tilde{B}\tilde{F}}{\partial \theta} + \dot{f_r}\frac{\partial \tilde{B}\tilde{F}}{\partial f_r} = \tilde{B}.\tilde{Q}\left(x,y,\theta,f_r,t\right) \tag{5.13}$$

with

$$\tilde{B}.\tilde{F}\left(x,y,f_r,\theta,t\right) = N(x,y,k_x,k_y,t) = \frac{CC_g}{2\pi\sigma}\tilde{N}\left(x,y,f_r,\theta,t\right) \tag{5.14}$$

$$\tilde{B} = \frac{CC_g}{2\pi\sigma^2} = \frac{C_g}{(2\pi)^2 k f_r} \tag{5.15}$$

θ is the direction of the waves, C the celerity of waves and C_g the wave group velocity. $F(f_r,\theta)$ represents the variance directional spectrum and it is related with the action density spectrum through $N = F/\sigma$.

In a general form, equation (5.13) can be re-written as:

$$\frac{\partial BF}{\partial t} + \vec{V}.\vec{\nabla}(BF) = BQ \tag{5.16}$$

where $\vec{V} = (\dot{x}, \dot{y}, \dot{\theta}, \dot{f}_r)$ represents the transport vector.

5.3.2 Source and sink terms

The TOMAWAC model takes into account several physical processes that affect the spectrum evolution towards the coast. Furthermore, it has a number of options available to choose the parametrization for each of the sink and source terms. The variable Q, presented in the R.H.S. of (5.12), can be subdivided into different contributions:

$$Q = Q_{in} + Q_{ds} + Q_{nl} + Q_{tr} + Q_{bf} + Q_{br} \tag{5.17}$$

where:

- Q_{in} is the wind input term;
- Q_{ds} represents the waves breaking in deep waters, i.e., the whitecapping;
- Q_{nl} refers to the non-linear quadruplet interactions;
- Q_{tr} is the non-linear triad interactions;
- Q_{bf} takes into account the bottom-induced dissipation;
- Q_{br} represents the depth-induced wave breaking.

As waves propagate towards the coast, they start to feel the bottom and therefore the last three terms mentioned above become more important to take into account.

In order to take into account the depth-induced wave breaking, the model proposed by Thornton and Guza (1983) (5.18) was used in this work.

$$Q_{br}(f_r, \theta) = -12\sqrt{\pi} B^3 f_{car} \frac{(2m_0)^{2/3}}{H_m^2 h} \left[1 - \left(1 + \frac{8m_0}{H_m^2} \right)^{-5/2} \right] F(f_r, \theta) \tag{5.18}$$

f_{car} is a characteristic wave frequency that can be chosen by the user. In TOMAWAC the default value is the average frequency computed from the spectral zero-th order m_0 and first order m_1 moments. H_m is the maximum wave height compatible with the water depth and it is controlled by γ through $H_m = \gamma h$. B is a parameter that ranges between 0.8 and 1.5.

For the bottom friction induced energy dissipation $Q_{bf}(f_r, \theta)$, TOMAWAC uses an empirical formulation obtained from the JONSWAP campaign (Hasselmann et al., 1973).

$$Q_{bf}(f, \theta) = -\Gamma \frac{2k}{g \sinh(2kh)} F(f_r, \theta) \tag{5.19}$$

Γ is a constant that assumes the value $\Gamma = 0.038\ m^2 s^{-3}$ for swell conditions and $\Gamma =\ 0.067\ m^2 s^{-3}$ for wind sea conditions (values achieved in JONSWAP campaign).

5.3.3 Numerical discretization

The wave directional spectrum is discretized in a number of directions and frequencies. The wave action balance equation is solved for each component of frequency and direction.

The frequencies are discretized following a progressive geometric function. For a number of frequencies n_f, n varies between 1 and n_f:

$$f_n = f_{min} q^{n-1} \tag{5.20}$$

q is the frequential ratio.

Besides the frequency discretization, TOMAWAC discretizes the domain into a number of directions (ND) the propagation direction that range from 0° to 360°. The directions are then:

$$\theta_m = (m-1)360°/ND \tag{5.21}$$

with $1 \leq m \leq ND$.

TOMAWAC uses unstructured grids and the computational domain is discretized by triangular elements. This method gives the great advantage of being able to work with a finer mesh resolution where required and thus represent bathymetric features or irregularities found in the coastline.

Like TELEMAC-3D, TOMAWAC uses the method of characteristics for the propagation step. If currents are taken into account, the method is applied in a dimension-4 space (it will apply to a dimension-3 otherwise). The convection step is made at this stage.

In the following description, the values after the propagation step and before the source term integration step are denoted by $()^*$. The exponents $()^{n+1}$ are the values after the source term integration step.

The solution is achieved through a fractional-step method, in which the convection and source terms integration steps are solved separately. Therefore for a time instant $t = n\Delta t$ in which the variance spectrum F^n is a known variable in all the computational domain points.

First, the convection step,

$$\frac{\partial BF}{\partial t} + \vec{V}.\vec{\nabla}(BF) = 0 \tag{5.22}$$

is discretized without the source terms:

$$\frac{(B.F)^* - (B.F)^n}{\Delta t} = \left[\vec{V}.grad(B.F)\right]^n \tag{5.23}$$

Here the intermediate values of $(B.F)^*$ are obtained.

The source and sink terms are integrated using a semi-implicit scheme:

$$\frac{\partial F}{\partial t} = Q \tag{5.24}$$

$$\frac{F^{n+1} - F^*}{\Delta t} = \frac{Q^{n+1} + Q^*}{2} \tag{5.25}$$

The variance density spectrum is then obtained for t^{n+1}.

Please see Benoit et al. (1996) and TOMAWAC documentation (2011) for further details on the numerical scheme.

5.4 Governing equations to take into account the effects of waves on the mean flow

5.4.1 Modified equations

The hydrodynamic model had to be modified to take into account the wave forcing terms and consequently to model the 3D effects of waves and current interactions. For that purpose, the recent formulation proposed by Ardhuin et al. (2008b) was included in TELEMAC-3D. The implementation follows the work of Bennis and Ardhuin (2011) in which the vertical current shear is neglected in the wave forcing terms. Considering an incompressible fluid and the hydrostatic assumption, the equations of mass (5.26) and horizontal momentum conservation ((5.27) and (5.28)) are solved.

$$\frac{\partial \hat{u}}{\partial x}+\frac{\partial \hat{v}}{\partial y}+\frac{\partial \hat{w}}{\partial z}=0 \tag{5.26}$$

$$\begin{aligned}\frac{\partial \hat{u}}{\partial t}+\hat{u}\frac{\partial \hat{u}}{\partial x}+\hat{v}\frac{\partial \hat{u}}{\partial y}+\hat{w}\frac{\partial \hat{u}}{\partial z}=S_x-g\frac{\partial \hat{\eta}}{\partial x}+\frac{\partial}{\partial x}\left(\nu_H\frac{\partial \hat{u}}{\partial x}\right)+\frac{\partial}{\partial y}\left(\nu_H\frac{\partial \hat{u}}{\partial y}\right)\\+\frac{\partial}{\partial z}\left((\nu_z+\nu_{wbz})\frac{\partial \hat{u}}{\partial z}\right)+\left[f_c+\frac{\partial \hat{v}}{\partial x}-\frac{\partial \hat{u}}{\partial y}\right]V_s-W_s\frac{\partial \hat{u}}{\partial z}-\frac{\partial J}{\partial x}\end{aligned} \tag{5.27}$$

$$\begin{aligned}\frac{\partial \hat{v}}{\partial t}+\hat{u}\frac{\partial \hat{v}}{\partial x}+\hat{v}\frac{\partial \hat{v}}{\partial y}+\hat{w}\frac{\partial \hat{v}}{\partial z}=S_y-g\frac{\partial \hat{\eta}}{\partial y}+\frac{\partial}{\partial x}\left(\nu_H\frac{\partial \hat{v}}{\partial x}\right)+\frac{\partial}{\partial y}\left(\nu_H\frac{\partial \hat{v}}{\partial y}\right)\\+\frac{\partial}{\partial z}\left((\nu_z+\nu_{wbz})\frac{\partial \hat{v}}{\partial z}\right)-\left[f_c+\frac{\partial \hat{v}}{\partial x}-\frac{\partial \hat{u}}{\partial y}\right]U_s-W_s\frac{\partial \hat{v}}{\partial z}-\frac{\partial J}{\partial y}\end{aligned} \tag{5.28}$$

$(\hat{u},\hat{v},\hat{w})$ are the so-called quasi-Eulerian mean velocities (Jenkins, 1989). They are given by the difference between the mean drift velocity (Lagrangian mean current) $(\overline{u}^L,\overline{v}^L,\overline{w}^L)$ and the Stokes drift (U_S,V_S,W_S).

The equations above are valid from the bottom $(z=-h)$ to the phase-averaged quasi-Eulerian free surface $(z=\hat{\eta})$.

The new terms included in the hydrodynamic model momentum equations are representative of the wave forcing terms, namely, the Stokes-Coriolis force (f_cV_S,f_cU_S), the vortex force $\left[\left(\frac{\partial \hat{v}}{\partial x}-\frac{\partial \hat{u}}{\partial y}\right)V_S-W_s\frac{\partial \hat{u}}{\partial z},\left(\frac{\partial \hat{v}}{\partial x}-\frac{\partial \hat{u}}{\partial y}\right)U_S-W_s\frac{\partial \hat{v}}{\partial z}\right]$ and the wave-induced pressure horizontal gradients $\left(\frac{\partial J}{\partial x},\frac{\partial J}{\partial y}\right)$.

The wave-induced pressure (J) and the horizontal components of the Stokes velocity (U_s, V_s) were also included and calculated in TOMAWAC model. For a spectrum of random directional waves, these terms read:

$$J = \iint g \frac{kF(f_r,\theta)}{\sinh(2kD)} df d\theta \tag{5.29}$$

$$(U_S, V_S) = \iint \sigma k(\sin\theta, \cos\theta) F(f_r,\theta) \frac{\cosh(2k(z+h))}{\sinh^2(kD)} df d\theta \tag{5.30}$$

Moreover, the Stokes flow is at lowest order divergence-free (Ardhuin et al., 2008b). Therefore the Stokes vertical velocity component, W_s, is given at lowest order by the horizontal divergence of U_S and V_S:

$$W_S = -U_S|_{z=-h}\frac{\partial h}{\partial x} - V_S|_{z=-h}\frac{\partial h}{\partial y} - \int_{-h}^{z}\left(\frac{\partial U_S}{\partial x} + \frac{\partial V_S}{\partial y}\right) dz \tag{5.31}$$

Furthermore, the vertical diffusion velocity coefficient value was modified in order to take into account the wave-induced enhanced vertical mixing (ν_{wbz}).

5.4.2 Boundary conditions

5.4.2.1 Free surface boundary conditions

At the free surface, a kinematic boundary condition has to be imposed for an impermeable boundary (Andrews and McIntyre, 1978a). In the glm2z-RANS approach it is expressed by:

$$\frac{\partial \hat{\eta}}{\partial t} + (\hat{u} + U_S)\frac{\partial \hat{\eta}}{\partial x} + (\hat{v} + V_S)\frac{\partial \hat{\eta}}{\partial y} = \hat{w} + W_S \tag{5.32}$$

Through the free surface boundary condition defined above, it is guaranteed that the convergence of the Stokes drift is compensated by a source of mass at the free surface. This condition is equivalent to a modified depth-integrated continuity equation expressed by:

$$\frac{\partial \hat{\eta}}{\partial t} + \frac{\partial\left(D\bar{\hat{u}}\right)}{\partial x} + \frac{\partial\left(D\bar{\hat{v}}\right)}{\partial y} = -\frac{\partial\left(D\overline{U}_S\right)}{\partial x} - \frac{\partial\left(D\overline{V}_S\right)}{\partial y} \tag{5.33}$$

In this work, an injection of all the momentum lost by the waves due to wave breaking and bottom friction at the surface and bottom boundaries of the hydrodynamic model was chosen. Other authors followed the same approach (Newberger and Allen (2007a), Delpey (2012)). However, Uchiyama et al. (2010) point out that a parametrization of the momentum fluxes vertical distribution throughout the water depth could be more appropriate. Nevertheless, as stated by Rascle et al. (2006), the strong vertical mixing caused by waves breaking allows the injected momentum to be diffused along the water depth.

Therefore, at the free surface, the momentum flux due to waves breaking (whitecapping and nearshore depth-induced breaking) is imposed as a surface stress (τ_{wbr}). This term will be calculated by the wave model using (5.36). The momentum flux transferred by the wind to the waves (τ_{watm}) is subtracted from the total momentum flux transferred by the atmosphere to the ocean (τ_{wind}) to avoid double counting (Bennis and Ardhuin, 2011).

$$\rho(\nu_z + \nu_{wbz}) \left.\frac{\partial \hat{u}}{\partial z}\right|_{z=\hat{\eta}} = \tau_{wind,x} - \tau_{watm,x} + \tau_{wbr,x} \tag{5.34}$$

$$\rho(\nu_z + \nu_{wbz}) \left.\frac{\partial \hat{v}}{\partial z}\right|_{z=\hat{\eta}} = \tau_{wind,y} - \tau_{watm,y} + \tau_{wbr,y} \tag{5.35}$$

$$(\tau_{wbr,x}, \tau_{wbr,y}) = \int\int g\rho \frac{k}{\sigma}(\sin\theta, \cos\theta) Q_{br}(f_r, \theta) df d\theta \tag{5.36}$$

5.4.2.2 Bottom boundary conditions

At the bottom, the momentum lost by waves due to bottom friction dissipation effects (τ_{wbot}) is added to the bottom shear stress (τ_{bot}) in the hydrodynamic model. The value of τ_{wbot} is obtained by the wave model with the expression (5.39).

$$\rho(\nu_z + \nu_{wbz}) \left.\frac{\partial \hat{u}}{\partial z}\right|_{z=-h} = \tau_{bot,x} + \tau_{wbot,x} \tag{5.37}$$

$$\rho(\nu_z + \nu_{wbz}) \left.\frac{\partial \hat{v}}{\partial z}\right|_{z=-h} = \tau_{bot,y} + \tau_{wbot,y} \tag{5.38}$$

$$(\tau_{wbot,x}, \tau_{wbot,y}) = \int\int g\rho \frac{k}{\sigma}(\sin\theta, \cos\theta) Q_{bf}(f_r, \theta) df d\theta \tag{5.39}$$

5.4.2.3 Offshore boundary conditions

At the open boundary, offshore, two conditions are imposed to guarantee a zero mass flux: one for the phase-averaged elevation (5.40) and another one for the horizontal velocities (5.41) (Rascle, 2007). It is considered that the wave-induced pressure and Stokes drift do not vary along the open boundary.

$$\hat{\eta} = -\frac{J}{g} \tag{5.40}$$

$$(\hat{u}, \hat{v}) = -(U_s, V_s) \tag{5.41}$$

5.4.3 Vertical mixing

5.4.3.1 At the free surface

The action of wind on the ocean generates waves. Some part of the wind momentum (τ_{wind}) is transferred to the waves as a surface stress (τ_{watm}). In turn, when waves break there is a transfer of momentum to the mean flow (τ_{wbr}). When waves break, by white-capping or due to depth-induced effects, there is the conversion of the wave′s mechanical energy into a turbulence kinetic energy (TKE) source (Donelan, 1998) that is transferred to the ocean surface. Craig and Banner (1994) showed that the turbulence effects due to breaking waves is confined to the surface boundary layer.

Here, the enhanced mixing due to wave breaking was implemented following the formulation proposed by Uchiyama et al. (2010). They assumed a vertical distribution over the water depth for this term and proposed a parametrization of this effect. The wave-enhanced momentum mixing due to surface breaking is then taken into account by adding ν_{wbz} to the vertical diffusion velocity coefficient ν_z.

$$\nu_{wbz}(z) = c_b (Q_{brv})^{\frac{1}{3}} \frac{H_s}{\sqrt{2}} D f^{wb}(z) \tag{5.42}$$

where:

$$Q_{brv} = \int\int g Q_{br}(f_r, \theta) df d\theta \tag{5.43}$$

c_b is a constant and H_s the significant wave height. Following the work of Uchiyama et al. (2010) this function is normalized and the vertical shape represented in (5.44) is assumed.

$$f^{wb}(z) = \frac{1 - tanh\left[k_b(\hat{\eta} - z)\right]^2}{\int_{-h}^{\hat{\eta}} \left(1 - tanh\left[k_b(\hat{\eta} - z)\right]^2\right) dz} \tag{5.44}$$

The penetration depth of the wave breaking induced vertical mixing is controlled by the parameter $k_b = \frac{\sqrt{2}}{a_b H_s}$, where a_b is an $O(1)$ parameter. After some sensitivity tests, Uchiyama et al. (2010) arrived at the pair of values $a_b = 1.2$ and $c_b = 0.03$, values which were also used in the applications made in this work.

5.4.3.2 At the bottom

As shown in the first part of this thesis when the waves interact with the currents, the bottom shear stress is modified comparatively with a only current case. A brief discussion was made in section 3.3.2 about the apparent roughness concept. This change in the bottom shear stress is related to viscosity effects. The oscillatory motion of waves is felt by the mean flow above the bottom boundary layer (Longuet-Higgins, 1953).

To take into account this effect in this study, the bottom shear stress condition is ensured by the calculation of a new friction coefficient C_{fwc} that includes the effects of waves on the current shear stress. Here it is obtained from the Christoffersen and Jonsson (1985) theoretical framework. It is calculated through the knowledge of the depth-integrated horizontal current velocity values and direction, the Nikuradse roughness (k_S) and the wave parameters.

Therefore the bottom shear stress is calculated in the hydrodynamic model including a new friction coefficient C_{fwc}, calculated by TOMAWAC, corresponding to a current friction coefficient affected by the presence of waves (5.45).

$$\vec{\tau}_{bot} = -\frac{1}{2}\rho C_{fwc}||u_{z=-h}||\vec{u} \tag{5.45}$$

5.5 Coupling system

In the following, we present the way the coupling system works.

First, the hydrodynamic model starts the calculation with a number of parameters imposed by the user, the computational mesh domain and bathymetry. It sends the information of depth-integrated velocities, mean surface elevation, z-levels and the Nikuradse roughness to the wave model after the first time step.

The wave model is forced with a spectral sea state offshore together with the definition of the mesh and bathymetry of the domain.

With the information given by the hydrodynamic model, the wave model computes, over a time step, the wave forcing terms: the Stokes drift components (U_s, V_s, W_s) which are dependent on the z-levels, the wave-induced pressure (J), the depth-induced wave breaking and the bottom-induced dissipation momentum contributions. The last two terms are imposed as surface (τ_{wbr}) and bottom (τ_{wbot}) stresses, respectively, in the hydrodynamic model. Furthermore, the wave model calculates the wave-enhanced diffusion coefficient (ν_{wbz}) that is added to the vertical diffusion velocity coefficient in TELEMAC-3D. This process is repeated each time step or made within a coupling period defined by the user.

The coupling period between TELEMAC-3D and TOMAWAC can be larger than the time step of the models. The time step of each of the models does not have to be the same, just a multiple of each other. Both models run with the same horizontal mesh.

Figure 5.3 shows a simplified scheme with the interaction terms exchanged in the coupling system implemented between TELEMAC-3D and TOMAWAC.

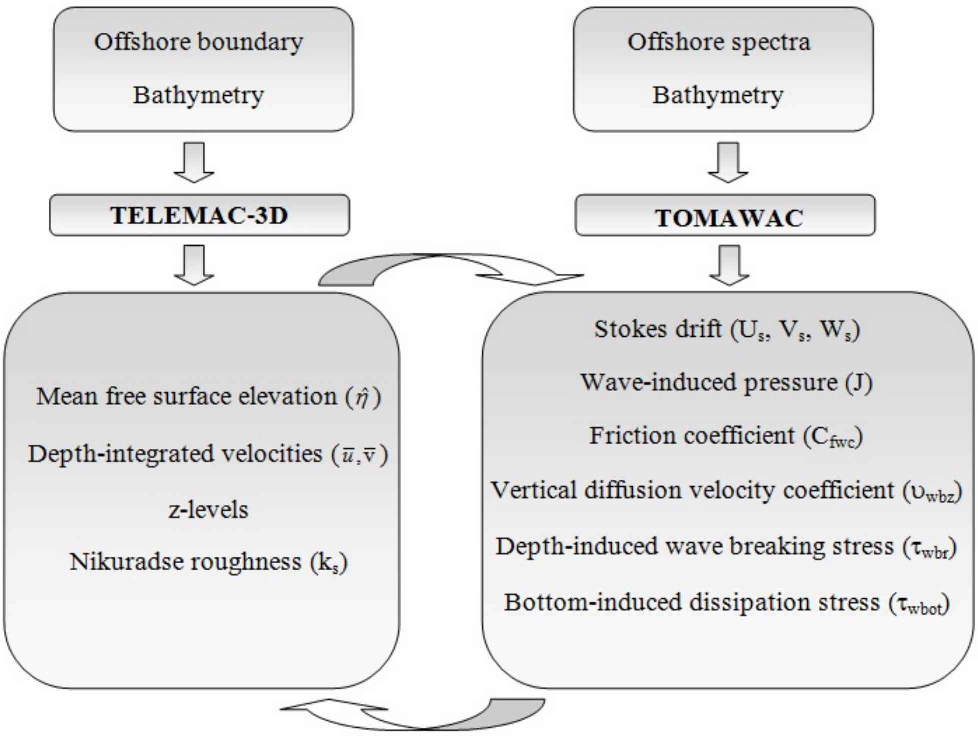

Figure 5.3: Representation of the exchanged terms in the coupled system implemented between the hydrodynamic model TELEMAC-3D and the wave spectral model TOMAWAC.

5.6 Validation - Adiabatic test

In order to validate the new coupling system obtained with the implementation of the glm2z-RANS equations (Ardhuin et al., 2008b) together with the simplifications made by Bennis and Ardhuin (2011), an academic test proposed by Bennis and Ardhuin (2011) was first made. This test has a known numerical solution and it is adapted from Ardhuin et al. (2008b).

The test presented in Bennis and Ardhuin (2011) corresponds to steady monochromatic waves, with a known frequency and incident amplitude, propagating over a bottom slope that develops from a depth of $h_1 = 6\ m$ offshore to $h_2 = 4\ m$ (Figure 5.4). The numerical solution can be achieved through a Laplace equation together with the defined boundary conditions, since no dissipation occurs and therefore the flow induced by shoaling waves over a bottom slope is irrotational.

The bottom geometry is defined as given by Roseau (1976) in which the reflection coefficient can be obtained analytically. The expression for the bottom profile is given in (5.46). x and z coordinates give the real and imaginary parts of the complex parametric function of the real variable x' (Ardhuin et al., 2008b). The bottom topography is uniform along the y direction (Figure 5.4).

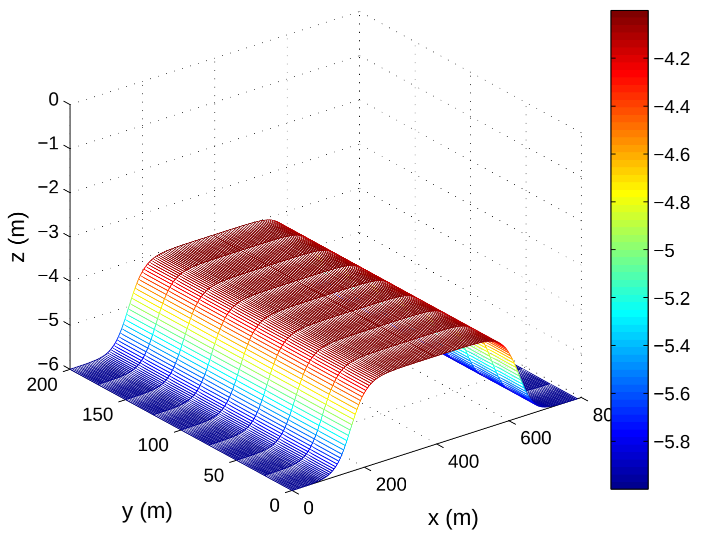

Figure 5.4: Bathymetry representation for the adiabatic test. The color scale represents the bottom elevation (m).

$$Z(x') = x + iz = \frac{h_1\,(x' - i\alpha_0) + (h_2 - h_1)\,ln\left(1 + e^{x' - i\alpha_0}\right)}{\alpha_0} \tag{5.46}$$

For notation simplicity, hereinafter the mean quasi-Eulerian velocities and the mean quasi-Eulerian surface elevation are referred to as ($u = \hat{u}$, $v = \hat{v}$) and $\overline{\eta} = \hat{\eta}$, respectively.

The upstream ($x = 0\ m$) and downstream ($x = 800\ m$) boundaries are defined as open boundaries. At these lateral boundaries, the mean surface elevation is considered zero ($\overline{\eta} = 0$) and the condition (5.41) is applied.

The hydrodynamic model was used with 10 horizontal planes equally spaced throughout the water depth and the horizontal mesh was discretized with $\Delta x = 5\ m$ and $\Delta y = 25\ m$ for which it is defined a triangular basis for each element. No viscous effects were taken into account.

TOMAWAC is a spectral wave model and therefore a spectrum or parametrized values have to be imposed at the offshore boundary. In order to represent monochromatic waves, a value for the directional spectrum of variance density was imposed for a single frequency and direction. The incident steady monochromatic waves were then characterized by a wave height of $H = 1.02\ m$, wave period $T = 5.24\ s$ and wave direction of $\theta = 90°$ (waves propagate along the positive x axis). On the upstream boundary the wave length was $L = 34.28\ m$ and over the step $L = 29.57\ m$. The sink and sources terms are all deactivated (there is no input nor dissipation).

For the hydrodynamic model the time step used was $\Delta t = 0.2\ s$ and for the wave model $\Delta t = 2\ s$. The computation ran until a stationary solution was achieved.

Due to the bottom profile, the incident wave amplitude increases. The non-dimensional water depth kD varies between $0.85 < kD < 1.1$. The group velocity varies a little from $4.89\ ms^{-1}$ (on the upstream boundary) to $4.64\ ms^{-1}$ (over the step).

The group velocity in deep water is given by linear theory through:

$$C_{g0} = g\frac{T}{4\pi} \approx 4.085 ms^{-1} \tag{5.47}$$

The shoaling coefficient from deep water to the upstream boundary of the test domain, where $C_g = 4.89\ ms^{-1}$ is thus given by:

$$K_{s1} = \sqrt{\frac{C_{g0}}{C_g}} \approx 0.914 \tag{5.48}$$

From the shoaling coefficient it is possible to obtain the wave height in deep waters $H_0 = H/0.914 \approx 1.115\ m$. Over the step the shoaling coefficient is $K_{s2} \approx 0.939$ and therefore, based on linear theory, the wave height over the step should be $H = K_{s2}H_0 \approx 1.047\ m$.

In Figure 5.5, it can be observed the wave height evolution over the domain and that TOMAWAC computes the right shoaling of wave over the bottom profile.

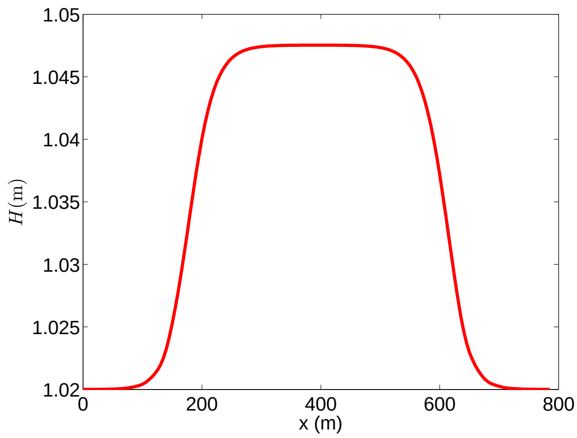

Figure 5.5: Wave height evolution. Incident wave parameters: $H = 1.02\ m$ and $T = 5.24\ s$.

The mean surface elevation obtained by the coupled system is shown in Figure 5.6. It is compared with the analytical solution for the mean surface horizontal gradient, deduced by Longuet-Higgins (1967), for slowly varying wave amplitudes over a bottom slope (5.49).

$$\overline{\eta(x)} = -\frac{kE}{sinh(2kD)} + \frac{k_0 E_0}{sinh(2k_0 D_0)} \tag{5.49}$$

The subscript ”0” corresponds to any horizontal position and E is the wave energy.

It can be seen that the horizontal mean surface elevation computed by the coupled system is in good agreement with the analytical solution given by Longuet-Higgins (1967).

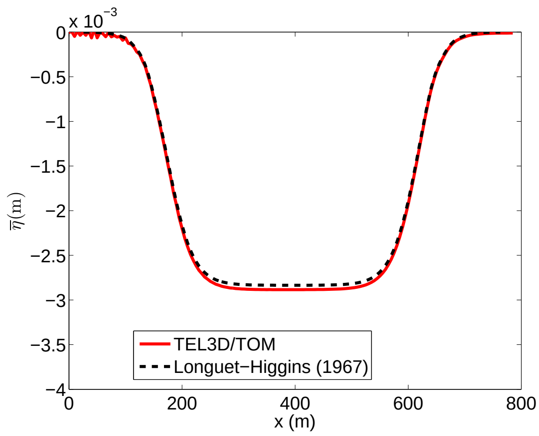

Figure 5.6: Comparison of mean surface elevation values obtained by the coupling system (TEL3D/TOM) and calculated from Longuet-Higgins (1967) analytical expression. Incident wave parameters: $H = 1.02\ m$ and $T = 5.24\ s$.

The shoaling of the incident waves is going to induce a mass transport in the shallower part of the domain (over the step). Therefore, in order to compensate the divergence of the Stokes drift (in the upper panel of Figure 5.7), a mean quasi-Eulerian steady current is generated in the opposite direction to the propagating waves (in the lower panel of Figure 5.7). Therefore the total mass conservation is ensured.

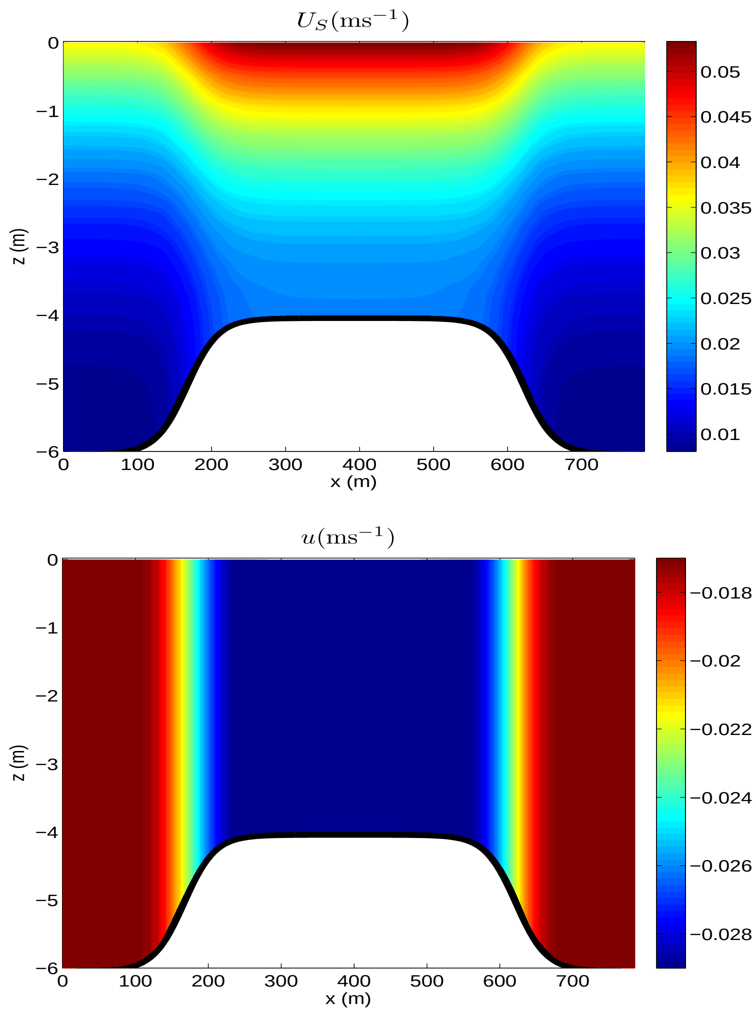

Figure 5.7: Horizontal Stokes velocity (on the top) and quasi-Eulerian velocity (on the bottom) obtained with $H = 1.02\ m$ and $T = 5.24\ s$.

Finally, the Lagrangian mean velocity $\overline{u}^L$ (Figure 5.8) is obtained by the sum of the horizontal Stokes velocity U_S with the quasi-Eulerian velocity u. Since the quasi-Eulerian velocity is nearly constant throughout the water depth, it can be seen that the contribution for the Lagrangian mean velocity shear comes entirely from the Stokes drift.

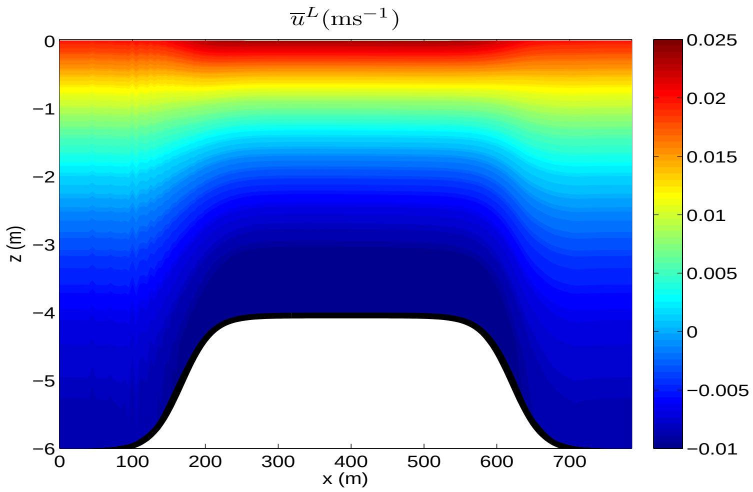

Figure 5.8: Lagrangian mean velocity obtained for $H = 1.02\ m$ and $T = 5.24\ s$.

The vertical pseudomomentum compensates for the divergence of the horizontal pseudomomentum (Ardhuin et al., 2008b), obtaining the distribution shown in Figure 5.9 for the vertical component of the Stokes drift.

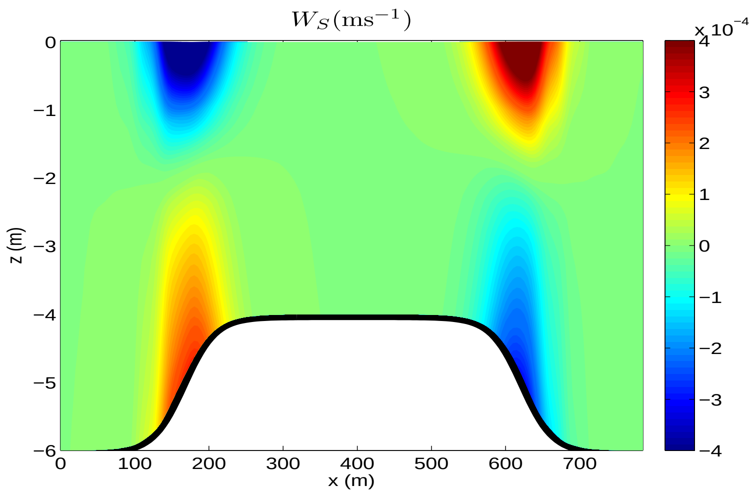

Figure 5.9: Vertical Stokes velocity for $H = 1.02\ m$ and $T = 5.24\ s$.

Since the mean current vertical shear is nearly zero and the source and sink terms are neglected, the momentum balance for this test case simplifies to:

$$u\frac{\partial u}{\partial x} = -g\frac{\partial \eta}{\partial x} - \frac{\partial J}{\partial x} \tag{5.50}$$

In Figure 5.10, it is possible to observe the evolution of the wave-induced and hydrostatic pressure gradients obtained by the numerical models. When analysing the horizontal velocity advection by itself (Figure 5.11), also obtained by the coupling system, it can be verified that it corresponds to the sum of the wave-induced pressure gradient with the hydrostatic pressure gradient. Therefore, it can be concluded that the momentum balance is achieved in the numerical solution.

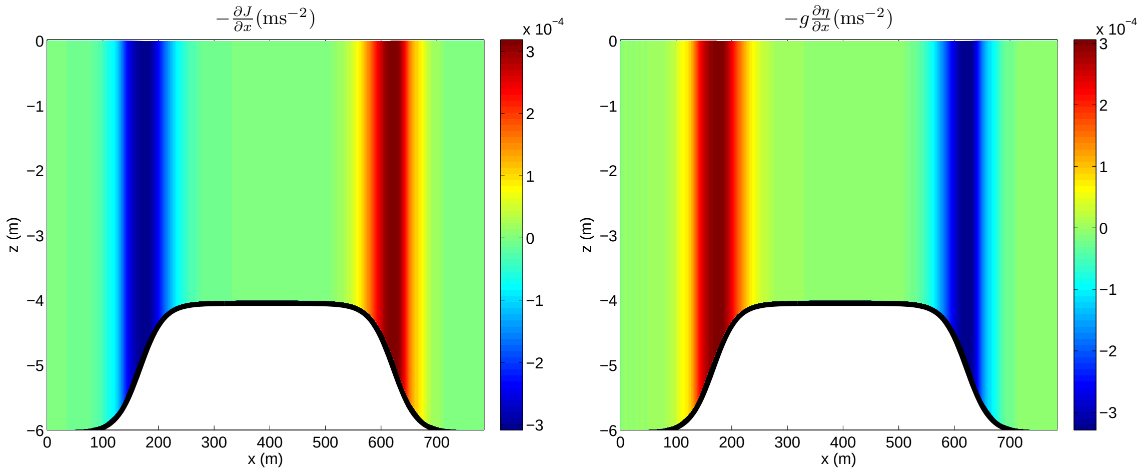

Figure 5.10: Wave-induced pressure (on the left) and hydrostatic pressure horizontal gradients (on the right) evolutions. Incident wave parameters: $H = 1.02\ m$ and $T = 5.24\ s$.

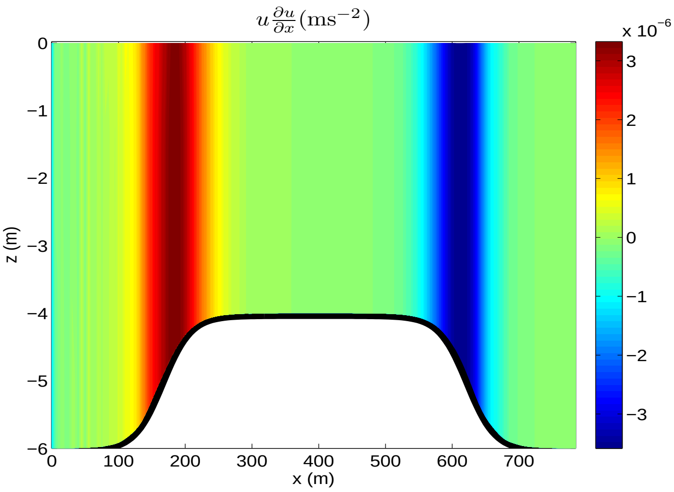

Figure 5.11: Evolution of the velocity advection by itself. Incident wave parameters: $H = 1.02\ m$ and $T = 5.24\ s$.

From the analysis made above with the adiabatic test case presented in Bennis and Ardhuin (2011) it can be concluded that the modified equations introduced in the coupled system TELEMAC-3D/TOMAWAC are well implemented. Therefore, this gives the motivation to continue with more complex test cases where, for instance, viscous effects on one hand and sink or source terms for wave dynamics on the other hand are taken into account. This is subject of the next chapter.

Chapter 6

Numerical modelling of wave-current interaction at a regional scale

6.1 Introduction

Within the coastal zone, processes like intense wave breaking and the consequent induced current generation can create a dangerous environment for humans. For instance, the rip currents can drag a swimmer several tens of meters offshore quite easily since such currents can achieve a velocity of order of magnitude $O(1)$ ms^{-1}. Unfortunately, most of swimmers are often not aware of that threat (Figure 6.1). Furthermore these currents can have a strong impact on nearshore morphodynamics. A number of studies were made in order to better understand this phenomenon (e.g. Dalrymple (1975), Putrevu et al. (1995), Haller and Dalrymple (2001), Yu (2006)). Additionally some experiences in laboratory facilities were also conducted to reproduce and study at model scale the structure of these currents (among others: Haller et al. (2002), Haas and Svendsen (2002), Castelle et al. (2010)).

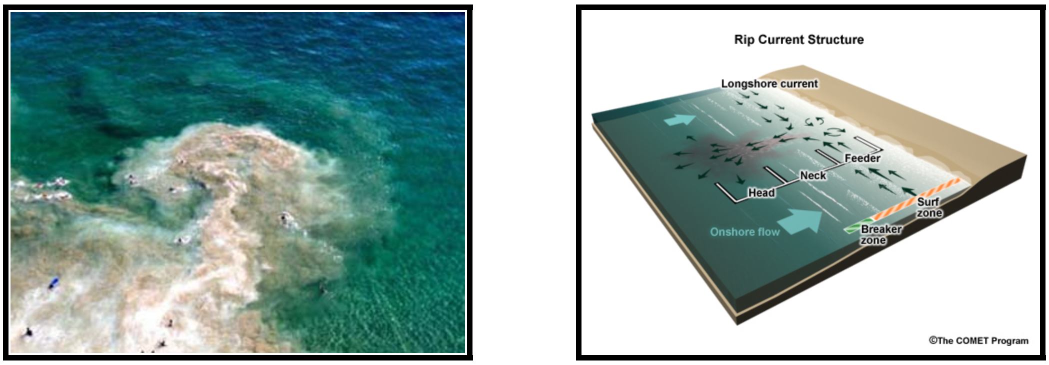

Figure 6.1: Photo and representation of a rip current. Sources: www.fire.lacounty.gov and www.comet.ucar.edu.

Longshore currents can also drag swimmers and surfers into rip currents or other hazardous areas (Figure 6.2). Moreover, the longshore drift of sediment transport is also a point of concern for coastal engineers to be aware of in areas of sand deposition or/and erosion.

In the past, Visser (1982, 1984b, 1984a, 1991) realized an extensive study about the generation of alongshore currents through experimental studies in laboratory basins. Hamilton et al. (1997) made a literature review about the different designs used in laboratory basins to study the longshore currents. More recently, Hamilton and Ebersole (2001) also used a large wave basin where the longshore uniformity of the wave-induced currents was established and measurements through a number of cross-shore and longshore sections were made. Furthermore the vertical structure of longshore currents was assessed.

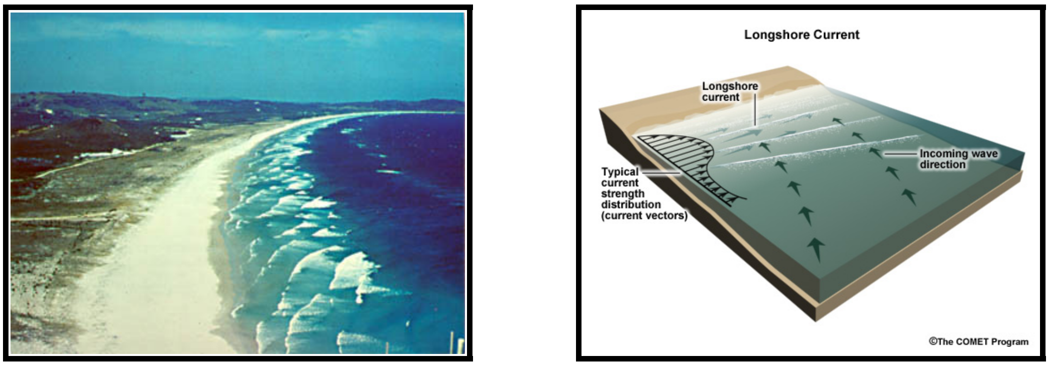

Figure 6.2: Photo and representation of a longshore current. Sources: www.indiana.edu and www.comet.ucar.edu.

Therefore, nearshore hydrodynamics are essential to study to be able to know and better predict how the different mechanisms occur and how one can prevent a number of different kinds of dangerous situations.

In this chapter, the modified equations implemented in the hydrodynamic model

TELEMAC-3D together with the coupling made with the wave model TOMAWAC are validated against two test cases realized in laboratory basins:

- on a plane beach with longshore currents (Hamilton and Ebersole, 2001);
- on a barred beach with rip currents (Haller et al. (2002) and Haas and Svendsen (2002))

Through the first test case, realized on a plane beach, it is possible to verify the capability of the coupled system to reproduce the longshore current generated by an incident wave field oblique to the beach. Moreover, the vertical structure of the mean flow is analysed. This will be addressed in section 6.2, where firstly, the experimental data is described (subsection 6.2.1) and then the model set-up (subsection 6.2.2) is presented. Finally the comparisons with the numerical model will be analysed and discussed in subsection 6.2.3.

The second test case is applied on a barred beach, where a rip current is generated by waves propagating and breaking on the bars. It will be possible to verify the capability of the model to properly reproduce the rip current system and the magnitude of this current. This will be presented in section 6.3. The experimental data is described in subsection 6.3.1, followed by the model set-up definition in subsection 6.3.2. The numerical results together with the experimental data are shown and analysed in subsections 6.3.3, 6.3.4 and 6.3.5.

6.2 Plane beach test-case

6.2.1 LSTF Data

In this present section, the capability of the coupling system between TELEMAC-3D and TOMAWAC to reproduce alongshore currents when waves propagate obliquely onto a uniform plane beach is tested. Furthermore, the vertical structure of the mean flow is also analysed.

For that purpose, data from experiments conducted in the Large-scale Sediment Transport Facility (LSTF) installed at the Coastal and Hydraulics Laboratory (CHL), Vicksburg (Figure 6.3) was used.

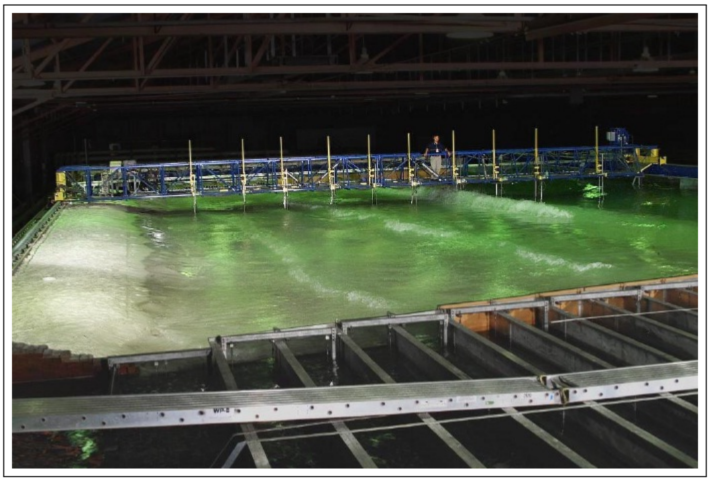

Figure 6.3: Photo from the LSTF laboratory basin. The wave-maker is on the right and the beach on the left. Source: Hamilton and Ebersole (2001).

This facility is one of the largest wave basins in the World, allowing a large scale for wave generation. It is equipped with a recirculation system in the lateral walls which ensures the uniformity of generated currents within the alongshore direction (Hamilton and Ebersole, 2001).

The laboratory basin has dimensions of approximately 30 m cross-shore and 50 m longshore. The concrete beach has a slope of 1 : 30 in the main section and 1 : 18 slope at the toe of the beach. To reproduce the natural sand roughness, the plane beach was broomed finished. So, sediments were not present in these experiments.

The wave basin has four piston-type wave generators installed. Regular and irregular long-crested waves were generated. Hereinafter, only tests with irregular waves will be referred to. These tests correspond to the series T8E from Hamilton and Ebersole (2001) where irregular waves with significant wave height of $H_S = 0.225$ m and peak period of $T_p = 2.5$ s were generated. The incident angle was $\theta = 10^\circ$ relative to the beach.

The values of surface elevation and velocity were obtained by ten capacitance-type wave gauges and ten Acoustic-Doppler Velocimeters (ADVs) respectively, that were co-located along a cross-shore direction of the wave basin. Vertical profiles of the flow velocity were obtained across the same direction. The ADVs were also located at approximately one third of the water depth above the bottom.

One of the main concerns during this experimental campaign was to guarantee a proper structure and magnitude of longshore currents. Hamilton and Ebersole (2001) followed the criteria proposed by Visser (1982) and Visser (1984b) to generate the wave-induced longshore currents that would be generated along an infinitely long beach by the breaking waves.

In Figure 6.4, it is possible to observe the general flow pattern obtained during the LSTF experiments.

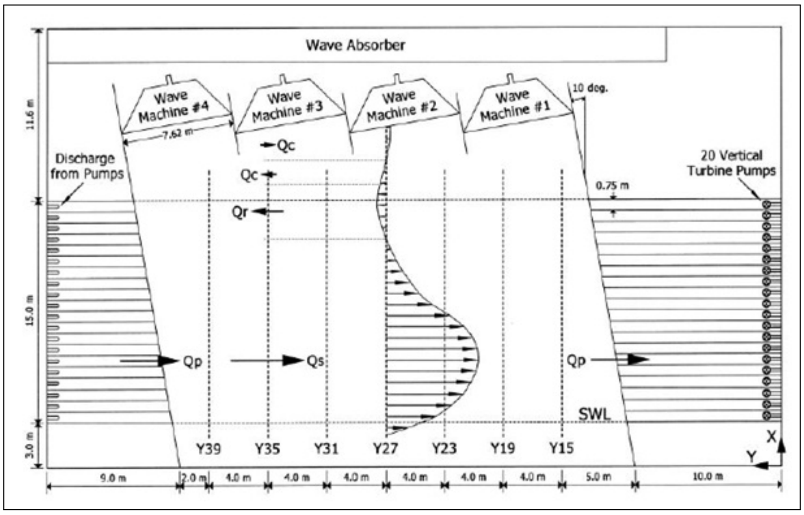

Figure 6.4: Scheme of the laboratory basin and wave-induced longshore currents in LSTF (top view). Source: Hamilton and Ebersole (2001).

On this figure, Q_s is the total longshore current between the wave set-up limit and the point of transition where the longshore current changes direction. It has two contributions:

$$Q_s = Q_p + Q_r \tag{6.1}$$

Q_p is the total longshore flow rate generated by the external pump system and Q_r represents the total longshore flow rate that internally recirculates in the offshore region. Hamilton and Ebersole (2001) found that this last contribution induced a secondary offshore circulation cell (Q_c). Therefore if Q_r is reduced so does Q_c.

6.2.2 Model setup

The numerical model domain has approximately the same dimensions as the real wave basin (Figure 6.5). The coordinate system has its origins at the offshore side of the wave basin. Positive x-axis is directed shoreward while y-axis is directed upstream. The z-axis is directed upwards with its origin at the still water level. The offshore depth was set to $h = 0.67\ m$. In the numerical model, the minimum depth shoreward was $h_{min} = 0.003\ m$.

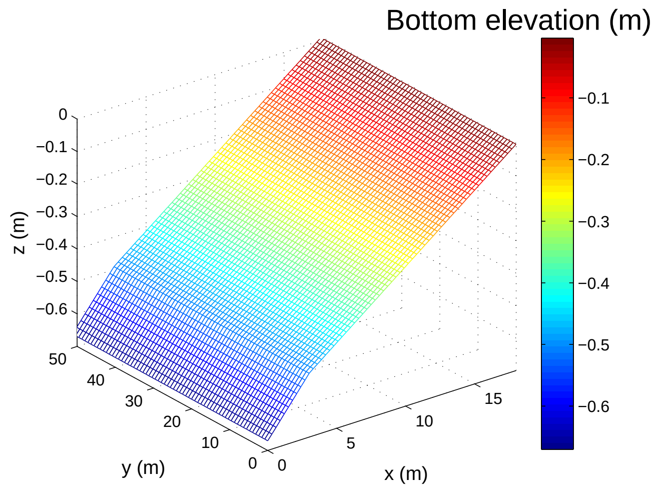

Figure 6.5: Computational domain for the reproduction of the LSTF test.

The computational domain was discretized equally for both models, with $\Delta x = 0.3\ m$ and $\Delta y = 0.8\ m$. Throughout the water depth, ten evenly spaced horizontal planes were defined in the 3D flow model. The time step was set to $\Delta t = 0.2\ s$ for both the hydrodynamic and the wave models.

Since uniform longshore currents were recreated in LSTF experiments, periodic conditions within the alonghsore direction were imposed at the lateral boundaries of the numerical wave basin.

At the offshore boundary of the hydrodynamic model, the boundary conditions defined at (5.40) and (5.41) were imposed. Moreover, a value of the Nikuradse roughness equal to $k_s = 0.0001\ m$ was assumed. This value nearly corresponds with the broomed finished concrete beach.

The $k - \varepsilon$ LP (with Linear Production) version was chosen for the turbulence closure model. While the vertical diffusion velocity coefficient is computed from the turbulence closure model, the horizontal diffusion velocity coefficient is imposed. The later was shown to be an important parameter to be adjusted to better fit experimental data. After some experiments, a constant value ($\nu_H = 0.2\ m^2 s^{-1}$) was set along the domain. Besides better fitting with experimental data, it was possible to get smoother solutions. The obtained value for the horizontal diffusion velocity coefficient is in the range of values used in other similar applications (Uchiyama et al. (2010), Kumar et al. (2012)).

The enhanced mixing due to wave breaking was taken into account through the expressions (5.42) and (5.44) with $c_b = 0.03$ and $a_b = 1.2$ (Uchiyama et al., 2010).

Furthermore, it must be noted that, as a laboratory basin is being reproduced numerically, there is no effect of wind and the Coriolis force is neglected, since at this scale it will not have any effect.

A JONSWAP spectrum was imposed with a peak enhancement factor $\gamma_e = 7$. The following parameters were forced at the offshore boundary of the wave model: significant wave height ($H_s = 0.225$ m), peak wave period ($T_p = 2.5$ s) and mean wave direction ($\theta_m = 80°$). The minimum frequency was set to 0.1 Hz, the number of frequencies $n_f = 25$ and the frequency ratio was $q = 1.07$. For the depth-induced breaking, Thornton and Guza (1983)$'$s model was chosen with the parameters $B = 1.25$ and $\gamma = 0.75$.

Both the effects of waves on the current and of the current on the propagation of waves were taken into account. The model ran continuously until a stationary state was achieved.

6.2.3 Wave-induced longshore current

First, the cross-shore distributions of significant wave height, mean surface elevation and velocity at one third of the water depth above the bottom were analysed and compared with measurements. Both measurements and numerical results were obtained by averaging the values over four cross-shore arrays.

From the left panel of Figure 6.6, it can be observed that the variation of the wave height is well modelled by the coupled system. Following the criteria used by Hamilton and Ebersole (2001), the breaking position is established when the significant wave height starts to decrease at the highest rate ($x \approx 8$ m).

The flux of momentum lost by the breaking waves induces a rise in the mean water level, the so-called wave set-up. Comparing the numerical results with data (right panel of Figure 6.6), it can be seen that the modelled mean surface elevation follows quite closely the measured values in the cross-shore array, although the wave set-down is a bit underestimated.

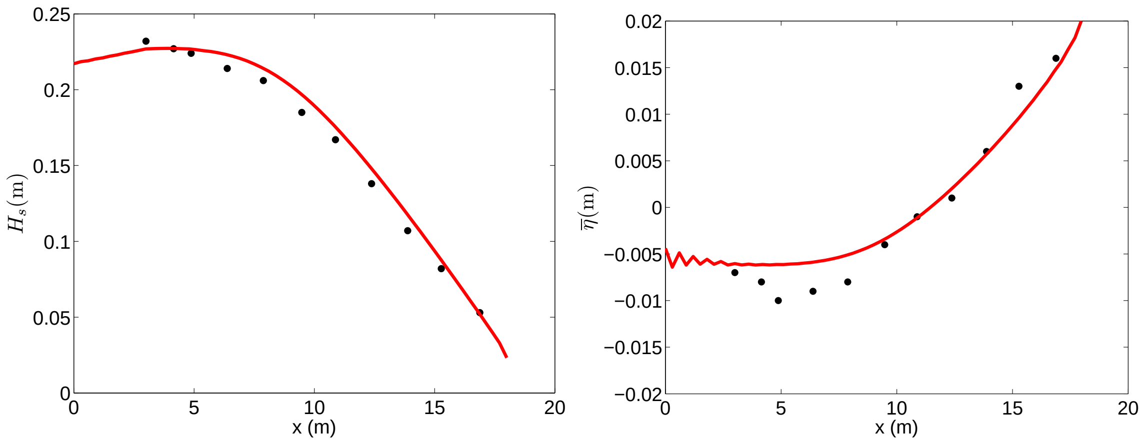

Figure 6.6: Cross-shore evolution of the significant wave height (H_s) and the mean surface elevation ($\overline{\eta}$). Comparison between numerical results (line) and experimental data (dots).

After waves start to break, the flux of momentum in the longshore direction associated with wave dissipation reaches its maximum absolute value ($x \approx 11\ m$) (Figure 6.7).

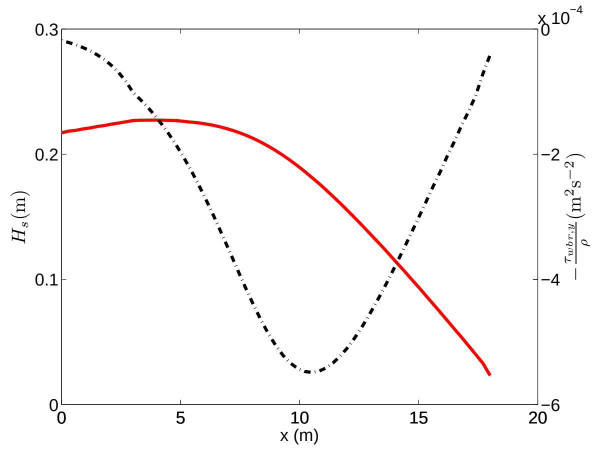

Figure 6.7: Cross-shore evolution, from numerical results, of the significant wave height (H_s) and of the longshore stress component of depth-induced wave breaking ($\tau_{wbr,y}/\rho$).

Since the waves have an oblique incidence towards the beach, when they break, a longshore current is generated as first explained by Longuet-Higgins and Stewart (1964). The longshore current velocity at one third of the water column above the bottom reaches a maximum value of $v \approx 0.34\ ms^{-1}$ around $x \approx 14\ m$ (Figure 6.8), just after the cross-shore section where the maximum dissipation rate occurs (Figure 6.7). It can be seen, when compared to the measurements, that the evolution of the longshore current profile and also its magnitude are very well modelled by the coupled system.

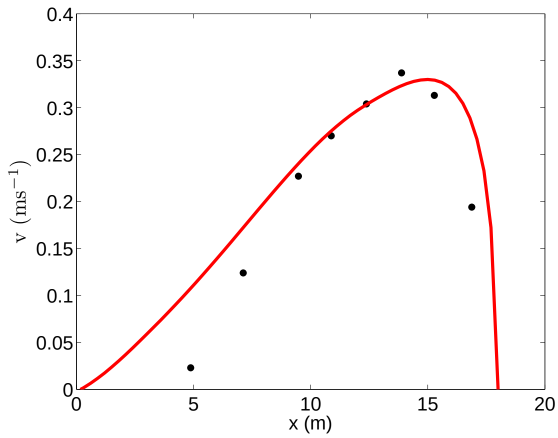

Figure 6.8: Cross-shore evolution of the longshore quasi-Eulerian velocity at one third of the water depth above the bottom. Comparison between numerical results (line) and experimental data (dots).

The slight differences observed in the offshore part of the domain, between numerical results and experimental data, can be caused by the difficulties felt in the laboratory basin in controlling a longshore flow that internally recirculated in the offshore region. Considering the scheme of a longshore current profile presented by Visser (1984a) (Figure 6.9), it can be seen that, at the cross-section where waves start to break (x_{br}), the longshore velocity should have approximately half the value of the maximum longshore velocity. From the numerical results obtained with the coupled system (Figure 6.8), this feature can be seen: for $x_{br} \approx 8\ m$, the longshore velocity is $v \approx \frac{v_{max}}{2} \approx 0.17\ ms^{-1}$.

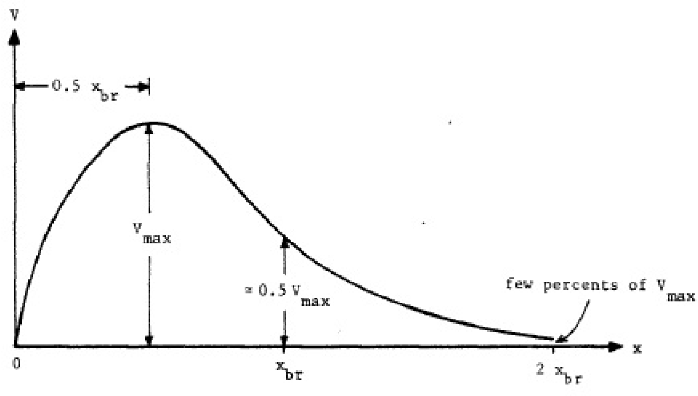

Figure 6.9: Scheme of a longshore current profile. Here the coastline is located at $x = 0\ m$. Source: Visser (1984a).

In order to guarantee the conservation of mass, an offshore oriented cross-shore depth-integrated quasi-Eulerian velocity has necessarily to be generated (Uchiyama et al., 2010). In Figure 6.10 it can be seen that it is about one order of magnitude smaller than the longshore quasi-Eulerian velocity. The cross-shore section for which the maximum value occurs is in accordance with the one obtained for the maximum value of the momentum flux lost by the breaking waves.

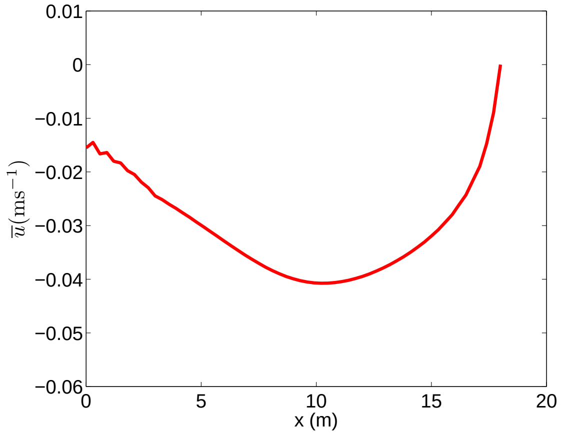

Figure 6.10: Cross-shore evolution, from numerical results, of the depth-integrated cross-shore quasi-Eulerian velocity.

6.2.4 Analysis of vertical structure of the flow

6.2.4.1 Cross-shore and longshore dynamics

In this section we present and analyse the vertical distribution of the quasi-Eulerian velocity, Stokes drift, Lagrangian mean velocity and new wave forcing terms incorporated in the momentum equation along a cross-shore array in the centre of the wave basin ($y = 27\ m$).

In Figure 6.11 the horizontal component of the cross-shore quasi-Eulerian velocity is presented. Outside the surf zone, the cross-shore velocity is weakly directed offshore throughout the water depth. Within the surf zone its vertical shear is clear, showing the importance of taking into account the vertical structure of the mean flow. It is essential, for instance, to analyse the sediment transport near the bed. A near-surface onshore flow with $u \approx 0.08\ ms^{-1}$ can be observed, which appears due to the transfer of momentum from the breaking waves to the mean flow (τ_{wbr}). An oriented offshore undertow with $u \approx -0.15\ ms^{-1}$ close to the bottom occurs to compensate the mass transport induced by the Stokes horizontal velocity (Figure 6.12).

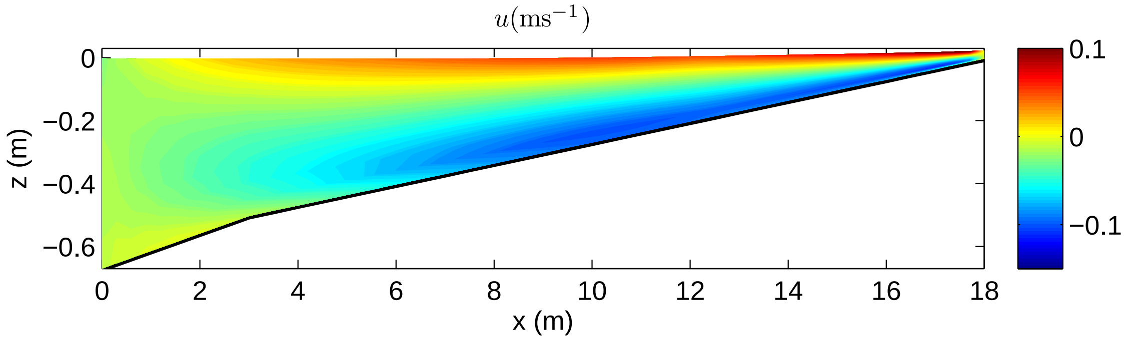

Figure 6.11: Cross-shore section at $y = 27$ m, from the numerical results, of the cross-shore quasi-Eulerian horizontal velocity.

The cross-shore Stokes horizontal velocity (Figure 6.12) shows an increase within the surf zone approximately between $x = 8$ m and $x = 12$ m. It has a maximum value of approximately 0.055 ms^{-1}, which is the same order of magnitude as the quasi-Eulerian current shown above. It can be observed that throughout the water depth the Stokes horizontal velocity is quite sheared.

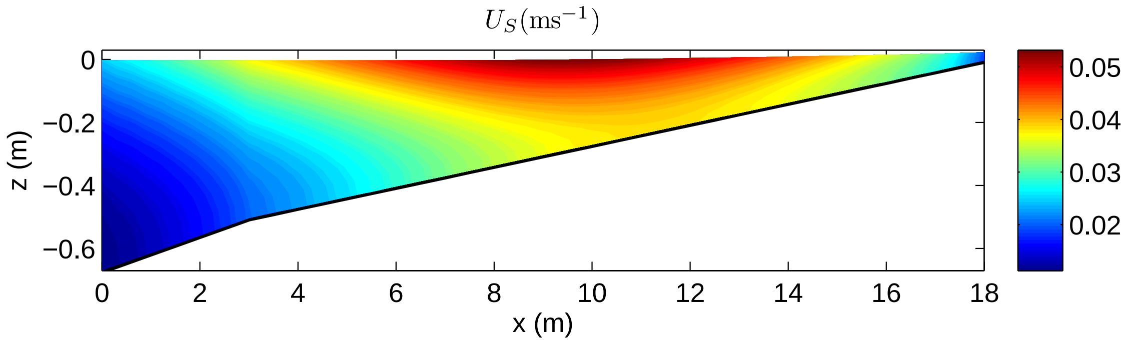

Figure 6.12: Cross-shore section at $y = 27$ m, from the numerical results, of the cross-shore Stokes horizontal velocity.

Finally, the cross-shore Lagrangian mean velocity is obtained by adding the contribution of the Stokes drift to the quasi-Eulerian velocity (Figure 6.13). It is seen that near the free surface, the Lagrangian mean velocity is onshore directed and near the bed, the undertow predominates.

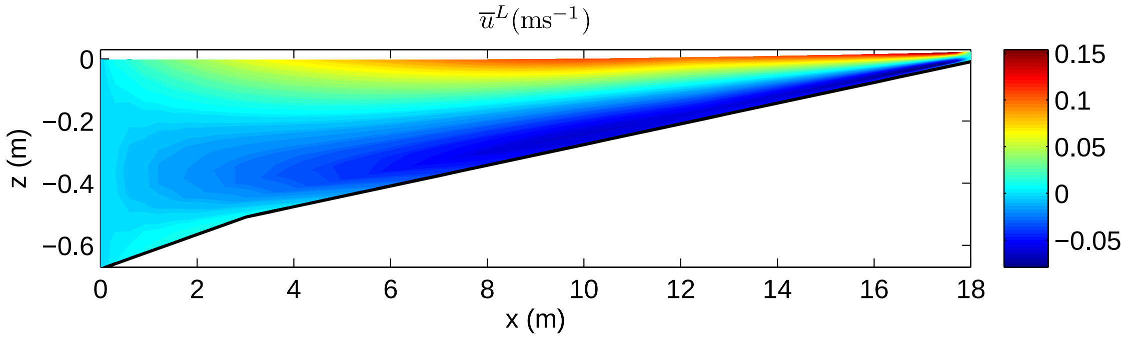

Figure 6.13: Cross-shore section at $y = 27\ m$, from the numerical results, of the cross-shore Lagrangian mean velocity.

Figure 6.14 and Figure 6.15 show the cross-shore distributions of the longshore current and longshore Stokes horizontal velocity, respectively. It can be observed that the longshore quasi-Eulerian velocity is one order of magnitude stronger than what was obtained for the cross-shore velocity plotted in Figure 6.11. The longshore velocity reaches a maximum value of $v \approx 0.35\ ms^{-1}$ at $x \approx 15\ m$ and decreases towards offshore. The longshore velocity vertical shear is not as significant as the cross-shore velocity shear. Due to the small wave incidence angle relative to the beach line, the Stokes drift in the longshore direction (Figure 6.15) is one order weaker than the one in the cross-shore direction. It reaches a maximum of $V_S \approx 0.008\ ms^{-1}$ between $x \approx 7\ m$ and $x \approx 10\ m$.

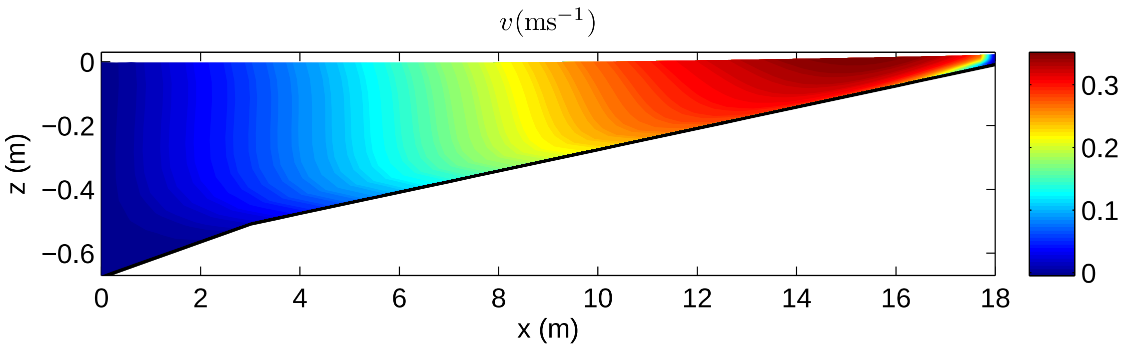

Figure 6.14: Cross-shore section at $y = 27\ m$, from the numerical results, of the longshore quasi-Eulerian velocity.

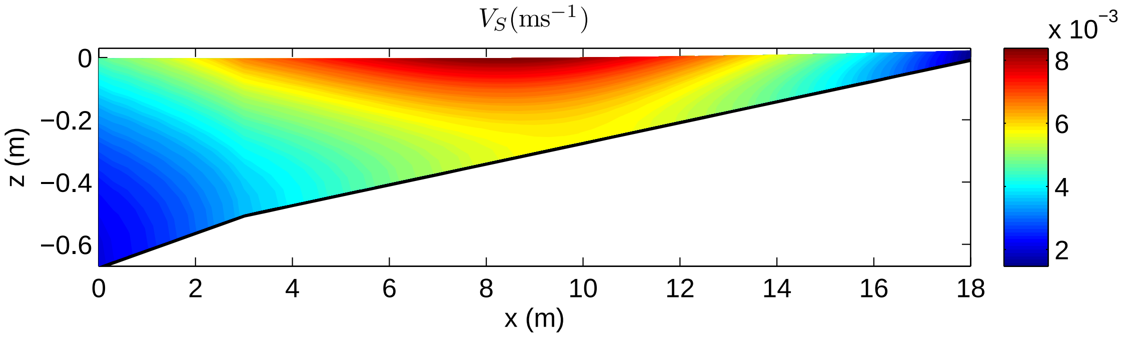

Figure 6.15: Cross-shore section at $y = 27\ m$, from the numerical results, of the longshore Stokes horizontal velocity.

In the same way as the cross-shore component of the Lagrangian mean velocity was obtained, the longshore component of the Lagrangian mean velocity is calculated and plotted in Figure 6.16.

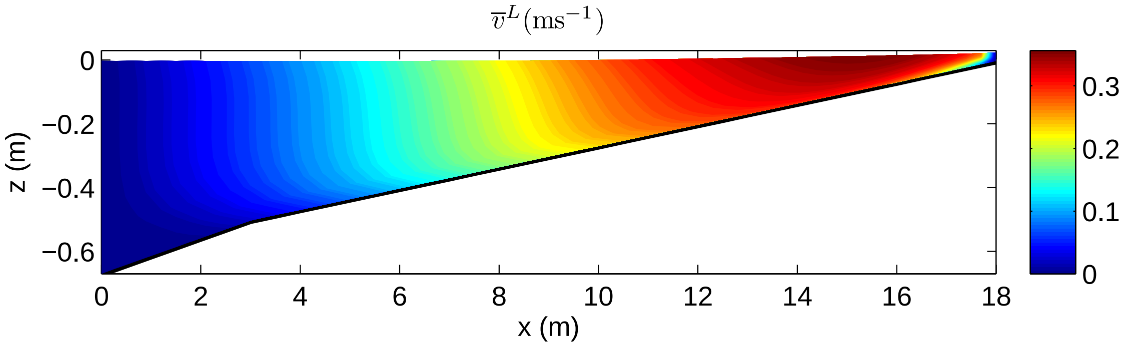

Figure 6.16: Cross-shore section at $y = 27\ m$, from the numerical results, of the longshore Lagrangian mean velocity.

The vertical component of the Stokes velocity (W_S) is presented in Figure 6.17. This variable is calculated with expression (5.31). Approximately where the waves start to break, W_s is equal to zero near the free surface. It becomes negative towards offshore and increases in the direction of the coastline.

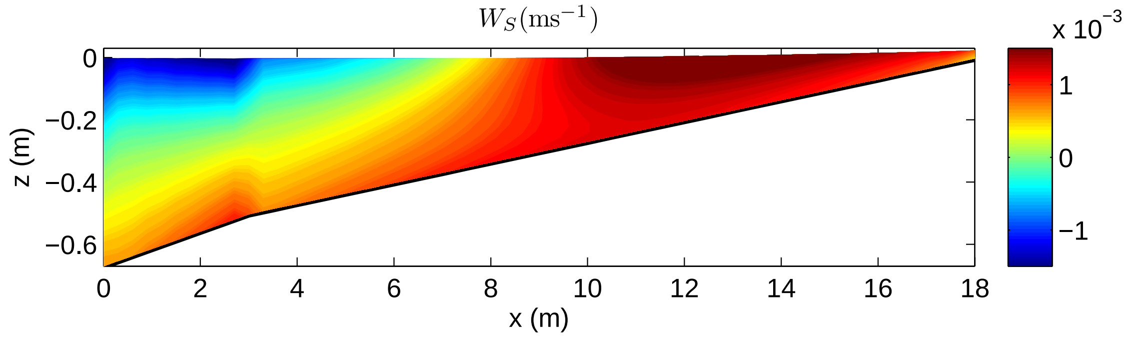

Figure 6.17: Cross-shore section $y = 27$ m, from the numerical results, of the vertical component of the Stokes drift.

As the effects of wind and Coriolis force are neglected, the wave-induced forcing terms on the hydrodynamic model are the vortex force, the wave-induced pressure and the momentum flux induced by wave dissipation (wave-enhanced vertical mixing (ν_{wbz}), waves breaking (τ_{wbr}) and bottom friction induced wave dissipation (τ_{wbot})).

The momentum equations presented in section 5.4.1 are simplified within this test case, where a longshore uniformity is achieved. For the stationary solution the cross-shore (x component) momentum balance reads:

$$u\frac{\partial u}{\partial x} + w\frac{\partial u}{\partial z} = -g\frac{\partial \eta}{\partial x} + \frac{\partial}{\partial x}\left(\nu_H\frac{\partial u}{\partial x}\right) + \frac{\partial}{\partial z}\left((\nu_z + \nu_{wbz})\frac{\partial u}{\partial z}\right) + \left(V_s\frac{\partial v}{\partial x} - W_s\frac{\partial u}{\partial z}\right) - \frac{\partial J}{\partial x} \tag{6.2}$$

In addition to the momentum balance presented in (6.2), the free surface and bottom stresses due to depth-induced wave breaking ($\tau_{wbr,x}/\rho$) and bottom-induced wave dissipation ($\tau_{wbot,x}/\rho$) cross-shore components have to be associated (Figure 6.18). The former is distributed throughout the water depth due to vertical mixing (Uchiyama et al. (2010), Kumar et al. (2012)). It can be seen that the term ($\tau_{wbot,x}/\rho$), representative of the bottom streaming effect, is an order of magnitude lower than ($\tau_{wbr,x}/\rho$).

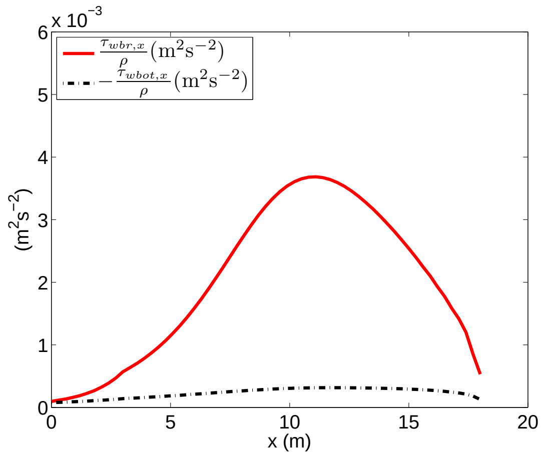

Figure 6.18: Evolution of the cross-shore stress components of depth-induced wave breaking ($\tau_{wbr,x}/\rho$) and bottom-induced wave dissipation ($\tau_{wbot,x}/\rho$).

In Figure 6.19 the cross-shore wave-induced pressure gradient is shown. It is uniformly distributed over the water depth and it increases toward the shoreline. One can observe that offshore, the gradient is negative, which produces a decrease in the water level, the so-called wave set-down. On the contrary, after wave breaking the wave-induced pressure gradient is positive creating a water level raise, the wave set-up.

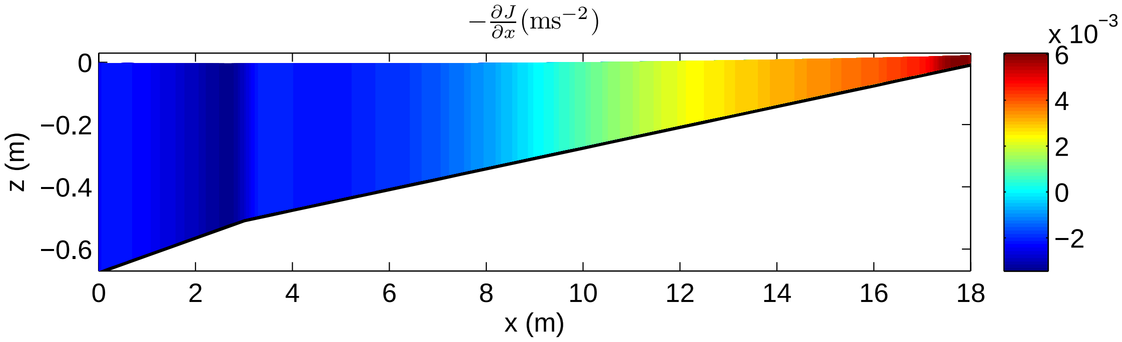

Figure 6.19: Cross-shore section at $y = 27\ m$, from the numerical results, of the wave-induced pressure gradient.

To complete the analysis of the wave forcing terms, in Figure 6.20 it can be seen that, within the surf zone, the vortex force cross-shore component is quite sheared throughout the water depth.

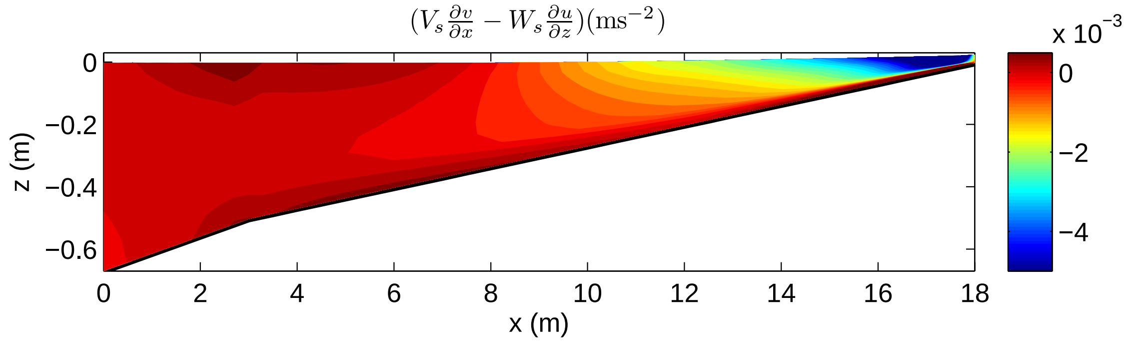

Figure 6.20: Cross-shore section at $y = 27$ m, from the numerical results, of the vortex force cross-shore component.

Moreover, in Figure 6.21, the hydrostatic pressure gradient is presented. It can be observed that, likewise the wave-induced pressure, it is uniformly distributed over the water depth and with increasing values toward the shoreline.

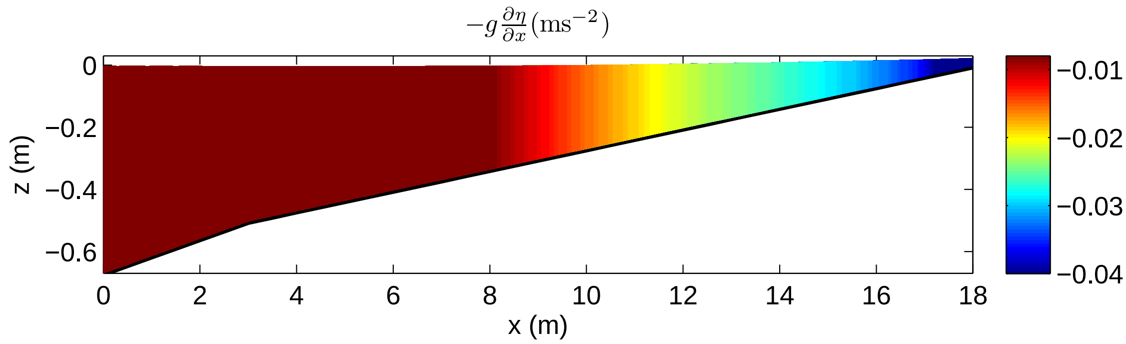

Figure 6.21: Cross-shore section at $y = 27$ m, from the numerical results, of the hydrostatic pressure gradient.

Among the different terms presented above, the most relevant ones to the cross-shore momentum balance appear to be the hydrostatic pressure gradient and the momentum lost by waves due to depth-induced wave breaking. The later term is vertically distributed over depth due to the vertical mixing.

Finally, the cross-shore velocities obtained by the coupled system are compared with the experimental data. An overview of the cross-shore evolution at $y = 27$ m of the cross-shore quasi-Eulerian velocity vertical profiles is presented in Figure 6.22. It can be verified that the numerical results represent well the magnitude and vertical structure of the cross-shore velocities.

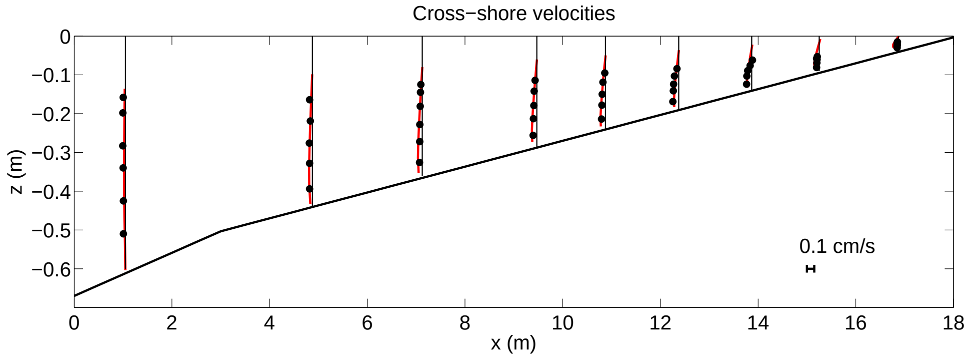

Figure 6.22: Comparison of vertical profiles of cross-shore velocity vertical profiles at $y = 27\ m$ from numerical results (lines) and LSTF experimental data (dots). The vertical lines represent the measurement sections.

It is possible to take a closer look at the vertical distributions of the cross-shore quasi-Eulerian velocities presented in Figure 6.22. In Figure 6.23 they are shown again for $y = 27\ m$, but with more detail for each analysed cross-section in order to analyse more closely the vertical structure of the flow. The vertical shear is clearly seen in model results for each cross-shore location, with positive velocities near the free surface and negative velocities near the bed. In general the numerical results are quite close to the measurements, showing a good trend of the velocity vertical profiles over the water column. Nevertheless there is an overestimation of the velocities magnitude, especially in the inshore zone. The differences found could be caused by the chosen turbulence closure model which influences the vertical distribution of the turbulence viscosity and therefore the velocity profile (this will be confirmed in section 6.2.4.4). Moreover, the momentum lost by waves due to depth-induced breaking is imposed at the free surface boundary of the hydrodynamic model. A vertical distribution of this source of momentum over the water column would certainly induce some changes on the vertical profile of the cross-shore velocities.

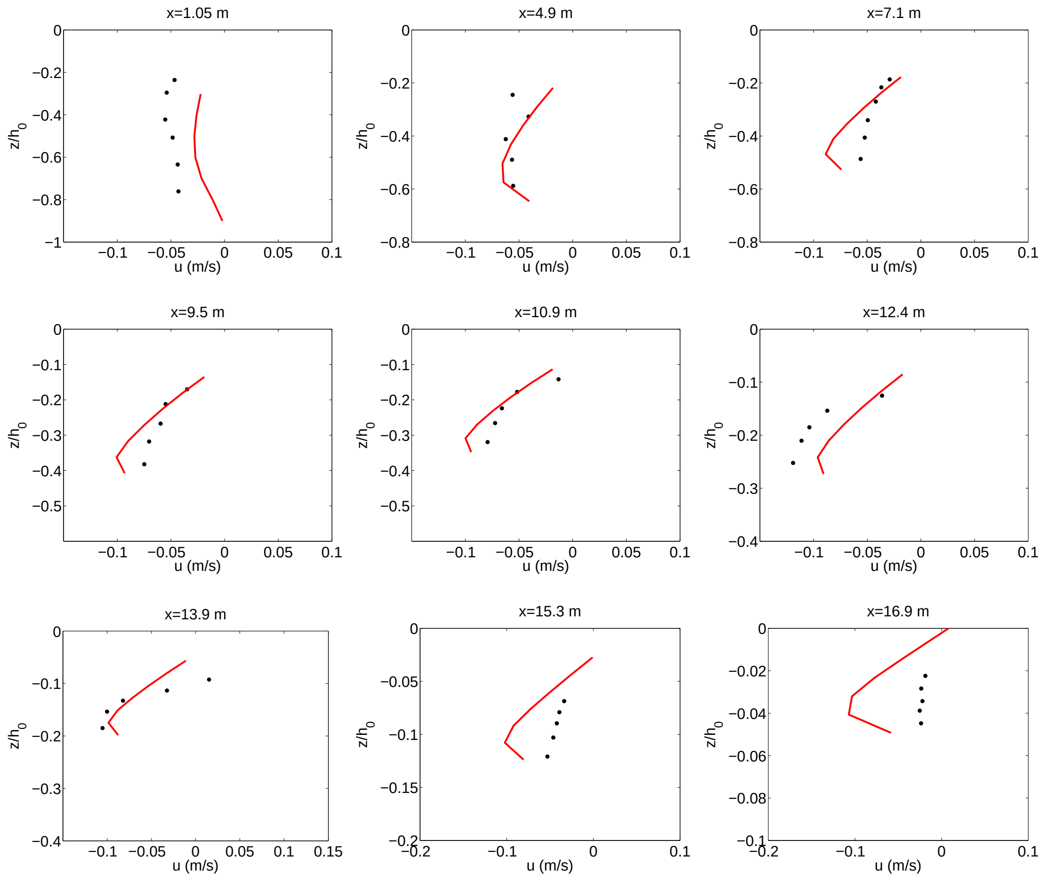

Figure 6.23: Comparison at $y = 27$ m between the cross-shore velocities obtained by the numerical model (line) and measured from LSTF experimental data (dots).

In what concerns the longshore (y component) momentum balance, the same is done as for the analysis in the cross-shore direction. The momentum equation is also simplified as the following:

$$u\frac{\partial v}{\partial x} + w\frac{\partial v}{\partial z} = \frac{\partial}{\partial x}\left(\nu_H \frac{\partial v}{\partial x}\right) + \frac{\partial}{\partial z}\left((\nu_z + \nu_{wbz})\frac{\partial v}{\partial z}\right) + \left(-U_s\frac{\partial v}{\partial x} - W_s\frac{\partial v}{\partial z}\right) \tag{6.3}$$

Here, as it can be seen in (6.3), the longshore component of the vortex force and the wave-enhanced mixing effects are the main wave forcing terms that contribute to the momentum balance. Additionally, the depth-induced wave breaking and bottom-induced wave dissipation have to be associated to it. In Figure 6.24 the longshore component of the vortex force is shown along a cross-shore array. It can be observed that it is quite sheared throughout the water depth, with the maximum located near the free surface (due to the Stokes drift).

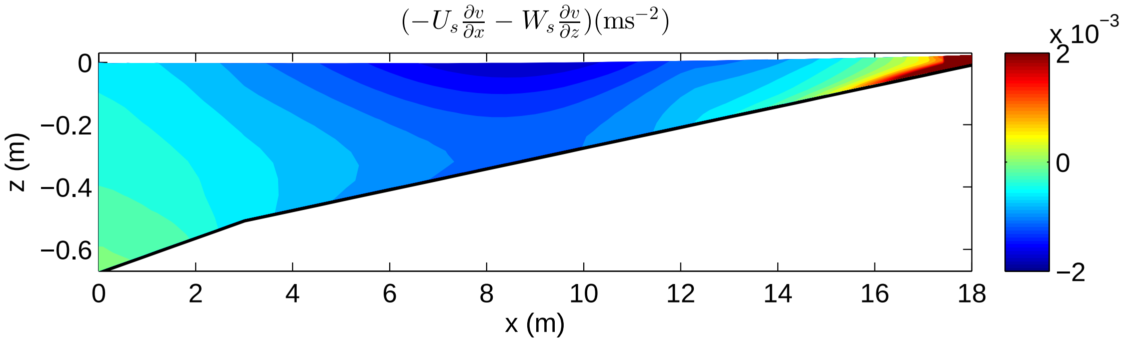

Figure 6.24: Cross-shore section at $y = 27\ m$, from the numerical results, of the vortex force longshore component.

In what concerns the surface and bottom stresses due to waves breaking and bottom-induced wave dissipation, they play an important role in the longshore balance. Already, in the past, Longuet-Higgins (1970) showed that the longshore balance is given by the radiation stresses gradient and the bottom friction dissipation. Within the vortex force formulation, the longshore dynamics are controlled by the bottom friction contribution ($\tau_{wbot,y}/\rho$) together with the longshore component of the vortex force ($-U_s\frac{\partial v}{\partial x} - W_s\frac{\partial v}{\partial z}$) and the momentum flux lost by depth-induced wave breaking ($\tau_{wbr,y}/\rho$).

The evolution of the longshore stress components of depth-induced wave breaking and bottom-induced wave dissipation ($\tau_{wbr,y}/\rho$, $\tau_{wbot,y}/\rho$) are presented on the left panel of Figure 6.25. The same contributions but divided by the total water depth ($\tau_{wbr,y}/(\rho D)$, $\tau_{wbot,y}/(\rho D)$) (giving the equivalent to an acceleration) are shown on the right panel of the same figure.

After waves start to break, the longshore vortex force is going to be balanced, near the free surface, with the longshore surface stress component of depth-induced wave breaking ($x \approx 9\ m$). Then the contribution of the former force starts to decrease and the latter continues to increase. It can be observed, on the right panel of Figure 6.25, that the maximum contribution of the surface stress is seen at $x \approx 15\ m$ which is the location where the longshore velocity reaches its maximum.

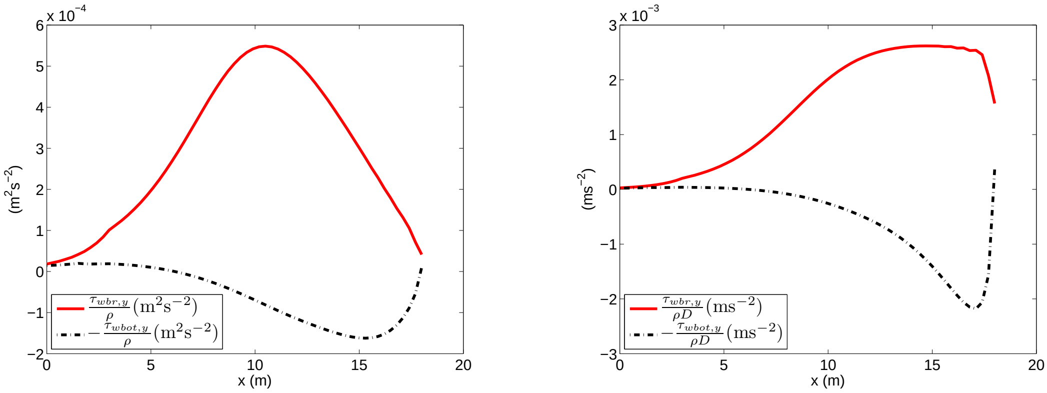

Figure 6.25: Evolution of the longshore stress components of depth-induced wave breaking and bottom-induced wave dissipation ($\tau_{wbr,y}/\rho$, $\tau_{wbot,y}/\rho$) on the left panel and the same contributions but divided by the total water depth ($\tau_{wbr,y}/(\rho D)$, $\tau_{wbot,y}/(\rho D)$) on the right panel.

In Figure 6.26, an overview of the comparisons made between the cross-shore evolution of longshore quasi-Eulerian velocities obtained by the numerical results and experimental data are shown. In general, a good agreement is achieved.

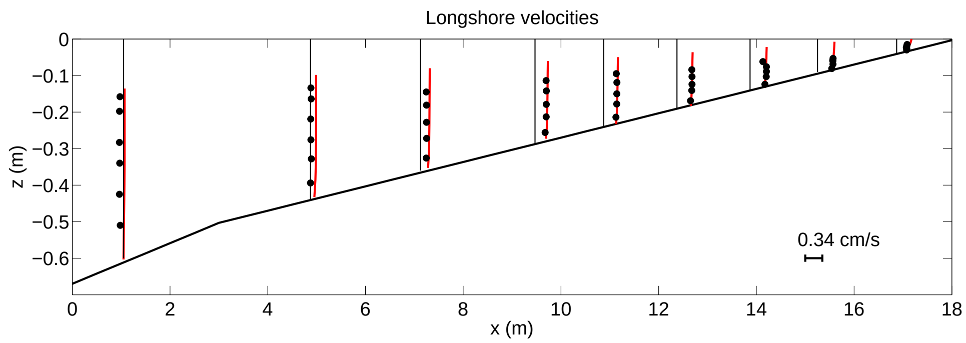

Figure 6.26: Comparison at $y = 27\ m$ of the longshore quasi-Eulerian velocity vertical profiles from numerical results and LSTF experimental data. The vertical lines represent the measurement sections.

In order to take a closer look at the figure above, in Figure 6.27, the vertical distributions of the longshore quasi-Eulerian velocities for each cross-shore direction are shown. In the offshore part the domain (upper panels of Figure 6.27), it can be confirmed that the model overestimates the longshore velocity throughout the water depth. As stated before this can be caused by the difficulties felt in the laboratory basin in controlling a longshore flow that internally recirculated in the offshore region. Regarding the other cross-shore sections, the same features can be seen as in the previous analysis, i.e., the vertical velocity shear is smaller than the one observed for the cross-shore velocities. Nevertheless, the longshore velocities reach a maximum value with an order of magnitude greater than the cross-shore velocities. The measurements show a slight increase in the current velocity towards the free surface. The numerical results also show the same behaviour throughout the water column, fitting quite well the experimental data.

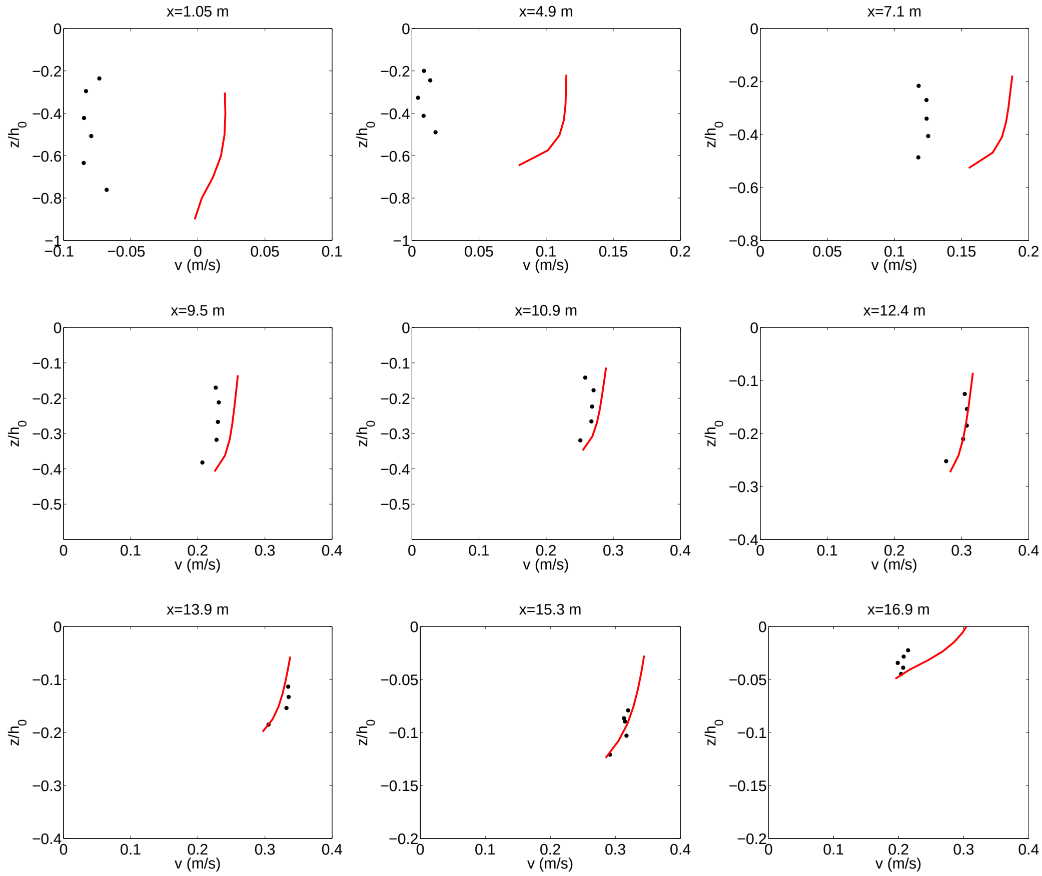

Figure 6.27: Comparison between the quasi-Eulerian longshore velocities obtained by numerical results (line) and measured from LSTF experimental data (dots).

6.2.4.2 Sensitivity tests on radiation stress and vortex force

In order to check the results obtained if the coupling between the hydrodynamic and wave models was made only through the radiation stress concept (Longuet-Higgins (1953), Longuet-Higgins and Stewart (1962, 1964)), comparisons were made with both the new implementation based on the vortex force approach and the data. The forces induced by the radiation stresses were distributed uniformly over depth in the hydrodynamic model.

In Figure 6.28, six profiles of the cross-shore velocity are shown. It is observed that in the case of simply forcing the radiation stress induced forces, there is no cross-shore velocity component. In fact, since no Stokes drift is included, there is no induced mass flux to be compensated.

In Figure 6.29 the longshore velocity profiles are presented for the same cross-shore sections. It can be observed that in the case of using the radiation stress formalism, the vertical shear of the longshore velocities is quite different from the one obtained using the vortex force approach. These differences could be caused by the fact that in the former case, no surface nor bottom stresses were included in the hydrodynamic model from the momentum lost by waves due to depth-induced breaking and bottom friction. Additionally, in this case the wave-enhanced mixing is also absent.

The improvement on the numerical results when the new version of the coupling system is applied can be confirmed.

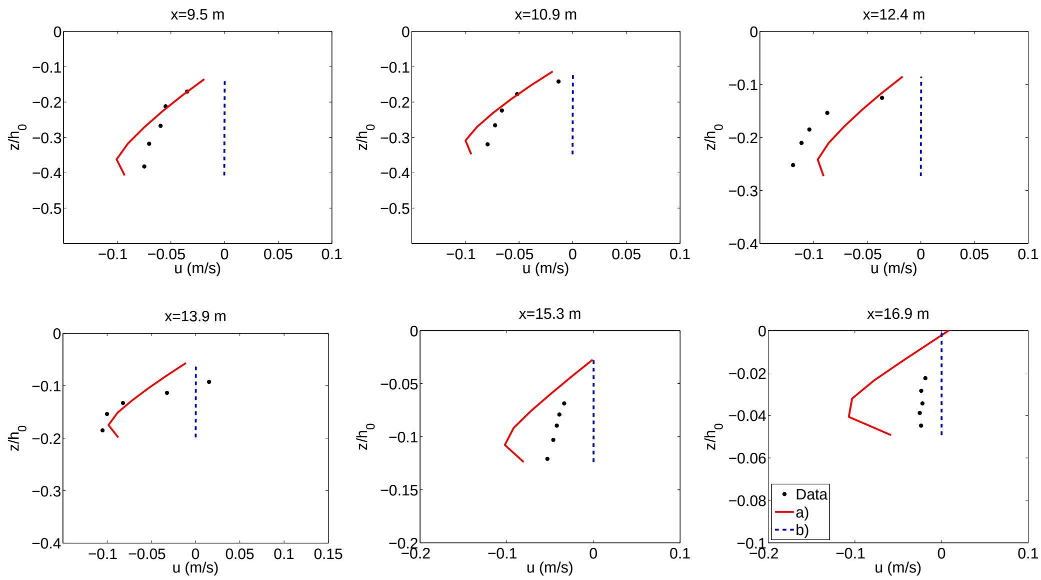

Figure 6.28: Comparison of the cross-shore velocities between the measurements from LSTF experimental data (dots) and the numerical results applying the vortex force (Ardhuin et al., 2008b) (a) and the radiation stress (Longuet-Higgins (1953), Longuet-Higgins and Stewart (1962, 1964) (b) approaches.

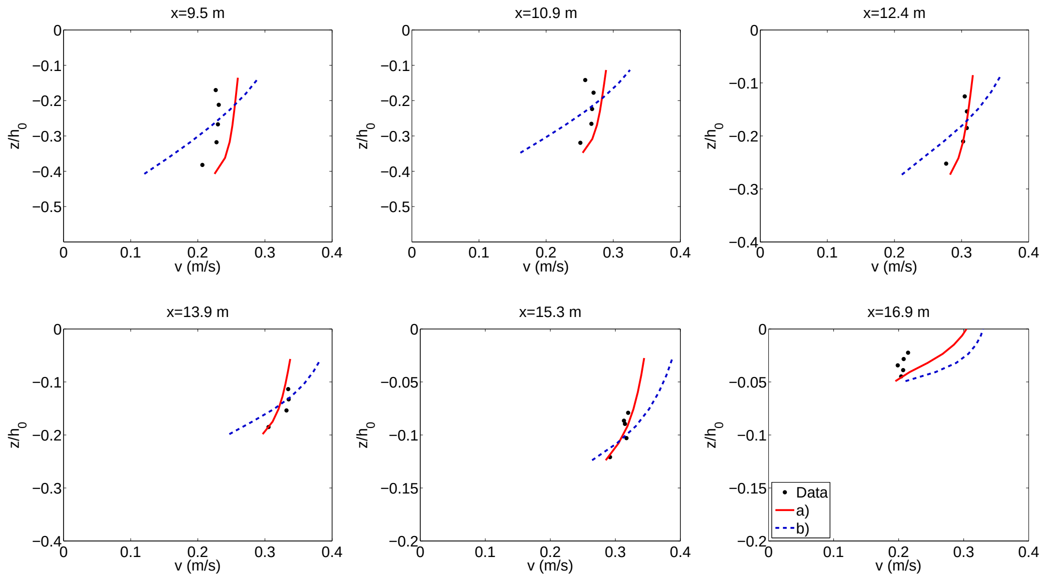

Figure 6.29: Comparison of the longshore velocities between the measurements from LSTF experimental data (dots) and the numerical results applying the vortex force (Ardhuin et al., 2008b) (a) and the radiation stress (Longuet-Higgins (1953), Longuet-Higgins and Stewart (1962, 1964) (b) approaches.

6.2.4.3 Sensitivity tests on bottom roughness and streaming

Bottom friction plays an important role in the longshore momentum balance. Therefore, some tests were made to see the sensitivity of the coupled system to the bottom roughness parameter. Different Nikuradse roughness values were imposed in the hydrodynamic model ($k_S = 0.001\ m$, $k_S = 0.0005\ m$, $k_S = 0.0001\ m$, $k_S = 0.00005\ m$) obtaining the results shown below. First, it can be verified that no great influence can be observed in the cross-shore velocities vertical profiles (Figure 6.30). Then, in Figure 6.31, it can be seen that increasing the Nikuradse roughness parameter, the longshore velocities tend to decrease both in the surf and inshore zones.

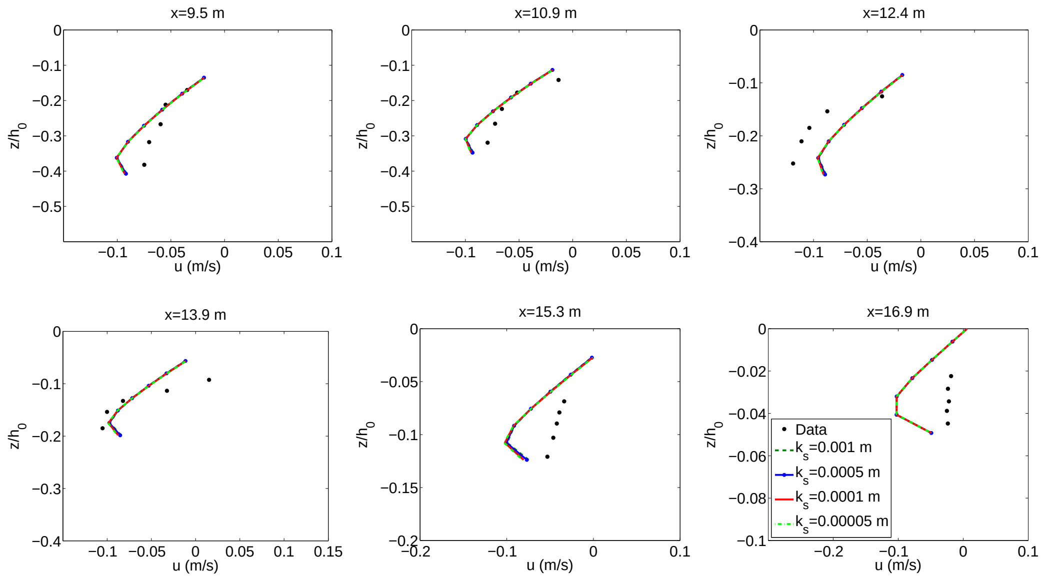

Figure 6.30: Comparison of the cross-shore quasi-Eulerian velocities between the measurements from LSTF experimental data (dots) and the numerical results with different and decreasing imposed Nikuradse roughness: $k_s = 0.001\ m$, $k_s = 0.0005\ m$, $k_s = 0.0001\ m$, $k_s = 0.00005\ m$.

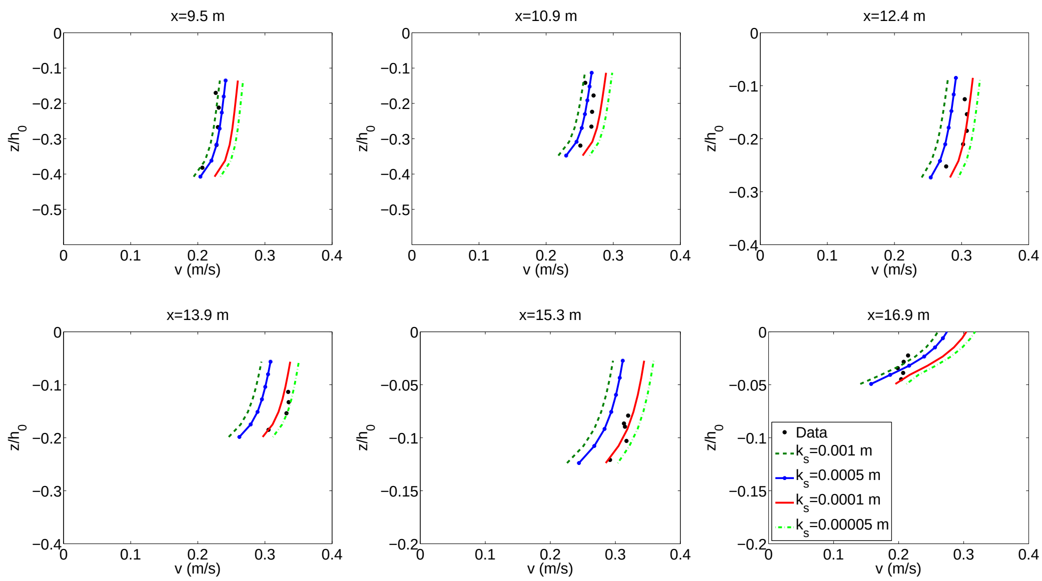

Figure 6.31: Comparison of the longshore quasi-Eulerian velocities between the measurements from LSTF experimental data (dots) and the numerical results with different and decreasing imposed Nikuradse roughness: $k_s = 0.001\ m$, $k_s = 0.0005\ m$, $k_s = 0.0001\ m$, $k_s = 0.00005\ m$.

It was also decided to make a sensitivity test regarding the relative importance of the bottom streaming effect. Two different tests were made: one in which the τ_{wbot} term is introduced as a bottom stress in the hydrodynamic model and another where $\tau_{wbot} = 0$. With the former option it is possible to reproduce the bottom streaming flow.

It can be seen in Figures 6.32 and 6.33 that, in general, taking into account the bottom streaming effect improves the numerical results, particularly near the bottom for the cross-shore velocities and throughout the water depth for the longshore velocities.

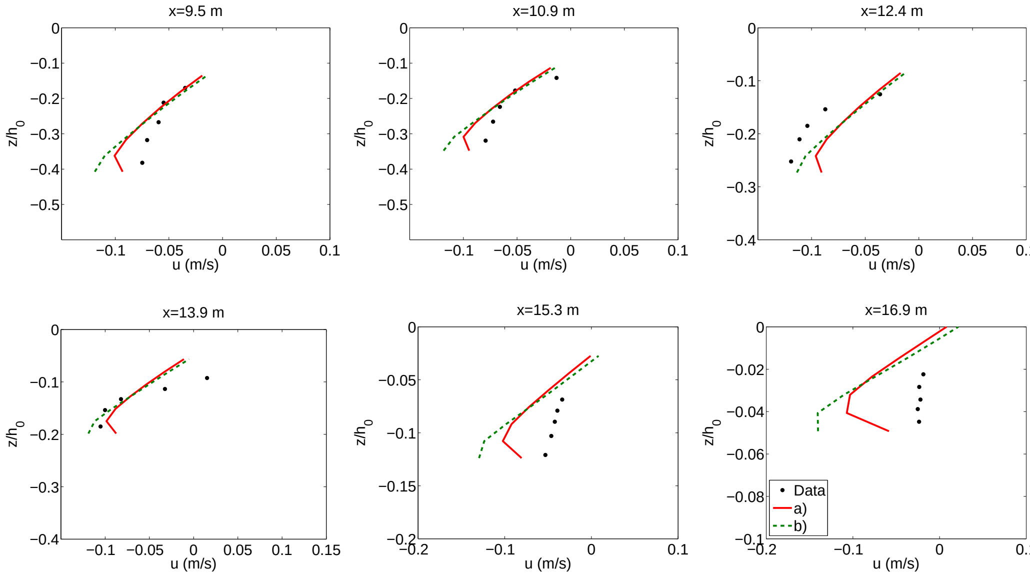

Figure 6.32: Comparison of the cross-shore velocities between the measures from LSTF experimental data (dots) and the numerical results taking (a)) and not taking into account (b)) the bottom streaming effect.

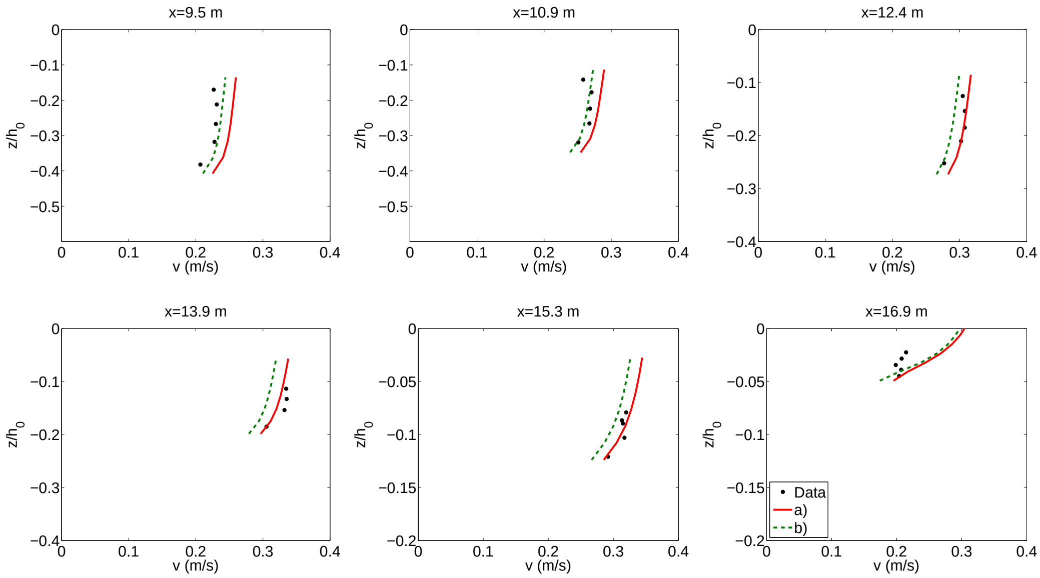

Figure 6.33: Comparison of the longshore velocities between the measurements from LSTF experimental data (dots) and the numerical results taking (a)) and not taking into account (b)) the bottom streaming effect.

6.2.4.4 Vertical mixing

Since the surface stress injected in the hydrodynamic model due to the loss of momentum when waves break has an important role in the cross-shore and longshore momentum balance, the way that this force is then distributed throughout the water depth is essential. This is controlled by vertical mixing.

In Figure 6.34, the cross-shore sections of the vertical diffusion velocity coefficient computed by the $k-\epsilon$ LP model only (ν_z) and the contribution of the wave-enhanced vertical mixing only (ν_{wbz}) are shown.

It can be seen that the values of the vertical eddy velocity diffusivity, from both contributions, reach their maximum near the free surface and in the cross-section where waves start to break ($x_{br} \approx 8\ m$). Nevertheless, it can be verified that in the present test case, the wave-enhanced vertical mixing values (on the right panel of Figure 6.34) are significantly lower than the values of the vertical diffusion velocity coefficient computed by the $k-\epsilon$ LP model (on the left panel of Figure 6.34). Please note that the additional contribution of the wave-enhanced vertical mixing was calculated based on the values ($c_b = 0.03$ and $a_b = 1.2$) used by Uchiyama et al. (2010).

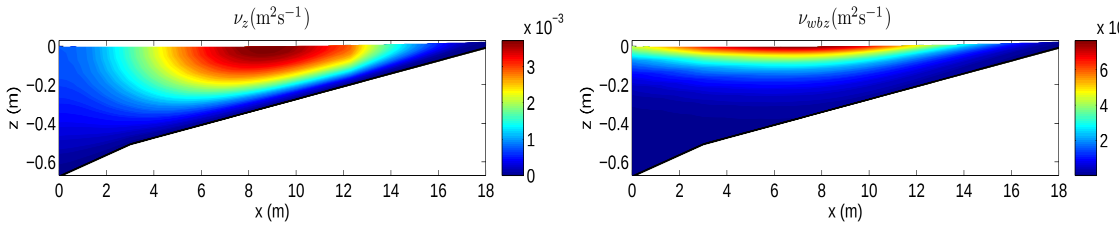

Figure 6.34: Cross-shore sections at $y = 27\ m$, from the numerical results, of the vertical eddy velocity diffusivity computed by $k-\epsilon$ LP model only, ν_z (m^2s^{-1}) (on the left panel) and the contribution of the wave-enhanced vertical mixing only ν_{wbz} (m^2s^{-1}) (on the right panel). Please note that the color scale is different on the two panels.

In Figure 6.35, it can be verified how the vertical eddy velocity diffusivity (vertical mixing) is distributed over a cross-shore array of the computational domain within different choices of the turbulence closure model applied in the hydrodynamic model: the $k-\varepsilon$ LP, the standard $k-\varepsilon$, the Prandtl (Prandtl, 1925) and the Nezu and Nakagawa (Nezu and Nakagawa, 1993) models. Additionally, the contribution from the wave-enhanced vertical mixing is also included in these representations.

It can be observed, as would be expected, that different distributions are obtained depending on the chosen turbulence closure model.

It can be seen that the vertical mixing values have their maximum near the free surface with the two versions of the $k-\varepsilon$ model. On the other hand, with Prandtl and Nezu and Nakagawa′s models the vertical diffusion velocity coefficient decreases when approaching the free surface.

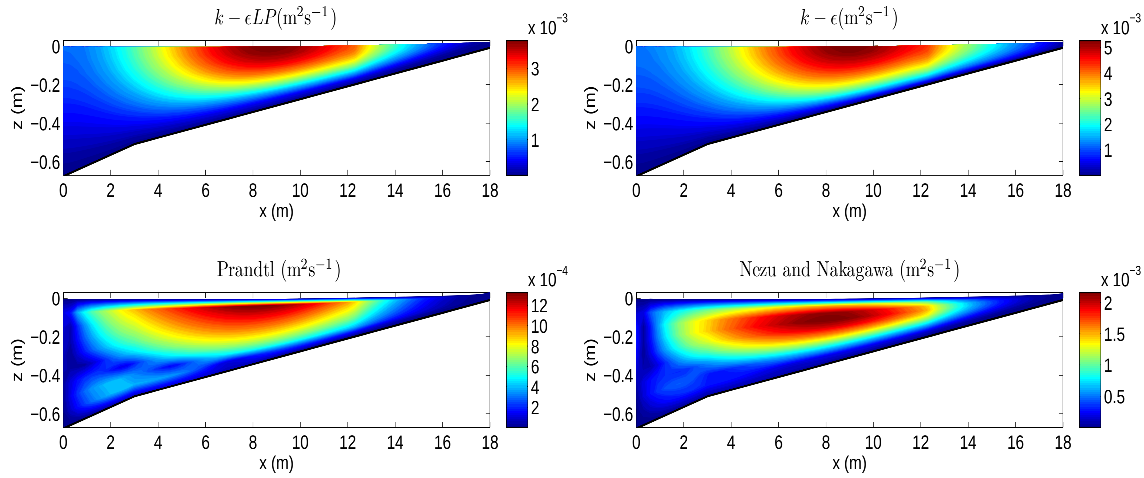

Figure 6.35: Cross-shore sections at $y = 27\ m$, from the numerical results, of the vertical eddy velocity diffusivity $(\nu_z + \nu_{wbz})$ $(m^2 s^{-1})$ using different turbulence closure models. Please note that the color scale is different on the four panels.

The vertical velocity profiles obtained with the different turbulence closure models are shown below. It can be seen that the two $k-\varepsilon$ model versions fit quite well the experimental data, both the cross-shore and longshore velocity profiles. What was stated earlier can be confirmed, regarding the influence of the vertical mixing on the vertical profiles of the cross-shore velocity in the inshore zone. For instance, if the standard model $k-\varepsilon$ is used instead of $k-\varepsilon$ LP version the vertical profile of the cross-shore velocity at $x = 15.3\ m$ fit the data better.

If the Prandtl or the Nezu and Nakagawa models are applied, we observe firstly an overestimation of the cross-shore velocity magnitude from the bottom to the middle of the water depth, and secondly an underestimation of the longshore velocities throughout of the water column.

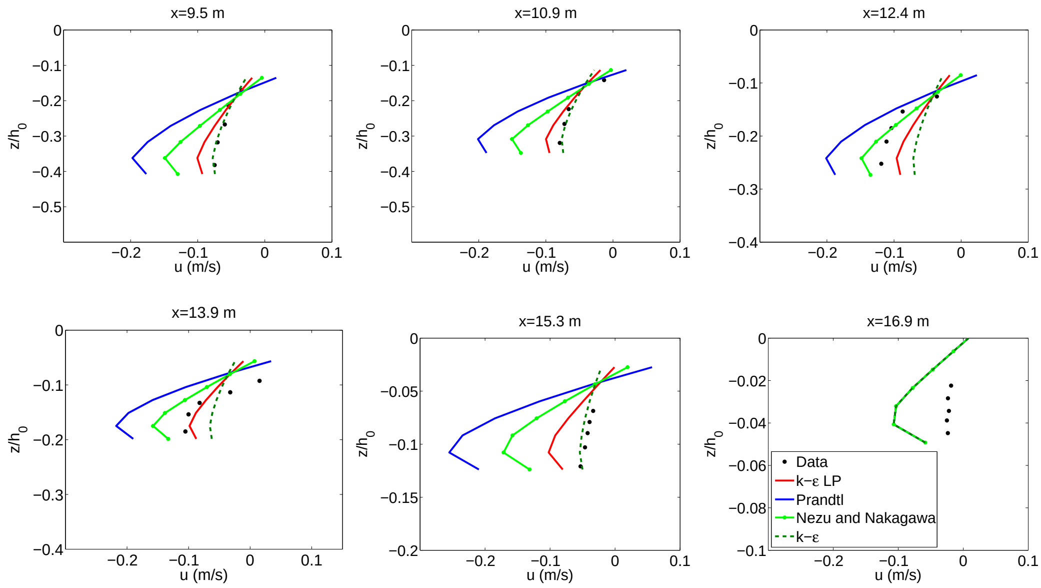

Figure 6.36: Comparison of the cross-shore quasi-Eulerian velocities between the measurements from LSTF experimental data (dots) and the numerical results using different turbulence closure models.

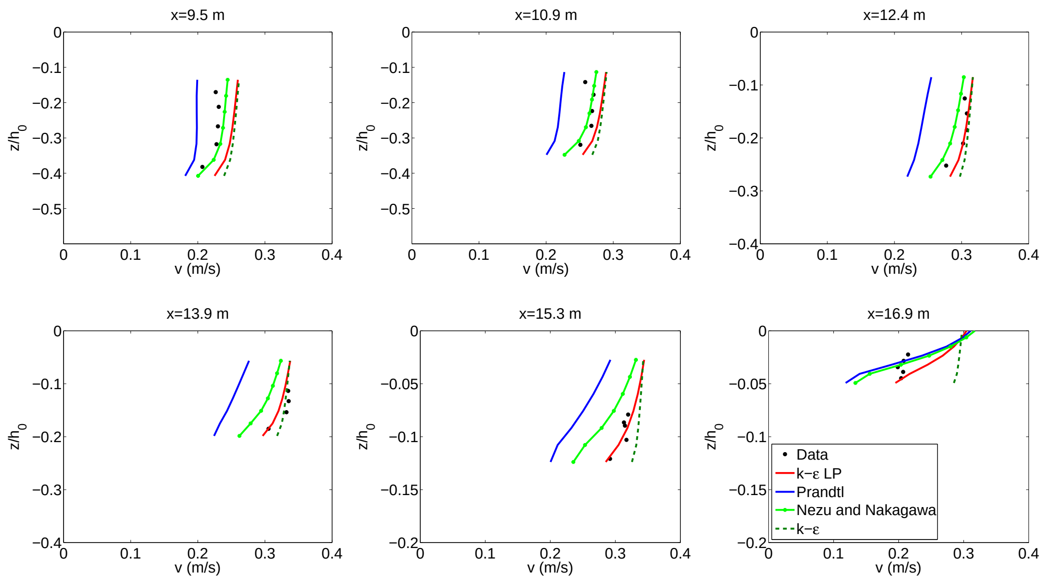

Figure 6.37: Comparison of the longshore quasi-Eulerian velocities between the measurements from LSTF experimental data (dots) and the numerical results using different turbulence closure models.

Furthermore, the coupled system was tested with and without taking into account the effect of waves on the bottom friction coefficient. This was done by implementing the theoretical framework by Christoffersen and Jonsson (1985). No important differences were found. Maybe the cause for the similarities found is that the physical bottom roughness of the wave basin is characterized by a small Nikuradse roughness value ($k_s = 0.0001\ m$) and thus no significant changes are induced by the propagation of the wave field.

6.3 Barred beach test-case

6.3.1 Experimental data

In the previous section, wave-induced longshore currents were analysed. The bathymetry was made of contour lines parallel with the beach line, with no variations in the longshore direction. Therefore the wave-induced currents were uniform in the alongshore direction.

If longshore variations of the bathymetry are taken into account, such as the existence of bars or other bathymetry patterns in the nearshore zone, the currents will no longer be uniform. Instead, if a channel is created between the bars, a rip current system can form.

In order to test the capability of the coupled system to model the flow patterns of a rip current system on a barred beach, experimental data from Haller et al. (2002) was used. Furthermore, to complete the analysis, the vertical structure of rip currents was also assessed and compared with data from Haas and Svendsen (2002).

The facility is located in the basin of the Ocean Engineering Laboratory (University of Delaware, U.S.A.). It has dimensions of 17.2 *m* in the cross-shore direction and 18.7 *m* in the alongshore direction. The cross-shore bathymetry profile is divided into two sections: offshore there is a slope of 1 : 5 between 1.5 *m* to 3 *m* from the wave maker and then a slope with 1 : 30 takes place until the end of the wave basin. Parallel to the coastline there is a fixed bar with two channels which have approximately 1.82 *m* of longshore length and 6 *cm* height (Figure 6.38). They are located approximately 11.8 *m* from the offshore wave-maker.

Figure 6.38: Photo from the barred beach installation at the University of Delaware. Source: www.coastal.udel.edu/faculty/basin.

Haller et al. (2002) used ten capacitance gauges and three two-dimensional side-looking Doppler Velocimeters (ADVs) to get a horizontal coverage over the wave basin. They measured at different cross-shore and longshore sections, the time series of surface elevation and they obtained the velocity values at approximately 3 cm above the bed. All measured quantities were time-averaged over $t \approx 1500$ s.

Despite the great advantage of these experiments, there was a lack of information regarding the three-dimensionality of the rip current system. Furthermore, Haas et al. (2003) showed that the three-dimensionality of the rip currents had a significant effect on the overall flow patterns. Consequently, Haas and Svendsen (2002) have also included in their facility three Sontek Acoustic Doppler Velocimeters that had the possibility of being located at three different positions over the water column. Therefore vertical profiles of the cross-shore velocity were obtained.

During the recorded time series ($t \approx 1800$ s), the velocities showed several fluctuations in the rip channels. These fluctuations were analysed by a number of authors (e.g. Haller and Dalrymple (2001), Kennedy and Zhang (2008)) and were associated with the unstable nature of rip currents. Instead of time-averaging the velocities over all the time record as done by Haller et al. (2002), Haas and Svendsen (2002) applied a bin-averaging technique.

6.3.2 Model setup

The computational domain was discretized equally for both models, with $\Delta x = \Delta y = 0.2$ m, and was divided in eight horizontal planes in z direction for the 3D flow model. The offshore depth was $h = 0.68$ m. The minimum depth shoreward was set to $h_{min} = 0.001$ m in the model. The time step was set to $\Delta t = 0.03$ s for both the hydrodynamic and wave models.

The lateral and shoreward boundaries were defined with walls. At the offshore boundary of the hydrodynamic model the conditions (5.40) and (5.41) were imposed. At the bottom it was assumed in the hydrodynamic model a value of the Nikuradse roughness equal to $k_s = 0.01$ m. This value was chosen based on the bottom nature of this experimental basin (Haas et al. (1998) estimated for this wave basin an interval of friction coefficient values $0.005 < C_f < 0.018$).

For the turbulence closure model, the $k - \varepsilon$ LP model was chosen. Likewise the plane beach test-case, the horizontal diffusion velocity coefficient was the parameter used to better fit experimental data and achieve a smoother solution. It was set to $\nu_H = 0.2$ $m^2 s^{-1}$. This value is in accordance with, for instance, the one used in a similar application by Kumar et al. (2012).

To take into account the wave-enhanced mixing in the hydrodynamic model due to wave breaking, the expressions (5.42) and (5.44) were used with $c_b = 0.03$ and $a_b = 1.2$ (Uchiyama et al., 2010).

In both Haller et al. (2002) and Haas and Svendsen (2002) experiments, monochromatic waves were imposed with parameters that correspond to test B from Haller et al. (2002). This test corresponds to the values of mean wave height $H_{mean} = 0.0475\ m$, wave direction $\theta = 90°$ and wave period $T = 1\ s$. The same wave parameters were imposed at the offshore boundary of TOMAWAC likewise in test B. The significant wave height was set to $H_s = 0.067\ m$. This value was obtained, such that the energy associated to the significant wave height was equal to the one associated to the mean wave height. The minimum frequency was set to $0.187\ Hz$, the number of frequencies $n_f = 7$ and the frequential ratio $q = 1.4$. The direction discretization was made through 24 direction bins. For the depth induced breaking the model proposed by Thornton and Guza (1983) was chosen with $\gamma = 0.9$ and $B = 1$.

In Figure 6.39, the wave basin topography is shown.

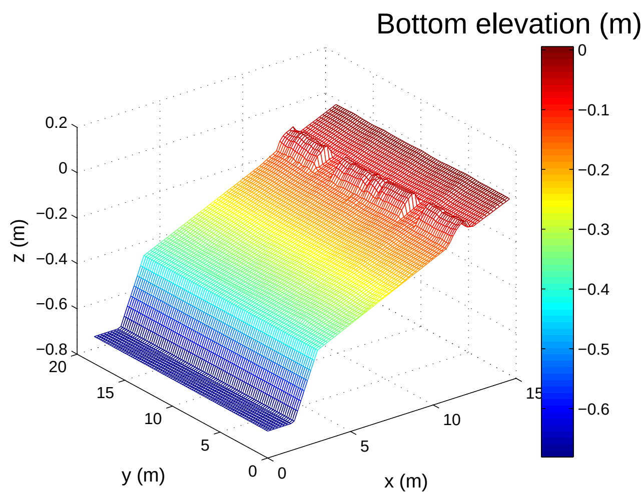

Figure 6.39: Wave basin topography of the barred beach test-case.

6.3.3 The rip current system

Throughout this section, data from Haller et al. (2002) was used in order to compare the significant wave height and mean surface elevation evolution across different cross-shore sections. Moreover, the flow patterns of the rip current system are analysed.

A time average was applied to all the variables over a period of 1500 s, being the total simulation time $t = 1800\ s$. Therefore, the first five minutes of simulation were not taken into account, in conformity to the time-averaged applied by Haller et al. (2002).

The wave height evolution over the domain is of major importance to correctly get the flow patterns of a rip current system. Moreover, the current is going to have a significant role on the wave height evolution (Haas et al., 2003). Therefore a great influence is also noticed on the rip currents from the interaction with waves.

In Figure 6.40, an overview of the significant wave height field can be observed for the case of taking into account the effects of the currents on waves (in the left panel) and deactivating those effects (in the right panel). If both panels are compared, it can be seen that the main differences lay in the cross-shore direction that passes through the rip channel. Here, if the effects of currents are taken into account on the wave propagation, a greater shoaling occurs than the one found if no effects of currents are included on wave dynamics. This shoal is a consequence of the strong offshore and opposed direction current from the wave propagation. This was also confirmed in Haas et al. (2003). Moreover, the rip current causes the refraction of waves towards the channel (Figure 6.41).

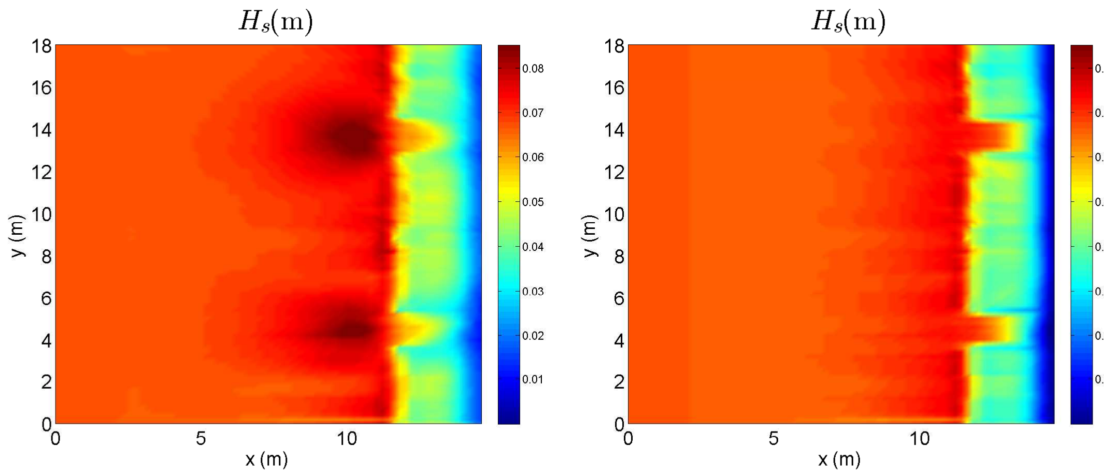

Figure 6.40: Planview of the wave height evolution in the wave basin with (in the left panel) and without (in the right panel) taking into account the effects of currents on waves.

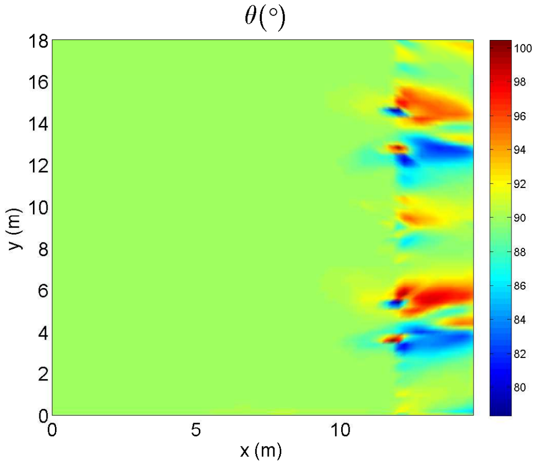

Figure 6.41: Planview of the waves mean direction evolution in the wave basin.

In Figure 6.42, the comparison between numerical results and measurements of the significant wave height along the transects over the bar ($y = 8.2$ m, $y = 9.2$ m, $y = 11.2$ m) and through the rip channel ($y = 13.25$ m, $y = 13.4$ m, $y = 13.65$ m) are shown. Moreover, within the numerical results, both the simulations taking into account the effects of currents on waves (WEC) and not taking them into account (NEC) are presented.

It can be seen that, over the bar, the comparisons between the numerical simulations (both for WEC and NEC) and data are quite similar. The waves break suddenly when encountering the bar. Through the rip channel the waves have a significant shoaling before breaking. This feature is only reproduced if the effects of currents on the waves are accounted for. Nevertheless, even if a correct shoaling is found, some difficulties were encountered by the coupled system in reproducing the correct location where waves start to break through the rip channel. This could be caused by having stronger opposing currents that induce the waves breaking earlier than observed in the experiments.

It can be confirmed that the breaking pattern is quite distinct between the bar and the rip channel. While over the bars the waves break suddenly and then, near the shoreline a second less intense breaking is observed, in the channel, due to the greater water depth, the waves break more progressively and penetrate further into the inshore zone of the channel.

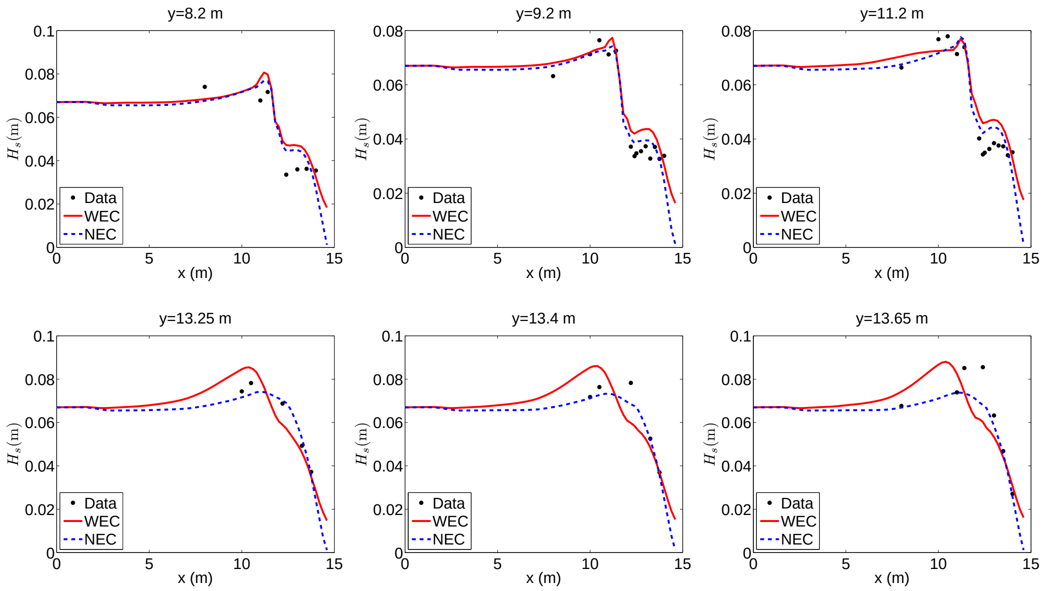

Figure 6.42: Cross-shore evolution of significant wave height over the bar ($y = 8.2$ m, $y = 9.2$ m, $y = 11.2$ m) and through the rip channel ($y = 13.25$ m, $y = 13.4$ m, $y = 13.65$ m) taking (WEC) and not taking (NEC) into account the effects of currents on the wave field. Comparison between numerical results (lines) and data (dots) from Haller et al. (2002).

The comparison between the cross-shore profiles of the mean surface elevation obtained from numerical results (for WEC and NEC) and experimental data can also be observed in Figure 6.43. Over the bar, a sudden and significant raise of the water level occurs due to the strong wave breaking that occurs in this region. Taking into account the two-way effects between waves and currents the numerical results are slightly improved. Nevertheless it can be seen that the first wave set-up over the bar is overestimated by the coupled system either for WEC and NEC. On the other hand, through the rip channel the wave set-up has a more progressive evolution up to the shoreline. Here, the numerical model results fit quite well the data.

From the analysis of the two locations, it can be observed that there is a longshore variability of the mean surface elevation that slopes downward from the bars to the rip channel.

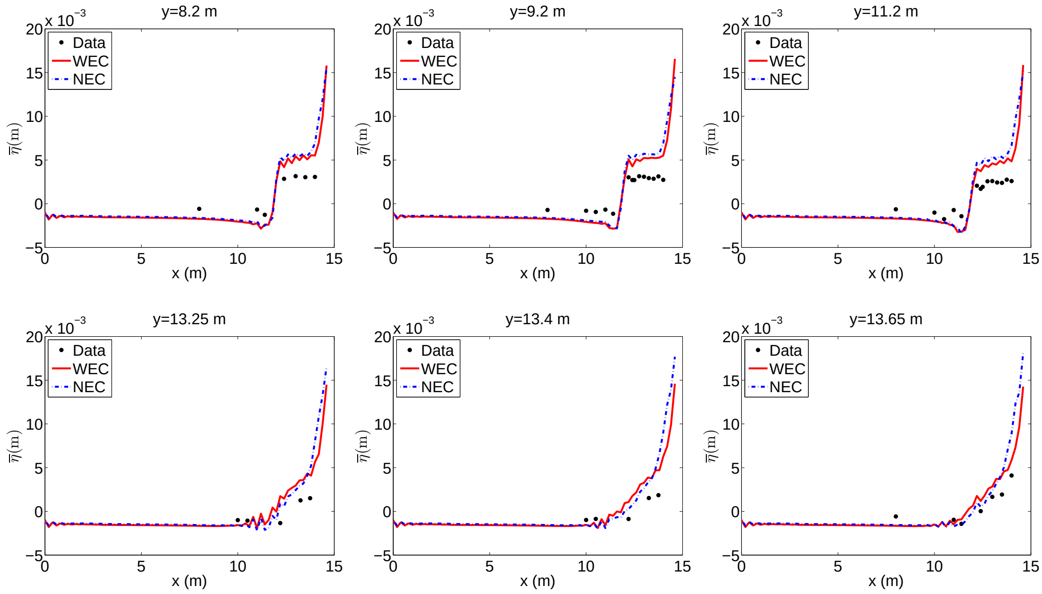

Figure 6.43: Cross-shore evolution of mean surface elevation over the bar ($y = 8.2\ m$, $y = 9.2\ m$, $y = 11.2\ m$) and through the rip channel ($y = 13.25\ m$, $y = 13.4\ m$, $y = 13.65\ m$) taking (WEC) and not taking (NEC) into account the effects of currents on the wave field. Comparison between numerical results (lines) and data (dots) from Haller et al. (2002).

From now on, only the simulations taking into account the effects of currents on the wave field (WEC) will be shown and discussed.

The momentum lost by waves due to depth-induced breaking effects transferred to the hydrodynamic model as a surface stress is represented in the left panel of Figure 6.44. The maximum values are obtained over the bar, confirming the strong wave breaking that occurs in this zone. In the middle and right panels of the same figure, the wave-induced pressure horizontal gradient and hydrostatic pressure horizontal gradient are also shown. This confirms the longshore variability of the longshore pressure gradients from the bars to the rip channels.

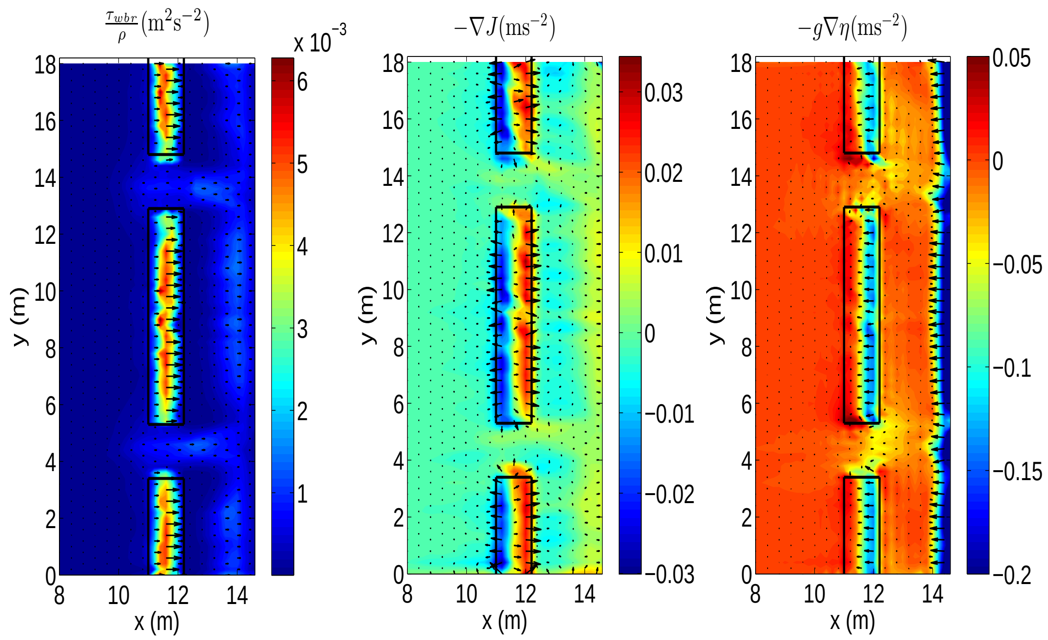

Figure 6.44: Evolution of the stress associated to the momentum lost by waves breaking due to depth-induced effects (left panel), wave-induced pressure horizontal gradient (middle panel) and hydrostatic pressure horizontal gradient (right panel), obtained by the numerical model near the free surface.

In Figure 6.45, an adaptation of the scheme presented in Haas et al. (2003) is shown. It is an overview of the wave basin flow patterns within a barred beach. It can be seen that there are clearly two recirculation cells in both rip channels. The same flow patterns were observed numerically (Haas et al. (2003), Kumar et al. (2012)) and experimentally (Haller et al. (2002), Haas and Svendsen (2002)).

The observed longshore variability of the mean surface elevation causes longshore pressure gradients which are going to induce feeder currents that converge in the rip channel oriented offshore, and an onshore directed flow over the bar. One recirculation cell is then generated.

Another recirculation cell is located between the bar and the shoreline, caused by the waves that break further inshore in the channel. When the waves break close to the shoreline, they induce longshore currents near the shoreline that flow away from the channel. This will be more evident if the level of penetration of waves in the channel is greater (Haller et al., 2002).

Outside the surf zone, the rip current starts to decrease until it disappears.

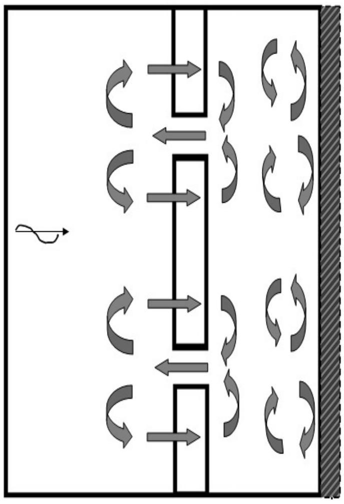

Figure 6.45: Scheme of a rip current system on a barred beach with normal incident waves. Adapted from Haas et al. (2003).

Finally, the time-averaged velocity vectors computed by the numerical model, at approximately 3 *cm* from the bottom, are represented in the left panel of Figure 6.46. It can be clearly seen the recirculation cells generated between the bar and the channel. Near the shoreline, the recirculation cell is not so evident. This is probably due to the fact that the waves in the numerical model break earlier than in the laboratory basin.

In the right panel of Figure 6.46, the velocity vectors measured in the wave basin by Haller et al. (2002), at approximately 3 *cm* from the bottom, are presented. The generation of the rip current and the associated feeder currents can be confirmed. If both left and right panels are compared, it can be inferred that the general flow patterns are quite well represented by the coupled system.

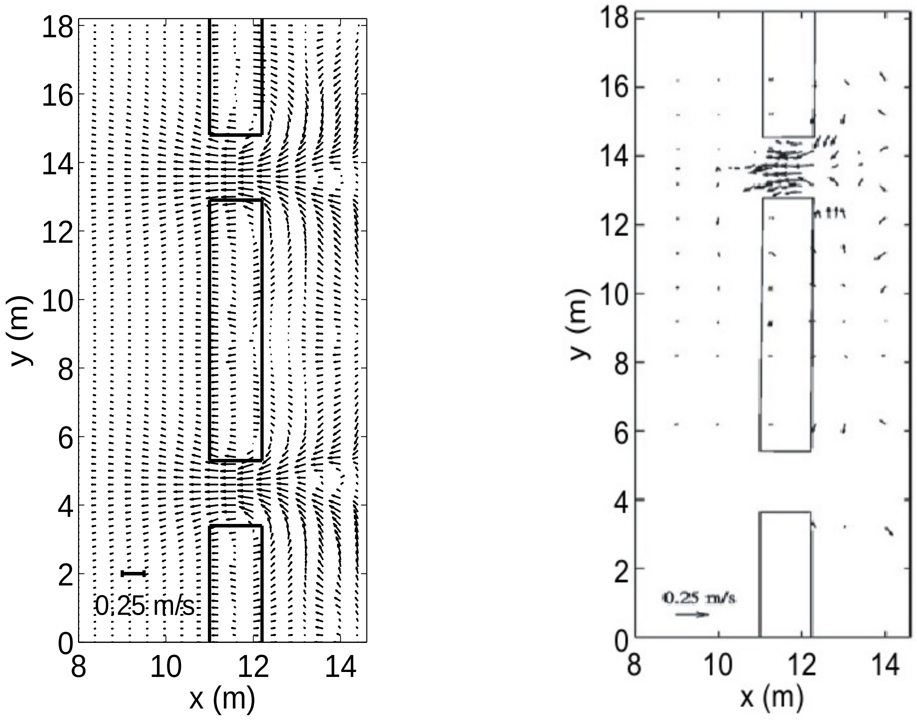

Figure 6.46: Time-averaged velocity vectors at approximately 3 *cm* from the bottom obtained by the numerical model (left panel) and by experimental data (Haller et al., 2002) (right panel).

Additionally, both in the experimental data and numerical simulations, some vortex patterns could be observed. The propagation of the vortices interact with the Stokes drift induced by the incoming waves, generating a strong vortex force. This feature was also observed in numerical results performed to reproduce the same experiments (Haller and Dalrymple (2001), Haas et al. (2003), Kumar et al. (2012)).

When the radiation stress approach (Longuet-Higgins (1953), Longuet-Higgins and Stewart (1962, 1964)) is applied, despite the good results for the mean flow, the interpretation of the results is quite difficult to achieve (Lane et al., 2007). On the contrary, one of the great advantages the vortex force formalism to describe waves and current interactions, is that the vortex force is clearly distinguished and therefore it is possible to study the circulations and water motions in the mean flow.

As observed in the above analyses, the variations of the bathymetry induce longshore pressure gradients and different wave breaking patterns on the barred beach. In the left panel of Figure 6.44, it can be seen that there is a stronger loss of momentum from waves breaking over the bars than through the channel. As a result, the flow is oriented to the shoreline over the bars and directed offshore through the channels. Therefore a circulation cell is generated in the longshore transition between the bars and the channel.

This feature can be observed in the left panel of Figure 6.47 where the generated vortices are represented together with the flow vectors. A pair of vortices is found with opposite signs. In the zone near the shoreline, two other weaker vortices, also with opposite signs, can be observed.

In the right panel of Figure 6.47, the vortex force is also represented. It can be observed that it shows greater values in the zones corresponding to the vortices shown in the left panel of the same figure. Over the rest of the domain, the vortex force is negligible. Therefore it can be confirmed that the vortex force has an essential contribution in forming and maintaining these vortices.

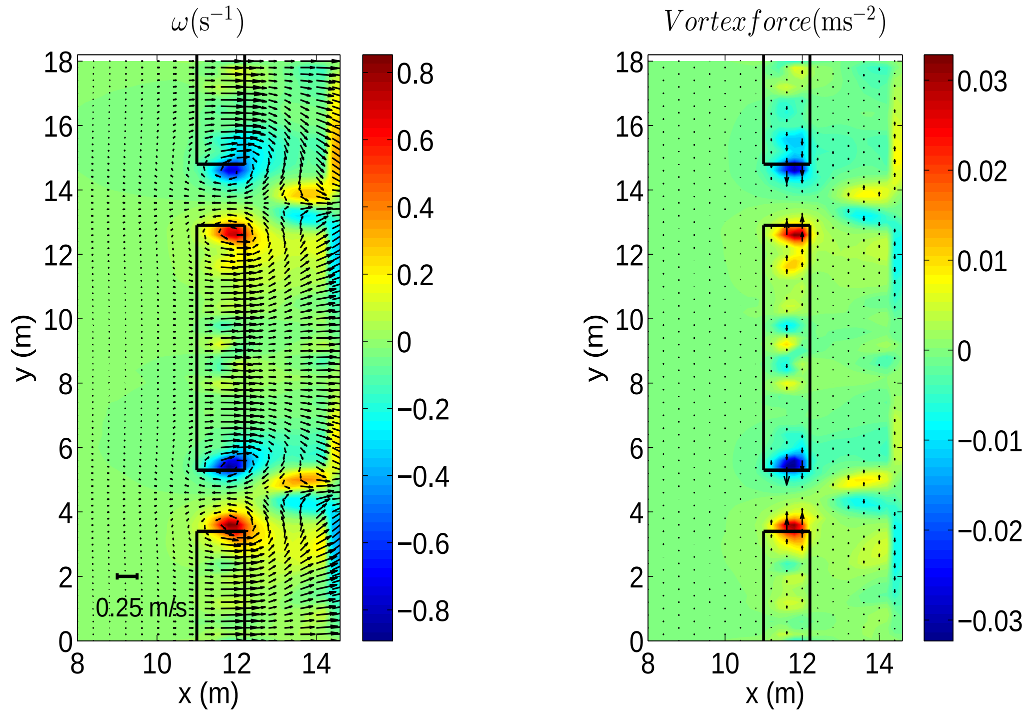

Figure 6.47: Vorticity obtained by the numerical model together with the flow vectors (in the left panel) and vortex force with corresponding vectors (in the right panel). Variables are represented near the free surface.

Through the analysis made above it can be confirmed that the coupled system behaves quite well in reproducing the significant wave height, mean surface elevation evolutions and associated flow patterns within the rip current system induced by a barred beach. Nevertheless, the cross-shore component of the flow seems to have a relevant shear throughout the water depth, as shown in different measurements in the field and laboratory experiments (Haas and Svendsen (2002)). Therefore in the following section the vertical structure of the rip current is analysed.

6.3.4 Vertical structure of the flow

6.3.4.1 Longshore variability

In the following analysis, the main purpose is to show and confirm that the bars on the beach induce a longshore variability in the different variables. The analysed longshore section was set at $x = 11.6\ m$, which corresponds to the longshore array across the bars and the channels.

In Figure 6.48, the longshore variability of the quasi-Eulerian velocities and Stokes drift can be observed. A strong vertical shear of the quasi-Eulerian cross-shore velocity component is observed above the bar crest (Figure 6.48, left and upper panel). It is negative near the bottom (with $u \approx -0.15\ ms^{-1}$), oriented offshore, then increases towards the free surface, being oriented towards the shoreline (with $u \approx 0.4\ ms^{-1}$). In the region over the bars, a strong mass flux induced by the waves occurs as it can be seen by the distribution of the cross-shore component of the Stokes drift in Figure 6.48 (left and lower panel).

Within the rip channels, the vertical profile of the cross-shore velocities is not so sheared, but it shows high negative velocities ($u \approx -0.25\ ms^{-1}$) approximately in the middle of the water column. Then it starts to slightly decrease in magnitude towards the free surface and the bottom.

The longshore components of the quasi-Eulerian velocity and Stokes drift are presented in the right panels of Figure 6.48. They are one order of magnitude lower than the quasi-Eulerian cross-shore velocities. This is caused by the weak longshore component of the Stokes drift. Nevertheless, they present high variability along the longshore bars and channels. At least three inflexion points for the velocities can be clearly identified: two in each channel and one over the bar.

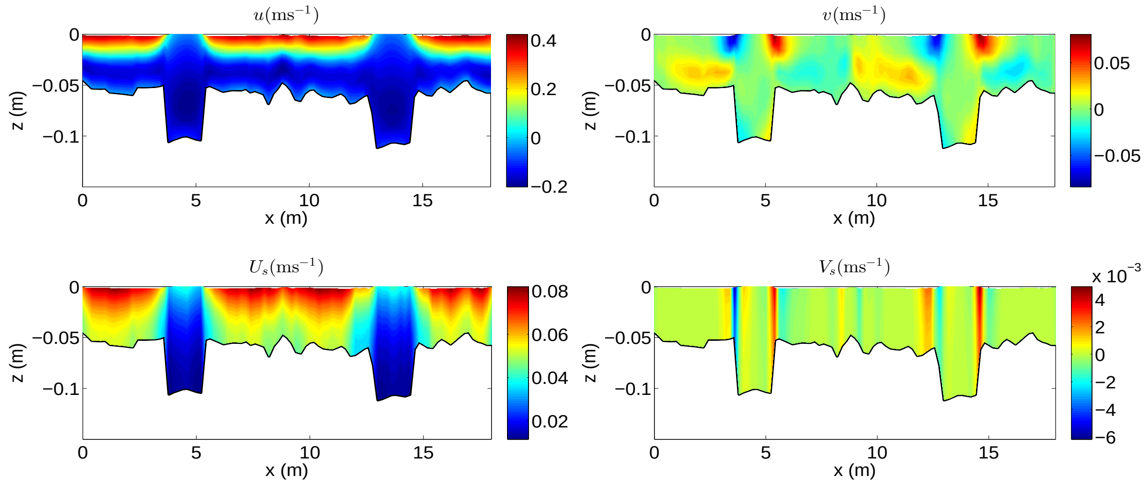

Figure 6.48: Longshore section at $x = 11.6\ m$ of the quasi-Eulerian velocity and Stokes drift cross-shore components (left panels) and of the quasi-Eulerian velocity and Stokes drift longshore components (right panels) from the numerical results.

Finally, in Figure 6.49, the cross-shore and longshore Lagrangian mean velocity components are obtained by adding the contribution of the Stokes drift with the quasi-Eulerian velocity.

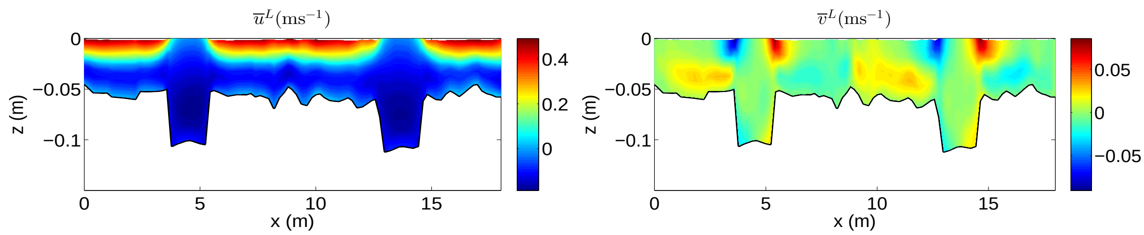

Figure 6.49: Longshore sections at $x = 11.6\ m$ of the Lagrangian mean velocity cross-shore (left panel) and longshore (right panel) components from the numerical results.

In Figure 6.50, the longshore distribution of the wave-induced pressure gradient (upper panels), hydrostatic pressure gradient (middle panels) and vortex force (lower panels) are presented at the same abscissa ($x = 11.6\ m$). In the left panels of Figure 6.50 the cross-shore components are shown, while the right panels show the longshore components.

It can be seen that the wave-induced and hydrostatic pressure cross-shore gradient components have lower values in the rip channel than over the bar. These differences arise from the strong transfer of momentum lost by breaking waves in the latter region. The corresponding longshore components show inflexion points. It can be confirmed that these inflexion points are located at the same sections as in the case of the longshore quasi-Eulerian velocity. These inflexion points are generated by the variability of the mean surface elevation in the longshore direction which in its turn is due to the different dissipation rates of the incident waves field.

Regarding the cross-shore component of the vortex force, it can be observed that is almost zero in the channels and with higher values over the bars. The longshore component of the vortex force presents its maximum absolute values in the sections where there is higher vorticity.

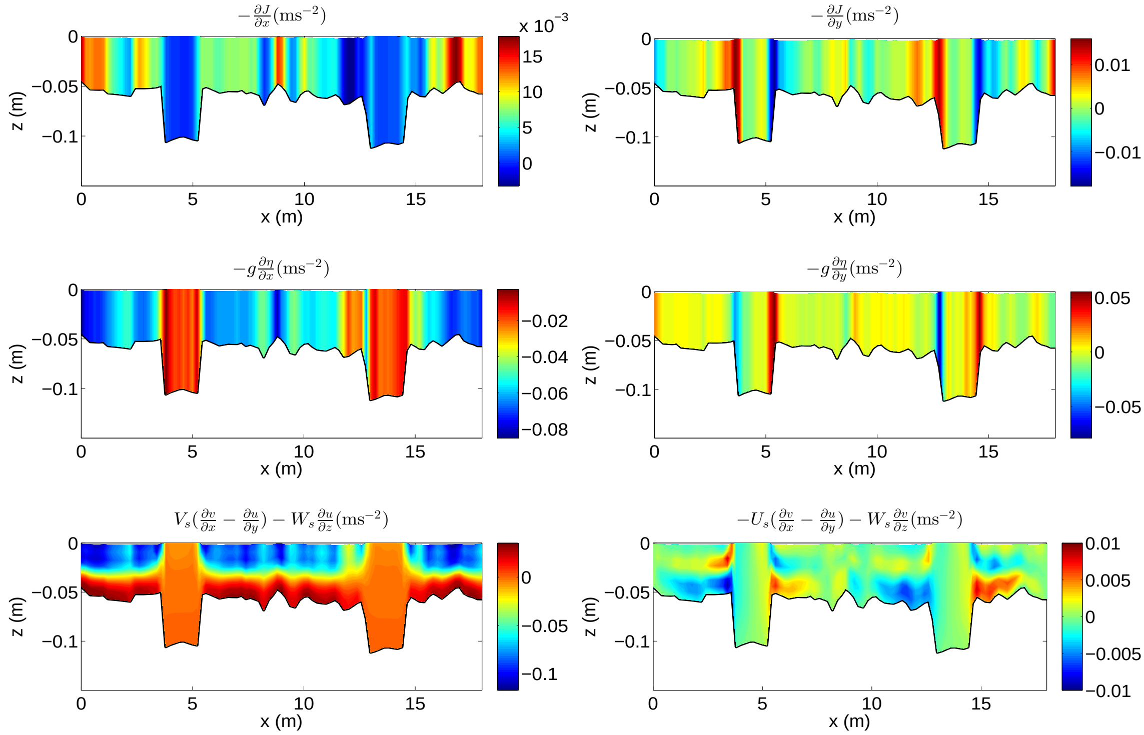

Figure 6.50: Longshore sections at $x = 11.6\ m$ of the wave-induced pressure gradient, hydrostatic pressure gradient and vortex force cross-shore (on the left panels) and longshore (right pannels) components.

6.3.4.2 Longshore dynamics

Hereinafter, the analysis of the rip current system will be focused on two cross-shore arrays: over the bar (in the left panels of the next figures) and through the rip channel (in the right panels). Over the bar crests and through the rip channel, it can be observed that the quasi-Eulerian velocity longshore component is relatively weak (Figure 6.51). This is due to the small longshore component of the Stokes drift (Figure 6.52).

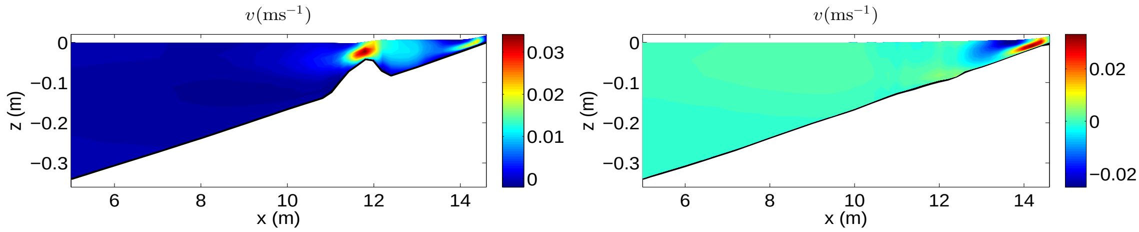

Figure 6.51: Cross-shore sections at $y = 9.2$ m (in the left panel) and $y = 13.6$ m (in the right panel) of the quasi-Eulerian longshore velocities from the numerical results.

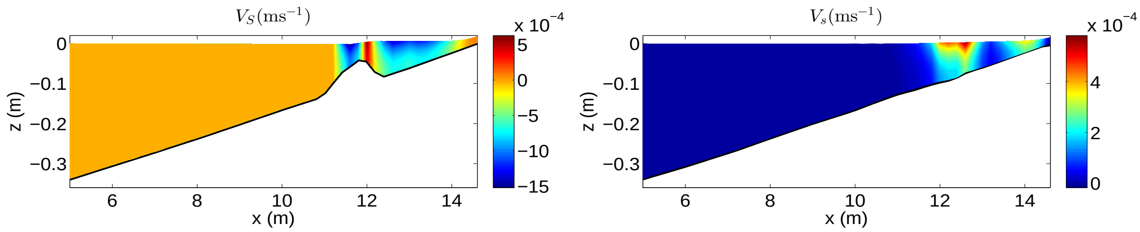

Figure 6.52: Cross-shore sections at $y = 9.2$ m (in the left panel) and $y = 13.6$ m (in the right panel) of the longshore component of the Stokes drift from the numerical results.

Finally, the longshore component of the Lagrangian mean velocity is also obtained for each cross-shore section (Figure 6.53).

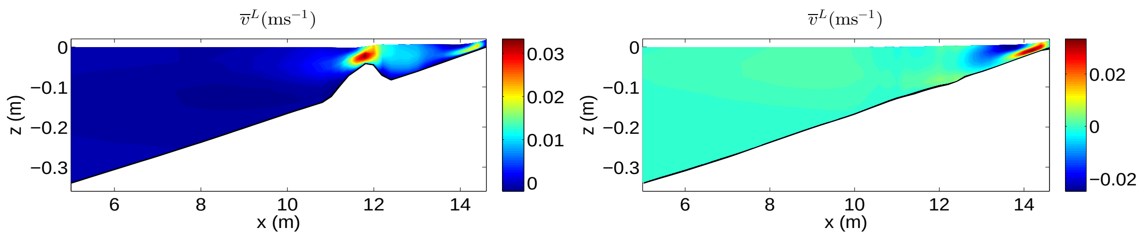

Figure 6.53: Cross-shore sections at $y = 9.2$ m (in the left panel) and $y = 13.6$ m (in the right panel) of the longshore component of the Lagrangian mean velocity from the numerical results.

Unlike the plane beach test-case, here there is no longer longshore uniformity. Therefore, the longshore components of the wave-induced pressure gradient (upper panels), hydrostatic pressure gradient (middle panels) and vortex force (lower panels) gain relevance in the longshore momentum balance (Figure 6.54).

It can be seen that in the vicinity of the bar there are strong wave-induced and hydrostatic pressure gradients. They induce the feeder currents that converge to the rip current.

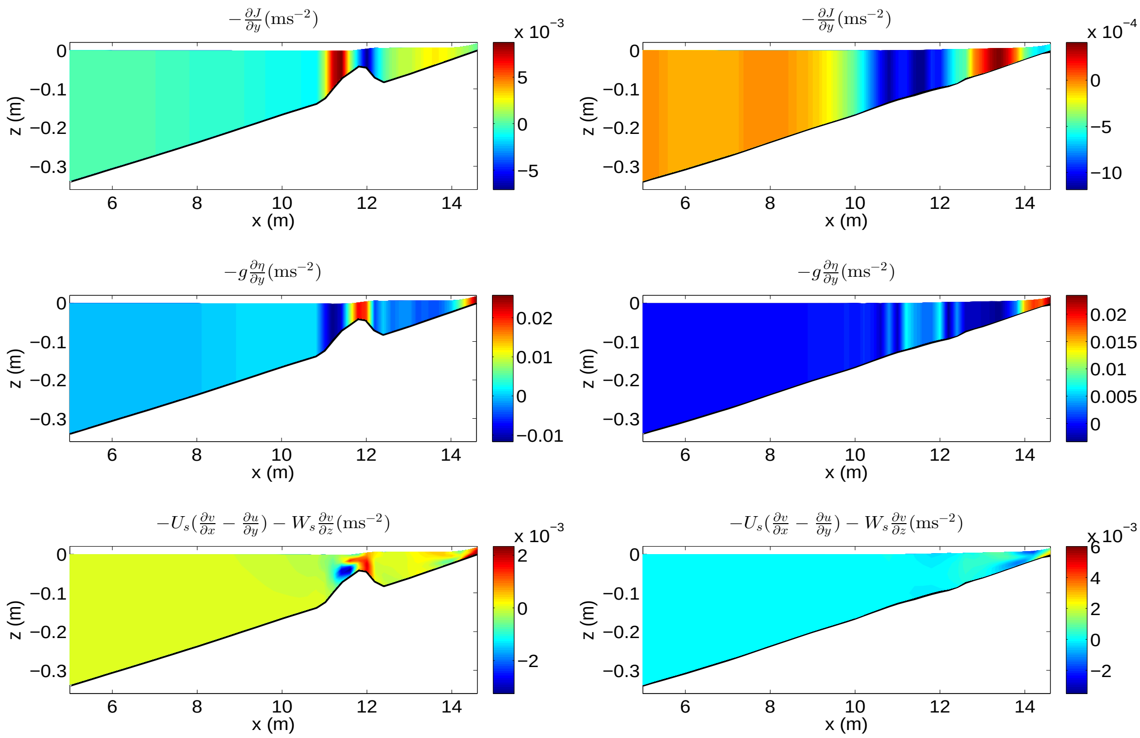

Figure 6.54: Cross-shore sections of numerical results at $y = 9.2\ m$ (in the left panel) and $y = 13.6\ m$ (in the right panel) of the longshore component of the wave-induced pressure gradient (upper panels), hydrostatic pressure gradient (middle panels) and vortex force (lower panels).

In Figure 6.55, the contribution of the momentum lost by waves in the longshore direction is shown over the bar and through the rip channel. Compared with the terms presented above, this contribution is weaker.

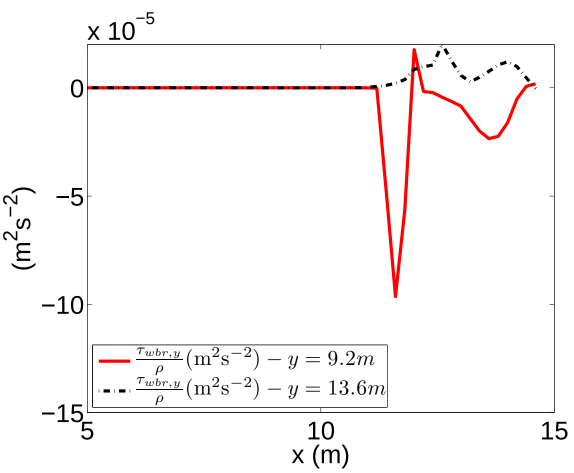

Figure 6.55: Cross-shore sections at $y = 9.2\ m$ and $y = 13.6\ m$ of the longshore stress component associated to the momentum lost by waves due to depth-induced effects, from the numerical results.

6.3.4.3 Cross-shore dynamics

Hereinafter, the cross-shore dynamics of the rip current system is focused on. In Figure 6.56, it is possible to observe the numerical results of the cross-shore quasi-Eulerian velocities in the two sections previously analysed: one over the bar (in the left panel) and another along the rip channel (right panel).

As observed in the previous sections, waves break over the bar crest and near the shoreline. It can be seen, over the bar, that in both wave breaking locations, there is a strong vertical shear of the cross-shore quasi-Eulerian velocities: near the free surface they are directed onshore with a magnitude of $u \approx 0.3\ ms^{-1}$, while near the bottom an undertow with $u \approx -0.2\ ms^{-1}$ is verified (Figure 6.56, left panel).

When analysing the rip current through the rip channel (in the right panel of Figure 6.56), at $x \approx 11.6\ m$, the velocities oriented offshore are stronger than the ones observed over the bar. The maximum values are reached approximately in the middle of the water column with $u \approx -0.25\ ms^{-1}$. The velocities then show a decrease toward the free surface and the bottom. Inshore of the rip channel, for $x > 12.5\ m$ the cross-shore quasi-Eulerian velocities are oriented onshore near the free surface and an undertow can be observed within the bottom boundary layer. Offshore of the rip channel, the flow is oriented seaward and it starts to decrease until it becomes negligible.

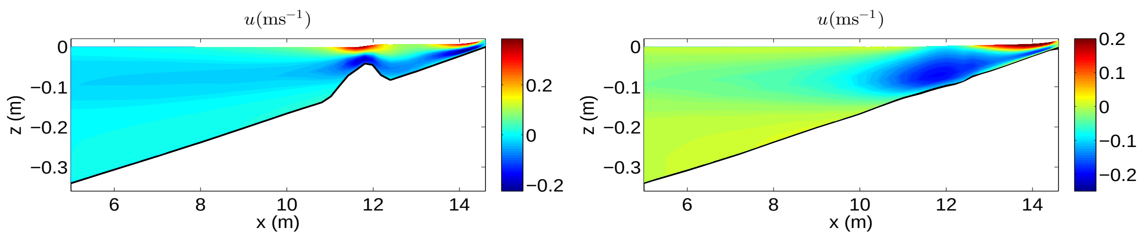

Figure 6.56: Cross-shore sections at $y = 9.2\ m$ (in the left panel) and $y = 13.6\ m$ (in the right panel) of the quasi-Eulerian cross-shore velocities from the numerical results.

In Figure 6.57, the cross-shore components of the Stokes drift in the same cross-shore arrays (over the bar (in the left panel) and through the rip channel (in the right panel)) are represented. Additionally, in Figure 6.58 the cross-shore components of the Lagrangian mean velocities are also shown. It can be confirmed that the Stokes drift has a stronger magnitude near the free surface over the bar crest than through the rip channel. Inshore the bar it presents also a positive value even if weaker. Through the rip channel, it has a continuous positive value near the free surface up to the shoreline, corresponding to the progressive wave breaking that occurs in that region.

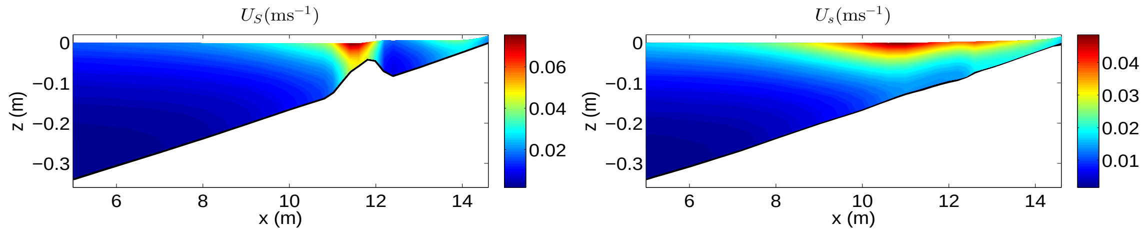

Figure 6.57: Cross-shore sections at $y = 9.2\ m$ (in the left panel) and $y = 13.6\ m$ (in the right panel) of the cross-shore component of the Stokes drift from the numerical results.

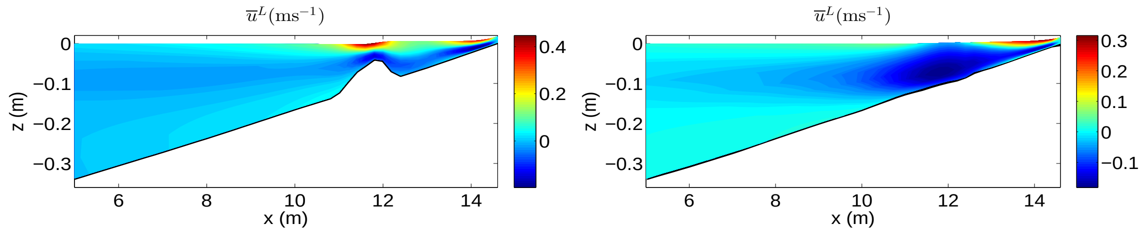

Figure 6.58: Cross-shore sections at $y = 9.2\ m$ (in the left panel) and $y = 13.6\ m$ (in the right panel) of the cross-shore component of the Lagrangian mean velocity from the numerical results.

In Figure 6.59 the cross-shore components of the wave-induced pressure horizontal gradient (upper panels), hydrostatic pressure gradient (middle panels) and vortex force (lower panels) are represented.

Along the cross-shore section over the bar, it can be confirmed that the wave-induced pressure is negative just before the bar which corresponds to the wave set-down, and just after the bar it has a positive value, which corresponds to the high elevation of the mean water level - the wave set-up.

In the cross-shore section along the rip channel a similar distribution is found relative to the plane beach test case presented in the previous section. The wave-induced pressure gradient is negative at $x \approx 12.5\ m$, inducing a decrease in the mean water level. After a positive gradient towards the shoreline and a rise of the mean water level is verified. The features mentioned above of the mean surface elevation evolution can be confirmed in Figure 6.43.

The cross-shore component of the vortex force has a weak contribution for the momentum balance through the rip channel due to the incident waves being perpendicular to the shoreline. Nevertheless, over the bar, the waves refract, and the vortex force becomes stronger above the bar crest.

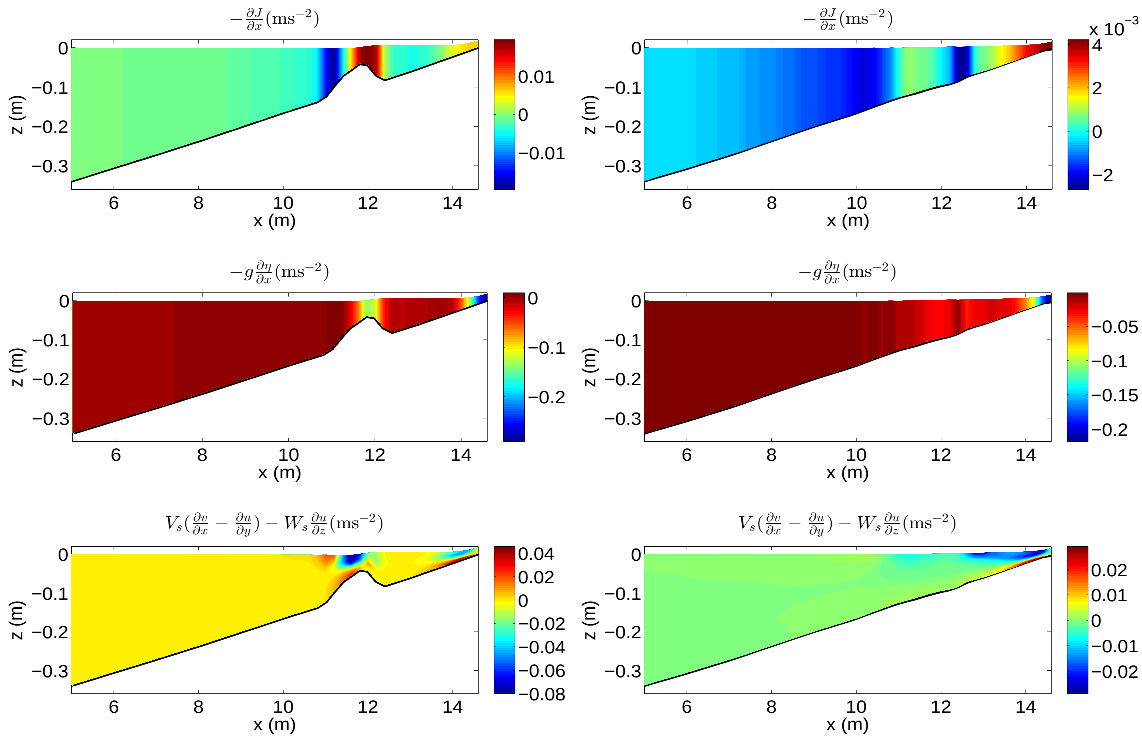

Figure 6.59: Cross-shore sections of numerical results at $y = 9.2\ m$ (in the left panel) and $y = 13.6\ m$ (in the right panel) of the cross-shore component of the wave-induced pressure gradient (on the top), hydrostatic pressure gradient (on the middle) and vortex force (on the bottom).

In Figure 6.60 the cross-shore stress component associated to the momentum lost by waves due to wave breaking is presented within the two cross-shore sections. It can be found that its greatest contribution occurs over the bar where there is strong wave breaking and then near the shoreline. Through the rip channel, this term starts to be greater at $x \approx 10.5\ m$ where the waves start to break, increasing towards the shoreline.

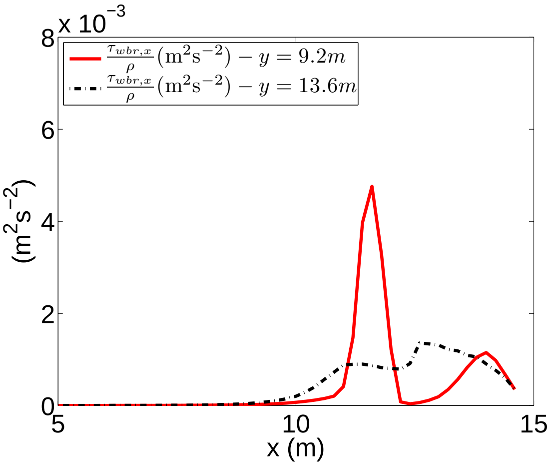

Figure 6.60: Cross-shore section at $y = 9.2\ m$ and $y = 13.6\ m$ of the cross-shore stress component associated to the momentum lost by waves due to depth-induced effects, from the numerical results.

Moreover, the distributions obtained of the vertical diffusion velocity coefficient are shown in Figure 6.61. The maximum values are concentrated near the free surface over the bar and in the rip channel.

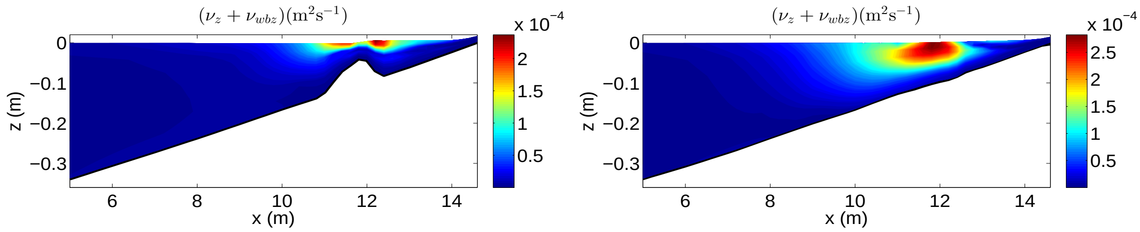

Figure 6.61: Cross-shore sections of numerical results at $y = 9.2\ m$ (in the left panel) and $y = 13.6\ m$ (in the right panel) of vertical diffusion velocity coefficient.

6.3.5 Detailed analysis of the instabilities of cross-shore velocities

6.3.5.1 Sensitivity study on the horizontal diffusion velocity coefficient and bottom friction values and wave-current interaction effects

In this section the numerical results are compared with the experimental data obtained by Haas and Svendsen (2002). Here, the same wave basin of the University of Delaware was used with the same imposed wave characteristics as for test B by Haller et al. (2002). The main purpose of this set of measurements was to analyse the vertical structure of the rip currents, since in data from Haller et al. (2002) a single location in the vertical was used.

Haas and Svendsen (2002) complemented the wave basin instrumentation with three Sontek Acoustic Doppler Velocimeters (ADVs) installed to measure the velocities. The probes were positioned at three water depths. Several cross-shore and longshore sections were used. The following analysis is focused on the corresponding test series R from Haas and Svendsen (2002) where a higher resolution of the rip current vertical structure (between three to six positions throughout the water depth) along one cross-shore section was achieved.

An important characteristic of a rip current system is that the rip current velocity values exhibit fluctuations in the order of $5-10\ cms^{-1}$ at this (model) scale, as observed by several authors (Haller et al. (2002), Haas and Svendsen (2002)). This is associated with the rip current unstable nature, which is explored and explained in Haller and Dalrymple (2001). It seems that the rip current instabilities become more evident if the wave height is greater or if the wave period decreases (Kennedy and Zhang, 2008), which indicates that this instability is related to the steepness of incident waves.

The instabilities of the rip currents modelled, can be more evident by decreasing the imposed bottom friction coefficient, decreasing the horizontal diffusion velocity coefficient in the hydrodynamic model or taking into account the two-way effects of waves and currents.

We therefore study and plot the time evolution of the rip current, obtained in the numerical results, near the free surface, depending on the choice of the horizontal diffusion velocity coefficient, ν_H, (Figure 6.62), Nikuradse roughness, k_S, (Figure 6.63) and taking (WEC) or not taking into account (NEC) the effects of current on waves (Figure 6.64).

It can be confirmed that the three parameters influence the unstable nature of the rip currents. When increasing the value set to the horizontal diffusion velocity coefficient, the rip current quickly becomes stationary. If the Nikuradse value roughness is decreased, it seems that the rip current is more unstable, having, in general, velocities lower than what it is obtained with greater values of k_S. Additionally, when the effects of currents are not taken into account in the wave field, the current is almost stationary.

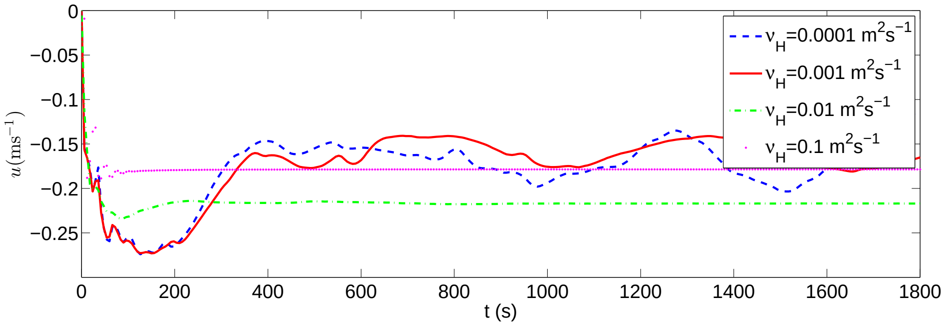

Figure 6.62: Time evolution of the cross-shore velocity near the free surface ($z \approx -0.03\ m$) at $x = 11.4\ m$ and $y = 13.6\ m$, depending on the choice of the horizontal diffusion velocity coefficient, ν_H. All simulations were made with $k_S = 0.01\ m$.

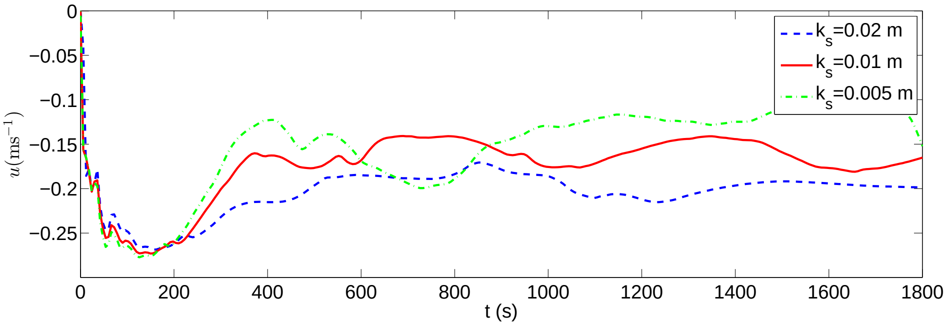

Figure 6.63: Time evolution of the cross-shore velocity near the free surface ($z \approx -0.03\ m$) at $x = 11.4\ m$ and $y = 13.6\ m$, depending on the choice of the Nikuradse roughness, k_S. All simulations were made with $\nu_H = 0.001\ m^2 s^{-1}$.

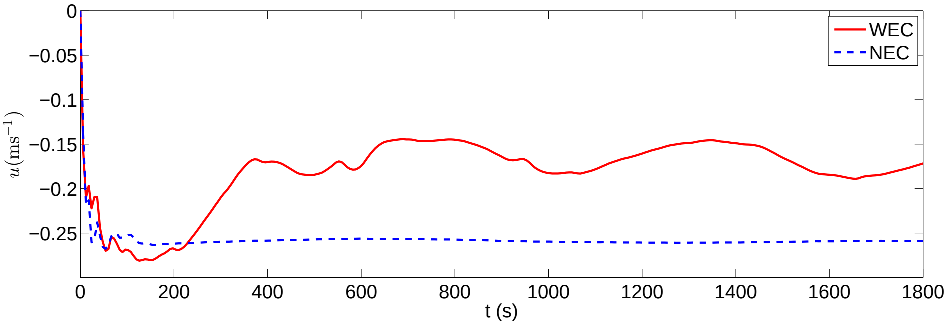

Figure 6.64: Time evolution of the cross-shore velocity near the free surface ($z \approx -0.03\ m$) at $x = 11.4\ m$ and $y = 13.6\ m$, taking (WEC) or not taking into account (NEC) effects of currents on waves. Both simulations were made with $\nu_H = 0.001\ m^2 s^{-1}$ and $k_S = 0.01\ m$.

6.3.5.2 Refined analysis on the cross-shore velocity vertical profiles

Haas and Svendsen (2002) made an extensive analysis regarding the time evolution of the rip current along several water depths and cross-shore and longshore sections. They found that if a time average was applied over the time series, the rip signal would be virtually eliminated outside the surf zone due to the unstable nature of the rip current. Therefore they applied a bin average technique to analyse the measured velocities.

We used the same procedure as the experimental one for the model outputs in order to analyse the vertical structure of the rip currents and compare it with data. According to Haas and Svendsen (2002), the different bins were defined and grouped depending on the magnitude of the near surface ($z \approx -0.035$ m) cross-shore instantaneous velocity (u_1). The criteria used were:

- bin 25 : $u_1 > 0.25$ (ms^{-1});
- bin 20 : $0.25 > u_1 > 0.2$ (ms^{-1});
- bin 15 : $0.2 > u_1 > 0.15$ (ms^{-1});
- bin 10 : $0.15 > u_1 > 0.1$ (ms^{-1}).

After distinguishing the four bins, the velocity profiles are time-averaged within each bin, creating four velocity profiles for each cross-shore measurement location.

Hereinafter, in order to get the instabilities mentioned above, the horizontal diffusion velocity coefficient was decreased to $\nu_H = 0.001$ $m^2 s^{-1}$. The other parameters are maintained comparing with the above sections ($k_S = 0.01$ m and taking into account the effect of currents on the wave field (WEC)).

In Figure 6.65, the comparison, within bins 10, 15, 20 and 25, from top to bottom, respectively, between the cross-shore velocities vertical profiles and the numerical results is made along the array $y = 13.6$ m.

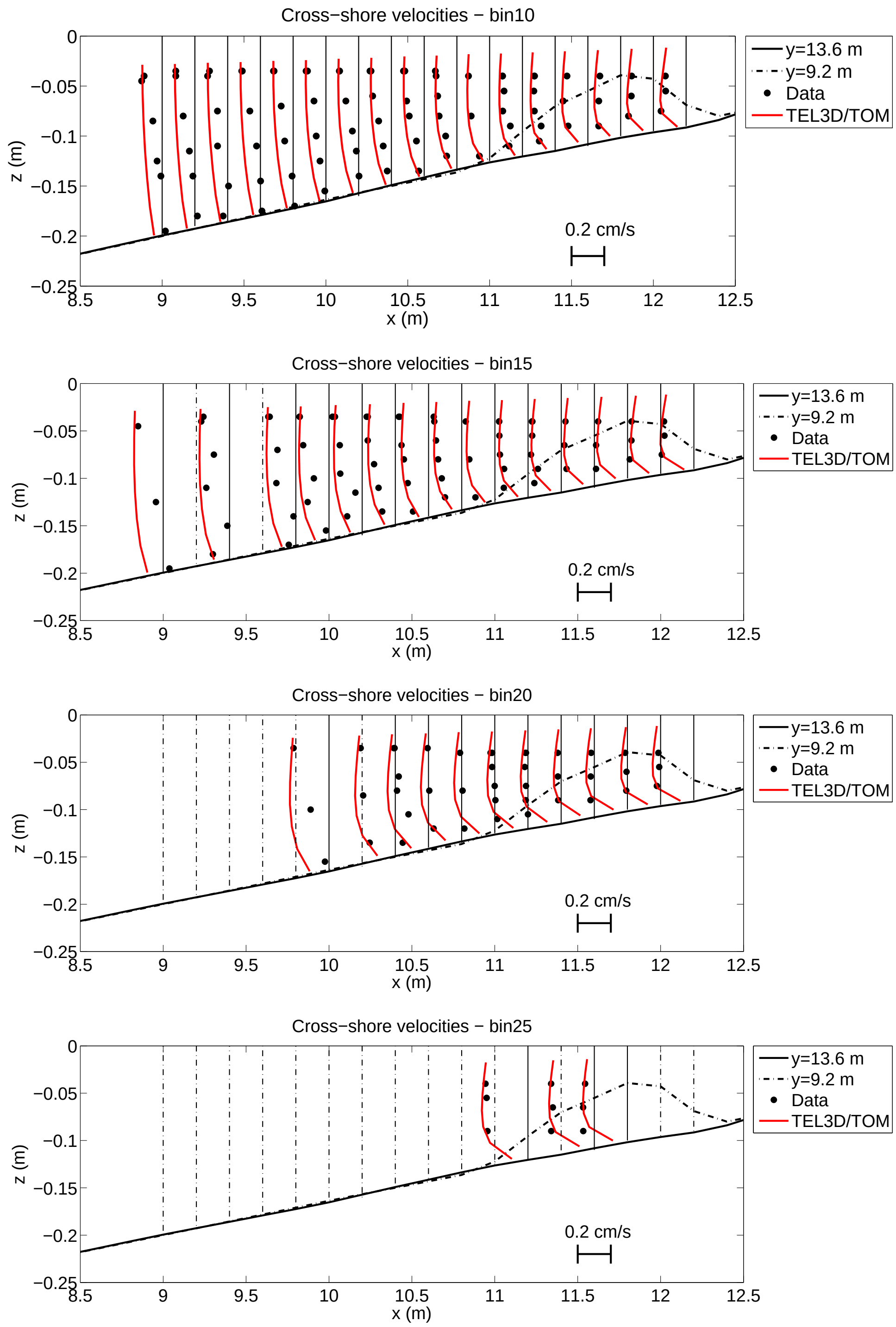

Figure 6.65: Comparison of the cross-shore velocity vertical profiles through the rip channel from numerical model and from Haas and Svendsen (2002) experimental data within bins 10, 15, 20 and 25. The full vertical lines represent the measurement sections.

It can be seen that the vertical distribution of the cross-shore velocities is quite well represented by the numerical model within all the bins. It can be even confirmed that the coupled system is able to reproduce the highest velocities seen in the wave basin near the free surface ($u \approx -0.25\ ms^{-1}$) (in the bottom panel of Figure 6.65).

Within bins 10 and 15, the evolution of the vertical structure of the rip currents with the depth variation can be clearly observed. Offshore the cross-shore velocity magnitude increases from the bottom towards the free surface, being directed offshore. From $x \approx 11\ m$ to the shoreline, the velocity sees its maximum below the bar-crest level and starts to slightly decrease near the free surface. For all the bins, a reduction in velocity is observed near the bed, due to the bottom boundary layer.

From the analysis made throughout the previous sections it can be concluded that, in general, the coupled system give good results in the present barred beach test-case. Not only the evolution of significant wave height, mean surface elevation and flow patterns given by numerical results fitted well the experimental data, but also the vertical structure of the flow was well reproduced.

6.4 Conclusions of Part II

A fully coupled system between the three-dimensional hydrodynamic model TELEMAC-3D and the spectral wave model TOMAWAC was developed. The hydrodynamic model TELEMAC-3D was adapted to include the recent formulation proposed by Ardhuin et al. (2008b) together with the simplifications made by Bennis and Ardhuin (2011). The theoretical framework is based on the Generalized Lagrangian Mean (GLM) theory within a vortex force formalism. Moreover, different parameterizations to take into account the non-conservative forces of the wave forcing terms were included.

The capabilities of the 3D coupled system were tested with two types of experiments. The first test considers longshore currents generated by obliquely incident waves on a uniform planar beach. The second test refers to the generation of rip currents induced by perpendicular incident waves on a barred beach.

For the first test, numerical results were compared with experimental data obtained at the Large Scale Sediment Transport Facility (LSTF) in Vicksburg (USA). In this set of experiments, values of mean water levels and velocities were measured.

The numerical results showed to fit quite well the experimental data, not only the wave-averaged parameters (e.g. significant wave height and mean surface elevation), but also the vertical structure of cross-shore and longshore velocities. It was shown that, while the vertical shear of the longshore component of the mean flow is relatively weak, a strong shear is observed in the cross-shore component. An onshore oriented flow is observed near the free surface and a stronger offshore oriented flow near the bottom is verified, the so-called undertow. This feature highlights the importance of taking into account the three-dimensionality of the flow in coastal applications.

The new terms implemented in the hydrodynamic model were analysed in the cross-shore and longshore directions. It was shown that, among these terms, the relevant contributions for the longshore balance are the wave dissipation due to bottom friction, the longshore vortex force component and the momentum flux due to depth-induced waves breaking.

Additionally, a number of sensitivity tests were carried out regarding some of the effects included in the coupled system.

First, a comparison was made using two different formulations to take into account wave-current interaction: one based on the radiation stress concept (Longuet-Higgins (1953), Longuet-Higgins and Stewart (1962, 1964)) (where the forces induced by the radiation stresses are distributed uniformly throughout the water depth in the hydrodynamic model) and another with the new implementation based on vortex force formalism (Ardhuin et al., 2008b). It is shown that the latter gives a great improvement on results, both for the cross-shore and longshore components of the mean flow.

Then some tests were also made within the bottom boundary layer. It was verified that increasing the bottom roughness value, a significant decrease of the longshore velocities is observed throughout the water depth. Additionally, the incorporation of the bottom streaming effect improves the results within the bottom boundary layer for the cross-shore velocities and throughout the water depth for the longshore velocities.

A sensitivity analysis was realized concerning the choice of the turbulence closure model. The comparisons were made between the standard $k-\varepsilon$ model, the $k-\varepsilon$ LP version, the Nezu and Nakagawa (Nezu and Nakagawa, 1993) and Prandtl (Prandtl, 1925) models. A great improvement of results is observed when both versions of $k-\varepsilon$ and $k-\varepsilon$ LP models are applied. Here, the vertical diffusion velocity coefficient shows its maximum values near the free surface and within the surf zone.

The turbulence modelling approach used in this analysis is quite simple when comparing, for instance, with the application of a second order turbulence closure model. The horizontal diffusion velocity coefficient was set to a constant value. One should test more complex turbulence closure models to see the influence on the numerical results.

In what concerns the modified bottom friction coefficient to take into account the effects of the interaction between waves and currents, incorporated through the Christoffersen and Jonsson (1985) theoretical framework, there were no noticeable differences found when this option was activated/deactivated. The similarities observed can be due to the small value of the bottom roughness in the wave basin, for which probably no significant changes occur with the presence of waves.

With experimental data obtained on a barred beach with rip channels (Haller et al. (2002), Haas and Svendsen (2002)), the capability of the coupled system to reproduce rip currents, where more complex flows are modelled, was also tested.

First, the data set obtained by Haller et al. (2002) was used. Comparisons of the cross-shore distribution of wave height and mean surface elevation were made. A good agreement was found between numerical results and experimental data. It was shown that, in order to reproduce the correct shoaling through the cross-shore array of the rip channel, the effects of currents on waves have to be taken into account. It was also observed that in the same cross-shore array, when effects of currents are taken into account on waves propagation, waves tend to break earlier than which is observed in data.

Over the bar a sudden, strong breaking occurs. The generated dissipation gradients between the bar and the channel induce longshore pressure gradients that in turn induce feeder currents which converge in the channel. These features generate a recirculation cell between the bar and the channel. Furthermore, the waves in the channel break further inshore, inducing longshore currents that flow away from the rip channel and therefore, another recirculation cell is generated.

The model showed to be capable of reproducing the overall flow patterns presented in the rip current system. Moreover, within this approach, based on the vortex force formalism, it was possible to show the distribution of the vortex force over the domain that in its turn contributes to the vortices located between the bar and the channel and near the shoreline.

Next, the vertical structure of the rip current system was also analysed. First, a section parallel to the shoreline passing through the bar and the channels was shown in order to confirm the longshore variability of the different terms of the momentum equations.

Afterwards, an analysis of the new terms included in the hydrodynamic model in the cross-shore and longshore momentum equations was made within two cross-shore arrays: one over the bar and another through the rip channel. Among the analysed terms, the most important for the longshore balance were shown to be the longshore pressure gradients and the vortex force longshore component. The cross-shore balance is mainly dominated by the momentum lost by depth-induced wave breaking together with the wave-induced and hydrostatic pressure gradients.

Finally, the vertical structure of the cross-shore component of the rip current was compared with data from Haas and Svendsen (2002). The unstable nature of the rip current was observed by imposing a smaller value of the horizontal diffusion velocity coefficient in the hydrodynamic model.

Once again, in the barred beach test-case, the horizontal diffusion velocity coefficient was set by using a simple approach (imposing a constant value along the domain). One should test different and more complex turbulence modelling approaches such as URANS (Unsteady RANS) or LES modelling in order to get a better representation of the real flow.

It was also shown that the values for the horizontal diffusion velocity coefficient, the Nikuradse roughness and taking into account the two-way effects between waves and currents influence the unstable nature of the rip current.

In general, the numerical results fit quite well the measurements obtained in the wave basin. Not only the magnitude but also the vertical shear. Offshore, the cross-shore velocity increases from the bottom towards the free surface, being directed offshore. Between the rip channel and the shoreline, the velocity sees its maximum below the bar crest elevation and starts to slightly decrease towards the free surface and bottom.

With the two tests presented, it can be concluded that the numerical model has a good performance in modelling the nearshore circulation in the coastal and surf zones, at least in a primary stage. The next purpose would be to test the coupled system with data from the field, where one has to deal more complex batymetries and some other external and non-stationary forcing terms, such wind forcing.

Chapter 7

Concluding remarks

7.1 Summary of the main goals of the thesis

The main goal of this thesis was to study and model the effects of waves-current interactions at local and regional scales. Therefore the thesis was divided into two parts.

In the first part of the thesis, the main objective was to improve our knowledge of the changes in vertical profiles of mean horizontal velocity and amplitude of orbital horizontal velocity for waves as well as shear stresses when waves are superimposed on currents. Furthermore we wished to get a better representation of these subscale phenomena for possible coastal and harbour applications.

For that purpose the *Code_Saturne* software (Archambeau et al., 2004), an advanced CFD solver based on the RANS (Reynolds Averaged Navier-Stokes) equations, was used. The Arbitrary Lagrangian-Eulerian (ALE) method was used to model the time-varying free surface dynamics. Some adaptations had to be made in order to make the code suitable to model the effects of the combined flow (waves + currents) in a numerical flume. Therefore the waves and currents were modelled simultaneously, including turbulence effects. Since the turbulence closure model plays an important role in the numerical results, a sensitivity analysis was made between the $k-\varepsilon$, $k-\omega$ and $R_{ij}-\varepsilon$ models to compare their results and see which would be more appropriate to model this kind of flows.

In the second part of the thesis, the numerical modelling of waves and currents interactions was also addressed, but following another approach. Instead of solving simultaneously the total motion, a separation is made between the waves and the current components. The main goal was to develop a numerical tool capable of reproducing the combined flow at a nearshore scale. The objective was focused on characterizing the hydrodynamics in coastal waters, particularly in the generation of currents induced by breaking waves. For that purpose, a new coupled system using a three-dimensional (3D) hydrodynamic model, TELEMAC-3D (Hervouet, 2007) and a spectral wave model, TOMAWAC (Benoit et al., 1996) was developed. Sensitivity analyses were made in order to assess the influence of the parameterizations included in the coupled system to take into account the effects of the waves on the mean flow.

7.2 Overview of results of the study at local scale

In the local analysis, where a CFD code was used, the results of the numerical simulations were compared to the experimental data of Klopman (1994) and Umeyama (2005). Four different hydrodynamic conditions were considered: only currents, only waves, waves following currents, and waves opposing currents. Particular attention was paid to the vertical profiles of the mean flow velocity, as well as the amplitude of the horizontal orbital velocity and Reynolds shear stress for each of the test cases.

After a sensitivity test regarding the most appropriate turbulence closure model to simulate this kind of flows it was concluded that the second order turbulence model $R_{ij} - \varepsilon$ SSG version by Speziale et al. (1991) gave quite good results. This turbulence model has the great advantage of solving the Reynolds stresses directly and no *a priori* assumptions are made relatively to the eddy viscosity distribution.

A boundary condition for the turbulence dissipation had to be imposed at the free surface. The turbulence dissipation at the free surface by Celik and Rodi (1984) was implemented and allowed to reproduce correctly the vertical profile of the Reynolds shear stress and turbulence viscosity.

The various comparisons showed that the model is capable of resolving the vertical structure of the combined flow. The model reproduces well the change in the vertical gradient of the mean horizontal velocity profile caused by the presence of waves following or opposing a mean flow. When waves are superimposed in the same direction as the current, there is a significant reduction in the mean horizontal velocity near mid-depth. When waves propagate in the opposite direction from the current, the vertical shear of the horizontal velocity increases. These effects are caused by wave induced stresses, non-uniformity of the flow and secondary currents.

A linear extrapolation was applied to the mean horizontal velocities vertical profiles estimated from the *Code_Saturne* model. The values for which the mean horizontal velocity is zero are then obtained. It was observed that those values were higher than the initially imposed physical roughness (z_0), both for the waves following and waves opposing the currents cases. This effect is a common feature of the wave and current combined environments. This is equivalent to an enhanced roughness which is modelled as the so-called apparent roughness.

It is worth to point out that, as a consequence of using a *High Reynolds* number modelling strategy in *Code_Saturne* (i.e. a wall function is used in the vicinity of the bottom), the model is not able to fully resolve the bottom boundary layer.

When comparing the model with experiments by Umeyama (2005), it could be seen that with the superposition of waves and currents, regardless of if they were opposing or went in the the same direction, there was a reduction in Reynolds shear stress observed not only near the bottom, but also throughout the water column.

Since the $R_{ij} - \epsilon$ turbulence closure model offers the advantage of solving for the turbulence dissipation and Reynolds stresses, it was also attempted to exploit the numerical results of the second-order scheme to propose a simple parametrization of the turbulence viscosity profile as a function of the Ursell number and elevation from the bottom.

The knowledge gained from this study on the effects of wave-current interaction at local scale was shown to have a great advantage in the subsequent steps when modelling waves and currents interactions at a regional scale.

7.3 Overview of results of the study at regional scale

After a literature review about the different theories to describe the wave-current environment it was decided to pursuit the work on the basis of the theoretical framework recently proposed by Ardhuin et al. (2008b). The hydrodynamic model TELEMAC-3D was adapted to include the simplified equations from Bennis and Ardhuin (2011) derived from the formulation by Ardhuin et al. (2008b), the so-called glm2z-RANS equations.

The implementation was first validated against an adiabatic test proposed in Bennis and Ardhuin (2011). The main features in the variation of wave heights and mean flow induced by the wave propagation and consequent Stokes drift on a slope were verified.

The coupled system was then tested against measurements obtained from two kinds of laboratory experiments. First, the coupled model is applied to a plane beach test-case where longshore currents are induced by wave breaking. Comparisons were made between numerical results and experimental data obtained from the Large Scale Sediment Transport Facility (LSTF) at the US Army Engineer Research and Development Centers Coastal and Hydraulics Laboratory (Hamilton and Ebersole, 2001), Vicksburg, USA. Second, experimental data obtained on a barred beach with rip channels (Haas and Svendsen (2002), Haas and Svendsen (2002)) was used to test the capability of the coupled system to reproduce the structure of rip currents.

Therefore, additional parameterizations were included to take into account the non-conservative forces, namely the wave induced breaking, the bottom friction induced dissipation and the wave-enhanced vertical mixing.

A number of conclusions can be drawn from the tests we have realized.

First, the capability of the model to reproduce the longshore current induced by obliquely incident waves breaking on the plane beach was shown to be successful. Not only the magnitude, but also the evolution of the longshore current, obtained at one third of the water depth from the bottom, in a cross-shore array, was well modelled by the coupled system. Additionally, a good reproduction of the evolution of the significant wave height and mean surface elevation, including the wave set-up, was obtained.

Furthermore, the vertical structure of the two components of the mean flow obtained by the numerical results fit well the experimental data. While the longshore current does not show a relevant shear throughout the water depth, the opposite is found for the cross-shore component. An onshore current was observed near the free surface while an offshore oriented current, the undertow, was verified near the bottom. The strong shear of the vertical cross-shore velocities seen in the results confirms the importance of working within a 3D framework. For instance, in this test case, to model the sediment transport in an accurate way it would be essential to take into account the strong undertow that occurs near the bed.

A sensitivity test was made, forcing the radiation stress induced forces to be distributed uniformly along the water depth in the hydrodynamic model. As the Stokes drift is not included within this approach, a zero cross-shore velocity is found. Moreover, the vertical distribution of the longshore current was significantly degraded in comparison with the new implementation, confirming thus the improvement brought by the present work.

Additionally, the importance and relevance of some of the effects included in the coupled system were assessed. It was found that the bottom friction model can have a strong influence on the magnitude of the lonsghore current. The inclusion of the bottom streaming shows some differences and improvements within the bottom boundary layer.

A sensitivity analysis was also made regarding the choice of the turbulence closure model. A great improvement in results is observed when either versions of $k-\varepsilon$ or $k-\varepsilon$ LP models are applied comparatively to the use of Nezu and Nakagawa and Prandtl models.

Nevertheless, more complex turbulence closure models, such as second order closure models, should be tested to see the impact on the numerical results.

In what concerns the modified bottom friction coefficient to take into account the effects of the interaction between waves and currents, no differences were observed when this option was activated. The observed similarities can be due to the small value of the bottom roughness in the wave basin, for which probably no significant changes occur with the inclusion of the effect of waves.

Regarding the second test case, relative to the rip current system, comparisons of the cross-shore distribution of wave height and of mean surface elevation were made with data from Haller et al. (2002). A good agreement was found between numerical results and experimental data. It was shown that, in order to reproduce the correct shoaling through the cross-shore array that passes in the channel, the effects of currents have to be taken into account. Nevertheless, it was also observed that in the same cross-shore array, when effects of currents on wave propagation are taken into account, waves break more offshore compared to what is observed in the data. This is possibly caused by a stronger opposing rip current generated in the numerical model that induces this early wave breaking.

Over the bar a sudden and strong breaking occurs. These different wave breaking patterns between the bar and the channel induce longshore pressure gradients. The latter induce feeder currents which converge in the channel. These features generate a recirculation cell in the longshore direction between the bar and the channel. Another recirculation cell is located between the bar and the shoreline, caused by the fact that waves break more progressively through the channel. When the waves break close to the shoreline, they will induce longshore currents near the beach.

Within the vortex force approach, there is the great advantage of distinguishing the vorticity effects, which cannot be done when the radiation stress approach is used.

Finally, the vertical structure of the rip currents was compared with data from Haas and Svendsen (2002). The numerical results fit quite well the measurements obtained in the wave basin, not only the magnitude of cross-shore current velocities but also the vertical shear. Offshore, the cross-shore velocity increases from the bottom towards the free surface, being directed offshore. In the region between the bars and the shoreline, the velocity reaches its maximum below the bar crest level and starts to slightly decrease towards the free surface and bottom. The unstable nature of the rip currents was obtained by imposing a smaller value of the horizontal diffusion velocity coefficient than the one initially imposed to compare with data from Haller et al. (2002).

Here, the horizontal diffusion velocity coefficient was set by using a simple approach (imposing a constant value along the domain). Different and more complex turbulence modelling approaches should be tested.

An analysis was made of the cross-shore and longshore dynamics of the flow in the two test cases and the main contributions were found.

In the case of the longshore current generation induced be breaking waves, the bottom friction induced wave dissipation, the longshore vortex force component and the momentum flux lost by depth-induced wave breaking are the main contributions to longshore balance.

For the rip current system, among the analysed terms, the most important for the longshore balance were shown to be the longshore pressure gradients and the vortex force longshore component. The cross-shore balance is mainly dominated by the momentum lost by depth-induced wave breaking together with the wave induced and hydrostatic pressure gradients.

Furthermore, the set of equations implemented in the coupled system offers the great advantage of getting a complete description of the flow. It was possible to analyse either the quasi-Eulerian current (comparable with measurements at fixed locations) and the Lagrangian mean current used in several applications.

As a general conclusion, through this work it was possible to understand the different processes present in hydrodynamic circulation in nearshore and coastal areas as well as to get a good prediction of the 3D structure of wave-induced currents.

7.4 Perspectives

Regarding the combined waves + flow simulation with a CFD solver (first part of the thesis), some improvements could be made. First, the implementation of an active wave absorber would be desirable, in order to be able to reduce the computational domain and thus the computational time cost. It would be also necessary to run parallel computation to reduce the simulation time. *Code_Saturne* offers this possibility.

Furthermore, the effects of some numerical parameters were not explored in *Code_Saturne*, which could improve the efficiency of the model. Moreover, the turbulence closure models were used with their default options and parameters. If some numerical aspects are tuned, some differences could be found on the numerical results.

Another constraint in this project was to apply *High Reynolds* number models as turbulence closure models. Near the bottom, the mesh grid size could not be too refined and a wall function had to be used to bridge the viscous sublayer near the wall. To improve the prediction within the bottom boundary layer it would be recommendable to apply *Low Reynolds* number models for which a finer grid near the bottom needs to be used.

Also a further analysis of the results should be made in order to find more parameterizations (such as the one found for the turbulence viscosity) to describe some of the phenomena that manifest during the wave and current interactions. These parameterizations could then be applied to large-scale models. One of our results in this directions is a simple turbulence viscosity parameterization regarding non-breaking waves propagating on a turbulent current.

In what concerns the coupled waves/flow simulations (second part of the thesis), it should be noted that Ardhuin et al. (2008b) state that their set of equations, approximated up to second order, can show some limitations in the surf zone due to the strong non-linearities found in that region. Furthermore, it should be noted that the set of equations implemented in the coupled system were made following the approach proposed by Ardhuin et al. (2008b) together with the simplifications made by Bennis and Ardhuin (2011). Here, the vertical current shear is ignored within the wave forcing terms. A first step in improving the coupled system could be the inclusion of this vertical current shear.

Furthermore, the non-conservative forces induced by the wave field, such as the momentum lost by waves due to depth-induced breaking and bottom friction were imposed as surface and bottom stresses in the hydrodynamic 3D model. Their vertical distribution could be tested throughout the water depth to see the influence on the numerical results.

In terms of the vertical mixing, a simple parameterization was used to take into account the wave breaking effect on the near free surface mixing. This effect shows to have a significant role on the vertical distribution of the mean flow (Bennis et al., 2012). In our case, it did not show such significant differences. A sensitivity analysis on the chosen empirical values used in the implemented parameterization should be made. Moreover, different parametrizations should be tried or the turbulence closure model should be improved to take those effects into account in a more precise way.

Additionally, in the second part of the thesis, the applied turbulence modelling approach is quite simple (a constant value was imposed for the horizontal diffusion velocity coefficient). More tests and analysis should be made to see the impact on the numerical results when using more complex turbulence modelling approaches, such as second order turbulence closure models, URANS or LES models.

The analysis with tracers was not done due to the nature of validation tests that were used. Nevertheless, it is essential to validate and verify the numerical results of the coupled system with data from the field. More complex bathymetries could be tested, the effect of wind could be taken into account and therefore also the whitecapping effect. For that purpose, it would also be desirable to make the computations paralleled to reduce the computational time cost. TOMAWAC offers this possibility in the most recent release.

The coupled system developed can be used not only to study wave-current interaction, as in this work, but also for the analysis and understanding of other phenomena or risks in the nearshore zone. For instance, another possible application for this coupled system could be the study of particle drift on the surface ocean such as cases where oil spills occur, or where radioactive particles are released during a nuclear disaster.

Also, the following step after this coupling between the hydrodynamic model TELEMAC-3D and spectral wave model TOMAWAC, could be the coupling with a sediment transport module, such as SISYPHE (also integrated in the TELEMAC-MASCARET system). Therefore, a complete description of the sediment transport could be possible, allowing to model the morphodynamics of the coastal zone. Finally, an atmospheric module could also be included to get a complete numerical platform.

References

Andrews, D. G., McIntyre, M. E., 1978a. An exact theory of nonlinear waves on a Lagrangian mean flow. Journal of Fluid Mechanics, Vol. 89, pp 609-646.

Andrews, D. G., McIntyre, M. E., 1978b. On wave-action and its relatives. Journal of Fluid Mechanics, Vol. 89, pp 647-664.

Apsley, D., Hu, W., 2003. CFD simulation of two- and three-dimensional free-surface flow. International Journal for Numerical Methods in Fluids, Vol. 42, pp 465-491.

Archambeau, F., Guimet, V., Bastin, G., 1999. Application du prototype de module ALE du Solveur Commun à des cas de surface libre. Technical report EDF HE-41/99/054/A, EDF Research and Development, Chatou, France (in French).

Archambeau, F., Méchitoua, N., Sakiz, M., 2004. Code_Saturne: a finite volume method for the computation of turbulent incompressible flows - industrial applications. International Journal on Finite Volumes, Vol. 1 (1), pp 1-62.

Ardhuin, F., 2006. On the momentum balance in shoaling gravity waves : Comment on "Shoaling surface gravity waves cause a force and a torque on the bottom" by K. E. Kenyon. Journal Oceanography, Vol. 62, pp 917-922.

Ardhuin, F., Jenkins, D., Belibassakis, K. A., 2008a. Commentary on "The Three-Dimensional Current and Surface Wave Equations" by George Mellor. Journal of Physical Oceanography, Vol. 38, pp 1340-1350.

Ardhuin, F., Rascle, N., Belibassakis, K. A., 2008b. Explicit wave-averaged primitive equations using a generalized Lagrangian mean. Ocean Modelling, Vol. 20 (1), pp 35-60.

Ardhuin, F., Rogers, E., Babanin, A. V., Filipot, J. F., Magne, R., Roland, A., van der Westhuysen, A., Queffeulou, P., Lefevre, J. M., Aouf, L., Collard, F., 2010. Semi-empirical dissipation source functions for wind-wave models: part I, definition, calibration and validation at global scales. Journal of Physical Oceanography, doi :10.1175/2010JPO4324.1.

Battjes, J., Sobey, R., Stive, M., 1990. Nearshore circulation. The Sea, Ocean Engineering Science, Vol. 9, Part A, Edited by B. Le Mehaute and D.M. Hanes, Wiley-Interscience Publication, pp 467-493.

Bennis, A., Ardhuin, F., 2011. On the coupling of wave and three-dimensional circulation models: Choice of theoretical framework, practical implementation and adiabatic tests. Ocean Modelling, Vol. 40 (3-4), pp 260-272.

Bennis, A., Dumas, F., Ardhuin, F., Blanke, B., 2012. Mixing and bottom friction: parameterization and application to the surf zone. Geophysical Research Abstracts, Vol. 14, EGU2012 - 11929-1.

Benoit, M., Marcos, F., Becq, F., 1996. Development of a third generation shallow water wave model with unstructured spatial meshing. Proc. 25^{th} International Conference on Coastal Engineering (ICCE′1996), 2-6 September 1996, Orlando (Florida, USA), pp 465-478.

Blumberg, A., Mellor, G., 1987. A description of a three-dimensional coastal ocean circulation model. In: Heaps, N.S. (Ed.), Three-Dimensional Coastal Ocean Models, Coastal Estuarine Science. American Geophysical Union, pp 1-16.

Bolanos, R., Osuna, P., Wolf, J., Monbaliu, J., Sanchez-Arcilla, A., 2011. Development of the POLCOMS-WAM current-wave model. Ocean Modelling Vol. 36, pp 102-115.

Booij, N., Ris, R. C., Holthuijsen, L. H., 1996. The SWAN wave model for shallow waters. Proc. 25^{th} International Conference on Coastal Engineering (ICCE′1996), 2-6 September 1996, Orlando (Florida, USA), pp 668-676.

Boussinesq, J., 1877. Essai sur la théorie des eaux courantes. Mémoires présentés par divers savants à l′Académie des Sciences 23 (1): pp 1-680 (in French).

Bruneau, N., 2009. Modélisation morphodynamique des plages sableuses. Ph.D. thesis, Universite Bordeaux I (in French).

Bühler, S., McIntyre, M., 1998. On non-dissipative wave-mean interactions in the atmosphere or oceans. Journal of Fluid Mechanics, Vol. 354, pp 301-343.

Burchard, H., Bolding, K., 2002. GETM- a general estuarine transport model. Scientific documentation. Tech. Rep., EUR 20253 EN, European Commission.

Castelle, B., Michallet, H., Marieu, V., Leckler, F., Dubardier, B., Lambert, A., 2010. Laboratory experimetn on rip current circulations over a moveable bed: Drifter measurements. Journal of Geophysical Research, Vol. 115 (C12008).

Celik, I., Rodi, W., 1984. Simulation of free surface effects in turbulent channel flows. Physicochemical Hydrodynamics, Vol. 5, pp 217-227.

Chang, 1969. Mass transport in deep-water long-crested random gravity waves. Journal of Geophysical Research, Vol. 74, pp 1515-1536.

Chawla, A., Kirby, J., 2002. Monochromatic and random wave breaking at blocking points. Journal of Geophysical Research, Vol. 107 (C7), 3067.

Christoffersen, J. B., Jonsson, I. G., 1985. Bed friction and dissipation in a combined current and wave motion. Ocean Engineering, Vol. 12, pp 387-423.

Code_Saturne documentation, 2013. Code_Saturne 3.0.0 Theory Guide (www.code-saturne.org/cms/).

Cozzi, O., 2010. Free surface flow simulation: correcting and benchmarking the ALE method in Code_Saturne. M.Phil. thesis, University of Manchester, UK.

Craig, P. D., Banner, M. L., 1994. Modeling wave-enhanced turbulence in the ocean surface layer. Journal of Physical Oceanography, Vol. 24 (12), pp 2546-2559.

Craik, A. D. D., Leibovich, S., 1976. A rational model for Languimir circulations. Journal of Fluid Mechanics, Vol. 73, pp 401-426.

Dalrymple, R. A., 1975. A mechanism for rip current generation on an open coast. Journal of Geophysical Research, Vol. 80, pp 3485-3487.

Dean, R. G., Dalrymple, R. A., 1991. Water wave mechanics for engineers and scientists. Advanced Series Ocean Engineering, Vol. 2, World Scientific.

Delft3D-FLOW, 2012. Delft3D-FLOW User Manual, Deltares (http://www.deltares.nl/en).

Delpey, M., 2012. Étude de la dispersion horizontale en zone littorale sous l′effet de la circulation tridimensionelle forcée par les vagues. PhD thesis, Université de Bretagne Occidentale, France (in French).

Dingemans, M. W., 1997. Water wave propagation over uneven bottoms. Part 1 - Linear Wave propagation. World Scentific, Vol. 13.

Dingemans, M. W., van Kester, J. A. T. M. V., Radde, A. C., Uittenbogaard, R. E., 1996. The effect of the CL-vortex force in 3D wave current interaction. Proc. 25^{th} International Conference on Coastal Engineering (ICCE′1996), Orlando (Florida, USA), pp 4821-4832.

Donelan, M. A., 1998. Air-water exchange processes. Physical processes in Lakes and Oceans, Vol. 27, pp 18-36.

Dore, B. D., 1978. Some effects of the air-water interface on gravity waves. Geophysics Astrophysics Fluid Dynamics, Vol. 10, pp 215-230.

Flather, R. A., 1976. Results from surge prediction model of the North-West European continental shelf for April, November and December 1973. Institute of Oceanography (UK), Report n 24.

Fredsœ, J., 1984. Turbulent boundary layer in wave-current motion . Journal of Hydraulic Engineering, ASCE 110, pp 1103-1120.

Fredsœ, J., Andersen, K. H., Mutlu Sumer, B., 1999. Wave plus currents over a ripple-covered bed. Coastal Engineering, Vol. 38, pp 177-221.

Garret, C., 1976. Generation of Langmuir circulations by surface waves - a feedback mechanism. Journal of Marine Research, Vol. 34, pp 117-130.

Grant, W. D., Madsen, O. S., 1979. Combined wave and current interaction with a rough bottom. Journal of Geophysical Research, Vol. 84 (C4), pp 1797-1808.

Groeneweg, J., 1999. Wave-Current Interactions in a Generalized Lagrangian Mean Formulation. PhD thesis, Delft University of Technology, The Netherlands.

Groeneweg, J., Battjes, J. A., 2003. Three dimensional wave effects on a steady current. Journal of Fluid Mechanics, Vol. 478, pp 325-343.

Groeneweg, J., Klopman, G., 1998. Changes of the mean velocity profiles in the combined wavecurrent motion described in a GLM formulation. Journal of Fluid Mechanics, Vol. 370, pp 271-296.

Guimet, V., Laurence, D., 2002. A linearised turbulent production in the $k-\epsilon$ model for engineering applications. 5^{th} International Symposium on Engineering Turbulence Modelling and Measurements, Mallorca, Spain, W. Rodi & N. Fueyo Edts, Elsevier.

Haas, K. A., Svendsen, I., 2002. Laboratory measurements of the vertical structure of rip currents. Journal of Geophysical Research, Vol. 107 (C5), 3047.

Haas, K. A., Svendsen, I., Haller, M., Zhao, Q., 2003. Quasi-three-dimensioal modeling of rip current systems. Journal of Geophysical Research Vol. 108 (C7), 3217.

Haas, K. A., Svendsen, I. A., Haller, M. C., 1998. Numerical modeling of nearshore circulation on a barred beach with rip channels. Coastal Engineering: Proceedings of the 26^{th} International Conference, pp 801-814, Am. Soc. of Civ. Eng., New York.

Haas, K. A., Warner, J. C., 2009. Comparing a quasi-3D to a full 3D nearshore circulation model: SHORECIRC and ROMS. Ocean Modelling, Vol. 26, pp 91-103.

Haller, M. C., Dalrymple, R. A., 2001. Rip current instabilities. Journal of Fluid Mechanics, Vol. 443, pp 161-192.

Haller, M. C., Dalrymple, R. A., Svendsen, I. A., 2002. Experimental study of nearshore dynamics on a barred beach with rip channels. Journal of Geophysical Research, Vol. 107 (C6), 3061.

Hamilton, D. G., Ebersole, B. A., 2001. Establishing uniform longshore currents in a large scale sediment transport facility. Coastal Engineering, Vol. 42, pp 199-218.

Hamilton, D. G., Neilans, P. J., Rosati, J. D., Fowler, J. E., Smith, J. M., 1997. Hydraulic design of a large-scale longshore current recirculation system. Proc. Coastal Dynamics, Plymouth, United Kingdom, ASCE, pp 516-525.

Hasselmann, K., 1971. On the mass and momentum transfer between short gravity waves and larger-scale motions. Journal of Fluid Mechanics, Vol. 50, pp 189-205.

Hasselmann, K., Barnett, T. P., Bouws, E., Carlson, H., Cartwright, D. E., Enke, K., Ewing, J. A., Gienapp, H., Hasselmann, D. E., Kruseman, P., Meerburg, A., Muller, P., Olbers, D. J., Richter, K., Sell, W., Walden, H., 1973. Measurements of wind-wave growth and swell decay during the Joint North Sea Wave Project (JONSWAP). Deutschen Hydrographischen Zeitschrift, Reihe A (8), N12.

Hervouet, J.-M., 2007. Hydrodynamics of free surface flows, modelling with the finite element method. Editions Wiley and Sons.

Holmedal, L. E., Myrhaug, D., Rue, H., 2003. The sea bed boundary layer under random waves plus current. Continental Shelf Research, Vol. 23 (7), pp 717-750.

Holmedal, L. E., Myrhaug, D., Rue, H., 2009. Wave-induced steady streaming, mass transport and net sediment transport in rough turbulent ocean bottom boundary layers. Continental Shelf Research, Vol. 29, pp 911-926.

Holt, J. T., James, I. D., 2001. An s coordinate density evolving model of the northwest European continental shelf: 1, Model description and density structure. Journal of Geophysical Research, Vol. 106, pp 14015-14034.

Houwman, K. T., van Rijn, L. C., 1999. Flow resistance in the coastal zone. Coastal Engineering, Vol. 38, pp 261-273.

Huang, Z., Mei, C. C., 2003. Effects of surface waves on a turbulent current over a smooth or rough seabed. Journal of Fluid Mechanics, Vol. 497, pp 253-287.

Jenkins, A. D., 1987. Wind and wave induced currents in a rotating sea with depth-varying eddy viscosity. Journal of Physical Oceanography, Vol. 17, pp 938-951.

Jenkins, A. D., 1989. The use of a wave-prediction model for driving a near-surface current model. Deutsche Hydrographische Zeitschrift, Vol. 42, pp 133-149.

Kemp, P. H., Simons, R. R., 1982. The interaction between waves and a turbulent current: waves propagating with the current. Journal of Fluid Mechanics, Vol. 116, pp 227-250.

Kemp, P. H., Simons, R. R., 1983. The interaction between waves and a turbulent current: waves propagating against the current. Journal of Fluid Mechanics, Vol. 130, pp 73-89.

Kennedy, A., Zhang, Y., 2008. The stability of wave-driven rip current circulation. Journal of Geophysical Research, Vol. 113 (C3).

Klopman, G., 1994. Vertical Structure of the flow due to waves and currents: laser-Doppler flow measurements for waves following or opposing a current. Progress report H840.30 PartII, Delft Hydraulics, Delft.

Klopman, G., 1997. Secondary circulation of the flow due to waves and current: laser-Doppler flow measurements for waves following or opposing a current. Techincal Report, Delft Hydraulics Z2249, Delft.

Kumar, N., Voulgaris, G., Warner, J., 2011. Implementation and modification of a 3-D radiation stress formulation for surf zone and rip-current applications. Coastal Engineering, Vol. 58 (12), pp 1097-1117.

Kumar, N., Voulgaris, G., Warner, J., Olabarrieta, M., 2012. Implementation of the vortex force formalism in the coupled ocean-atmosphere-wave-sediment transport (COAWST) modeling system for inner shelf and surf zone applications. Ocean Modelling, Vol. 47, pp 65-95.

Lane, E. M., Restrepo, J. M., McWilliams, J. C., 2007. Wave-currents interaction: a comparison of radiation-stress and vortex-force representations. Journal of Physical Oceanography, Vol. 37, pp 1122-1141.

Launder, B. E., Reece, G. J., Rodi, W., 1975. Progress in the Development of a Reynolds-Stress Turbulent Closure. Journal of Fluid Mechanics, Vol. 68, Part 3, pp 537-566.

Launder, B. E., Spalding, D. B., 1974. The Numerical Computation of Turbulent Flow. Computer Methods in Applied Mechanics and Engineering, Vol. 3, pp 269-289.

Lazure, P., Dumas, F., 2008. An external-internal mode coupling for a 3D hydrodynamical model for applications at regional scale (MARS). Advances in Water Resources Vol. 31, pp 233-250.

Lewis, J. K., 1997. A three-dimensional ocean circulation model with wave effects. In: Spaulding, M.L., Blumberg, Af.F. (Eds.), Proceedings of the Fifth International Conference on Estuarine and Coastal Modelling, Alexandria, VA. American Society of Civil Engineers, Reston, VA, pp 584-600.

Longuet-Higgins, M. S., 1953. Mass transport in water waves. Philosophical Transactions of the Royal Society of London, Vol. 245, pp 535-581.

Longuet-Higgins, M. S., 1967. On the wave-induced difference in mean sea level between the two sides of a submerged breakwater. Journal of Marine Research, Vol. 25, pp 148-153.

Longuet-Higgins, M. S., 1970. Longshore Currents Generated by Obliquely Incident Sea Waves, 1. Journal of Geophysical Research, Vol. 75 (33), pp 6778-6789.

Longuet-Higgins, M. S., Stewart, R. W., 1961. The changes in amplitude of short gravity waves on steady non-uniform currents. Journal of Fluid Mechanics, Vol. 10, pp 529-549.

Longuet-Higgins, M. S., Stewart, R. W., 1962. Radiation stress and mass transport in gravity waves, with applications to surf beats. Journal of Fluid Mechanics, Vol. 13, pp 481-504.

Longuet-Higgins, M. S., Stewart, R. W., 1964. Radiation stresses in water waves: a physical discussion with applications. Deep Sea Research, Vol. 11, pp 529-562.

Lundgren, H., 1972. Turbulent currents in the presence of waves,. Proc. 13^{th} International Conference on Coastal Engineering (ICCE$'$1972), Vancouver (Canada), pp 623-634.

Marsaleix, P., Estournel, C., Kondrachoff, V., Vehil, R., 1998. A numerical study of the formation of the Rhone river plume. Journal of Marine Systems, Vol. 14 , pp 99-115.

Martins, F., 2000. Modelação matemática tridimensional de escoamentos costeiros e estuarinos usando uma abordagem de coordenada vertical generica. Ph.D. thesis, Instituto Superior Técnico, Lisbon, Portugal (in Portuguese).

McWilliams, J. C., Restrepo, J. M., Lane, E. M., 2004. An asymptotic theory for the interaction of waves and currents in coastal waters. Journal of Fluid Mechanics, Vol. 511, pp 135-178.

Mei, C. C., 1989. The Applied Dynamics of Ocean Surface Waves. World Scentific, Vol. 1, 738 pp.

Mellor, G., 2003. The Three-Dimensional Current and Surface Wave Equations. Journal of Physical Oceanography, Vol.33, pp 1978-1989.

Mellor, G., 2005. Some consequences of the three-dimensional currents and surface wave equations. Journal of Physical Oceanography, Vol.35, pp 2291-2298.

Mellor, G., 2008. The depth-dependent current and wave interaction equations : A revision. Journal of Physical Oceanography, Vol.38, pp 2587-2596.

Mellor, G., 2011a. Corrigendum. Journal of Physical Oceanography, Vol. 41, pp 1417-1418.

Mellor, G., 2011b. Wave radiation stress. Ocean Dynamics, Vol. 61, pp 563-568.

Mellor, G., 2013. Waves, circulation and vertical dependence. Ocean Dynamics, Vol. 63, pp 447-457.

Menter, F. R., 1994. Two-equation eddy-viscosity turbulence models for engineering applications. AIAA Journal, Vol. 32 (8), pp 1598-1605.

Michaud, H., Marsaleix, P., Leredde, Y., Estournel, C., Bourrin, F., Lyard, F., Mayet, C., Ardhuin, F., 2012. Three-dimensional modelling of wave-induced current from the surf zone to the inner shelf. Ocean Sciences, Vol. 8, pp 657-681.

Moghimi, S., Klingbeil, K., Gräwe, U., Burchard, H., 2013. A direct comparison of a depth-dependent Radiation stress formulation and a Vortex force formulation within a three-dimensional coastal ocean model. Ocean Modelling, Vol. 70, pp 132-142.

Muzaferija, S., Peric, M., 1997. Computation of free-surface flows using the finite-volume method and moving grids. Numerical Heat Transfer, Part B, Vol. 32, pp 369-384.

Newberger, P. A., Allen, J. S., 2007a. Forcing a three-dimensional, hydrostatic primitive-equation model for application in the surf zone, 1: Formulation. Journal of Geophysical Research, Vol. 112 (C08018).

Newberger, P. A., Allen, J. S., 2007b. Forcing a three-dimensional, hydrostatic primitive-equation model for application in the surf zone, 2. Application to DUCK94. Journal of Geophysical Research, Vol. 112 (C08019).

Nezu, I., Nakagawa, H., 1993. Turbulence in Open-Channel Flows, A.A. Balkema, Rotterdam. CRC Press.

Nezu, I., Rodi, W., 1986. Open channel flow measurements with a laser Doppler anmometer. Journal of Hydraulic Engineering, Vol. 112 (5), pp 335-355.

Nielsen, P., You, Z., 1996. Eulerian mean velocities under non-breaking waves on horizontal bottoms. Proc. 25^{th} International Conference on Coastal Engineering (ICCE$'$1996), Orlando (Florida, USA), pp 4066-4078.

Olabarrieta, M., Medina, R., Castanedo, S., 2010. Effects of wave-current interaction on the current profile. Coastal Engineering, Vol. 57 (7), pp 643-655.

Peregrine, D. H., Jonsson, I. G., 1983. Interaction of waves and currents. Misc. Report No 83-6 U.S. Army, Corps of Engineers, Coastal Engineering Research Center, Fort Belvior, Va, 88 pp.

Perlin, A., Kit, E., 2002. Roughness in wave-current flow: implication for coastal studies. Journal of Hydraulic Engineering, Vol. 128 (8), pp 729-741.

Phillips, O. M., 1977. The Dynamics of the Upper Ocean. Cambridge Monographs on Mechanics and Applied Mathematics, 2d ed. Cambridge University Press, Vol. 2, 336 pp.

Pierson, 1962. Perturbation Analysis of the Navier-Stokes Equations in Lagrangian Form with Selected Linear Solutions. Journal of Geophysical Research, Vol. 67 (8), pp 3151-3160.

Prandtl, L., 1925. Bericht uber die Entstehung der Turbulenz. Zeitschrift für Angewandte Mathematik und Mechanik, Vol. 5, pp 136-139.

Putrevu, U., Oltman-Shay, J., Svendsen, I. A., 1995. Effect of alongshore nonuniformities on longshore current predictions. Journal os Geophysical Research, Vol. 100, pp 16119-16130.

Putrevu, U., Svendsen, I. A., 1999. Three-dimensional dispersion of momentum in wave-induced nearshore currents. European Journal of Mechanics - B/Fluids, Vol. 18, pp 410-426.

Rascle, N., 2007. Impact of waves on the ocean circulation. PhD thesis, Université de Bretagne Occidentale, France.

Rascle, N., Ardhuin, F., Terray, E. A., 2006. Drift and mixing under the ocean surface : A coherent one-dimensional description with application to unstratified conditions. Journal of Geophysical Research, Vol. 111 (C3), pp 1-16.

Reynolds, O., 1895. On the dynamical theory of incompressible viscous flows and the determination of the criterion. Philosophical Transactions of the Royal Society, London Ser. A 186, pp 123-161.

Ris, R. C., Holthuijsen, L. H., 1996. Spectral modeling of current induced wave-blocking. Proc. 25^{th} Int. Conf. on Coastal Eng., pp 1246-1254.

Roland, A., Zhang, Y. J., Wang, H. V., Meng, Y., Teng, Y. C., Maderich, V., Brovchenkod, I., Dutour-Sikiric, M., Zanke, U., 2012. A fully coupled 3D wave-current interaction model on unstructured grids. Journal of Geophysical Research, Vol. 117 (C00J33).

Roseau, M., 1976. Asymptotic wave theory. Elsevier.

Shchepetkin, A. F., McWilliams, J. C., 2005. The regional oceanic modeling system (ROMS) : a split-explicit, free-surface, topography-following-coordinate oceanic model. Ocean Modelling, Vol. 9 (4), pp 347-404.

Sheng, Y., Liu, T., 2011. Three-dimensional simulation of wave-induced circulation: comparison of three radiation stress formulations. Journal of Geophysical Research, Vol. 116 (C5).

Sheng, Y. P., 1986. A three-dimensional numerical model of coastal and estuarine circulation and transport in generalized curvilinear grids. Tech. Rep. 587, 255 pp., Aeronaut. Res. Assoc. of Princeton, Princeton, N. J.

Smagorinsky, J., 1963. General simulation experiments with the primitive equations. Monthly Weather Review, Vol. 91, pp 99-164.

Smith, J., 2006. Wave-Current Interactions in Finite Depth. Journal of Physical Oceanography, Vol. 36 (7), pp 1403-1419.

Song, T., 1994. Velocity and turbulence distribution in non-uniform and unsteady open-channel flow. PhD thesis, École Polytechnique Fédéral de Lausanne, Switzerland.

Soulsby, R., Hamm, L., Klopman, G., Myrhaug, D., Simons, R., Thomas, G., 1993. Wave current interaction within and outside the bottom boundary layer. Coastal Engineering, Vol. 21, pp 41-69.

Spalart, P. R., Allmaras, S. R., 1992. A One-Equation Turbulence Model for Aerodynamic Flows. AIAA Paper 92-0439.

Speziale, C. G., Sarkar, S., Gatski, T. B., 1991. Modeling the pressure-strain correlation of turbulence: an invariant dynamical systems approach. Journal of Fluid Mechanics, Vol. 227, pp 245-272.

Stokes, J., 1847. On the theory of oscillatory waves. Transactions of the Cambridge Philosophical Society, Vol. 8 (441), pp 441-455.

Tang, C. L., Perrie, W., Jenkins, A. D., DeTracey, B. M., Hu, Y., Toulany, B., Smith, P. C., 2007. Observation and modelling of surface currents on the Grand Banks: a study of the wave effects on surface currents. Journal of Geophysical Research, Vol. 112 (C10).

TELEMAC modelling system documentation, 2004. 2D hydrodynamics, TELEMAC-2D software, User Manual (www.opentelemac.org).

Teles, M. J., Benoit, M., Pires-Silva, A. A., 2013a. Modelling combined wave-current flows using a RANS CFD solver with emphasis on the effect of the turbulence closure model. Advances in Hydroinformatics: Simhydro 2012 - New Frontiers of Simulation (38), Ed. Philippe Gourbesville, Jean Cunge and Guy Caignaert, Springer Verlag. ISBN: 978-981-4451-41-3.

Teles, M. J., Pires-Silva, A. A., Benoit, M., 2013b. Numerical modelling of waves and current interactions at a local scale. Ocean Modelling, Vol. 68, pp 72-87.

Terray, E. A., Donelan, M. A., Agrawal, Y. C., Drennan, W. M., Kahma, K. K., Williams, A. J., Hwang, P. A., Kitaigorodskii, S. A., 1996. Estimates of kinetic energy dissipation under breaking waves. Journal of Physical Oceanography, Vol. 26 (5), pp 792-807.

Thompson, K. W., 1987. Time dependent boundary conditions for hyperbolic systems. Journal of Computational Physics, Vol. 68, pp 1-24.

Thornton, E. B., Guza, R. T., 1983. Transformation of wave height distribution. Journal of Geophysical Research, Vol. 88 (C10), pp 5925-5938.

Tolman, H. L., 2002. Validation of WAVEWATCH-III version 1.15. Technical Report 213, NOAA/NWS/NCEP/MMAB.

TOMAWAC documentation, 2011. Software for sea state modelling on unstructured grids over oceans and coastal seas. release 6.1 (www.opentelemac.org).

Uchiyama, Y., McWilliams, J. C., Shchepetkin, A. F., 2010. Wave-current interaction in an oceanic circulation model with a vortex-force formalism: Application to the surf zone. Ocean Modelling, Vol. 34, pp 16-35.

Uittenbogaard, R. E., 1992. Wave forces in three dimensions. Technical Report Z553, Delft Hydraulics.

Umeyama, M., 2005. Reynolds stresses and velocity distributions in a wave-currents coexisting environment. Journal of Waterway, Port, Coastal and Ocean Engineering, Vol. 131 (5), pp 203-212.

Uribe, J. C., 2006. An industrial approach to near wall turbulence modelling for unstructured finite volume methods. PhD thesis, University of Manchester, United Kingdom.

Van Rijn, L., 2007. Unified view of sediment transport by currents and waves. I: Initiation of motion, bed roughness, and bed-load transport. Journal of Hydraulic Engineering, Vol. 133 (6), pp 649-667.

Visser, P. J., 1982. The proper longshore current in a wave basin. Communications on Hydraulics Rep., Dept. of Civil Eng. Delft Univ. of Technology, Delft, The Netherlands, 86 pp.

Visser, P. J., 1984a. A mathematical model of uniform longshore currents and the comparison with laboratory data. Report No. 84 - 2, Dept. of Civil Eng. Delft Univ. of Technology, Delft, The Netherlands, 151 pp.

Visser, P. J., 1984b. Uniform longshore current measurements and calculations. Proc. 19^{th} International Conference on Coastal Engineering (ICCE$'$1984), Houston, ASCE, pp 2192-2207.

Visser, P. J., 1991. Laboratory measurements of uniform longshore currents. Costal Engineering, Vol. 15, pp 563-593.

Walstra, D. J. R., Roelvink, J. A., Groeneweg, J., 2000. Calculation of wave driven currents in a 3D mean flow model. Coastal Engineering, pp 1-4.

WAMDI-Group, 1988. The WAM model - A third generation ocean wave prediction model. Journal of Physical Oceanography, Vol. 18, pp 1775-1810.

Warner, J. C., Sherwood, C. R., Signell, R. P., Harris, C. K., Arango, H. G., 2008. Development of a three-dimensional, regional, coupled wave, current, and sediment transport model. Computers and Geosciences, Vol. 34, pp 1284-1306.

Wilcox, D. C., 1993. Turbulence modeling for CFD. Technical report, DCW Industries Inc, La Canada, CA.

Xia, H., Xia, Z., Zhu, L., 2004. Vertical variation in radiation stress and wave-induced current. Coastal Engineering, Vol. 51, pp 309-321.

Xie, L., Wu, K., Pietrafesa, L., Zhang, C., 2001. A numerical study of wave-current interaction through surface and bottom stresses : Wind-driven circulation in the South Atlantic Bight under uniform winds. Journal of Geophysical Research, Vol. 106 (C8), pp 16841-16855.

Yang, S., Tan, S.-K., Lim, S.-Y., Zhang, S.-F., 2006. Velocity distribution in combined wave-current flows. Advances in Water Resources, Vol. 29, pp 1196-1208.

You, Z., 1996. The effect of wave-induced stress on current profiles. Ocean Engineering, Vol. 23, pp 619-628.

Yu, J., 2006. On the instability leading to rip currents due to wave-current interaction. Journal of Fluid Mechanics, Vol. 549, pp 403-428.